Technische Universität München
TUM School of Natural Sciences

Advanced Characterization Methodologies for Automotive PEM Fuel Cells

Felix Haimerl

Vollständiger Abdruck der von der TUM School of Natural Sciences der Technischen Universität München zur Erlangung eines

Doktors der Naturwissenschaften (Dr. rer. nat)

genehmigten Dissertation.

Vorsitz: Prof. Dr. Ulrich Gerland

Prüfende der Dissertation:

1. Prof. Dr. Aliaksandr Bandarenka
2. Prof. Dr. Ian Sharp

Die Dissertation wurde am 13.09.2024 bei der Technischen Universität München eingereicht und durch die TUM School of Natural Sciences am 29.10.2024 angenommen.

I dedicate this dissertation to all the incredible people who made it possible:

To **Prof. Dr. Aliaksandr Bandarenka**, thank you for providing the opportunity for this dissertation and for your insightful and efficient guidance.

To **Claudia Stephan, Thomas Mertens, and the entire team at BMW**, your guidance, supervision, and enriching discussions were invaluable. It has been a genuine pleasure working with you over these past few years.

To **Sunil Kumar, Emilio Avellone, Julian Rumpfinger, Marco Sirbescu, and Anna-Lena Gerber**, your commitment exceeded all expectations. Many of the results presented in this work are based on your efforts.

Lastly, to my family and friends, your love and support made the last few years incredibly enjoyable. **Mama, Papa, Luis, and Luana**, my life would not be the same without you.

Abstract

Appealing and economically viable electric vehicle offers are pivotal for transitioning global energy provision to renewables. In this context, fuel cell electric vehicles utilizing polymer electrolyte membrane fuel cells (PEMFCs) emerge as a promising alternative to battery electric vehicles. However, commercialization of PEMFCs necessitates a reduction in production and development costs. This study aims to broaden the scope of electrochemical impedance spectroscopy (EIS) to accelerate fuel cell testing and reduce the associated development and production costs of PEMFCs.

A novel, cost-effective setup for spatially resolved EIS within automotive-sized PEMFCs was developed, bridging theoretical simulations with practical fuel cell applications. The results reveal correlations between high current density regions and decreased proton resistance, which we attribute to elevated water production, with relative humidity playing a moderating role. Moreover, lowering the cathodic stoichiometry accentuates mass transport issues at the air outlet, while anodic stoichiometry influences performance only below a threshold value of 1.2.

Notably, we report, for the first time, localized degradation patterns during PEMFC cold starts, attributing voltage degradation to carbon corrosion and ionomer degradation. Realistic tempera-

ture gradients during cold start cycling manifest in reduced current density and proton resistance in regions subject to the lowest temperatures.

Emerging as fast and non-destructive quality testing strategies in PEMFC production, EIS conducted at low hydrogen concentration offers valuable insights into fuel cell processes. This study introduces a novel equivalent circuit model to analyze impedance spectra under low hydrogen partial pressures. The proposed model effectively characterizes impedance responses and explains the performance decline observed at reduced hydrogen concentrations. Specifically, reduced hydrogen availability at the anode introduces reaction losses, subsequently affecting potential changes and influencing cathode processes. These findings suggest that impedance spectroscopy at low hydrogen partial pressures could be a dependable fuel cell quality control tool.

This investigation extends the understanding of EIS through spatially resolved analyses, local degradation phenomena, and the impact of reduced hydrogen concentrations. Collectively, this work showcases EIS as a cost-effective asset in development and production and its potential to advance PEMFC commercialization.

Published work

Publications

F. Haimerl, S. Kumar, M. Heere and A. S. Bandarenka, Electrochemical impedance spectroscopy of PEM fuel cells at low hydrogen partial pressures: efficient cell tests for mass production, RSC Industrial Chemistry & Materials, 2024, 2, 132-140.

F. Haimerl, J. P. Sabawa, T. A. Dao and A. S. Bandarenka, Spatially Resolved Electrochemical Impedance Spectroscopy of Automotive PEM Fuel Cells, ChemElectroChem, 2022, 9, e202200069.

J. P. Sabawa, **F. Haimerl**, F. Riedmann, T. Lochner and A. S. Bandarenka, Dynamic and Precise Temperature Control Unit for PEMFC Single-Cell Testing, Engineering Reports, 2021, 3, e12345.

J. Fichtner, S. Watzele, B. Garlyyev, R. M. Kluge, **F. Haimerl**, H. A. El-Sayed, W.-J. Li, F. M. Maillard, L. Dubau, R. Chattot, J. Michalička, J. M. Macak, W. Wang, D. Wang, T. Gigl, C. Hugenschmidt and A. S. Bandarenka, Tailoring the Oxygen Reduction Activity of Pt Nanoparticles

through Surface Defects: A Simple Top-Down Approach, ACS Catalysis, 2020, 10, 3131–3142.

Conference Presentations

F. Haimerl, E. Avellone and A. S. Bandarenka, Understanding the Break-in of PEM Fuel Cells: A Comprehensive Study of Break-in Methods and Underlying Mechanisms, presented at the ECS 244th Annual Meeting, Gothenburg, Sweden, Oct. 10, 2023.

F. Haimerl and A. S. Bandarenka, Enabling Fast and Efficient Testing Strategies for Fuel Cell Mass Production by Combining Impedance Spectroscopy and Forming Gas as Anode Stream, presented at the 74th Annual Meeting of the International Society of Electrochemistry, Lyon, Sep. 07, 2023.

F. Haimerl, J. P. Sabawa, T. A. Dao and A. S. Bandarenka, Spatially Resolved Electrochemical Impedance Spectroscopy of Automotive PEM Fuel Cells, presented at the 73rd Annual Meeting of the International Society of Electrochemistry, online, Sep. 14, 2022.

Contents

1 Introduction

1.1 Climate Change and Green Transport

Transitioning away from fossil fuel combustion emerges is a central challenge facing humanity: Air pollution from fossil fuel combustion leads to rising cardiovascular and respiratory mortality rates [1–4]. Global warming, linked to greenhouse gas emissions, is causing substantial changes in our climate system [5–7], and extreme weather events, including but not limited to floods, droughts, tornadoes, and hurricanes, are increasing in frequency and severity [8–10]. As commonly understood today, the human-caused rise in greenhouse gas concentration in the earth's atmosphere leads to a substantial increase in the planet's mean temperature (see Figure 1.1 (a) and (b)) [11–14]. Scientists predict further catastrophic events and economic damage if we do not respond promptly with significant transformations in all sectors of our life [15–18].

In a concerted effort to mitigate climate change and its consequences, the United Nations (UN) has formulated a global response. Embodied within the Paris Agreement is a consensus among all UN member states to constrain the temperature increase below $1.5\,^{\circ}\mathrm{C}$ relative to pre-industrial levels [22]. Achieving this objective necessitates substantial reductions in emissions over forth-

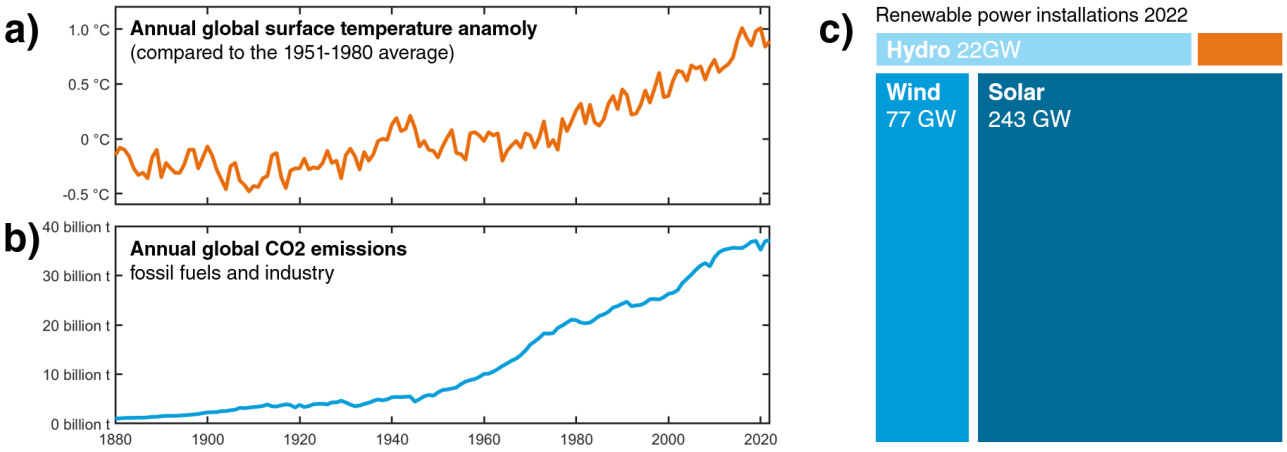

Figure 1.1 (a) The annual mean global temperature deviation from the baseline over 1880-2022. The baseline is the average temperature between 1951 and 1980. Data source: NASA, 2023 [19]. (b) The annual global CO_2 emission from fossil fuel combustion and industry. Data source: Ritchie, Rosado, and Roser, 2023 [20]. (c) The global renewable power generation capacities installed in 2022. Data source: REN21, 2023 [21].

coming decades [23]. Consequently, the European Union has introduced the European Green Deal, pledging to eliminate greenhouse gas emissions within its member states by 2050 [24].

Addressing the challenge of growing energy demands together with the imperative to reduce greenhouse gas emissions mandates a transition from fossil fuels to renewable energy sources. Solar, wind, and hydroelectric power installations are increasingly integrated into energy grids. In 2022, electricity constituted the predominant form of energy output from 98% of the global installed renewable energy capacity (see Figure 1.1 (c)). [21, 25]

Given the pivotal role of wind and solar energy in a net-zero emission energy landscape, direct or indirect electrification of the industry and transport sectors is crucial [26–28]. Within the transportation sector, battery electric vehicles (BEVs) represent a viable solution, with the sales market rapidly growing in recent years [29, 30]. BEVs exceed conventional internal combustion engine vehicles (ICEVs) in acceleration, demonstrate competitiveness in total cost of ownership

estimations, and, most importantly, drive emission-free. Still, challenges must be addressed, including the charging infrastructure, long recharging times, and high acquisition costs. [31–33]

1.2 Fuel Cell Electric Vehicles as Second Pillar for Electric Mobility

Fuel cell electric vehicles (FCEVs) can contribute to the future of electric mobility by offering consumers a choice between electrified drivetrains. State-of-the-art FCEVs drive up to $500\,\mathrm{km}$ with refueling times of $5\,\mathrm{min}$ and below, mirroring the familiar drive cycles of ICEVs. A FCEV utilizes the energy stored in hydrogen to power an electric motor. The core part of every FCEV is a fuel cell stack that converts the chemical energy stored in hydrogen into electrical energy, yielding only water as emission. [34, 35]

The most promising technology for automotive applications is polymer electrolyte membrane fuel cells (PEMFCs), as they enable fast starting times, high efficiency, and low degradation. Hydrogen tanks store the hydrogen fuel at up to $700\,\mathrm{bar}$, while the second reactant, air, is drawn from the environment. The high energy density of hydrogen compared to batteries makes FCEVs lighter than comparable long-range BEVs. [36–39]

As an increasing number of car manufacturers release commercially available FCEVs, the focus pivots towards scalability and mass production [40–44]. Oliver Zipse, the CEO of the BMW Group, stated that "hydrogen is the missing piece in the jigsaw when it comes to emission-free mobility" [45]. The recently released BMW iX5 Hydrogen is depicted in 1.2 (a) together with the

cockpit view displaying a range of $500\,\mathrm{km}$ on a full hydrogen tank at a hydrogen consumption of $1.2\,\mathrm{kg}/100\mathrm{km}$.

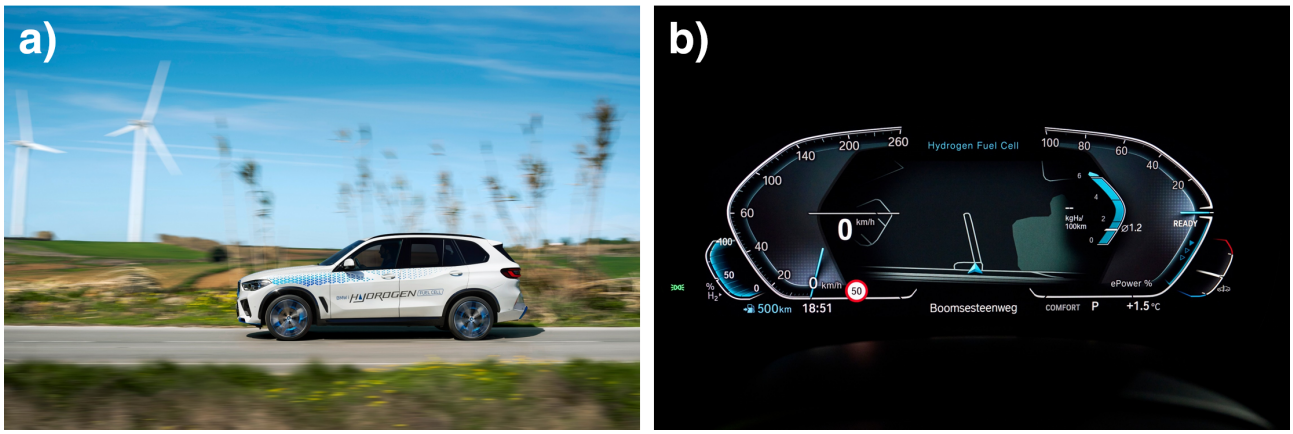

Figure 1.2 (a) Picture of the iX5 Hydrogen by BMW. (b) The cockpit displays a range of $500\,\mathrm{km}$ on a full hydrogen tank at a hydrogen consumption of $1.2\,\mathrm{kg}/100\mathrm{km}$. © Copyright BMW AG.

The major challenge to making FCEVs a viable alternative to widely used ICEVs, BEVs, and plugin hybrid electric vehicles (PHEVs) is the high production costs. While recent studies estimate the production costs for fuel cell systems at $\sim 200\,\$/\mathrm{kW}$ for mass production [46], the U.S. Department of Energy (DOE) expects that a cost reduction to $30\,\$/\mathrm{kW}$ is necessary for long-term competitiveness with alternative powertrains [47].

1.3 Enhancing the Industrialization of PEM Fuel Cells with Electrochemical Impedance Spectroscopy

Shifting to mass production, electrochemical impedance spectroscopy (EIS) can provide a powerful tool to accelerate cycle times in development and production. EIS is a well-established method that gains insights into the working principles of fuel cells while being fast and non-invasive [48, 49]. Therefore, it has the potential to speed up fuel cell design processes, reduce

costs for quality testing, and deepen the understanding of degradation mechanisms in automotive applications.

1.3.1 Electrochemical Impedance Spectroscopy in the Development Phase

Durability is one of the main challenges for automotive PEMFC applications [47]. Therefore, researchers look into making all fuel cell components more robust against chemical, mechanical, and thermal degradation by testing new or modifying known materials. [50–52]

Physical-chemical phenomena negatively impacting PEMFC performance can be categorized based on time scales. Short-term phenomena (minutes to hours) of particular significance include cathode flooding, membrane drying, anode catalyst poisoning by carbon monoxide, and contaminant absorption into the membrane. Conversely, long-term phenomena (hours to days to years) entail chemical processes characterized by slow reaction rates, such as ionomer degradation, carbon corrosion, and catalyst particle growth. [53–56]

PEMFC durability for vehicle applications has been closely linked to driving conditions and control strategies. Degradation testing is an essential and time-consuming step in the development of new membrane electrode assemblys (MEAs), as a wide range of scenarios and degradation mechanisms must be tested. Start-stop cycles, load changes, open-circuit voltage (OCV), high power operation, and cold starts contribute to a shortened lifetime. Over the years, single-cell accelerated stress tests have been standardized to accelerate the development of durable materials while minimizing costs and time. [57–60] Most degradation mechanisms heavily depend on

operating parameters like the potential, the temperature, the relative humidity, and the reactant supply [61, 62]. These parameters can differ significantly across larger automotive fuel cell stacks [63–67]. Hence, degradation is often a highly localized phenomenon [68–70].

In this context, EIS provides a non-destructive, *in situ* method for studying the degradation of PEMFCs. Even though interpreting impedance spectra and their characteristics can be complicated, EIS can help differentiate and track different degradation phenomena. [71–73] Still, conventional EIS cannot provide feedback on localized degradation processes. Advanced measurement techniques have emerged to address localized performance and degradation concerns in recent years. For instance, scanning electrochemical microscopy offers a high-resolution characterization of fundamental processes in half cells but lacks applicability to industrial fuel cells [74–76].

Alternatively, segmented fuel cell setups have been developed for the EIS of a complete fuel cell. Segmented cells utilize segmented flow fields and current collectors, electronically isolating each segment. [77–84]. Only recently, Liu et al. [85, 86] introduced a less invasive setup with an integrated printed circuit board (PCB). Although there is a growing interest in spatially resolved EIS for PEMFCs, existing literature only covers small-scale fuel cells with limited spatial resolution. In the scope of this thesis, we aimed to bridge this gap by investigating local impedance effects in PEMFCs relevant to commercial FCEV applications. Both the influence of operating conditions and the application to cold start stress testing were investigated.

1.3.2 Electrochemical Impedance Spectroscopy in the Production

The large-scale manufacturing of PEMFCs presents significant challenges for both material and component suppliers and fuel cell stack manufacturers. As the emphasis shifts to PEMFC mass production, one key advancement is developing time- and cost-effective quality control steps. Ensuring quality control throughout the production of automotive PEMFCs is essential, addressing safety concerns and economic viability. [87–91]

For quality checks on components, including catalyst layers, membranes, gas diffusion layers, and bipolar plates, optical tools provide a solution. Recent advances in this field include through-plane reactive excitation techniques for detecting pinholes in membrane electrode assemblies,[92] infrared thermography studies to detect membrane irregularities [93] or electrode defects [94–96], and deep learning implementations [97, 98].

However, optical quality control does not enable us to assess the internal functionality for cell and stack end-of-line testing. Hence, we have to look into other strategies.
The end-of-line test represents the final step in the production process, serving as the ultimate quality control before distribution to the respective customer [99]. In general, the end-of-line test has to fulfill the following tasks [100]:

- Identifying manufacturing and material flaws.
- Process control and feedback for quality management.
- Performance check and verification of user requirements specifications.

Given that the end-of-line cycle time significantly affects the required number of hydrogen test benches, reducing the time spent and maximizing the information acquired is critical.

EIS has proven to be a non-destructive testing method for automotive-scale Li-ion batteries. Significantly, this technique can rapidly discern between viable and nonviable cells in under one minute [101–103]. Further research has investigated the simultaneous testing of multiple cells within multi-cell setups to reduce the number of test channels [104, 105]. Overall, battery multicell testing yields a cost reduction of $\sim 42\,\%$ per tested cell [106].

In PEMFCs, the potential for EIS in end-of-line testing has yet to be investigated. A significant difference between EIS in batteries and fuel cells is the necessity to fuel the PEMFC with hydrogen. The operation with hydrogen requires high safety measures, as it permeates through various materials and can detonate at a volumetric ratio as low as 4.3%. [107–109]
Within this work, we investigate the potential of EIS for PEMFC end-of-line testing. A particular focus is understanding EIS interpretation at reduced hydrogen concentrations since quality testing at low hydrogen concentrations would significantly reduce safety measures and costs.

1.4 Scope and Structure of the Thesis

The aim of this thesis is to examine EIS applications to enhance the industrialization of PEMFCs. Therefore, experiments are conducted to deepen the understanding of EIS measurements in a wide range of implementations relevant to developing and producing commercial fuel cells. We will try to answer the following research questions:

- Which insights on operational strategies can we gain from spatially resolved EIS?
- Does degradation during realistic freeze-start cycling manifest itself in its EIS response?

- How can we interpret EIS data from experiments at low hydrogen concentrations?
- Can EIS detect faulty fuel cells in quality testing?

We will summarize the fundamentals of PEMFCs and EIS in Chapter 2. A particular emphasis lays on EIS in PEMFCs. The experimental setup with the different PEMFC tested in this work, the characterization methods, the data processing, and the test procedures are explained in Chapter 3. The results are presented in Chapter 4. The discussion includes the effects of temperature, humidity, and stoichiometries on the fuel cell performance, the investigation of local degradation effects due to starts from sub-zero temperatures, and EIS at low hydrogen partial pressure.

2 Theory

2.1 Fuel Cell Fundamentals

Before we discuss polymer electrolyte membrane fuel cells (PEMFCs) specifically in Chapter 2.2, we need to understand the electrochemical basics of a fuel cell. Therefore, this Chapter will briefly overview of the general setup, thermodynamics, kinetics, and mass transport of an electrochemical cell. An overview of fuel cell types can be found in the Appendix A.1.

2.1.1 The Electrochemical Cell

Electrochemistry is the science of chemical reactions that involve the transfer of electrons. It combines the study of chemical and electrical phenomena at interfaces between an electronic conductor (electrode) and an ionic conductor (electrolyte).

The charge transfer between an electrode and an electrolyte occurs via the uptake or the release of electrons by molecules in the electrolyte. The chemical reaction at the electrode-electrolyte interface involving the acceptance of an electron is called *reduction*. Vice versa, the release of electrons is called *oxidation*. Oxidation and reduction can not occur alone but only as a combined

reaction, called *redox reaction*. The simplest case of a redox reaction with one electron is given in equations 2.1 - 2.3.

$$\mathrm{A} + \mathrm{e}^- \longrightarrow \mathrm{A}^- \qquad \text{reduction} \qquad (2.1)$$

$$\mathrm{B} \longrightarrow \mathrm{B}^+ + \mathrm{e}^- \qquad \text{oxidation} \qquad (2.2)$$

$$\mathrm{A} + \mathrm{B} \longrightarrow \mathrm{A}^- + \mathrm{B}^+ \qquad \text{redox reaction} \qquad (2.3)$$

An *electrochemical cell* uses a redox reaction to transform chemical energy into electrical energy or vice versa. It comprises two electrodes connected by an electric circuit and an electrolyte separating the electrodes. The electrode associated with the oxidation is called *anode*, and the electrode linked to the reduction is called *cathode*. Due to the spatial separation of oxidation and reduction, ions and electrons must travel between the two electrodes. The ions move through the electrolyte, separating the two electrodes. The electrons move through the external electric circuit. [110–113]

We distinguish between two types of electrochemical cells: In *galvanic cells*, electrode reactions occur spontaneously, inducing an electric current. They convert chemical energy into electrical energy. In contrast, *electrolytic cells* transform electrical energy into chemical energy by promoting a reaction via an externally applied current.

Fuel cells are one form of galvanic cells. A fuel cell is solely an energy conversion device. The reactants are not stored in the fuel cell but supplied from external sources. Within this work, the main focus will be on fuel cells. However, the thermodynamic and kinetic basics apply to every electrochemical cell.

2.1.2 Thermodynamics

To describe the electrochemistry at an interface between two phases, the electrochemical potential $\tilde{\mu}$ is introduced. It is defined as the sum of the electric potential ϕ and the chemical potential μ of a phase.

$$\tilde{\mu} = \mu + e\phi \tag{2.4}$$

Here, e is the elementary charge. As the electrochemical potential aligns at the interface of two materials, we can compare the electrical and chemical potential differences. Together with the definition of free reaction enthalpy Δg_r (2.6), the difference in electrical potential can be given as

$$\Delta\phi = \frac{\Delta\mu}{e} = -\frac{\Delta g_r}{eF} \tag{2.5}$$

$$\Delta g_r = \sum v_k \mu_k \tag{2.6}$$

where F is the Faraday constant, the electrical charge of one mole elementary charges, and v_k are stoichiometric factors describing the relations of the reactants and products. The indices k denote the different substances of the reaction.

With the definition of the entropy s_k of a substance, we can expand the expression for the chemical potential and the corresponding expression for the free enthalpy.

$$\begin{aligned} \mu_k &= \mu_k^0 + T\Delta s_k \\ &= \mu_k^0 + RT \ln a_k \end{aligned} \tag{2.7}$$

$$\begin{aligned}\Delta g_r &= \Delta g_r^0 + RT \sum v_k \ln a_k \\ &= \Delta g_r^0 + RT \ln \left(\prod a_k^{v_k} \right)\end{aligned} \tag{2.8}$$

Here, R denotes the universal gas constant, and a_k are the reactants' activities. The exact definition of the activity depends on the chemical phase of the substance. For gases, it is equal to the partial pressure of the gas; for solutions, the concentration of the substance can replace it; and for liquids and solids, the activity is equal to one.

Combining eq. 2.5 and 2.8, we arrive at the Nernst equation:

$$\Delta \phi = \Delta \phi^0 + \frac{RT}{nF} \ln \left(\prod a_k^{v_k} \right) \tag{2.9}$$

$$\Delta \phi^0 = -\frac{\Delta g_r^0}{nF} \tag{2.10}$$

The Nernst equation describes the electrical potential difference at the interface between two phases. The voltage of an electrochemical cell in equilibrium V^{eq} equals the sum of potential differences across the cell.

$$U_{OCV} = U_0 + \frac{RT}{nF} \ln \left(\prod a_k^{v_k} \right) \tag{2.11}$$

The electrochemical cell is in equilibrium if the net current through the cell is zero. Therefore, the cell voltage in the equilibrium state is often called open-circuit voltage (OCV).

2.1.3 Kinetics

Once a current passes through the interface, the voltage will differ from the OCV. The difference between the theoretical value calculated with the Nernst equation and the measured potential is termed overpotential. The magnitude of the overpotential and the main contributions depend on the current passing through the cell. We will first focus on the kinetic overpotential associated with the electron transfer. The reaction rate of a chemical reaction k depends on the activation barrier e_b, which has to be surpassed on the reaction path. In equilibrium, the electrochemical potential at a surface is equal for both sides of the reaction. Therefore, the energetic barriers have the same magnitude in both directions. However, when charge transfer is involved, one direction is favored. A symmetry factor α is introduced to account for this variation from equilibrium.

$$k = k_0 \cdot \exp -e_b/RT \tag{2.12}$$

$$e_{b,ox}(\eta) = e_{b,ox}^{eq} - \alpha F \eta \tag{2.13}$$

$$e_{b,red}(\eta) = e_{b,red}^{eq} + (1-\alpha) F \eta \tag{2.14}$$

$$e_{b,ox}^{eq} = e_{b,red}^{eq} \tag{2.15}$$

Here, η is the overpotential at the interface. Figure 2.17 (a) shows a visual representation of this concept. Using equations 2.12-2.15 and the expression for the exchange current density j (eq. 2.16), we obtain a relation between the current density at one electrode-electrolyte interface and the corresponding overpotential (eq. 2.17).

$$j = Fkac_0 \tag{2.16}$$

$$= j_0 \left(\exp\left(\frac{\alpha F \eta}{RT}\right) - \exp\left(-\frac{(1-\alpha) F \eta}{RT}\right)\right) \tag{2.17}$$

$$j_0 = Fk_0ac_s \tag{2.18}$$

This relation is named the Butler-Volmer equation after the two scientists independently derived it. Here, c_s is the concentration of reactants at the surface. Figure 2.17 (b) shows a plot of the Butler-Volmer equation with a symmetry factor $\alpha = 0.5$ (solid line) and the contributions of the anodic and cathodic reaction (dashed lines).

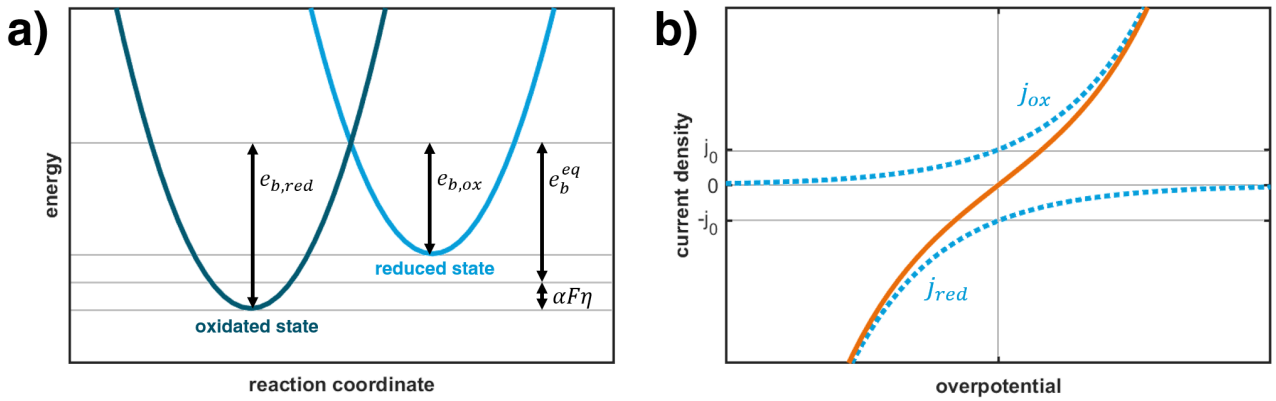

Figure 2.1 Schematic representation of the concept of activation barriers (a), as well as a plot of the Butler-Volmer equation with the symmetry factor $\alpha = 0.5$ (b).

For $\eta_{kin} >> \frac{RT}{F}$ the kinetic overpotential can be approximated by the Tafel equation:

$$\eta_{kin} = \frac{RT}{\alpha F} \ln\left(\frac{j}{j_0}\right) \tag{2.19}$$

Theoretically, both electrodes contribute to the difference in voltage. In a PEMFC, however, the slow reaction kinetics of the oxygen reduction reaction (ORR) mainly determines the overpotential. The overpotential of the anode is comparably small [111].

2.1.4 Mass Transfer

At high current densities, the reaction rapidly consumes reactants to establish concentration gradients. Both depletion of reactants and accumulation of the products become a problem. We learned from the Nernst equation 2.11 that the cell voltage depends on the concentration of the reactants at the electrode-electrolyte interface. Using the concentration at the electrode surface c_s in the Nernst equation yields

$$U_{OCV} = U_0 + \frac{RT}{nF} \ln c_s. \tag{2.20}$$

The overpotential caused by reactant depletion is therefore

$$\eta = \frac{RT}{nF} \ln \left(\frac{c_s}{c_b} \right), \tag{2.21}$$

where c_b denotes the bulk concentration of the reactant. Applying Fick's law, we obtain a proportionality between the current and the concentration gradient (eq. 2.22).

$$j = \frac{nFD(c_b - c_s)}{\delta} \tag{2.22}$$

Here, n is the flux of reactants per unit area, D is the diffusion coefficient of the reacting species, and δ is the Nernst diffusion layer thickness. Combining eq. 2.22 and 2.21, we arrive at a relation between the overpotential and the current density:

$$\eta_{mt} = \frac{RT}{nF} \ln \left(1 - \frac{\delta j}{nFDc_b} \right) \tag{2.23}$$

For $j = 0$ the overpotential is $\eta_{mt} = 0$. For $j \longrightarrow \frac{nFDc_b}{\delta}$ the mass transport overpotential approaches infinity $\eta_{mt} \longrightarrow \infty$. The current density $j = \frac{nFDc_b}{\delta}$ is called limiting current density j_L. It is the absolute maximum current a fuel cell can produce. Equation 2.23 predicts a sharp drop in the cell voltage when approaching the limiting current density. In realistic cells, the limiting current density is usually not reached uniformly across the catalyst surface. Instead, the reactant concentration and current density vary, leading to a softer voltage drop.

2.2 The PEM Fuel Cell in Automotive Applications

Due to its quick-start capabilities and comparably low operating temperatures, the PEMFC is the most promising candidate for fuel cell electric vehicles (FCEVs). This Chapter will guide you through the current understanding of PEM fuel cells. We will start with the fundamental chemical reactions in PEMFCs and provide an overview of state-of-the-art materials and design principles from the catalyst powder to stack components. Further explanations on the periphery and the working principles in an FCEV can be found in the appendix.

2.2.1 Chemistry of a PEM Fuel Cell

A PEMFC uses the highly exothermic reaction of hydrogen and oxygen to water to result in an electric current. At the anode side, hydrogen is oxidized to protons (*hydrogen oxidation reaction, HOR*). The proton-permeable membrane between the anode and cathode allows the transport of protons to the cathode side, where they reduce oxygen to water (*oxygen reduction reaction, ORR*). A potential builds up since the membrane prevents electrons from balancing the induced electron imbalance. A current is induced upon connecting the anode and cathode via an external circuit.

$$\mathrm{H_2} \longrightarrow 2\,\mathrm{H^+} + 2\,\mathrm{e^-} \qquad \text{HOR} \tag{2.24}$$

$$\frac{1}{2}\,\mathrm{O_2} + 2\,\mathrm{H^+} + 2\,\mathrm{e^-} \longrightarrow \mathrm{H_2O} \qquad \text{ORR} \tag{2.25}$$

$$\mathrm{H_2} + \frac{1}{2}\,\mathrm{O_2} \longrightarrow \mathrm{H_2O} \qquad \text{overall reaction} \tag{2.26}$$

While the potential of the relatively simple hydrogen oxidation reaction (HOR) is defined as $\phi = 0$, there are two distinct pathways with different potentials of the ORR in aqueous solutions. It either

occurs by the direct 4-electron pathway to water (eq. 2.27) or via the 2-electron pathway (eq. 2.28) to hydrogen peroxide. The hydrogen peroxide may react further with two protons and two electrons to water (eq.2.29). [114, 115]

$$\mathrm{O_2} + 4\,\mathrm{H^+} + 4\,\mathrm{e^-} \longrightarrow 2\,\mathrm{H_2O} \qquad 1.229\,\mathrm{V} \qquad (2.27)$$

$$\mathrm{O_2} + 2\,\mathrm{H^+} + 2\,\mathrm{e^-} \longrightarrow \mathrm{H_2O_2} \qquad 0.70\,\mathrm{V} \qquad (2.28)$$

$$\mathrm{H_2O_2} + 2\,\mathrm{H^+} + 2\,\mathrm{e^-} \longrightarrow 2\,\mathrm{H_2O} \qquad 1.76\,\mathrm{V} \qquad (2.29)$$

Additionally, the reaction between oxygen and the most common catalyst, platinum, induces a mixed potential at the cathode.

$$\mathrm{Pt} + \mathrm{H_2O} \longrightarrow \mathrm{PtO} + 2\,\mathrm{H^+} + 2\,\mathrm{e^-} \qquad 0.88\,\mathrm{V} \qquad (2.30)$$

The mixed cathode potential is around $1.06\,\mathrm{V}$ at standard conditions ($25\,^\circ\mathrm{C}$,$1.0\,\mathrm{bar}$) [116]. Other side reactions reduce the cathode potential further. One main contribution stems from hydrogen crossover. Even though the membrane separating the anode and cathode is built to prevent hydrogen and oxygen from moving to the other side, hydrogen crossover occurs at low rates. Consequently, the hydrogen oxidizes at the cathode, reducing the cathode potential. The current flowing due to hydrogen crossover is minimal in state-of-the-art fuel cells. It is negligible at higher currents. Nevertheless, it reduces the open-circuit voltage at equilibrium. [111, 116]

2.2.2 Catalyst Materials

The ORR is much slower than the HOR and is the rate-determining step. Hence, there is great interest in catalytically improving the sluggish kinetics.

Catalysis aims to bind reactants to a surface, thereby reducing the energetic activation barrier for a reaction. However, if intermediates bind too strongly to the catalyst surface, the reaction may not proceed, and the intermediates may block the catalyst's active sites. Therefore, a good catalyst should bind the reactants strong enough to reduce the activation barrier significantly but weak enough so that products can easily detach. This principle is called the Sabatier principle and leads to so-called volcano plots, indicating an absolute maximum of catalytic activity when plotted against the bonding energy. For the ORR, as well as for the HOR, platinum happens to be the best-known non-alloyed catalyst [114, 117]. The volcano plots for the ORR and the HOR, together with suitable candidates, are shown in Figure 2.2.

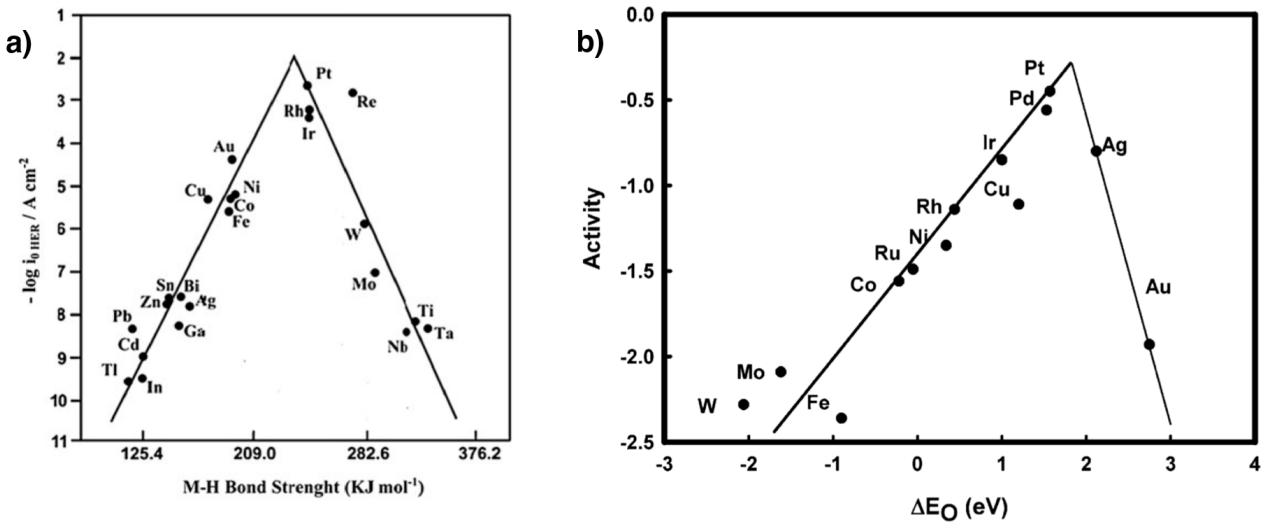

Figure 2.2 Volcano plots and suitable catalysts for the HOR (a) and the ORR (b). (a) Adapted from Lavacchi, A. et al. 2013. (b) Reprinted with permission from Norskov, J. K. et al. 2004 [117]. Copyright 2004 American Chemical Society.

However, the catalytic activity is not distributed uniformly over the catalyst surface. Contrarily, the catalytic activity mainly depends on individual active sites [118]. The binding energy of an atom depends on the number of closest neighbors. Hence, the catalytic activity depends on the structure of the surface. Under-coordinated edges and kinks bind oxygen too strongly for platinum and are less active than plain surface atoms. Over-coordinated cavities, in contrast, are even more active. [119, 120]

The activity of catalyst materials is commonly given as either specific or mass activity. The specific activity is the catalytic activity divided by the surface area of the catalyst. The mass activity is the catalytic activity per mass of catalyst material.
Since platinum is expensive, the main target is reducing the platinum content needed for PEMFCs while maintaining high catalyst activity and fuel cell efficiency. There are three ways to achieve lower platinum loadings: Increasing the surface area of platinum, increasing the specific activity, or finding platinum-free catalysts with equally high catalytic activity. [121]

Enhancing the surface area is achieved by using catalyst nanoparticles since nanoparticles lead to a higher surface-to-mass ratio. However, decreasing particle size leads to a higher percentage of step and kink surface sites with lower catalytic activity, reducing the specific activity. Considering both effects, the mass activity reaches a maximum at particle sizes around $3\,\mathrm{nm}$ [122]. Further, the utilization of active sites needs to be maximized. For a catalyst site to contribute to the reaction, it must be easily accessible by protons, electrons, and the reactant gas. Further details on electrode design principles to achieve a high catalyst utilization are explained in Chapter 2.2.4

To increase the specific activity of platinum, alloying with d-metals or lanthanides to craft bimetallic electrocatalysts is beneficial. Bimetallic catalysts like Pt_3Ni, Pt_3Co, and Pt_3Y have been demonstrated to enhance both the stability and the activity of Pt-based electrocatalysts. Further, the secondary metal can impede carbon monoxide adsorption on the catalyst surface, reducing the amount of blocked active sites. Taking the idea to the next step, researchers also look into ternary alloy catalysts for further improvements. [123–125]

Lastly, non-platinum catalysts are investigated based on several different approaches, including single-atom catalysts [126–128], high entropy alloy catalysts [129, 130], and metal-free catalysts [131–134]. Still, despite extensive efforts, state-of-the-art catalysts in commercial applications are platinum-based. Most commonly used are either pure platinum or Pt_3Co nanoparticles.

2.2.3 The Electrolyte

The primary function of the electrolyte in PEMFCs is to allow protons to move from the anode side to the cathode side. However, the electrolyte also acts as a separator between the anode and cathode catalyst layers, preventing electrons from moving through short circuits directly from the anode to the cathode and minimizing gas crossover. These requirements must be matched in a wide range of temperatures and humidities for commercial vehicle applications. Most widely used are perfluorinated sulfonic acid (PFSA) electrolytes like Nafion®, Gore-Select®, Aciplex®, or Flemion®. [135–138]

PFSA consists of a fluoropolymer backbone with pendant perfluoro side chains ending in sulfonic acid groups. The exact chemical formula varies between manufacturers but is shown schematically in Figure 2.3 (a). The fluoropolymer backbone is hydrophobic and provides chemical and thermal stability. The sulfonic acid groups are highly hydrophilic due to their high polarity. The high proton conductivity of PFSA membranes stems from the interconnections of water molecules bound to the sulfonic acid groups when hydrated. Within the polymer, superstructures form. Hydrophilic, water-rich domains form channels of high proton conductivity, separated by hydrophobic regions. The high conductivity within these channels stems from the *Grotthuss mechanism*. Instead of individual protons physically moving through the water channels, the proton is transported via rapid rearrangement of hydrogen bonds. The continuous *bond flipping* leads to virtually moving H_3O^+ ions. The Grothuss mechanism leads to almost ten times faster ion conduction than for any other ion. [139, 140]

Nafion®exhibits a conductivity of $0.2\,\mathrm{S/cm}$ at ideal conditions [141, 142]. In order to meet the desired resistance values between $0.01\,\Omega\,\mathrm{cm}^2$ and $0.02\,\Omega\,\mathrm{cm}^2$ this corresponds to a maximum membrane thickness of less than $20\,\mu\mathrm{m}$.

Challenges for PFSA membranes are still insufficient durability and the large dependence of the proton conductivity on humidification. Research to tackle these issues includes shortened side chains [143–145], reinforcing the fluoropolymer backbone [146–149], introducing radical scavengers to prevent free radicals from decomposing the ionomer chains [150, 151] as well as the introduction of new materials [152, 153].

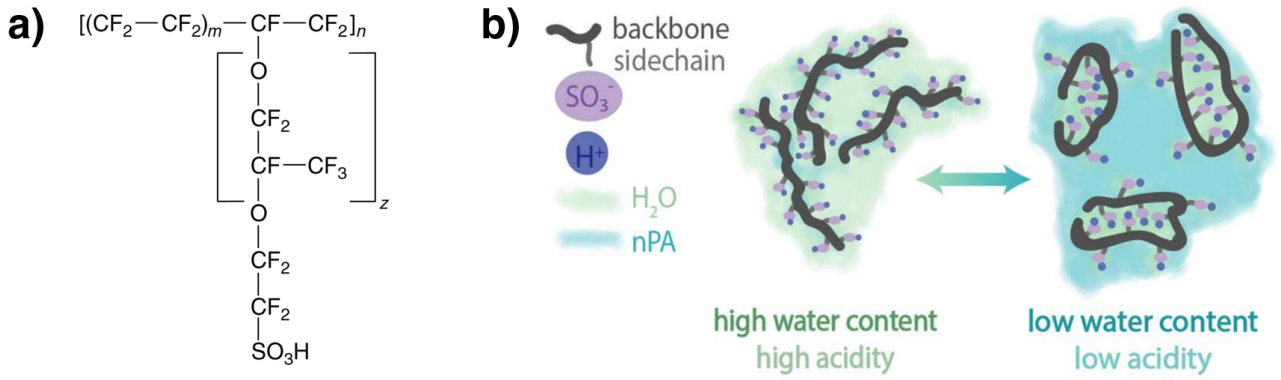

Figure 2.3 (a) The structural chemical formula of PFSA. (b) Schematic illustration of the ionomer structure as a function of water content. Reprinted with permission from Berlinger et al. 2018 [154]. Copyright 2018 American Chemical Society.

2.2.4 The Electrodes

State-of-the-art polymer electrolyte membrane (PEM) fuel cells are designed so that the reactions occur in the porous structure of the electrodes.

For the reaction to occur at a given spot in the electrode, the electrode must provide pathways to the reaction side for the three components: electrons, protons, and the reaction gas. An electrode is usually a porous structure of an electron-conducting material and a proton-conducting ionomer to enable those so-called triple-phase boundaries. An illustration of an exemplary electrode structure is shown in Figure 2.4.

The electrodes are also frequently called catalyst layers due to the presence of catalyst nanoparticles. To achieve high catalytic activity at minimal costs, the catalyst is dispersed on carbon support as nanoparticles. The carbon support acts as an electron pathway.

As discussed in the previous chapter, platinum is the most active catalyst for the ORR and the HOR. Consequently, anode and cathode are very much comparable regarding material requirements. Commercial cathodes contain around $0.2\,\mathrm{mg/cm^2}$ to $0.4\,\mathrm{mg/cm^2}$ platinum. The platinum loading on the anode is lower due to the better reaction kinetics of the HOR. Reduction of plat-

inum content at a simultaneous increase of mass activity is the main goal for future applications to reduce costs. The U.S. Department of Energy (DOE) targets a platinum loading of in total $0.125\,\mathrm{mg/cm^2}$ by 2025 to be competitive with other technologies. [47, 136, 138]

One key quantity to measure the accessible platinum surface is the electrochemical active surface area (ECSA). In order to increase the utilization rate of the platinum nanoparticles, the platinum must be in contact with the carbon support, the ionomer, and the gas phase. Porous carbon is commonly used as support to achieve a high gas permeability. It combines good electrical conductivity, low contact resistance, and high porosity. The carbon agglomerates in superstructures of agglomerates with different pore sizes provide a transport channel for the gaseous reactants and the liquid water the reaction produces. [155]

The carbon agglomerates are partially coated by a thin film of ionomer, providing proton pathways to the reaction site. Excess ionomer will, however, reduce the gas diffusion pathways. The optimum ionomer loading (*I/C ratio*) is around 30 wt%, and as described in Chapter 2.2.3, PFSA materials are most commonly applied. Water content is critical not only because it increases the proton conductivity in the ionomer. Additionally, water thin films and water-filled small pores provide further proton pathways, increasing the catalyst utilization rate. However, excess water may lead to an accumulation of water in larger pores and, therefore, a blocking of gas pathways (see Figure 2.4). [156–158]

The catalyst layers are prepared in two steps: Mixing an ink with all previously described components, an additional solvent, and possibly other additives. Subsequently, the ink is applied to a

substrate. [159]

The substrate might either be the gas diffusion layer (GDL) (see Chapter 2.2.5), the membrane, or a foil for a later transfer to the membrane. The electrode's exact structure is highly dependent on material choice and ink composition. Some essential variables are the catalyst material, the carbon material, the platinum weight loading, the Pt/C ratio, the I/C ratio, the ionomer, and the amount and kind of solvent used. [144, 154, 160]

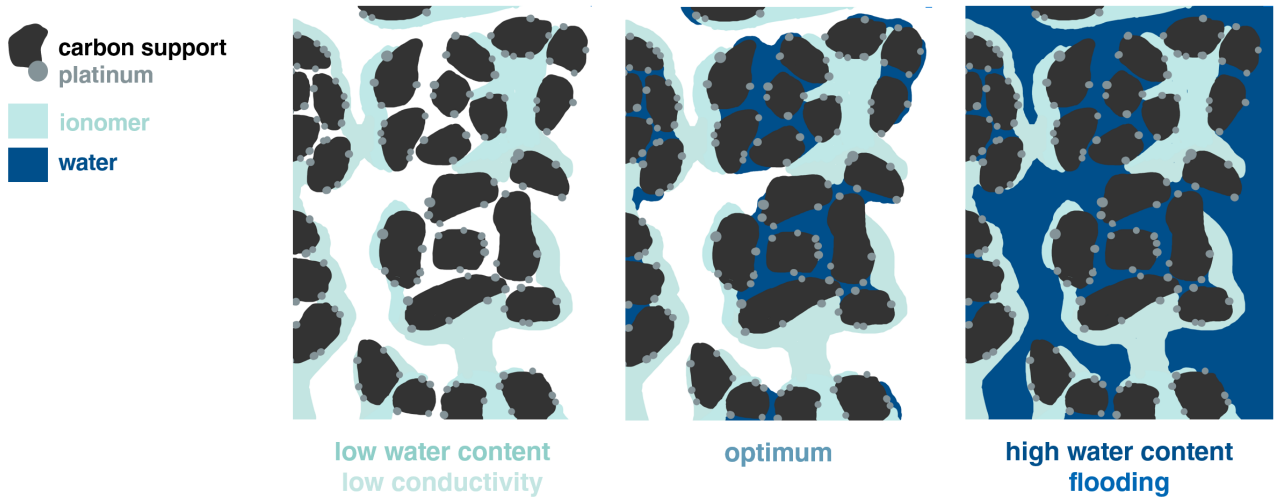

Figure 2.4 Illustration of the electrode structure in PEMFCs with the influence of the water content in the electrode.

2.2.5 The PEM Fuel Cell Stack

A full cell stack compromises membrane electrode assemblys (MEAs), which are essentially the electrochemically functional part of a fuel cell stack, and bipolar plates (BPPs). BPPs supply the cell with hydrogen and oxygen, electrically connect the cells, and guide the cooling medium of the stack. To achieve the power requirements for FCEV, up to 400 MEAs and BPPs are stacked in series. Figure 2.5 shows the alternate stacking of MEAs and BPPs.

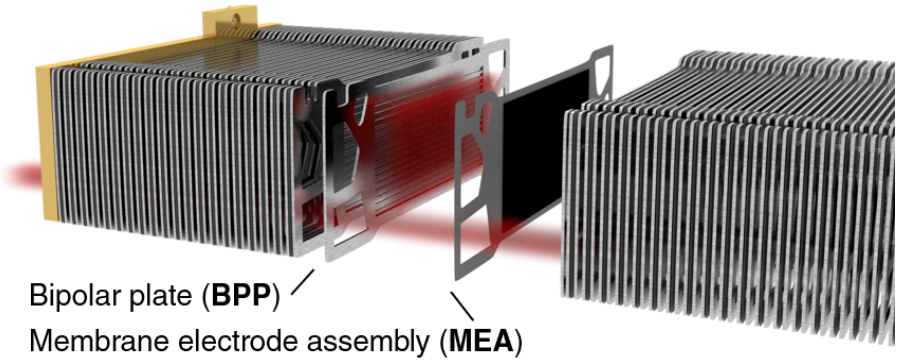

Figure 2.5 Exemplary CAD graphic of a PEMFCs stack for automotive applications.

The Membrane Electrode Assembly

The membrane electrode assembly (MEA) is the smallest functional part in a fuel cell stack. Talking solely about essential parts, the MEA combines all components of an electrochemical cell. It consists of a polymer electrolyte membrane (PEM) (see Chapter 2.2.3) sandwiched by anode and cathode layers (see Chapter 2.2.4). The electrode-electrolyte sandwich is completed with a sealing gasket, ensuring gas tightness and electrical isolation. In commercial fuel cell stacks, two additional layers, a gas diffusion layer (GDL) on the cathode and anode side, ensure good gas distribution across the catalyst layer. A graphic of a typical MEA for automotive applications is displayed in Figure 2.6.

The GDL serves in the following functions: diffusion and even distribution of the gas from the

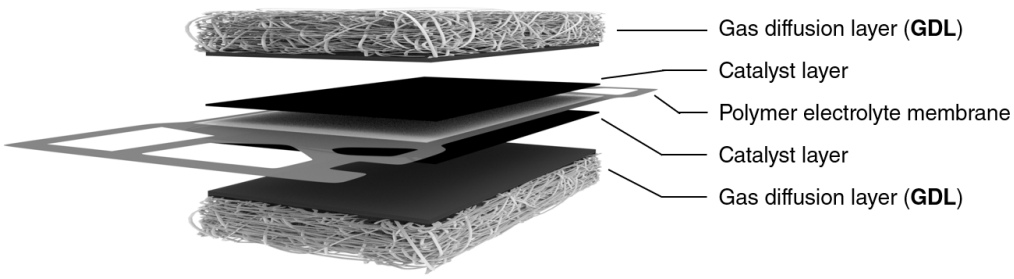

Figure 2.6 Exemplary CAD graphic of the essential components of MEAs for automotive applications.

flow channels towards the catalyst, transport of produced water from the MEA back to the flow field, conduction of electrons and heat, and mechanical support of the MEA across the uneven surface of the flow field design. Thus, it must exhibit good thermal and electrical conductivity and a high porosity. The GDL is built up by a substrate and a thin coat of a microporous layer (MPL). Commonly, carbon fiber material, hydrophobized with 5 wt% to 30 wt% polytetrafluoroethylene (PTFE), is used as a GDL-substrate. The MPL consists of carbon or graphite particles and between 10 wt% and 40 wt% hydrophobic binder. It enhances water transport and protects the MEA from substrate fibers. Without the additional MPL coating, liquid water films form at the electrode-GDL interface, blocking oxygen pathways. The smaller pore size of less than $500\,\mathrm{nm}$ compared to substrate pores of more than $10\,\mu\mathrm{m}$ within the MPL provides a barrier for condensed water in the GDL. [161–163]

The layer thickness is a crucial factor for the transport properties of the GDL. While thicker GDLs exhibit better oxygen diffusion, they flood more easily. Therefore, the optimal thickness depends on the application, ranging between $0.1\,\mathrm{mm}$ to $0.4\,\mathrm{mm}$. [163]

Bipolar plates

A BPP fulfills multiple functions in a fuel cell stack. It sits between each MEA, acting as anode contact on one side and cathode contact on the other side of the plate. A flow field is impregnated on each side, providing the fuels for the cell and removing the product water. Besides, BPPs must also inhibit channels for the cooling system and electrically connect adjacent cells. Thus, material requirements include good thermal and electrical conductivity, gas impermeability, and corrosion resistance [164]. Due to the demand for mass production capabilities in automotive applications, metal BPPs are commonly used in this sector. They are composed of two metal

plates, each stamped with a gas flow field on the outside. On the inside of the BPPs, a cooling medium flow field enables controlling the stack temperature. A typical geometry of BPPs inside a PEMFC-stack is shown in 2.5. [165, 166]
Since most metals are prone to corrosion, the metal plates are protected by an anti-corrosion coating [167, 168].

Effective water management and reactant distribution are pivotal as they directly impact cell performance and degradation. Water transport and gas distribution depend on the flow field design. In commercial PEM fuel cell stacks, a straight parallel flow field variation is usually utilized, where air and hydrogen are supplied to the MEA in multiple parallel channels. In straight parallel flow field designs, we distinguish *co-flow* and *counter-flow*. The first term means that air and hydrogen are fed from the same side and thus flow in the same direction; the latter means that air and hydrogen flow in opposite directions. Counter-flow usually leads to a more even water distribution. [169–171]

2.2.6 Current-Voltage Characteristics of a PEM Fuel Cell

According to the Nernst equation 2.11, we obtain the OCV by inserting the free enthalpies of hydrogen, oxygen, and water. For a PEMFC at ambient pressure, this results in a theoretical voltage of $1.229\,\mathrm{V}$. Accounting for the mixed potential at the cathode and side reactions, realistic OCV values are usually around ~$1.00\,\mathrm{V}$. Moving away from equilibrium conditions, the actual cell voltage decreases with increasing current drawn from the cell. The difference between the theoretical OCV calculated from the Nernst equation and the actual cell voltage is termed overpo-

tential η. The dependence of the overpotential on the current density defines the current-voltage characteristics depicted in Figure 2.7. The current-voltage curve is also called *polarization curve*.

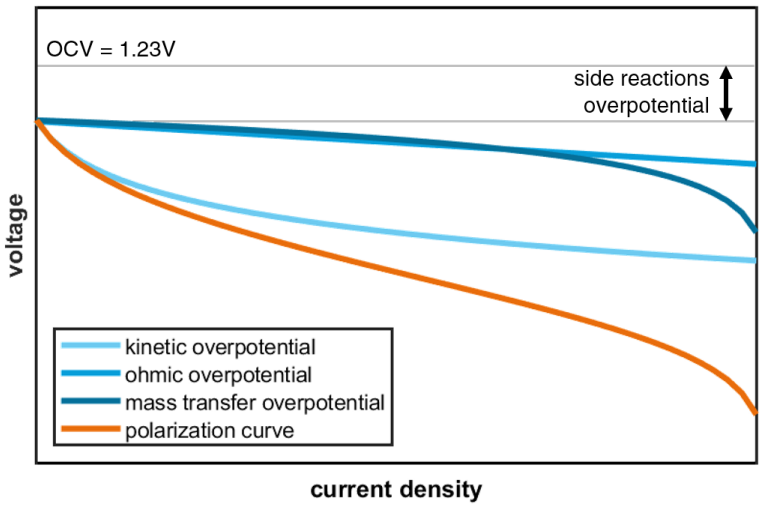

Figure 2.7 Polarization curve of a PEM fuel cell. We can distinguish four potential losses: side reactions, kinetics, ohmic losses, and mass transfer limitations.

We can differentiate between overpotentials stemming from different processes that shape the polarization curve in specific current ranges. Apart from the difference between theoretical and actual OCV, we can differentiate three regions in which three different overpotentials shape the curve:

Kinetic overpotential

At low current densities, the sluggish kinetics of the ORR, referred to as *kinetic overpotential*, dominate the current-voltage curve. The kinetic overpotential is associated with the energy barrier that must be overcome for the reaction to occur. For $\eta_{kin} >> \frac{RT}{F}$ the kinetic overpotential can be described by the Tafel equation:

$$\eta_{kin} = \frac{RT}{\alpha F} \ln\left(\frac{j}{j_0}\right) \tag{2.31}$$

The Tafel equation predicts a logarithmic dependency of the kinetic overpotential η_{kin} on the current density, which can also be seen in the polarization curve. For further explanation and the derivation, please refer to Chapter 2.1.3.

Ohmic overpotential

With increasing current density, the polarization curve flattens into a reasonably straight line attributed to ohmic losses, the *ohmic overpotential*. The ohmic overpotential is rather not one overpotential but a combination of three ohmic resistances: the proton resistance in the ionomer R_{proton}, the electronic resistance of fuel cell components R_e, and the contact resistance R_c.

$$\eta_{ohm} = IR \tag{2.32}$$

$$R = R_{proton} + R_e + R_c \tag{2.33}$$

The resistivity of metals and carbon materials used for electronically conductive components is in the order of $10^{-8}\,\Omega/\mathrm{m}$ to $10^{-6}\,\Omega/\mathrm{m}$ compared to an ionic resistivity in the order of $1\,\Omega/\mathrm{m}$ to $10^{10}\,\Omega/\mathrm{m}$ of the membrane. Hence, electronic resistances are almost negligible. Contact and ionic resistances are of approximately the same order of magnitude.[111, 142, 172]

Mass transport overpotential

At very high current densities, the reactants at the electrodes deplete, leading to a *mass transport overpotential*. The theory of this phenomenon was already discussed in Chapter 2.1.4.

We derived the equation for the mass transfer overpotential:

$$\eta_{mt} = \frac{RT}{nF} \ln\left(1 - \frac{\delta j}{nFDc_b}\right) \tag{2.34}$$

For large current densities ($j \longrightarrow \frac{nFDc_b}{\delta}$), the theoretical equation predicts a sharp drop in the cell voltage. To move the limiting current density to higher values, either the diffusion constant must increase or the diffusion distance must decrease. This means either reducing the thickness of electrodes and GDL or improving the permeability of the materials. To minimize mass transfer limitations, the fuel cell is usually operated on higher reactant supplies than theoretically necessary to maintain the applied current. The ratio of the supplied reactant to the theoretical reactant consumption rate is called stoichiometry and is denoted with the symbol λ.

2.3 Electrochemical Impedance Spectroscopy in PEM Fuel Cells

Electrochemical impedance spectroscopy (EIS) provides a well-established approach for fast and non-invasive PEMFC measurements. By applying small sinusoidal disturbances at different frequencies to the fuel cell, impedance spectroscopy can reveal vital insights into the electrochemical performance of the cell. [48, 49, 53, 173]

Based on the knowledge of PEMFCs from previous chapters, this Chapter aims to provide a common basis for EIS fundamentals. First, EIS is introduced, and the basics of EIS data analysis are explained. Secondly, a connection is drawn between electrochemical processes in a fuel cell and corresponding impedance contributions. Finally, common EIS models are described. For electrical basics and the concept of impedance, please refer to the Appendix A.3.

2.3.1 The Concept of Electrochemical Impedance Spectroscopy

The principle of electrochemical impedance spectroscopy (EIS) measurements is to apply an alternating current (AC) probing signal to an electrochemical system and measure the response. One can calculate the complex resistance called *impedance* from the phase shift and the amplitudes of signal and response. Applying different perturbation frequencies makes it possible to separate electrochemical processes due to their different relaxation times. The set of impedance values for different frequencies is called *impedance spectrum*.

EIS experiments are usually carried out on a three-electrode setup: the working electrode as the object under investigation, the counter electrode as the counterpart of the working electrode,

and the reference electrode as a reference point. In a PEM fuel cell, the anode might be used simultaneously as the counter and reference electrode due to practicability. This is, however, only possible since the HOR shows significantly faster kinetics than the ORR. [174, 175]

One differentiates between *galvanostatic* and *potentiostatic* EIS measurements. In galvanostatic measurements, the current perturbation is controlled while recording the voltage response; the potentiostatic mode is the opposite way of generating a voltage signal and measuring the current response. For both options, a potentiostat is most commonly used in combination with a frequency response analyzer. The combination is often built into a single device, providing four terminals: Two terminals for generating a voltage/current signal and two terminals measuring the current/voltage response. [174, 175]

The data obtained from an EIS measurement can be plotted in multiple ways, the most prominent being Nyquist and Bode plots. In a Nyquist plot, the data points are plotted in the complex plane, providing the imaginary part of the impedance as a function of the real part. This representation is very illustrative and allows for determining an electrochemical cell's fundamental properties at first glance. However, a Nyquist plot provides no information about the frequency range and dependency of the obtained EIS data. Therefore, a Bode plot can be a viable alternative, often providing additional information. A Bode plot maps the absolute value of the impedance $|Z|$ and the phase ϕ as functions of the angular frequency ω. $|Z|$ and ω are plotted on a logarithmic scale. Examples of a typical Nyquist plot (a) and the corresponding Bode plot (b) are given in Figure 2.8.

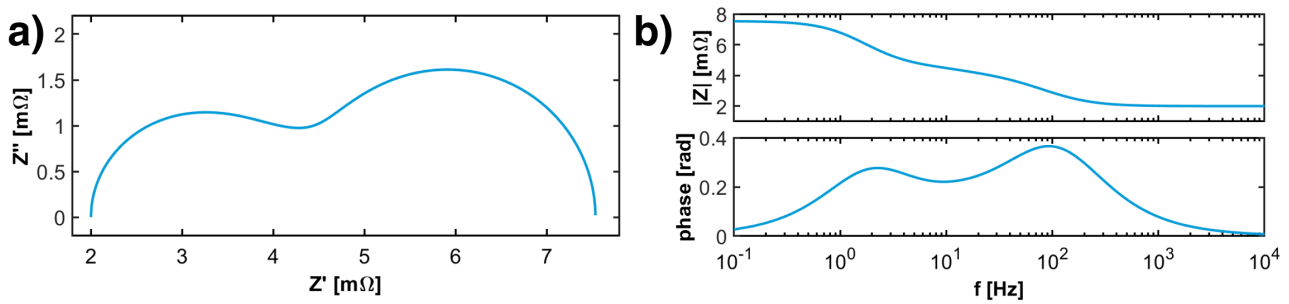

Figure 2.8 Examples of a typical Nyquist plot (a) and the corresponding Bode plot (b). Note that the Nyquist representation does not provide information about the frequency dependence. The data was obtained by simulating a modified Randles circuit with finite diffusion over a frequency range from 0.01 Hz to $10\,000$ Hz. The properties were $R_0 = 0.002\,\Omega$, $R_1 = 0.002\,\Omega$, $C_1 = 1$ F, $A_w = 0.005\,\Omega$ and $B = 0.5\,\Omega$.

2.3.2 Data Validation and Fitting

EIS can provide insights into the contributions of the impedance and, therefore, the chemical and physical processes in a fuel cell. Identifying the different contributions solves the inverse problem: We know the outcome and want to learn about the sources. The fitting process of impedance spectra consists of three steps: validation of the measured data, the proposal of a model representing the processes in a fuel cell, and fitting the model to the data. [176]

The Kramers-Kronig transformation validates the experimental data regarding stability, linearity, and causality. It states that the imaginary part of a valid EIS data set can be calculated from the real part. Since the Kramers-Kronig transformation is rather complicated, the data is often validated by fitting a model that fulfills the Kramers-Kronig relation. The data set fulfills the Kramers-Kronig relation if the relative residuals of the fit are distributed over the full range of frequencies. However, the data set is not necessarily invalid if the relative residuals are not distributed randomly. [177–179]

The validated impedance data is then commonly fitted with fuel cell models. Historically, the

most common fuel cell models are based on electric circuit diagrams aiming to simplify complex electrochemistry while providing information on the underlying physics. These so-called *equivalent circuit models (ECMs)* are easy to understand and, given a fundamental understanding of electrochemistry, easy to apply. [180] There is, however, the ambition to develop models solely based on physical equations. Due to the complexity of those models, the fitting is usually only possible with additional ex-situ measurements. [181, 182]
We will discuss the physical basics of PEMFC impedance models in Chapter 2.3.3 and introduce different ECMs in Chapter 2.3.4.

Nowadays, computer technology provides a fast and accurate way of fitting an equation to a measured data set. The complex non-linear least square (CNLS) fitting method is the most commonly used fitting approach. Most data analysis programs are based on the Levenberg-Marquardt minimization algorithm. The CNLS approach aims to minimize the chi-squared parameter, which is defined by

$$\chi^2 = \sum \left(\frac{y_i - f(x_i)}{\sigma_i} \right)^2 . \tag{2.35}$$

χ^2 is also called object function. (y_i/x_i) are the measured data points with a standard deviation σ_i and $f(x)$ is the model function. For the CNLS fit, the object function is defined as

$$\chi^2 = \sum Re(Z_i - Z(\omega_i))^2 + Im(Z_i - Z(\omega_i))^2. \tag{2.36}$$

Here, Z_i denotes the measured impedance for the angular frequency ω_i, and $Z(\omega_i)$ is the impedance calculated with the chosen equivalent circuit model for the angular frequency ω_i. The minimization

algorithm then aims to minimize the object function by varying the parameters of the impedance function. [174, 183]

Indicators often used to determine the quality of a fit are the relative residuals [174]:

$$\Delta_{re,i} = \frac{Re(Z_i - Z(\omega_i))}{|Z(\omega_i)|} \tag{2.37}$$

$$\Delta_{im,i} = \frac{Im(Z_i - Z(\omega_i))}{|Z(\omega_i)|} \tag{2.38}$$

The fitting process starts by selecting an appropriate equivalent circuit and estimating the initial values for all model parameters. The minimization algorithm then evaluates the resulting fit through the object function and adjusts the parameters. It will repeat the process of fitting, evaluating, and adjusting for a specified number of cycles or until reaching a given goal for accuracy. This, however, may result in a poor fit even for an appropriate model choice and good measurement data due to poor estimates of the initial values. Therefore, estimating the initial values requires good knowledge of the electrochemical system under investigation. [174]

2.3.3 Impedance and Its Corresponding Electrochemical Processes

A typical model of an electrolyte-electrode interface contains three main contributions: one part attributed to faradaic reactions at the interface, one contribution by the interface itself, and an ohmic contribution of the charge transport through the ionomer and electrode components. We will discuss each contribution in this Chapter in greater detail.

Ohmic Contribution

The charge transport of both electrons and ions leads to an ohmic contribution to the fuel cell impedance. Therefore, it is often modulated by a resistor R_u. The *uncompensated resistance* is connected to the conductivity σ by equation 2.40.

$$Z_u = R_u \tag{2.39}$$

$$R_u = \frac{l}{\sigma A} \tag{2.40}$$

Here, l denotes the length of the conduction pathway, and A denotes the cross-section of the conductor. Since the cross-section of the ionomer is much smaller in the porous ionomer structure of the electrodes, proton conduction within the electrodes significantly adds to the proton resistance.

Interface Impedance

The interface between the electrode and the electrolyte itself is usually modeled as capacitance. A charged zone builds up at the interface between proton-conducting material and electron-conducting material. This zone is negligibly small in electronic conductors but extends significantly into the electrolyte. Due to its characteristics of adsorbed species as a charge layer and a more extended charged volume built up by ions, it is often referred to as *double layer*. The corresponding capacitance is called *double layer capacitance* C_{dl}. Simple models approximate the interface capacitance as a plate capacitor (see eq. 2.42). This is a considerable simplification

of the electrode-electrolyte interface and reflects the physics only poorly but gives an intuitive understanding of related quantities.

$$Z_C = \frac{1}{i\omega C} \qquad \text{impedance of a capacitance} \tag{2.41}$$

$$C = \frac{\epsilon_0 \epsilon_r A}{d} \qquad \text{plate capacitor} \tag{2.42}$$

Here, Z_C is the impedance of a capacitance, i is the imaginary unit, C denotes the capacitance, A is the area, and d is the distance. ϵ_0 and ϵ_r are the relative and vacuum permittivity, respectively.

Following the simplification of a plate capacitor, we can estimate the electrode-electrolyte interface area from the capacitance. While the magnitude may vary from the actual values, the double layer capacitance indicates how the interface area changes over time. It is, however, essential to note that the interface area here describes the total area between ionic conductors (ionomer, water) and electronic conductors (platinum, carbon). It does, therefore, not translate to an indication of the ECSA.

Faradaic Impedance and Mass Transport Impedance

Regarding the faradaic impedance at an electrolyte-electrode interface, the simple model derived by Warburg [184] has been the scientific standard for over a century. When considering a simple redox reaction

$$\mathrm{Ox} + \mathrm{ne} \longleftrightarrow \mathrm{Re} \tag{2.43}$$

one can write the potential at the electrode as a function $V(j, c_{ox}, c_{red})$ of the current passing through the interface j as well as the concentrations of reductant c_{ox} and oxidant c_{red}. If we assume only mass transport according to Fick's diffusion law and neglect migration and convection, the time differentials of the concentration at the interface are given by

$$\frac{\partial c_{ox}(x,t)}{\partial t} = D_{ox}\frac{\partial^2 c_{ox}(x,t)}{\partial x^2} \tag{2.44}$$

$$\frac{\partial c_{red}(x,t)}{\partial t} = D_{red}\frac{\partial^2 c_{red}(x,t)}{\partial x^2}, \tag{2.45}$$

where D is the diffusion constant of the species.

As the length of the diffusion region δ, namely the electrode layer plus the GDL, is not significantly larger than the diffusion length, we have to consider a finite-length diffusion problem. In PEMFCs, a totally absorbing boundary is a good approximation. The boundary conditions can, therefore, be formulated as

$$c(x = L, t) = 0 \tag{2.46}$$

Inserting the boundary conditions and connecting the diffusion with the current density, we can solve the differential equations 2.44-2.45. Using the Fourier transformation, we arrive at the

Faradaic impedance as a combination of a charge transfer resistance plus the Warburg impedance [174, 175].

$$Z_{faradaic} = R_{ct} + Z_{ws} \tag{2.47}$$

$$R_{ct} = \frac{RT}{n^2 F^2 A c k_{app}} \tag{2.48}$$

$$Z_{ws} = Aw(i\omega)^{-0.5} \tanh(\sqrt{i\omega}B) \tag{2.49}$$

with

$$Aw = \frac{RT}{n^2 F^2 A c \sqrt{2D}}, \tag{2.50}$$

$$B = \frac{\delta}{\sqrt{D}} \tag{2.51}$$

The impedance Z_{ws} and the corresponding equivalent circuit element are called *Warburg short* [185]. We can determine characteristic properties of a fuel cell, like the diffusion constant, directly from the Warburg short parameters.

From the relation between Aw and R_{ct} we can derive an indication of the apparent reaction rate k_{app}:

$$\frac{Aw}{R_{ct}} = \frac{k_{app}}{\sqrt{2D}} \tag{2.52}$$

2.3.4 Equivalent Circuit Models for PEM Fuel Cells

With the knowledge of the most important contributions to the impedance of a PEMFC, we can think of possible models to describe a fuel cell. In the scope of this thesis, we will focus on so-called equivalent circuit models (ECMs). An ECM is an electric circuit diagram aiming to simplify complex electrochemistry while providing information on the underlying physics.

In this chapter, we will describe and discuss different ECMs and possible applications for them. We will start with the well-established and simple Randles equivalent circuit and gradually introduce complexity. An overview of the Randles model and possible additions is provided in Figure 2.9.

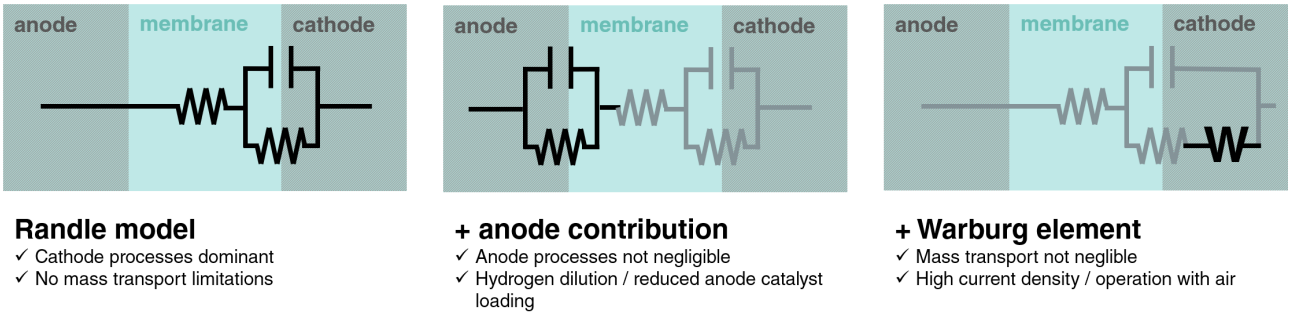

Figure 2.9 Diagram of the Randles ECM, as well as two possible additions: an anode contribution in case of operating conditions or design choices promoting a stronger impact of anode processes; a mass transport contribution in the form of a Warburg element as derived in Chapter 2.3.3

.

Randles model

The standard model for describing kinetic and interfacial effects at the electrode-electrolyte interfaces has been the Randles model for over 70 years [186]. The model consists of a parallel arrangement of a resistor and a capacitor. The resistor models the resistance associated with the electrochemical reaction itself. The capacitor is a simplified representation of the double layer

building up at the interface between an electric conductor and an ionic conductor (see Chapter 2.3.3).

For PEMFCs, we usually assume the anode reaction to be negligible. In the simplest case, we, therefore, model the fuel cell with a parallel connection of the charge transfer resistance R_{ct} and the double layer capacitor C_{dl} for the cathode and an additional resistor R_{Ω} for the ohmic losses associated with proton conduction and interface resistances. A representation of the simplest model is shown in Figure 2.10, together with the typical Nyquist response that we would expect from a simple Randles model.

The high-frequency intercept with the x-axis is attributed to the ohmic resistance. The semi-circle in the Nyquist plot is associated with the processes at the electrode-electrolyte interface. Therefore, the low-frequency intercept with the x-axis is $R_{\Omega} + R_{ct}$. [187]

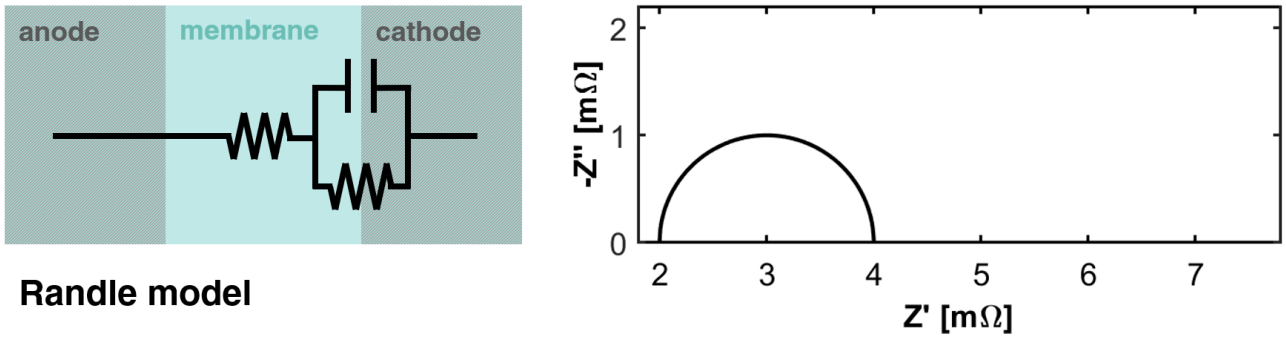

Figure 2.10 Diagram of the Randles model for PEMFCs and the corresponding Nyquist plot.

.

In real-world applications, the half-circle in the Nyquist plot is often depressed. Therefore, the capacitor is sometimes replaced with a constant phase element (CPE). A CPE is essentially an imperfect capacitor with the additional parameter n being a measure for the degree of deviation from a capacitor. $n = 1$ equals a pure capacitor. However, the exact physical meaning of CPEs

is still under debate in each particular case. [188–193]

The simple Randles model is primarily used in ideal use cases, as it neglects two factors that we will look at more closely in the following chapters.

Mass transport contribution

Moving away from ideal conditions to the operation with air at a realistic stoichiometry, we commonly see a second arc evolving in the impedance spectra of fuel cells. The mass-transport processes take place at a longer timescale and are therefore visible in the low-frequency domain between 0.1 Hz to 5 Hz. [178]

While there are publications fitting the mass transport arc with a second capacitance/resistance parallel circuit, the physically derived Warburg short element is the most common model for mass transport phenomena in PEMFCs [185]. The modified Randles circuit with the Warburg element for bound diffusion and the Nyquist plot of the resulting impedance spectrum are shown in Figure 2.11.

We usually see increasing mass transport contributions in the impedance spectrum at high current densities, low stoichiometries [194], or due to water management [195, 196]. Still, mass transport can become noteworthy at low current densities if hydrogen crossover is increased [197].

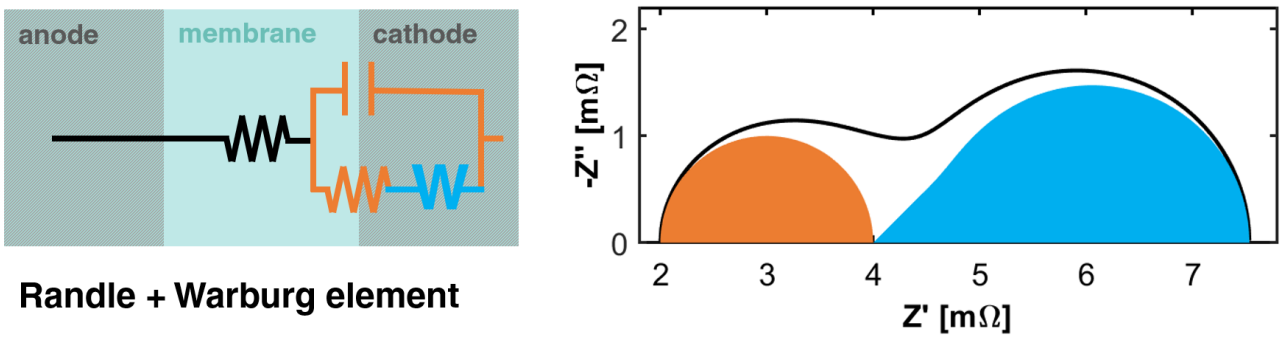

Figure 2.11 Diagram of a typically used ECM considering mass transport issues and the corresponding Nyquist plot. The contribution of the normal Randles model is orange, and the additional mass transport contribution is blue.

.

Anode contribution

While mass transport contributions are present in most full cell PEMFC impedance studies, the anode contribution is comparably small at realistic operating conditions. Since the HOR is extremely fast compared to the sluggish ORR, only small amounts of catalyst are required to keep the anodic voltage losses at a fraction of the cathodic voltage losses. [194, 198]

Still, at very low anode platinum loadings or low hydrogen stoichiometries, one sees an additional arc in the Nyquist plot that can be attributed to the anodic charge transfer process [199, 200]. One can model the electrode-electrolyte interface at the anode similarly to the cathode with a Randles circuit. Since the HOR takes place at short time scales, it is visible in the high-frequency range from $100\,\mathrm{Hz}$ to $1000\,\mathrm{Hz}$ [178, 201]. A simple model considering the anodic charge transfer and the resulting Nyquist plot is displayed in Figure 2.12.

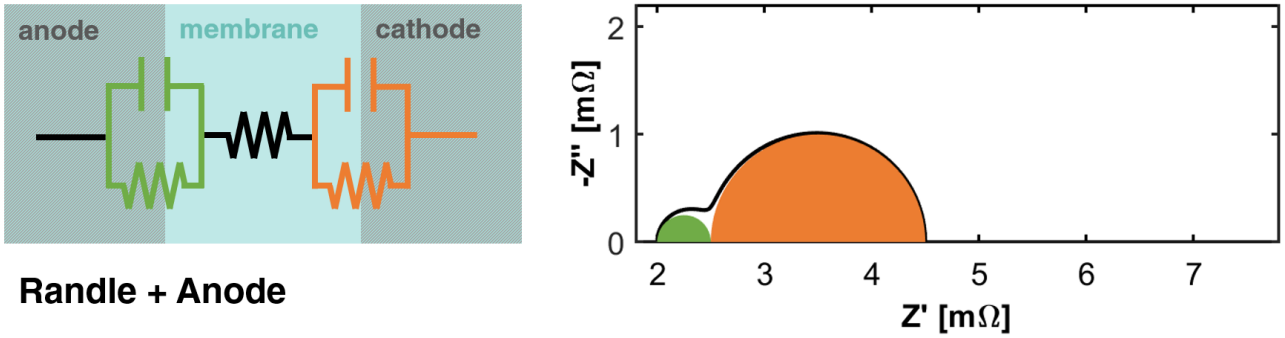

Figure 2.12 Diagram of a typically used ECM considering anode contributions and the corresponding Nyquist plot. The contribution of the normal Randles model is orange, and the additional anode contribution is green.

.

3 Experimental

This Chapter provides an overview of the experimental setups, characterization techniques, and test protocol used in this work.

3.1 Experimental Setup

The main tests were carried out on two different experimental setups: the spatially resolved EIS study and the freeze-start cycle experiment were conducted on automotive-sized PEMFCs; the tests on the influence of hydrogen partial pressure (hpp) were carried out on smaller lab-sized PEMFCs.

Both the hardware for the spatially resolved EIS measurements and the temperature control hardware for the freeze-start cycling were developed in the scope of the thesis. Therefore, they are discussed in more detail in separate chapters.

3.1.1 Lab-Sized Cell Setup

For the smaller lab-sized fuel cell testing, manually produced MEAs with an active area of $43.56\,\mathrm{cm}^2$ were utilized. Figure 3.1 shows the complete cell setup.

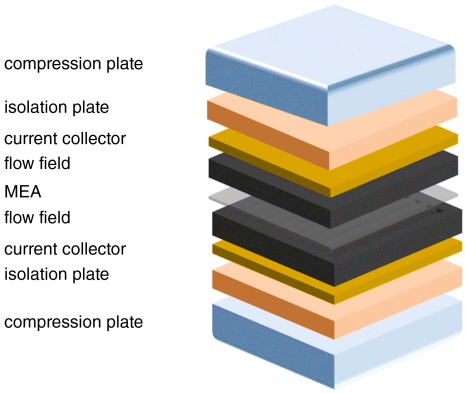

Figure 3.1 Graphic of the lab-sized cell setup used in this work.

The fuel cells were hand-assembled on a laboratory scale within BMW AG facilities. A proton exchange membrane supplied by Gore (M775.15) and commercial platinum/Vulcan catalyst layers with weight loadings of $0.08\,\mathrm{mg/cm^2}$ and $0.4\,\mathrm{mg/cm^2}$ are aligned and hot-pressed. The proton exchange membrane is a PTFE-reinforced composite membrane with a thickness of $15.5\,\mu\mathrm{m}$ and an equivalent weight of $800\,\mathrm{g/mol}$. A $25\,\mu\mathrm{m}$ PEN sub-gasket provides mechanical stability and ensures gas tightness. The lamination is achieved by hot-pressing the MEA in an additional step. Two GDLs are added on the anode (Toray MX003) and cathode side (Toray MX004). The setup in the test bench is completed by graphite flow fields, gold-coated current collectors, isolation plates, and compression hardware. The flow field supplies air and hydrogen in a parallel straight-channel counter-flow configuration. The cell is compressed at a constant $9\,\mathrm{bar}$.

3.1.2 Automotive-Sized Cell Setup

The cell setup is visualized in Figure 3.2. It compromises two compression plates, two temperature control plates (TCPs), two current collectors, two bipolar plates (BPPs), the membrane electrode assembly (MEA), and a printed circuit board (PCB) for spatially resolved measurements.

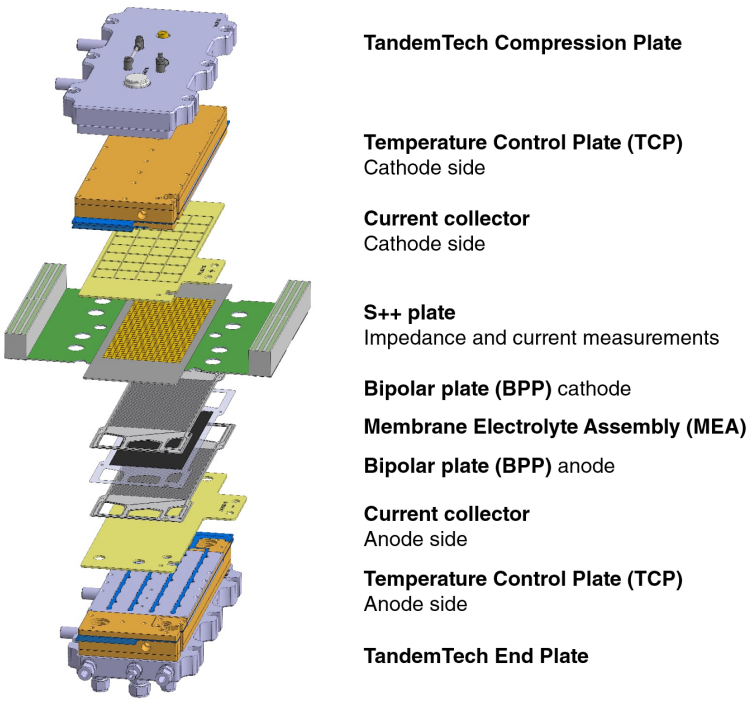

Figure 3.2 CAD graphic of the automotive-sized cell setup used in this work. The measurement plate for local impedance and current measurements is located between the cathodic bipolar plate and the cathodic current collector. The MEA, BPPs, current collectors, and the S++ plate package are sandwiched by the TCPs and the compression hardware.

All experiments in this setup were carried out on industrially produced MEAs with an active area of $285\,\mathrm{cm}^2$ provided by Johnson Matthey Fuel Cells. Platinum on porous carbon was used as catalyst material for the anode and cathode. The platinum loading was $0.05\,\mathrm{mg/cm}^2$ and $0.3\,\mathrm{mg/cm}^2$, respectively. The catalyst layers are applied on a $15\,\mu\mathrm{m}$ PFSA membrane. Commercial GDLs with a thickness of $235\,\mu\mathrm{m}$ and $220\,\mu\mathrm{m}$ on the anode and cathode side complete the MEA (type 29BC and 22BB by SGL Carbon SE).

Two BPPs made of stamped aluminum sheets supply the gases. The impregnated flow fields distribute hydrogen and air in a parallel counter-flow configuration with straight flow channels. The cooling flow is not directed through the BPPs as the TCPs provide thermal control. The

current collectors are solid copper plates with a gold coating to reduce contact resistance. The compression hardware by TandemTech compresses the whole setup with $9\,\mathrm{bar}$. The TCPs and the PCB supplied by S++ will be explained in more detail in chapters 3.1.3 and 3.1.4.

3.1.3 Spatially Resolved Impedance Measurement Setup

For the spatially resolved measurements of current and impedance, a PCB is incorporated between the cathode BPP and the cathode current collector. The PCB was developed and distributed by S++ for current distribution measurements. It comprises 612 measurement shunts on a grid of 18 x 34. Each shunt is made up of a golden contact plate on each side of the PCB, a resistor connecting the two contact plates, and the wiring to tap the voltage on both sides.

To enable EIS distribution measurements, the PCB was combined with an electrochemical workstation, a potentiostat, and a multiplexer. The workstation Zennium X by Zahner-Elektrik GmbH controls the PP241 potentiostat (also Zahner-Elektrik GmbH) and analyses the recorded responses of up to 16 channels. A multiplexer switches between four groups of measurement shunts to increase the number of channels. The wiring is illustrated in Figure 3.3.

The impedance spectra are recorded in galvanostatic mode by applying a current signal to the current collectors. The Zahner workstation records and analyzes the response of 46 measurement points distributed over the active area. An automated script runs the measurements.

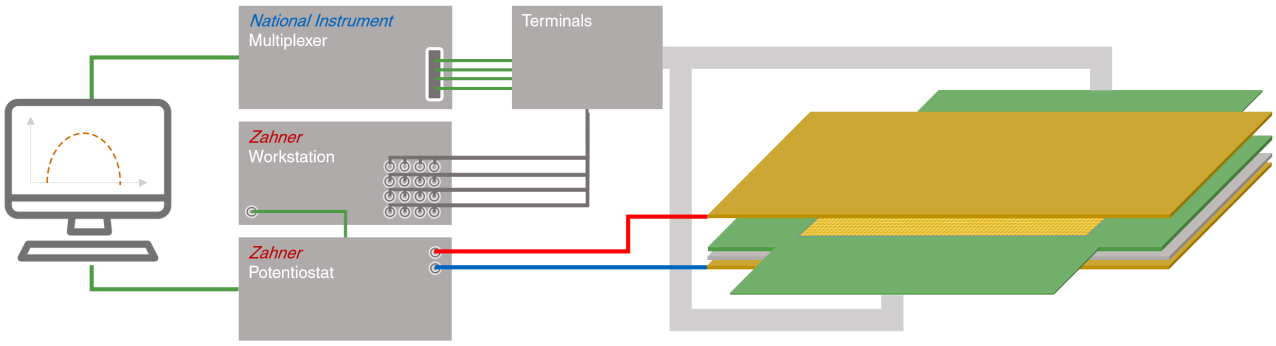

Figure 3.3 Schematic drawing of the setup for locally resolved impedance measurements.

3.1.4 Temperature Control Setup

In the scope of this thesis, a new temperature control unit consisting of an anodic and cathodic temperature control plate (TCP) and a control cabinet was developed.

Each TCP compromises 32 Peltier elements and 32 temperature sensors in a grid of 4 x 8. Logic, communication, and power supply are located in a separate control cabinet to mitigate safety risks. The Peltier elements and the temperature sensors are held in place and connected by two specifically designed PCBs. Each Peltier element measures $30\text{x}30\,\text{mm}$ and has a maximum cooling power of $37\,\text{W}$. The PT1000 temperature sensors are located directly above/below the Peltier elements and measure the temperature with an accuracy of $\pm 0.12\%$ RD. To thermally insulate the elements from each other and at the same time provide good thermal conduction towards the BPPs, the PCBs are embedded in four distinct layers of aluminum and Ultem. A flow field for the cooling medium provides heat removal on the backside of the Peltier elements.

The newly developed temperature control unit was extensively tested before being applied to fuel cell testing. The TCPs enable temperatures ranging from $-25\,°\text{C}$ to $125\,°\text{C}$. A maximum heating rate of $80\,°\text{C}/\,\text{min}$ can be achieved close to ambient temperature (see Figure 3.4 (a)).

According to Newton's law, the maximum heating rate decreases with increasing deviation from the ambient temperature. Applying the norm IEC 60068-3-6 for climate chambers, the standardized heating/cooling rates are 24 / $17\,°\mathrm{C/min}$ [202]. The accuracy is $\pm 0.3\,°\mathrm{C}$ for stable operation in the whole temperature range (see Figure 3.4 (b)).

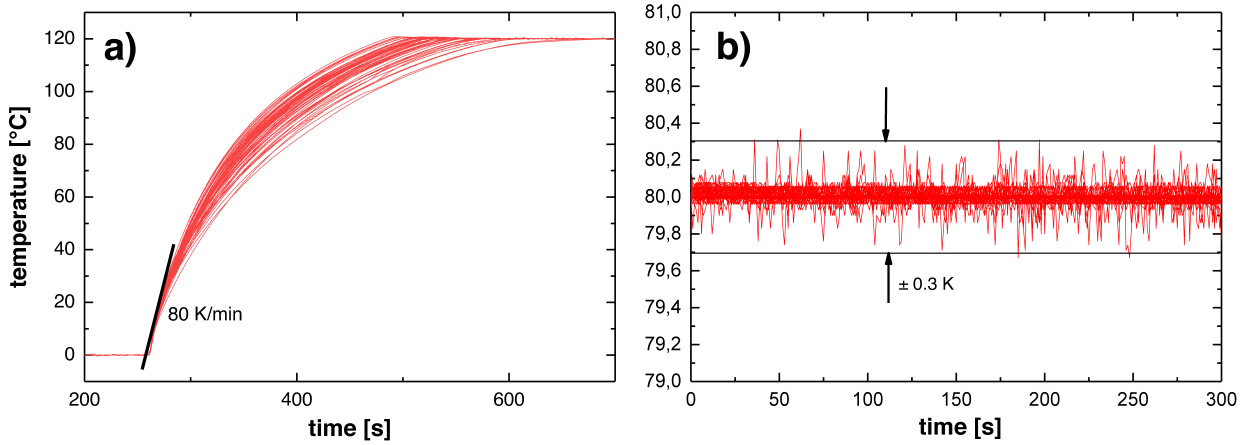

Figure 3.4 Measured temperatures plotted against the time for heating the cell from $0\,°\mathrm{C}$ to $120\,°\mathrm{C}$ (a) and a stable operation point at $80\,°\mathrm{C}$, displaying the control accuracy of the temperature control (b).

The method based on thermoelectric temperature control expands the scope of single-cell testing for PEMFCs. Water-cooled cells commonly only provide a control range of $25\,°\mathrm{C}$ to $95\,°\mathrm{C}$. Climate chambers extend the temperature range but are cost-intensive and lack dynamic temperature change rates. Commercially available climate chambers provide temperature change rates of up to $6\,°\mathrm{C}/\,\mathrm{min}$ according to the norm IEC 60068-3-6 [203, 204]. Temperature gradients, setting hot spots, or temperature differences between anode and cathode are unique to the new hardware. Each Peltier element is controlled autonomously, and temperature differences up to $10\,°\mathrm{C}$ between neighboring elements are possible. Figure 3.5 (a) shows the temperature of all Peltier elements over time when setting a temperature gradient from $10\,°\mathrm{C}$ to $80\,°\mathrm{C}$. The resulting

temperature distribution is captured with a thermal imaging camera in Figure 3.5 (b).

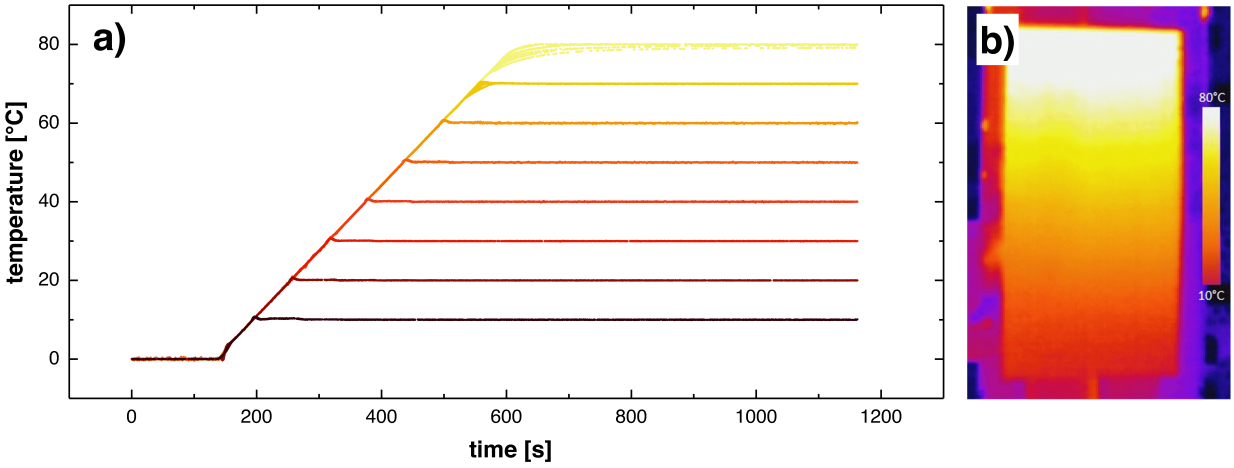

Figure 3.5 (a) Temperature profiles of all 64 temperature sensors while setting a horizontal temperature gradient from $10\,°C$ to $80\,°C$. (b) Image of the anodic TCP from above while applying a horizontal temperature gradient from $10\,°C$ to $80\,°C$. Taken with a thermal imaging camera.

3.1.5 Test Bench

All automotive-sized fuel cell tests were carried out on a FuelCon Evaluator-C1000LT test bench (see Figure 3.6 (a)). The experiments with smaller lab-sized fuel cells are conducted on an Evaluator-C50-LT test bench by FuelCon. Both FuelCon test benches are equipped with a water-cooled electronic load. Up to $1000\,A$ or $3\,kW$ electrical power can be drawn from the test item. The load can be controlled in galvanostatic or potentiostatic mode with an accuracy of $\pm 0.1\,\%$FS. It is connected to the test item via two $300\,mm^2$ cables. A cell voltage monitoring tracks the cell voltage and the current with an accuracy of $\pm 0.05\%$ FS plus $\pm 0.08\%$ RD.

Nitrogen, hydrogen, and carbon monoxide are supplied with a $\geq\ 99.999\%$ purity. The air is sourced from ambient air with several intermediary filter systems. Volume flows can be adjusted via a series of mass flow controllers (MFCs) with an accuracy of $\pm 0.5\,\%$RD $+0.1\,\%$FS. The hu-

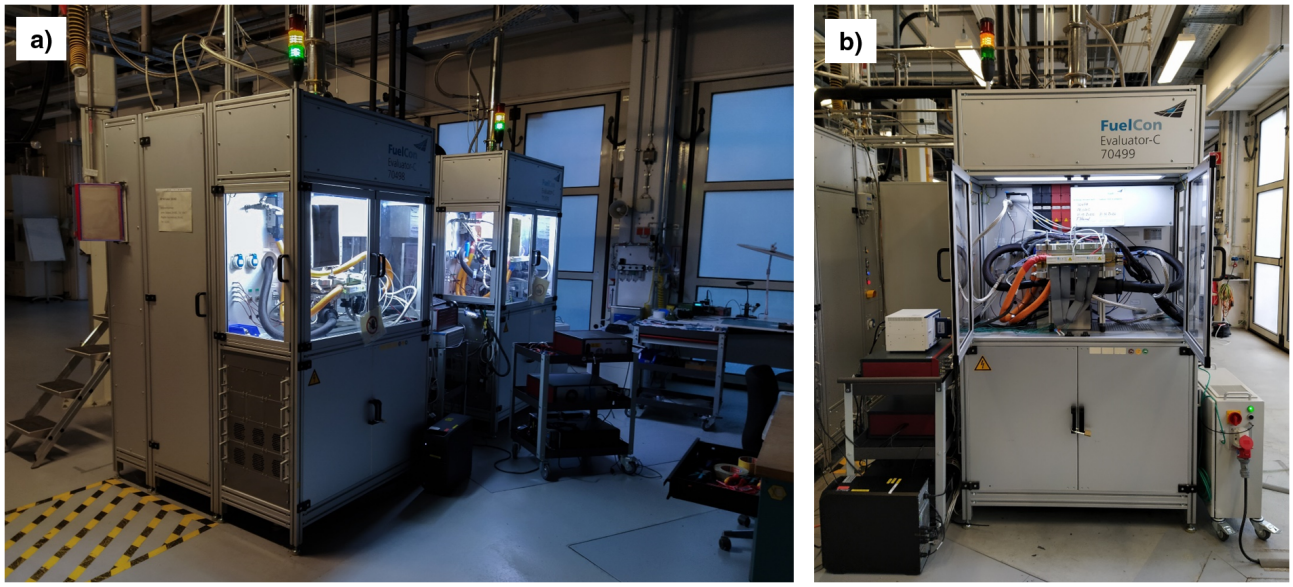

Figure 3.6 FuelCon test benches (a) and the test bench used in this work with the complete test and measurement setup (b).

midity can be adjusted via the dew point temperature T_{dp} with an accuracy of $\pm 1\,°\text{C}$. The dew point temperature and the relative humidity (rh) are connected via the Magnus formula.

$$T_{dp} = \frac{b\gamma}{a - \gamma} \tag{3.1}$$

$$\text{with } \gamma = \ln \frac{rh}{100} + \frac{aT}{b + T} \tag{3.2}$$

Here, T is the cell temperature, and $a = 17.67$ and $b = 243.5\,°\text{C}$ are empirical constants [205].

Heating hoses control the gas temperature with an accuracy of $\pm(0.15\,°\text{C} + 0.002 \cdot T)$, and all downstream pipes are thermally insulated to prevent condensation. The gas flow is controllable with an accuracy of $\pm 0.5\%$ RD plus $\pm 0.1\%$ FS. Additionally, two QPV1 Ultra Precision Electronic Regulators with an accuracy of $\pm 0.5\%$ FS enable gas pressure control.

3.2 Measurement Methods

In the experiments conducted in this work, four characterization techniques were applied: EIS of the cell, spatially resolved EIS, polarization curve measurements, and cyclic voltammetry (CV). This chapter will describe each method's measurement process and further data processing.

3.2.1 Spatially Resolved Electrochemical Impedance Spectroscopy

For the spatially resolved EIS, the spectra of the four groups of measurement points are recorded in series. The recording takes $2400\,\mathrm{s}$ in total. The impedance at each measurement point is recorded for 47 logarithmically distributed frequencies from $0.3\,\mathrm{Hz}$ to $10\,000\,\mathrm{Hz}$. The upper frequency range is measured in both directions to exclude hysteresis effects and ensure the stability of the electrochemical processes involved. The measurement starts at a frequency of $f = 1000\,\mathrm{Hz}$, going upwards to a frequency of $f = 10\,000\,\mathrm{Hz}$, at which the measurement direction is reversed, going down to a frequency of $f = 0.3\,\mathrm{Hz}$. Impedance measurements at frequencies above $f = 1000\,\mathrm{Hz}$ are averaged over ten cycles; lower frequency measurements are averaged over five cycles. The galvanostatic signal has an amplitude of $I_m = 10\,\mathrm{A}$. Due to practicability reasons, the anode acts both as a counter and reference electrode. The obtained data file tabulates the real and imaginary part of the impedance for each frequency.

The raw data is processed within Matlab. The data is checked for validity by applying the Kramers-Kronig check. A circuit model is fitted to the data points, the Nyquist and Bode plots, and the corresponding relative residuals are plotted, and a color map of each fitting parameter across the cell's surface is produced.

Data pre-evaluation demonstrated that inductive artifacts dominated the impedance spectra for

the frequency range above $f > 500\,\text{Hz}$. To eliminate these effects, all wires were shielded as much as possible. However, due to the complex wiring with the electrochemical workbench and the multiplexer, these adjustments could only improve the measurements slightly. Consequently, the fitting is only done for the frequency range from $0.3\,\text{Hz}$ to $500\,\text{Hz}$. As the equivalent circuit model, a modified Randles circuit was chosen. The circuit model consists of a proton resistance R_{proton}, a double layer capacitance C_{dl}, a charge transfer resistance R_{ct}, and a Warburg short element. The Warburg short element is connected in series with the charge transfer resistance and in parallel with the double layer capacitance. The impedance corresponding to the modified Randles circuit is given by equation 3.3, with A_w and B being parameters of the Warburg short element.

$$Z = R_{proton} + \frac{1}{\frac{1}{R_{ct}+A_w(i\omega B)^{-0.5}\tanh(\sqrt{i\omega B})} + i\omega C_{dl}} \tag{3.3}$$

The fitting is realized using the Matlab function *lsqnonlin* to minimize the relative residuals of the real and imaginary parts. The function *lsqnonlin* is based on the multi-dimensional least square fitting algorithm *Levenberg-Marquardt*. The starting parameters $R_{proton,0}$, $C_{dl,0}$, $R_{ct,0}$, $A_{w,0}$ and B_0 and the corresponding upper and lower limits are adjusted for different operating conditions.

The parameters obtained for all 46 measurement points separately are then displayed as a color map with the spatial plane of the cell on the x-y-plane and the fitting parameter plotted as color. The color map is smoothed using the Matlab functions *scatteredInterpolant* and *interp2* on a mesh grid with 120 x 64 interpolation points. The function *scatteredInterpolant* is used for a first natural interpolation to account for the irregular distribution of measurement points. The func-

tion *interp2* smoothes the surface based on a spline interpolation. The input and output of this process are shown in Figure 3.7.

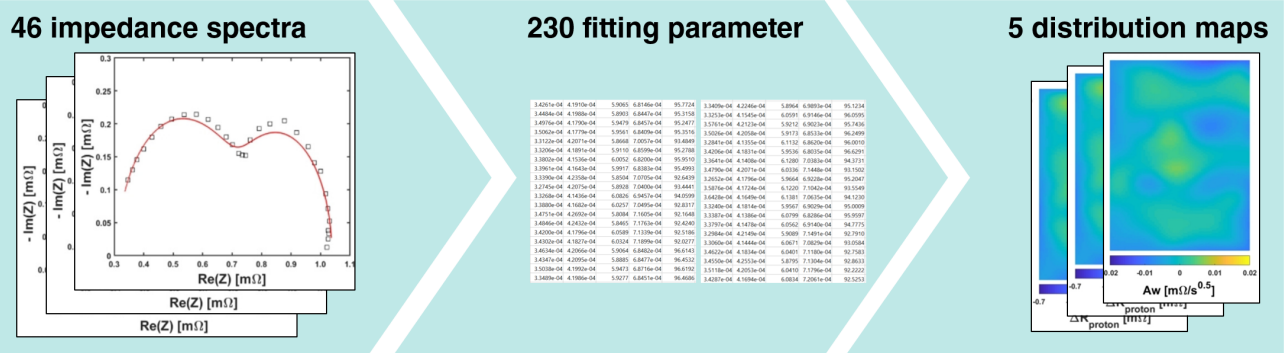

Figure 3.7 Graphical representation of the data visualization process. The 46 values obtained for each fitting parameter from the fitting of each measurement point are mapped in a color map. Smoothed, interpolated surfaces illustrate the spatial distribution of the quantities.

3.2.2 Cell Impedance Measurements

For the conventional EIS measurements, a Zennium X workstation in combination with a PP241 potentiostat by Zahner-Elektrik GmbH was utilized. The Zahner Zennium X workstation includes a frequency generator and analyzer. The EIS measurements were carried out in galvanostatic mode by drawing a direct current (DC) via the potentiostat and adding an AC signal on top. The amplitude for the DC and AC signal was $2\,\mathrm{A}$ for lab-sized fuel cells and $10\,\mathrm{A}$ for automotive-sized fuel cells. The workstation was automated via the Zahner Thales software on a measurement computer.

For the measurements on the automotive-sized fuel cell, a frequency range of $0.3\,\mathrm{Hz}$ to $500\,\mathrm{Hz}$ was found to provide reliable results. A frequency range from $3\,\mathrm{Hz}$ to $10\,000\,\mathrm{Hz}$ was applied on the smaller lab-sized fuel cells.

The Kramers-Kronig check was carried out to ensure the validity of the recorded data. The

ECM was used for the fitting of every recorded spectrum with a non-linear least square algorithm in MATLAB. The corresponding fitting parameters were then averaged over all measurements at each operating point. Regression models for discussing the effect of the hydrogen partial pressure (hpp) on fuel cell characteristics were also fitted in MATLAB, applying a non-linear least square algorithm.

3.2.3 Polarization Curve Measurements

The polarization curve is taken in galvanostatic mode. Starting from the OCV, the current density is increased by $0.1\,\mathrm{A/cm^2}$ every $30\,\mathrm{s}$ (automotive-sized cell) / $10\,\mathrm{s}$ (lab-sized cell). the process is reversed when the voltage drops below $V = 0.45\,\mathrm{V}$ / $0.3\,\mathrm{V}$. However, in the reverse process, the current is decreased by larger steps and longer holding times of $600\,\mathrm{s}$ / $60\,\mathrm{s}$. Longer holding times ensure that the cell is in stable operating conditions. An example of the current history of a polarization curve recording is shown in Figure 3.8 (a), together with the resulting polarization curve (b).

For the polarization curves shown in this work, the voltage values were averaged over $60\,\mathrm{s}$ / $25\,\mathrm{s}$

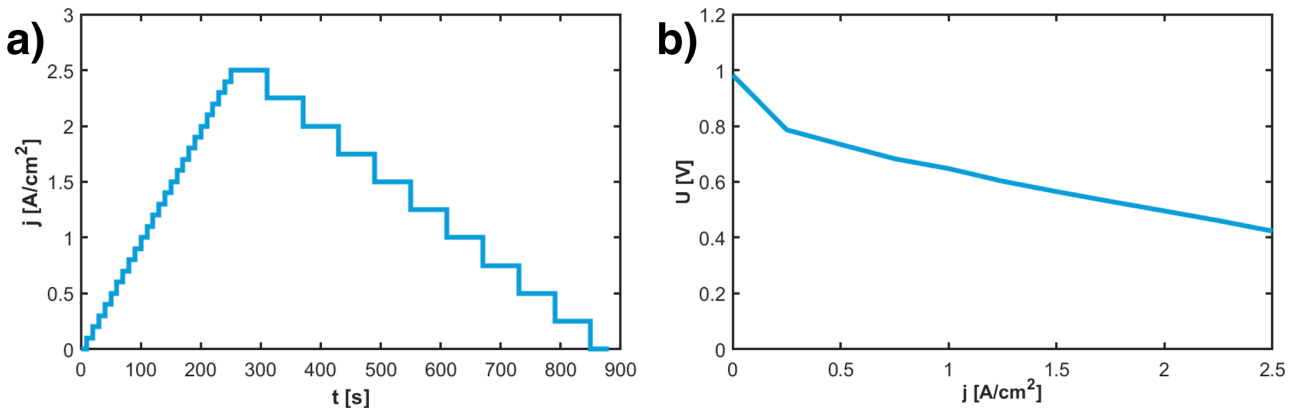

Figure 3.8 (a) Course of the current during the recording of a polarization curve for the lab-sized PEMFC. (b) An example of a resulting polarization curve.

after waiting for $500\,\mathrm{s}$ / $25\,\mathrm{s}$ for the voltage to stabilize at each step. If applicable, the resulting values were then averaged over multiple measurements.

3.2.4 Cyclic Voltammetry

For the determination of the electrochemical active surface area (ECSA), cyclic voltammetry (CV) measurements are conducted within the freeze-cycle degradation test. Similar to the setup for EIS measurements, the anode acts as a counter and reference electrode, and the cathode is the working electrode under investigation.

The cathode is flushed with and operated with nitrogen, while hydrogen is supplied to the anode. The Zahner potentiostat cycles the voltage from $0.1\,\mathrm{V}$ to $1.0\,\mathrm{V}$ and back five times with a voltage change rate of $0.05\,\mathrm{V/s}$. Meanwhile, the current response is recorded. In the final step, the cell is brought back to the stable operation point (SOP), returning to the initial state.

The recorded CV is analyzed with a Matlab script. To obtain the ECSA, the current of the hydrogen adsorption peak is integrated between $V = 0.1 - 0.4\,\mathrm{V}$. The obtained charge is divided by the surface charge of $210\,\mu\mathrm{C/cm^2}$. The ECSA is averaged over the five recorded CV cycles. The corresponding error is calculated using the student t distribution for a significance level of 0.05.

3.2.5 Current Distribution Measurements

The electronics for current distribution measurements are built into the S++ PCBs and can be controlled via the CurrentView software by S++ on a connected PC. The voltage drop over the resistor connecting the two golden plates is measured at each measurement shunt. The software

then calculates the corresponding current value via Ohm's law. The resulting tabulated values are processed with Matlab to plot color maps, with the plot being the active area of the MEA, and the current density plotted as color.

3.3 Test Protocols

In the scope of this work, we will discuss three different experimental studies. First, a parametric analysis of the impact of different operating conditions on the global and local cell impedance was conducted. The fundamental relations obtained were then used to interpret the freeze-start cycling degradation test results. Further, the effect of hydrogen partial pressure (hpp) on cell performance and cell impedance was investigated.

The tests were carried out using the automation software TestWork Enterprise by FuelCon. All operating parameters, including cell voltage and the total current drawn, are tracked by the Test-Work Enterprise Software.

3.3.1 Spatially Resolved Electrochemical Impedance Spectroscopy

Four key determinants were investigated to study the relation between operational conditions and the distribution of specific EIS fitting parameters: cell temperature, relative humidity of the supplied reactants, anodic stoichiometry, and cathodic stoichiometry. All other parameters were held constant. An overview of all operational determinants is shown in 3.1.

Before the actual measurement series, a startup script and a subsequent 9-hour activation step were utilized to achieve stable performance. During activation, a voltage-cycling protocol was employed, consisting of ten cycles between the OCV ($t = 300\,\mathrm{s}$), a galvanostatic step at $j =$

Quantity	Symbol	Value
anodic stoichiometry	λ_{H2}	1.1 to 2.0
cathodic stoichiometry	λ_{air}	1.1 to 2.0
gas temperature	T_{gas}	$85\,°C$
cell temperature	T_{cell}	$50\,°C$ to $80\,°C$
relative humidity	rh	$30\,\%$ to $90\,\%$
back pressure	p	2.00 bar
current density	j	$0.5\,A/cm^2$

Table 3.1 Specified values for the operation points of the experiment on the influence of operating conditions on the spatially resolved impedance.

$0.15\,A/cm^2$ ($t = 600\,s$) and a potentiostatic hold at $V = 0.55\,V$ ($t = 2700\,s$). During the break-in the flow rates are set to $Q_A = 0.13\,dm^3/s$ and $Q_C = 0.40\,dm^3/s$.

At each specified operating point, all parameters are held constant for $1800\,s$ before recording the current and impedance distribution at $j = 0.5\,A/cm^2$. Please refer to Chapter 3.2 for specifics on the measurement methods.

3.3.2 Freeze-Start Cycling Degradation Test

A degradation test was carried out to investigate the impact of temperature gradients during freeze-starts, combining temperature gradients from the TCPs and current and impedance distribution measurements with the S++ plate.

The test protocol is built up of three blocks: A begin of life (BOL) procedure prepares the cell for operation; A characterization step includes polarization curve and CV measurements every 20th freeze-start cycle; The actual freeze-cycle includes a cell shutdown, the subsequent freeze to $-8\,°C$ to $2\,°C$, the startup after the freeze, and a short characterization with current and impedance distribution measurements.

In the BOL phase, the cell is brought to the SOP by slowly ramping up the corresponding op-

erating parameters to prevent startup degradation. Table 3.2 displays the specified parameter values for the SOP.

Afterward, a load cycling break-in procedure brings the cell to its optimal performing state. Ten cycles between the OCV ($t = 300\,\mathrm{s}$), a galvanostatic step at $j = 0.15\,\mathrm{A/cm^2}$ ($t = 600\,\mathrm{s}$), and a potentiostatic hold at $V = 0.55\,\mathrm{V}$ ($t = 2700\,\mathrm{s}$) are carried out. During the break-in the flow rates are set to $Q_A = 0.13\,\mathrm{dm^3/s}$ and $Q_C = 0.40\,\mathrm{dm^3/s}$.

Quantity	Symbol	Value
anodic stoichiometry	λ_{H2}	2.0
cathodic stoichiometry	λ_{air}	2.0
gas temperature	T_{gas}	$85\,^\circ\mathrm{C}$
cell temperature	T_{cell}	$80\,^\circ\mathrm{C}$
relative humidity	rh	$50\,\%$
back pressure	p	$2.00\,\mathrm{bar}$
current density	j	$0.5\,\mathrm{A/cm^2}$

Table 3.2 Specified values for the stable operation point (SOP). These values are set whenever this work refers to a SOP.

The focus of the actual freeze-cycle was to mimic the process of shutting down and restarting an FCEV in sub-zero temperatures as closely as possible. The operational steps like setting flows, humidities, pressures, and temperatures were adapted from the processes implemented in the fuel cell system (FCS) control in FCEVs.

In the first step, the cell is shut down by setting the applied load to zero and ramping down the pressure. The cathode and anode are subsequently flushed with dry gas. The cathode is flushed until the high-frequency resistance (HFR) of the cell drops below $30\,\mathrm{m\Omega}$. The anode is in the following purged for $120\,\mathrm{s}$. After purging the cathode and anode, the cell is cooled and brought to a realistic freeze state. The temperature gradient in the fuel cell stack was simulated with the TCPs freezing the outer region of the cell at $-8\,^\circ\mathrm{C}$ while keeping the inner region at $2\,^\circ\mathrm{C}$. After

holding the cell in this freeze shutdown state, a startup brings the cell back to SOP. Hydrogen and air are supplied to the frozen cell. After reaching the OCV, current and temperatures ramp up in parallel. Finally, the humidification of the gases is switched back on. The characterization on every cycle includes impedance and current distribution measurements at $j = 0.5\,\mathrm{A/cm^2}$. A detailed description of those measurements can be found in Chapter 3.2.

The exact steps of one freeze-cycle are shown in Table 3.3.

Phase	Step	Describtion	Parameters
Shutdown & freeze	load off		$j = 0\,\mathrm{A/cm^2}$
	reduce pressure	ramp down the backpressure	$p_A = 1.2\,\mathrm{bar}$ $p_C = 1\,\mathrm{bar}$
	flush cathode	flush liquid water out of the cathode	$rh = 0\,\%$ $Q_C = 0.17\,\mathrm{dm^3/s}$ HFR<$30\,\mathrm{m\Omega}$
	cool cell	reduce cell temperature	$T_{cell} = 10\,°\mathrm{C}$
	flush anode	flush liquid water out of the anode	$rh = 0\,\%$ $Q_A = 0.15\,\mathrm{dm^3/s}$ $t = 120\,\mathrm{s}$
	freeze cell	set temperature gradient	$T_{cell} = -8\,°\mathrm{C} - 2\,°\mathrm{C}$
	wait	hold temperature gradient	$t = 1800\,\mathrm{s}$
Startup	initialize cell	supply gases & wait for OCV	$rh = 0\,\%$ $Q_A = 0.03\,\mathrm{dm^3/s}$ $Q_C = 0.08\,\mathrm{dm^3/s}$
	draw current		$j = 0.1\,\mathrm{A/cm^2}$
	set temperatures		$T_{cell} = 80\,°\mathrm{C}$ $T_{gas} = 85\,°\mathrm{C}$
	ramp up current	in case $U_{cell} < 0.3\,\mathrm{V}$ set $j = 0\,\mathrm{A/cm^2}$	
	set humidification		$rh = 50\,\%$ $U_{cell} = 0.7\,\mathrm{V}$
Characterization	stable operation point	hold at stable operation point (tab 3.2)	$t = 1800\,\mathrm{s}$
	current distribution		
	impedance distribution		

Table 3.3 Overview of the steps of a single freeze-start cycle.

The freeze-start cycle is repeated until the startup fails. A failure is defined as not reaching an OCV>0.85 V in the step 'initialize cell'. An additional characterization is triggered at BOL and after every 20th cycle. The characterization script contains two measurements: A polarization curve and a CV. Again, details on the characterization techniques are provided in Chapter 3.2.

3.3.3 Electrochemical Impedance Spectroscopy at Low Hydrogen Partial Pressures

Two investigate the impact of the hydrogen partial pressure (hpp) on the fuel cell performance, polarization curves and EIS were conducted in a wide range of hydrogen partial pressure from 36 kPa to 190 kPa. While the backpressure and the hydrogen flow were kept constant, reducing the hpp was achieved by diluting the anode stream with nitrogen. The hydrogen flow was kept at $19.2\,\mathrm{cm}^3/\mathrm{s}$, equalling a stoichiometric factor of 1.5 for the maximum current density of $2.5\,\mathrm{A}/\mathrm{cm}^2$. The airflow on the cathode side was also kept constant at a flow rate of $168.6\,\mathrm{cm}^3/\mathrm{s}$, corresponding to a stoichiometry of 5.5, to minimize the effect of mass transport limitations on the cathode side.

The operating conditions were chosen to be comparable with other experiments from the literature. The cell temperature was set to $60\,^\circ$C with a relative humidity of the cathode and anode gas stream of $50\,\%$. The backpressure in the experiments was held at 2 bar.

Each cell was brought to its optimal performing state by a startup script and a subsequent 9-hour activation step. a voltage-cycling protocol with three galvanostatic steps at $0.2\,\mathrm{A}/\mathrm{cm}^2$, $0.5\,\mathrm{A}/\mathrm{cm}^2$, and $1.2\,\mathrm{A}/\mathrm{cm}^2$ was carried out for the activation. The hold time at each step was 300 s. The cycle

was repeated 15 times before the cell achieved a stable performance.

The hpp was varied in the range between $190\,\mathrm{kPa}$, equaling pure hydrogen, and $36\,\mathrm{kPa}$ corresponding to a nitrogen volume flow of $87.7\,\mathrm{cm}^3/\mathrm{s}$. At each hpp, the cell was flushed with the corresponding gas mixture for $4800\,\mathrm{s}$ before recording a polarization curve. Within the polarization curve measurement, an EIS was measured at $1.0\,\mathrm{A}/\mathrm{cm}^2$.

The test protocol was designed to keep the cell exposure to harsh conditions at a minimal level. Still, to exclude degradation effects from our analysis, all measurements were carried out four times: Twice while decreasing the hpp and twice when ramping the hpp back up. Partial pressures were calculated starting with the total pressure ($200\,\mathrm{kPa}$) and subtracting the water vapor pressure at the relative humidity level ($50\,\%$). The result was divided according to the volumetric flow fraction of hydrogen.

4 Results and Discussion

The results and discussion are based on the following publications:

- **F. Haimerl**, J. P. Sabawa, T. A. Dao and A. S. Bandarenka, Spatially Resolved Electrochemical Impedance Spectroscopy of Automotive PEM Fuel Cells, ChemElectroChem, 2022, 9, e202200069.
- **F. Haimerl**, S. Kumar, M. Heere and A. S. Bandarenka, Electrochemical impedance spectroscopy of PEM fuel cells at low hydrogen partial pressures: efficient cell tests for mass production, RSC Industrial Chemistry & Materials, 2024, 2, 132-140.

4.1 Spatially Resolved Electrochemical Impedance Spectroscopy

Operational parameters like temperature, humidity, and stoichiometry influence the performance and degradation of a PEMFC. In order to get a better understanding of fuel cell operating strategies, it is essential to understand the relationship between spatial differences in electrochemical processes and operational parameters. We studied the spatially resolved impedance response to variations in the cell temperature T_{cell}, relative humidity of the supplied gas rh, and in anodic

λ_A and cathodic stoichiometry λ_C. For simplicity and clarity, only the most prominent effects will be discussed for each parameter.

4.1.1 Flow Field Configuration Aspects

In large PEMFCs, the flow field design is a major determinant of the fuel cell performance. Spatially resolved measurements can help understand the influence of the flow field design and provide verification for flow simulations. In our experiments, a parallel counter-flow configuration was chosen. Figure 4.1 shows the current distribution as a color map (top) and the corresponding average values along the parallel channels (bottom).

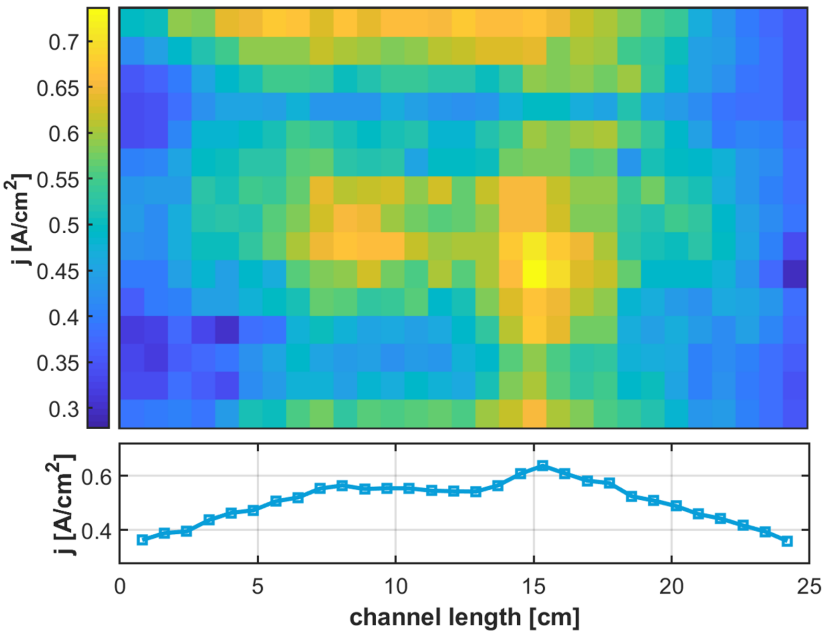

Figure 4.1 Color map of the current distribution (top) and the corresponding average values along the channel length (bottom) at $j = 0.5\,\mathrm{A/cm^2}$ with $T_{cell} = 80\,°\mathrm{C}$, $rh = 50\,\%$, $\lambda_C = 2.0$ and $\lambda_A = 2.0$.

Since most results in this Chapter will be discussed, looking at these two forms of plots, we will explain the two figures in more detail now. The color map shows the current density distribution, looking at the PEMFC from above. The plot area displays the active area of the cell. The flow

channels are oriented in horizontal lines. The air flows from left to right. The hydrogen flows from right to left. The current density is displayed as a color ranging from low values in blue to high values in yellow. Below the color map, the average values along the channel are plotted as a function of the distance from the air inlet. Those explanations will also be valid for all further figures of other parameters in plots similar to those shown here.

From Figure 4.1, we can learn that the current density reaches the highest values in the center region of the active area. Perpendicular to the flow field, one can see a "W-shape" in the current density. The two sides and the middle of the cell exhibit the highest current density. Two digs on either side of the center region with lower current densities are visible between those high current density regions. The W-pattern is characteristic of this exact flow field design [70]. The gas distribution zones, where the gas flow is split and guided into single channels, are crucial for an even flow distribution. Different angles and flow channel widths lead to characteristic patterns in the flow distribution and characteristic current density distributions.

One can see two distinct maxima along the flow field in the middle section, while the current density at the air inlet and air outlet is relatively small. Two different origins are responsible for the low current density at the air inlet and air outlet: The low values at the air outlet are mainly caused by mass transport losses due to reduced oxygen partial pressures. In contrast, the low current density at the air inlet is caused by an increased proton resistance due to a lack of liquid water in this region. Both effects are also visible in the parameter distributions gained by means of EIS. Figure 4.2 shows the average values along the airflow direction of the uncompensated resistance (b), the Warburg short parameter Aw (c), and the current density once again for refer-

ence (a).

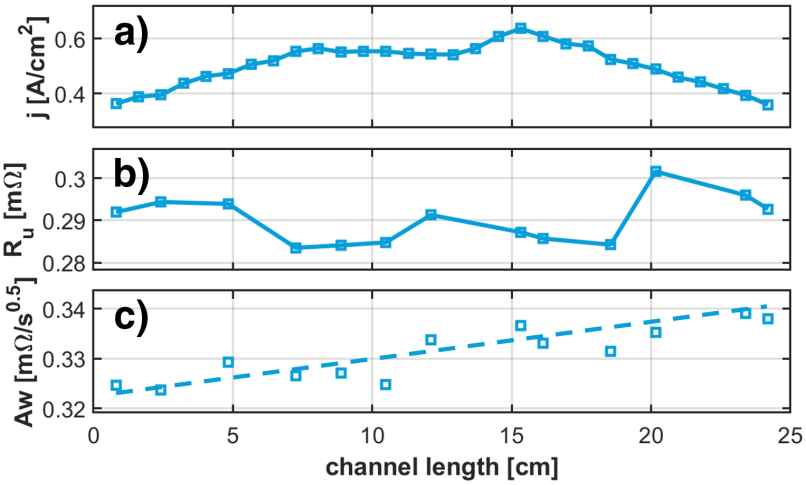

Figure 4.2 Average values along the flow channels of the current density j (a), the uncompensated resistance associated with proton transfer (b), and the Warburg short parameter Aw associated with mass transport (c). The dotted line serves as a guide for the eye.

The uncompensated resistance is associated with the proton transport through the ionomer. As we learned in Chapter 2.2.3, the proton conductivity in the ionomer depends strongly on the water content. At relatively low relative humidities, the gas flow does not supply enough water to humidify the ionomer. In contrast, low humidity gas flow can, in the worst case, draw water out of the ionomer. Therefore, we see maxima in the uncompensated resistance at both the air and hydrogen inlet. Along the flow field, the reaction produces water and hydrates the ionomer with increasing distance from the air and hydrogen inlet. Since the current constantly searches for the path of least resistance, high proton resistances lead to a current redistribution.

Oxygen diffusion to the catalyst sites is usually modeled with the Warburg short element when interpreting EIS data. The corresponding parameter Aw is a measure of the losses from the process of oxygen diffusion. A gradient of Aw along the flow channel is visible in Figure 4.2 (c). The oxygen concentration in the flow is the highest at the air inlet. With increasing channel length, more and more oxygen is consumed by the reaction. Consequently, the oxygen partial pressure

in the gas stream decreases, increasing mass transport losses [82, 170]. At a high stoichiometry, this effect is comparably small. We will see later in Chapter 4.1.5 that the gradient becomes increasingly dominant at low air stoichiometries.

In the literature, most current distribution measurements focus on small-sized $5\,\text{cm}$ x $5\,\text{cm}$ PEM fuel cells. On the smaller length scale, previous research mostly found a single maximum in current density along the channel. [63, 79, 81] Simulations [206] and experiments [70] for longer flow channels hint at two maxima in certain operating conditions. Still, the position and size of the maxima strongly depend on the cathodic stoichiometry, the humidification, and the operating pressure [66, 67].

If one takes a look at the distribution of Aw over the whole cell surface in Figure 4.3 (a), one can see that the region directly at the air outlet (top right corner) exhibits the highest values. This also translates to an increased charge transfer resistance in this area (see Figure 4.3 (b)). As discussed in Chapter 2.3.3, Aw and R_{ct} are directly connected as the charge transfer resistance depends on the surface concentration of the reactants. As visible from the scale of the color bar, the differences are, however, smaller than the variations in Aw.

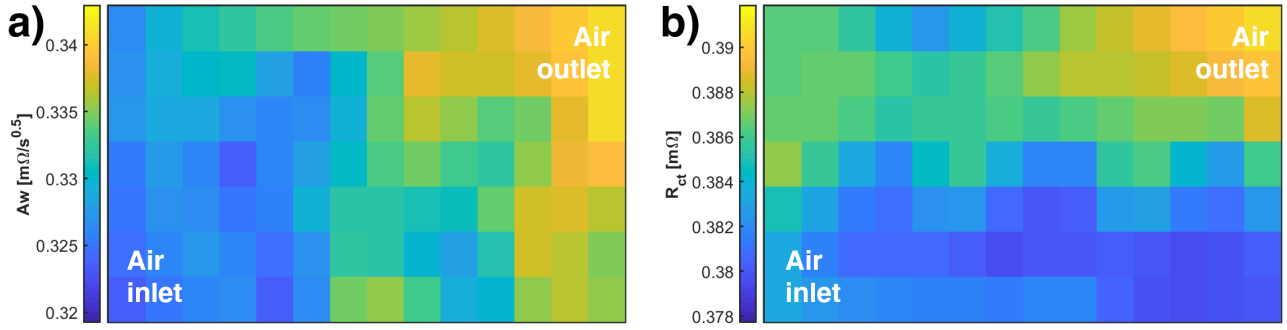

Figure 4.3 Color maps of the EIS fitting parameters A_w (a) and R_{ct} (b) across the cell surface. The distributions were obtained from EIS at $j = 0.5\,\text{A/cm}^2$ in a frequency range from $0.3\,\text{Hz}$ to $1000\,\text{Hz}$.

4.1.2 Humidity Effects

The performance of a PEMFC is largely influenced by the water content in the MEA. If the MEA is too dry, the proton conduction in the ionomer is hindered, and catalyst particles within carbon pores can not be accessed. If the water content is too high, oxygen channels are blocked, and the cell runs into mass transport issues. There are two sources of water for a PEMFC: The water produced by the reaction on the cathode side and the water brought into the cell by humidifying the reactant gases. The humidity of the reactant gases is usually given as relative humidity (rh).

Figure 4.4 (a) shows the cell voltage at $j = 0.5\,\mathrm{A/cm}$ versus the relative humidity of the cathode and anode gas streams. The general trend is that the cell voltage increases with increasing relative humidity of the supplied gas. We do not run into mass transport limitations at $j = 0.5\,\mathrm{A/cm}$, even for $rh = 90\,\%$. High relative humidity seems especially beneficial at high temperatures and high stoichiometries that lead to high flow rates (light blue curve). The combination of high temperatures and flow rates leads to drying out the MEA when not sufficiently humidifying the gas stream. [64, 207]

The EIS fitting values R_u, C_{dl}, R_{ct}, Aw, and B are displayed as a function of the relative humidity in Figure 4.4 (b)-(f). The strongest trends are visible in the uncompensated resistance R_u (b) and in the double layer capacitance C_{dl} (c). Both parameters are directly connected with the water content in the MEA. The double layer capacitance is a measure of the interface between ionic conductors and electric conductors. Increasing the water content increases the interface area between water and carbon/platinum, and, therefore, the capacitance increases.
The uncompensated resistance is associated with the proton conduction within the ionomer. As

the proton conduction in PFSA depends on the humidification level of the ionomer, the uncompensated resistance decreases with increasing water content. In both parameters, one can once again see that these trends are pronounced at high flow velocities and high temperatures.

The trends in the other three parameters are comparably small. Both Warburg short parameters Aw (e) and B (f) are fairly constant over the range of relative humidities. A slight trend is visible in the charge transfer resistance R_{ct}: The resistance decreases in the case of $T = 80\,°\text{C}$, $\lambda_C = 2.0$ with rising relative humidity. Increased water content in the MEA gives access to additional catalyst sites, leading to a higher ECSA and a lower charge transfer resistance [208].

The relative humidity of the reactant gases does not only influence the total performance of the fuel cell, but also the distribution of the characteristic cell descriptors. We will take a closer look at the local differences between a relative humidity of $30\,\%$ and $90\,\%$ at $T = 80\,°\text{C}$ and $\lambda_C = 2.0$. A plot of the corresponding current density distributions and average values along the flow channel is shown in Figure 4.5. Clearly, the maxima and minima are significantly pronounced at $rh = 30\,\%$. While the difference between the highest average value and the lowest value along the flow channel is $0.25\,\text{A/cm}^2$ at $rh = 90\,\%$, it is $0.46\,\text{A/cm}^2$ at $rh = 30\,\%$. At low relative humidities, the ionomer is only sufficiently hydrated in the high current regions in the center of the cell. The resulting low proton conductivity in edge regions leads to a shift of the current density towards the center region, which in turn pronounces the effect further.

Figure 4.6 displays the distributions of the uncompensated resistance at $rh = 30\,\%$ (a) and $rh = 90\,\%$ (b). The variation between center regions and edge regions also transfers to the

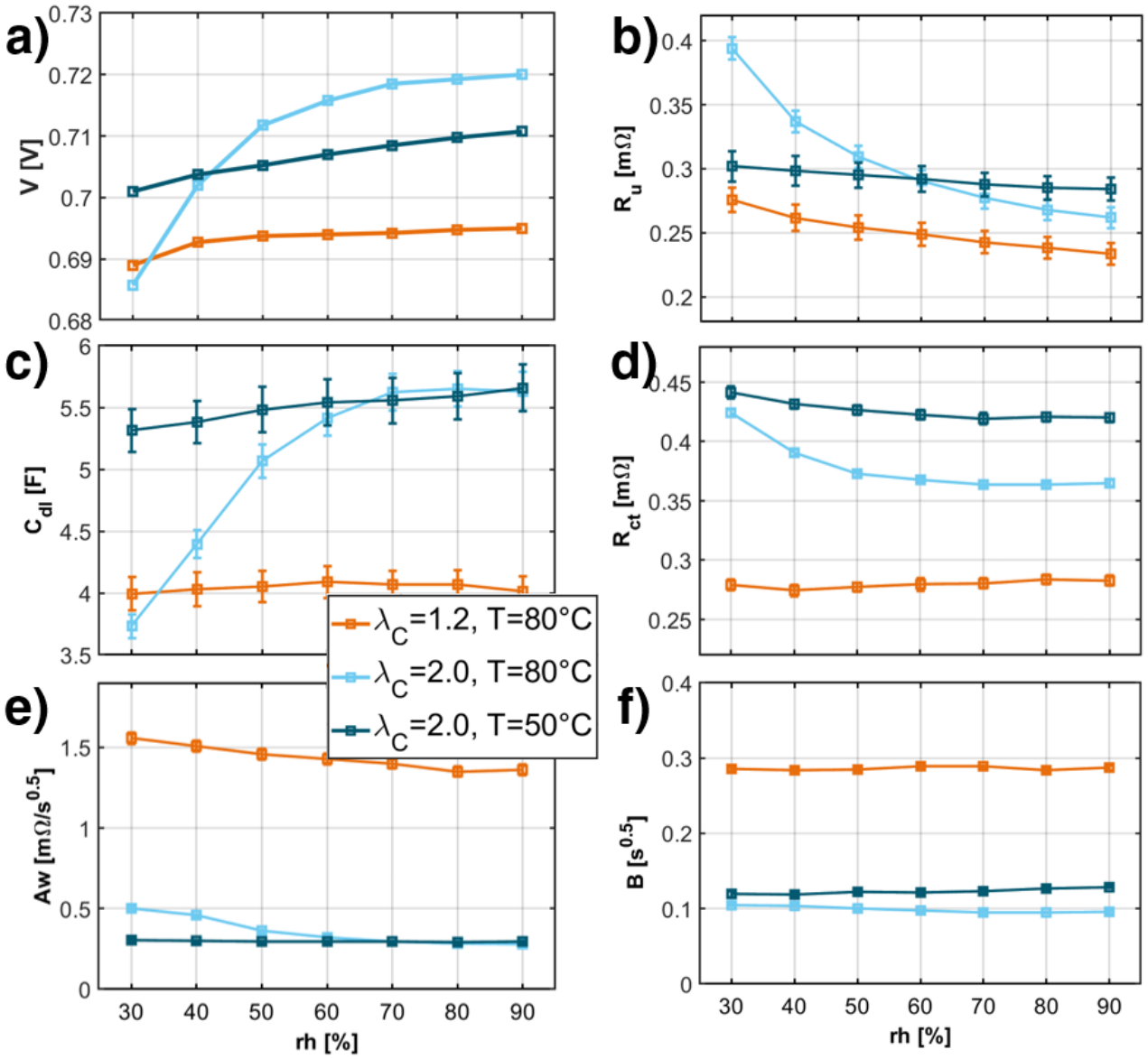

Figure 4.4 Plot of the cell voltage (a), the uncompensated resistance (b), the double layer capacitance (c), the charge transfer resistance (d), and the Warburg short parameters Aw (e) and B (f) as a function of the relative humidity. The relative humidity was varied between $rh = 30\%$ and $rh = 90\%$ at $\lambda_C = 2.0$ and $\lambda_A = 2.0$.

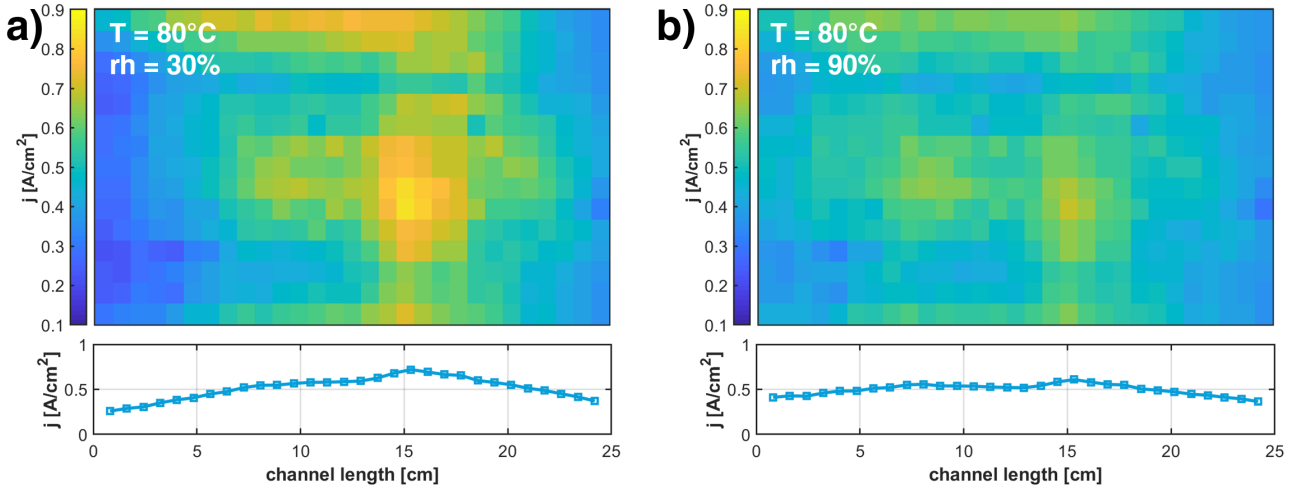

Figure 4.5 Color map of the current distribution (top) and the corresponding average values along the channel length (bottom) at $30\,\%$ (a) and $90\,\%$ rh (b). The measurements were conducted at $j = 0.5\,\mathrm{A/cm^2}$, $T = 80\,°\mathrm{C}$, $\lambda_C = 2.0$ and $\lambda_A = 2.0$.

uncompensated resistance. At $rh = 90\,\%$, the difference between the edge regions (average of the 6 points along the flow channels closest to the air inlet and outlet) and the center regions (average of the 7 points along the flow channels closest to the middle) is $7.9\,\mu\Omega$. At $rh = 90\,\%$, this value increases to $10.8\,\mu\Omega$, equalling a relative increase of $+37\,\%$.

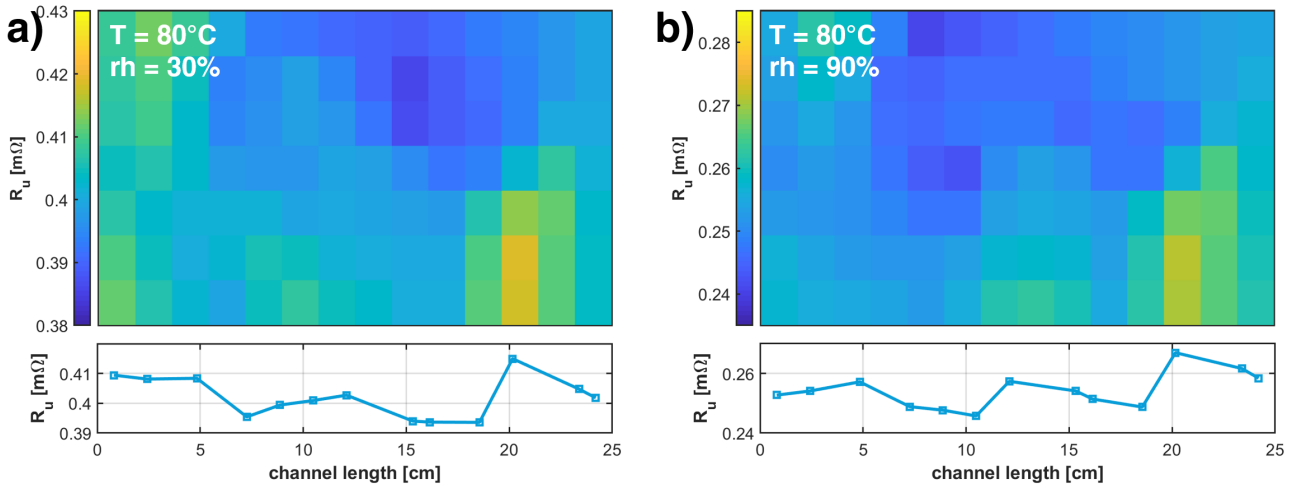

Figure 4.6 Color map of the uncompensated resistance distribution (top) and the corresponding average values along the channel length (bottom) at $30\,\%$ (a) and $90\,\%$ rh (b). The measurements were conducted at $j = 0.5\,\mathrm{A/cm^2}$, $T = 80\,°\mathrm{C}$, $\lambda_C = 2.0$ and $\lambda_A = 2.0$.

4.1.3 Temperature Effects

Besides the relative humidity, the cell temperature has a major influence on all relevant electrochemical processes in a PEMFC. Reaction rates depend on temperature, proton conduction is a function of temperature and the gas transport is affected via a dependence on the oxygen partial pressure. Therefore, we investigated the influence of temperature on global and local phenomena in the common PEMFC operating temperature range $50\,°\text{C}$ to $80\,°\text{C}$.

We will first discuss the effect on global cell descriptors and start with the most important magnitude: the cell voltage. The corresponding plot is shown in Figure 4.7 (a) for different rh between $30\,\%$ and $90\,\%$. Generally speaking, the cell voltage increases with rising temperature. However, the voltage plateaus at $70\,°\text{C}$. The cell voltage decreases for $rh < 80\,\%$ from $70\,°\text{C}$ to $80\,°\text{C}$.

The inconsistent trend originates from several opposing effects that we see in the corresponding EIS fitting parameters. We will go through the fitting parameters one by one and conclude on the most dominant effect at the end of this chapter.

The uncompensated resistance R_u in Figure 4.7 (b) provides a reversed trend to the cell voltage. Already here, two effects balance each other: The proton conduction in PFSA ionomer at a constant humidification level is directly proportional to the temperature [141]. However, in realistic scenarios, increased temperatures lead to drying out of the ionomer. Therefore, the uncompensated resistance decreases with rising temperature at high relative humidities of the supplied gases, but shows the opposite trend at high temperatures and low rhs.

A decreasing water content for $T > 60\,°\text{C}$ and $rh < 70\,\%$ is also confirmed by the double layer capacity C_{dl} trends in Figure 4.7 (d). Decreasing C_{dl} values hint at a reduction of the water-carbon

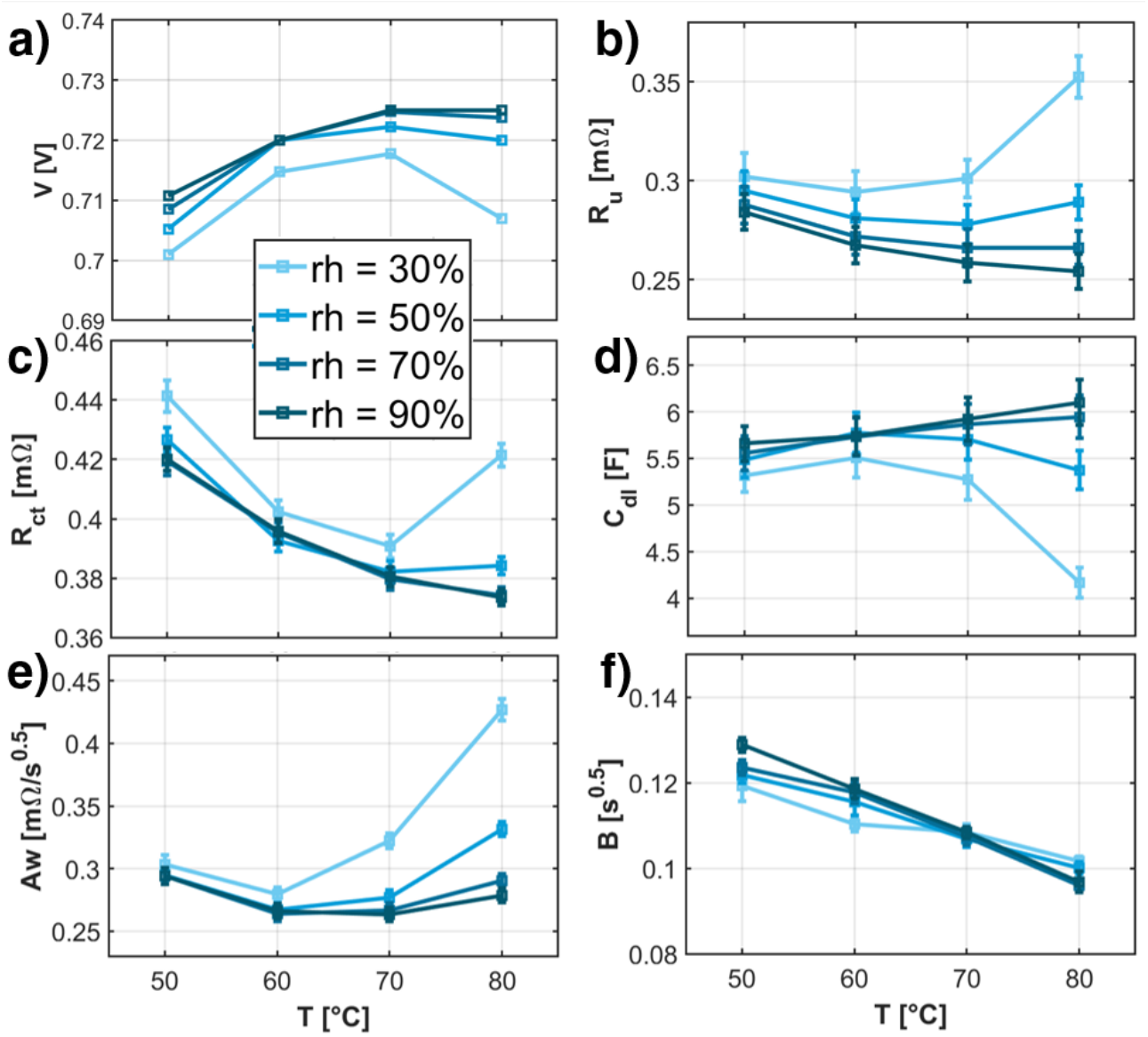

Figure 4.7 Plot of the cell voltage (a), the uncompensated resistance (b), the charge transfer resistance (c), the double layer capacitance (d), and the Warburg short parameters Aw (e) and B (f) as a function of the temperature. The temperature was varied between $T = 50\,°\text{C}$ and $T = 80\,°\text{C}$ at $\lambda_C = 2.0$ and $\lambda_A = 2.0$.

surface area.

Before we will discuss the faradaic phenomena associated with temperature, we will first look at the Warburg short parameter B. Figure 4.7 (f) displays B as a function of T. The fitting parameter is a function of the diffusion constant and the Nernst diffusion layer thickness $B = \delta/\sqrt{D}$. The diffusion layer thickness does not depend on the temperature. As long as the water content in the MEA is constant, we can assume that the diffusion layer thickness is constant. The diffusion constant increases with increasing temperature [209]. Hence, B should decrease with increasing temperature. A inverse proportionality between B and the temperature is observed for all relative humidities. The slope depends on the relative humidity, which we attribute to changes in the water content in the MEA and, thus, changes in the diffusion layer thickness.

Lastly, we will look at the two faradaic parameters R_{ct} and Aw in Figure 4.7 (c) and (e). There are two effects that we have to take into account. The Butler-Volmer equation predicts a relation between the current density and the temperature in the form of the Arrhenius equation: $ln(j/j_0) \propto 1/T$. The corresponding exponential decrease in R_{ct} can be seen for $rh \geq 70\,\%$. At $rh < 70\,\%$, the exponential decrease is over-layered with the second effect of increasing mass transport issues. The increase in mass transport losses is also displayed in the Warburg short parameter Aw: We see a rise of Aw for $T > 60\,°$C predominantly at low relative humidities.
The effects of temperature on mass transport are diverse. There are three factors influencing mass transport: the diffusion constant of oxygen, the partial pressure of oxygen in the gas stream, and the water management in the catalyst layer. From our measurements, one can conclude that dry conditions promote mass transport issues at high temperatures.

In the current density distribution in Figure 4.8, one can see a shift of current from the air inlet towards the center of the cell from $50\,°C$ to $80\,°C$. Both the minimum at the air inlet and the maximum at the center of the cell are enhanced. This again indicates that the dry, high-temperature gas flow at the inlet leads to significant performance losses.

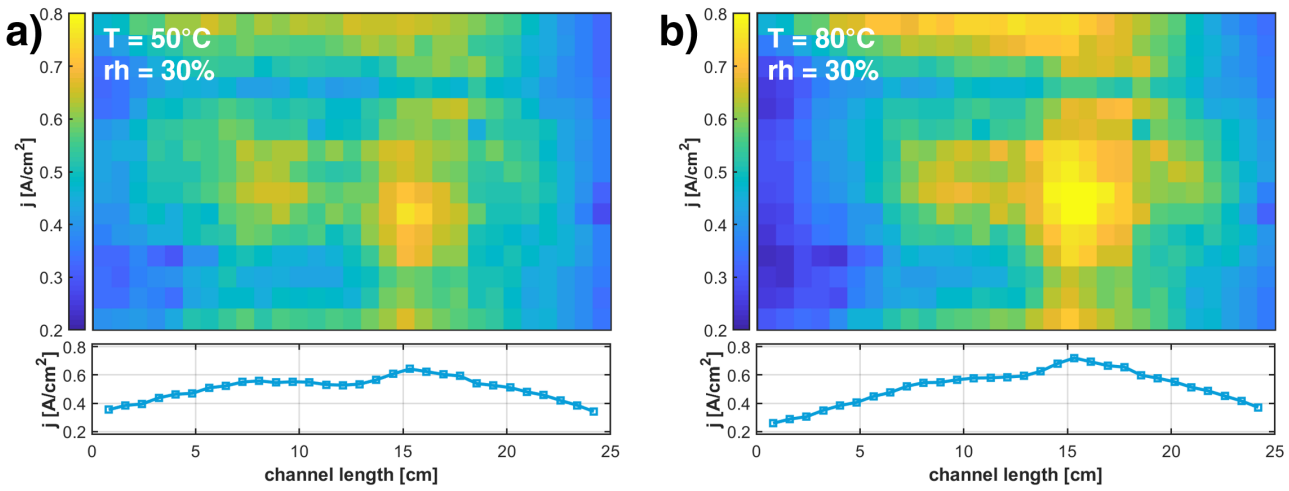

Figure 4.8 Color map of the current distribution at $50\,°C$ (a) and $80\,°C$ (b). The measurements were conducted at $j = 0.5\,\mathrm{A/cm^2}$, $rh = 30\,\%$, $\lambda_C = 2.0$ and $\lambda_A = 2.0$.

4.1.4 Anodic Stoichiometry Effects

Anode processes are usually thought to have minimal contributions to PEMFC losses. Thus, the anode is usually not considered in equivalent circuit models. To verify this simplification, the impact of the anodic stoichiometry on the cell impedance was investigated. The relation between the cell voltage and the anodic stoichiometry is displayed in Figure 4.9 (a). Figures 4.9 (b)-(f) show the corresponding plots of the EIS fitting parameters.

The curves for all parameters, including the cell voltage for $rh \geq 70\,\%$, are a straight line in the range $\lambda_A = 1.15 - 2.00$. As expected, the effect of the anodic stoichiometry is negligible in these

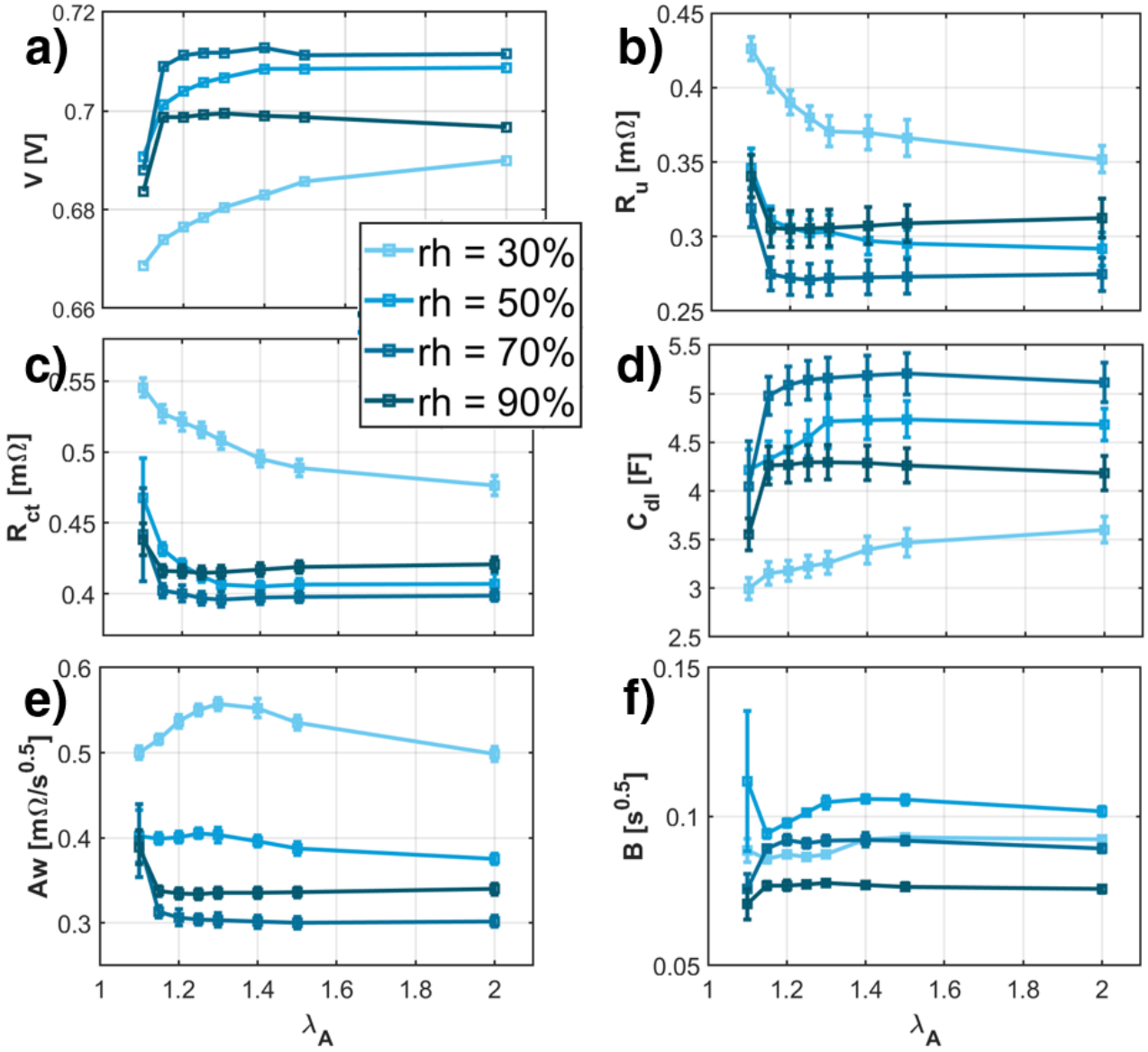

Figure 4.9 Plot of the cell voltage (a), the uncompensated resistance (b), the charge transfer resistance (c), the double layer capacitance (d), and the Warburg short parameters Aw (e) and B (f) as a function of the anodic stoichiometry. The anodic stoichiometry was varied between $\lambda_A = 2.00$ and $\lambda_A = 1.10$ at $T = 80\,°\text{C}$ and $\lambda_C = 2.0$.

operating conditions. However, for $\lambda_A = 1.10$ and for $rh < 70\,\%$ one can see a deviation from the constant behavior.

In the curves for $rh = 30\,\%$ and $rh = 50\,\%$, one can see a decrease in cell voltage with decreasing hydrogen stoichiometry. Similar trends of increasing charge transfer resistance and uncompensated resistance can also be observed. Note, however, that in this experiment, the anodic stoichiometry is directly correlated with the volume flow in the anode stream. Therefore, a decreased stoichiometry means smaller flow velocities and a lower absolute water content brought into the cell. Hence, we attribute the change in voltage and the other cell descriptors to the water management phenomena discussed previously. Still, it does hint that cathode and anode gas humidification impact the cell performance.

At $\lambda_A = 1.10$, the cell voltage diminishes for all rh levels. The drop in cell voltage indicates that the anode becomes relevant at a very low anodic stoichiometry. One can also observe spikes in nearly all fitting parameters at $\lambda_A = 1.10$. As anode processes get non-negligible, the fitting with only one electrode-electrolyte interface oversimplifies the system under investigation. Hence the ECM needs a modification at very low anodic stoichiometries.

To conclude, the disregard of anode processes in the modeling of PEMFC impedance is justified at a reasonably high anodic stoichiometry. However, the simplification might lead to wrong assumptions when operating on a very low anodic stoichiometry. Also, it is important to note that anodic flow velocities might impact the cell performance when operating at low humidities. Future experiments with independent investigations on anodic flow velocity and anodic stoichiometry are necessary to verify further and explain the observed patterns.

4.1.5 Cathodic Stoichiometry Effects

In contrast to the anodic stoichiometry, the cathodic stoichiometry is assumed to affect cell performance significantly. Oxygen transport is a relevant process in PEMFCs, especially when operated with air as a cathode supply. Since, in our experiments, the cell is operated in galvanostatic mode we see the influence of reduced cathodic stoichiometry in the cell voltage. The voltage values as a function of the stoichiometry for different relative humidities are displayed in Figure 4.10 (a).

The cell voltage increases with increasing stoichiometry. The voltage exhibits a monotonous rise at high relative humidities, $rh \geq 50\,\%$. Only at $30\,\%$ rh the voltage reaches a maximum at $\lambda_C = 1.30$, followed by a slight decrease for $\lambda_C > 1.30$. A similar behavior was already previously observed by Chen et al. [210].

Decreasing the air stoichiometry leads to an increase in mass transport issues. The Warburg short parameter Aw, which is directly associated with oxygen diffusion, rises significantly with decreasing stoichiometry (see Figure 4.10 (e)). According to equation 2.50, theory predicts a hyperbolic function of the concentration, which directly relates to the stoichiometry. Hence, the experimental data fits the theory very well. The difference in A_w for different relative humidities is minimal, suggesting that water transport is not an issue.

As mass transport is the dominant contribution in the impedance spectra at low air stoichiometries, the trends in other EIS fitting parameters must be evaluated carefully in the region $\lambda_C < 1.30$. Still, in Figure 4.10 (b), one can observe a trend of rising uncompensated resistance values with increasing cathode stoichiometry. The gradient is larger at low relative humidities, indicating

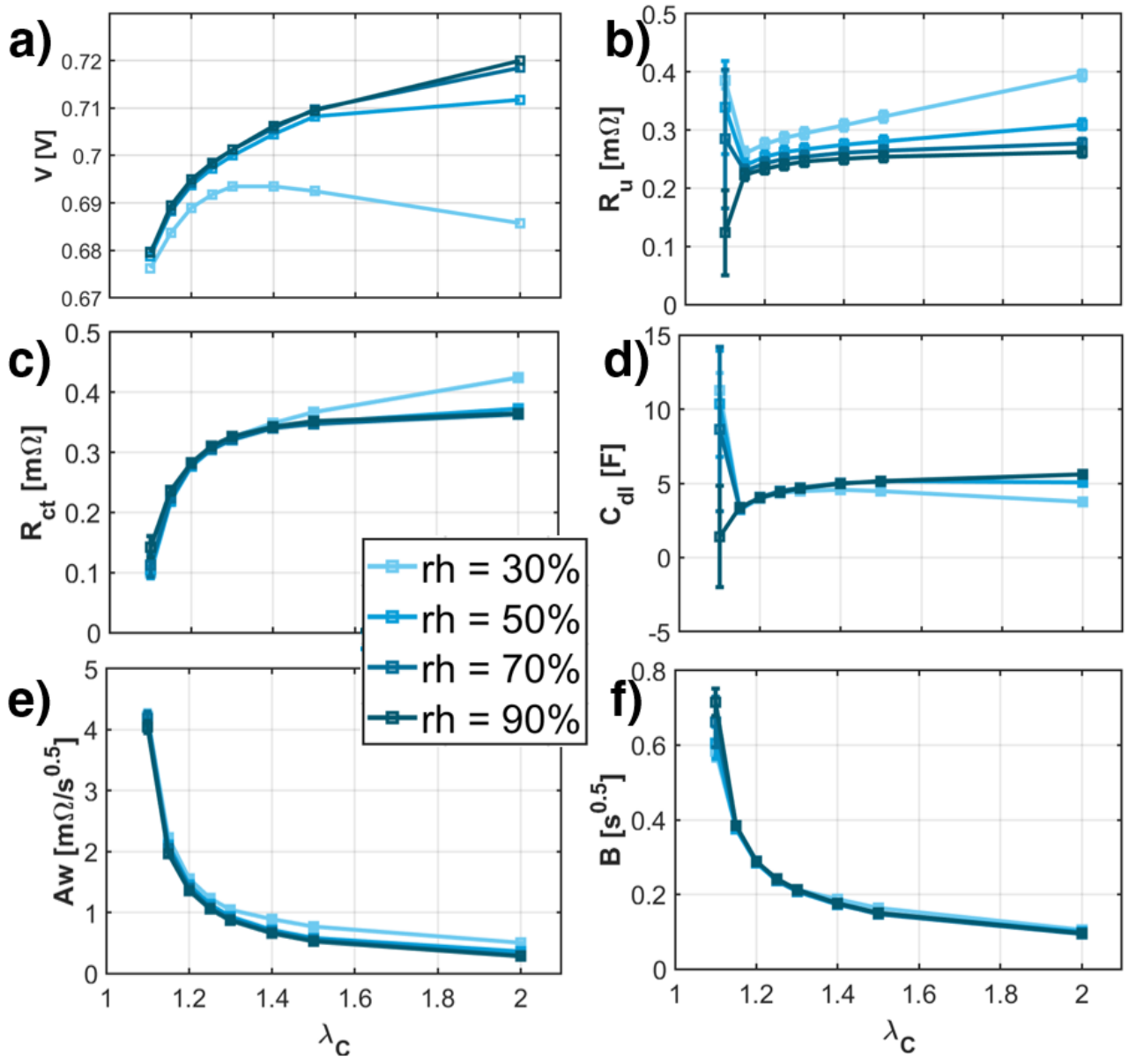

Figure 4.10 Plot of the cell voltage (a), the uncompensated resistance (b), the charge transfer resistance (c), the double layer capacitance (d), and the Warburg short parameters Aw (e) and B (f) as a function of the cathodic stoichiometry. The cathodic stoichiometry was varied between $\lambda_C = 2.00$ and $\lambda_C = 1.10$ at $T = 80\,°C$ and $\lambda_A = 2.0$.

that the water content in the MEA decreases with increasing flow velocities at low rh. This is once again confirmed by decreasing double layer capacitance values in the same region in Figure 4.10 (d). Thus, the cell voltage decrease at $30\,\%$ rh for $\lambda_C > 1.30$ can be explained by rising proton conduction losses due to insufficient humidification of the ionomer.

We will take a closer look at the mass transport issues correlated with decreased cathode stoichiometry and study the spatial distribution of the current density and the Warburg short parameter Aw. Figure 4.11 shows the current density distribution (top) and the corresponding average along the flow channel (bottom) for cathodic stoichiometries of 2.00 (a) and 1.15 (b). In both the color map and the profile along the flow channel, a shift of the current maximum towards the air inlet is clearly visible. The current density at the air outlet diminishes.

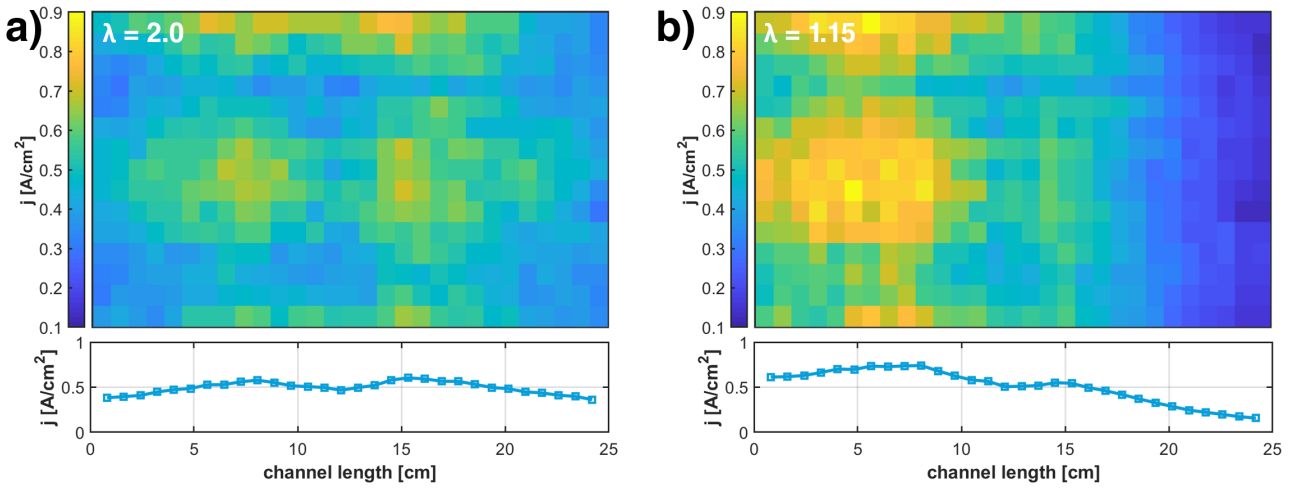

Figure 4.11 Current distributions for cathodic stoichiometries of $\lambda_C = 2.00$ (a) and $\lambda_C = 1.15$ (b) at $T = 80\,°\text{C}$, $rh = 80\,\%$ and $\lambda_A = 2.0$.

The corresponding distributions of the pseudo-resistance Aw are shown in Figure 4.12. For better comparability, the scale of the color bar was set to the same delta. One can observe an increase in the average value from $0.28\,\text{m}\Omega/\text{s}^{0.5}$ to $1.98\,\text{m}\Omega/\text{s}^{0.5}$ and an increase in the gradient

from $0.06\,\mathrm{m\Omega/s^{0.5}m}$ to $0.54\,\mathrm{m\Omega/s^{0.5}m}$. In relative numbers, this equals a 7-fold increase in the average Aw value and a 9-fold increase in the gradient when decreasing the stoichiometry from 2.00 to 1.15. The low cathodic stoichiometry induces mass transport problems and, ultimately, reactant starvation at the air outlet as more and more oxygen is consumed by the reaction along the channels. Simulations show that the partial pressure of oxygen shrinks along the flow direction [170, 211]. Chen et al. [210] found that the proportion of area suffering from oxygen starvation increases from approximately 5% at $\lambda_C = 2.0$ to 11% at $\lambda_C = 1.25$ when operating at $2\,\mathrm{bar}$ operating pressure.

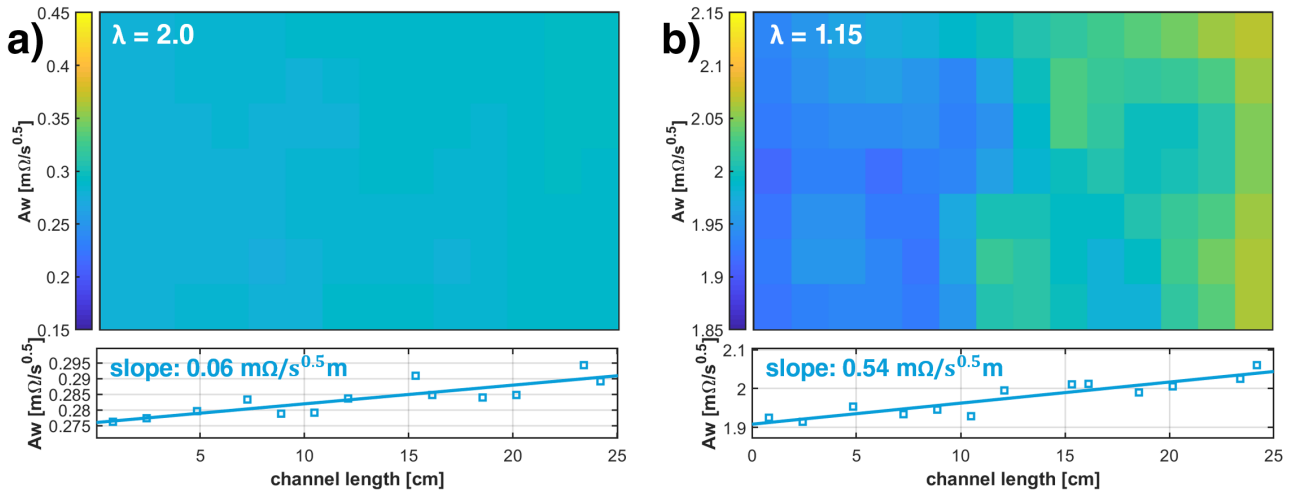

Figure 4.12 Distributions of the Warburg short parameter A_w for cathodic stoichiometries of $\lambda_C = 2.00$ (a) and $\lambda_C = 1.15$ (b) at $T = 80\,^{\circ}\mathrm{C}$, $rh = 80\,\%$ and $\lambda_A = 2.0$. Linear fits to the average values along the flow channel (solid line in the bottom graphs) show the effect of the cathodic stoichiometry on the gradient of Aw.

One can see a hyperbolic correlation when plotting the gradient of Aw versus the cathodic stoichiometry (see Figure 4.13). For large stoichiometries, the Aw gradient approaches $0\,\mathrm{m\Omega/s^{0.5}m}$. When approaching a stoichiometry of 1 ($\lambda_C \longrightarrow 1$), the gradient become indefinitely large $\frac{\delta Aw}{\delta x} \longrightarrow \infty$.

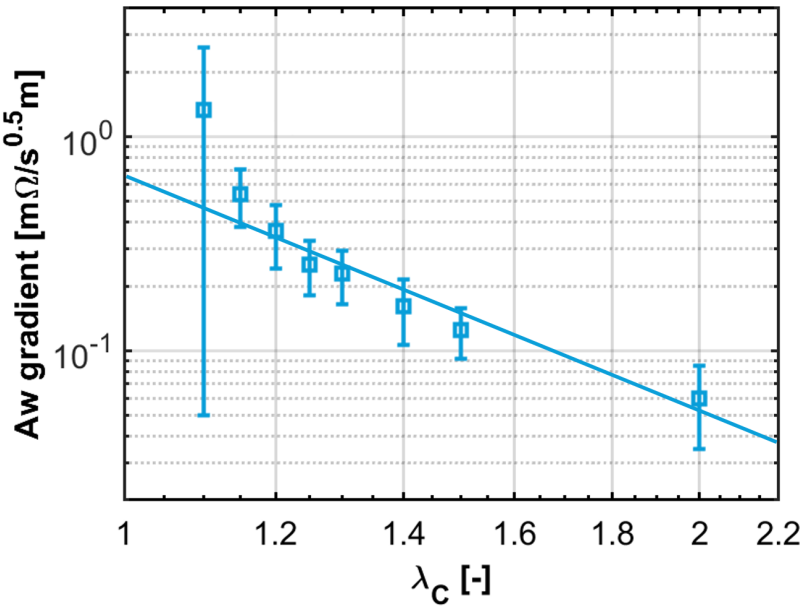

Figure 4.13 Double-logarithmic plot of the gradients of Aw along the channel length as a function of the cathodic stoichiometry at $T = 80\,°\text{C}$, $rh = 80\,\%$, and $\lambda_A = 2.0$. The solid line serves as a guide for the eye.

4.2 Investigation of Local Degradation Effects Caused by Realistic Freeze-Start Cycling

Starting from sub-zero temperatures is a major issue for PEMFCs in FCEVs. Local degradation phenomena due to hydrogen starvation and voltage reversal diminish the FCS lifetime. Therefore, a spatial and time-resolved analysis of EIS parameters could provide critical insights for future freeze-start strategies. In this work, a realistic freeze-start cycling test was performed with mild temperatures of $2\,°\text{C}$ at the middle of the cell and lower temperatures of $-8\,°\text{C}$ in the outer regions. The cell reached its end of life (EOL) after 131 cycles. In cycle 132, the cell did not achieve an open circuit voltage above $0.85\,\text{V}$. A first examination of the MEA revealed membrane pinholes within the outer areas of the cell associated with lower temperatures. The results obtained from repeated in-situ measurements of the polarization curve, the ECSA, current distribution, and EIS are illustrated in the following. We will start with the observed degradation in terms of conventional

measures and progress by discussing separate degradation phenomena with the help of spatially resolved impedance spectroscopy results.

4.2.1 Global Performance Degradation

The degradation is commonly quantified by measuring the voltage degradation at a specified current density. In this experiment, the voltage at $j = 0.5\,\mathrm{A/cm^2}$ is chosen as the degradation measure. The voltage course over 131 freeze-start cycles is shown in Figure 4.14 (a). A 10-point moving average with a $\pm 0.002\,\mathrm{V}$ band guides the eye. Figure 4.14 (b) displays the corresponding polarization curves at BOL and after 120 cycles.

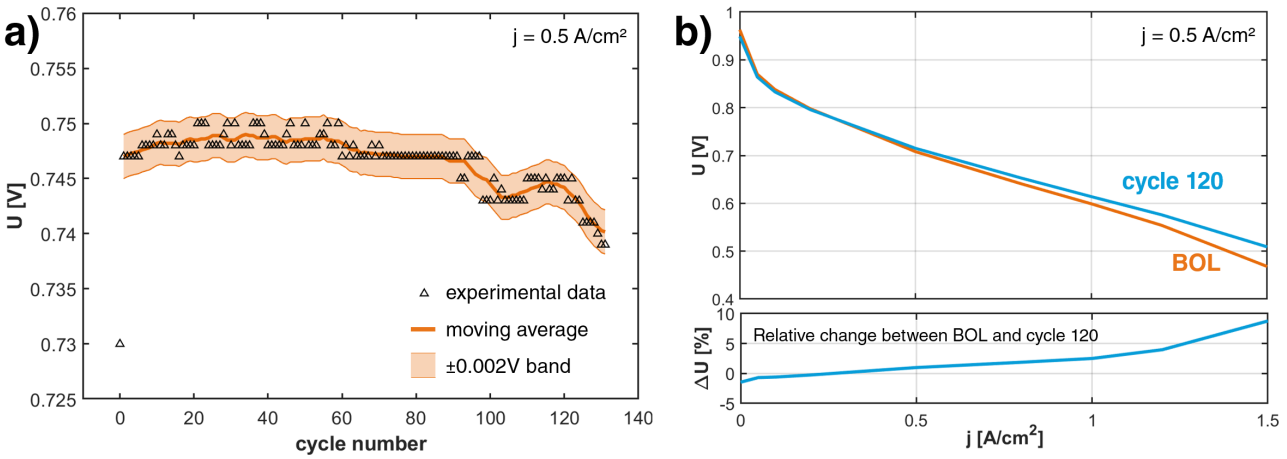

Figure 4.14 (a) Course of the cell voltage at $j = 0.5\,\mathrm{A/cm^2}$. The experimental data points are displayed as black triangles. A 10-point moving average with a $\pm 0.002\,\mathrm{V}$ band in orange illustrates the long-term trend. (b) Plot of the polarization curves at the BOL and after 120 freeze-start cycles (top) and the corresponding relative voltage change ΔU as a function of the current density j (bottom).

The polarization curves show that the voltage increases from BOL to cycle 120 at medium to large current densities. Only for $j < 0.25\,\mathrm{A/cm^2}$, the voltage decreases over the freeze-start cycle experiment. However, the increase in performance can be attributed nearly entirely to the first freeze-cycle. In the voltage history in Figure 4.14 (a) a jump in cell voltage is visible between

BOL and the first cycle. From cycle 1 onward, a slight increase can be observed before the cell voltage plateaus between cycles ~ 20 and ~ 60. After cycle ~ 60, the voltage degrades for the rest of the experiment with a short voltage recovery between cycles ~ 100 and ~ 120. Before approaching the EOL, the voltage decline accelerates.

The performance improvement in cycles 1-20 is attributed to a break-in behavior of the fuel cell. Even though a break-in protocol was performed before starting the freeze-start cycle experiment, phenomena that are associated with PEMFC degradation can also improve cell performance in the beginning. Previous freeze-start cycle experiments found more pronounced degradation rates right from the start. However, the result of certain degradation phenomena is dependent on the MEA composition. Sabawa and Bandarenka [212] proved that voltage degradation strongly depends on the ionomer-to-carbon weight ratio. For low ionomer-to-carbon weight ratios, they found a similar voltage course over freeze-start cycling experiments [212]. Further, in our experiment, degradation in the areas subject to sub-zero temperatures might be balanced by other regions. We will, therefore, look at the development of the current density distribution in the next chapter.

4.2.2 Current Redistribution

Investigating local differences in degradation is crucial to understanding the effect of the temperature gradient during the freeze phase. Current distribution measurements can provide a method to quantify local degradation differences. The current density distribution is displayed as a color map at the BOL and after cycle 120 in Figure 4.15 (a) and (b). The color map shows the active area of the MEA from above, with the air flowing from left to right and the hydrogen flowing from

right to left. The distribution is similar at both points in time. One can see two distinct maxima in the middle of the cell. The current density is comparably low at the air inlet and air outlet.

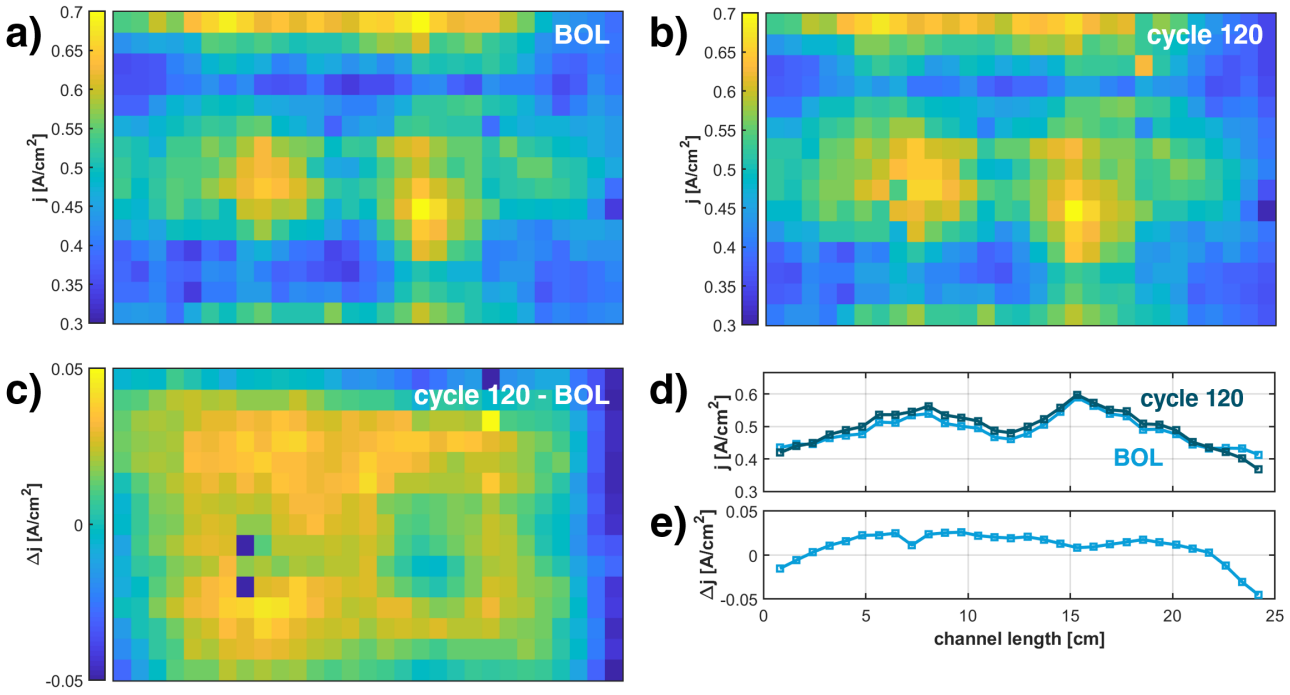

Figure 4.15 The current distribution at $0.5\,\mathrm{A/cm^2}$ at the BOL (a), and after cycle 120 (b). The color map in (c) displays the absolute change in the current density distribution between BOL and cycle 120. The corresponding profiles along the flow channel for the BOL (light blue) and the 120th cycle (dark blue) are plotted in (d). The change in the current profile can be seen in (e).

From the distributions at the BOL and the 120th cycle, the change is not apparent. To reveal local degradation, in Figure 4.15 (c), the current distribution at the BOL is subtracted from the one after 120 cycles. Positive values (yellow) indicate an increased current density at a specific spot. Negative values (blue) translate to a decreased current density. The resulting color map reveals that the current density in edge regions decreases by up to $-0.05\,\mathrm{A/cm^2}$. A higher current density across the rest of the cell compensates for the decrease in edge regions. However, the two peaks observed in Figure 4.15 (a) and (b) do not exhibit increased current densities. Generally, areas that showed a higher current density contribute less to the compensation than regions that showed a modest current density. The described trends can also be seen in the comparison

between the current density profiles for the BOL and the 12th cycle in Figure 4.15 (d) and the profile corresponding to the absolute change in Figure 4.15 (e). The decline in current density is most pronounced in areas close to the air outlet.

The current distribution measurements reveal, for the first time, compensation effects across the fuel cell in degradation testing. The temperature gradient that simulates realistic parking stops in FCEVs at sub-zero temperatures directly translates to a correlated degradation pattern: regions subject to the lowest temperatures of $-8\,^{\circ}\mathrm{C}$ at the edge show the highest decrease in current density. In contrast, the center of the cell, which is brought to mild $2\,^{\circ}\mathrm{C}$, compensates for the high degradation in edge regions. Previous freeze-start cycle degradation tests on small-sized MEAs and with even temperature distributions might not reflect real-world applications.

4.2.3 Electrochemically Active Surface Area Degradation

Degradation mechanisms like platinum dissolution, platinum poisoning, and carbon corrosion all impact the electrochemical active surface area (ECSA) of the MEA. Hence, the ECSA course over degradation experiments can give a more accurate degradation measure than voltage/current degradation rates.

The ECSA was determined every 20th cycle using the hydrogen adsorption peak in the recorded CVs. The plot of the resulting trend over the number of freeze-start cycles is given in Figure 4.16 (a). The ECSA decreases by $26.8\,\%$ over 120 cycles, equaling an average surface loss of $0.083\,\mathrm{m}^2/\mathrm{g}$ per cycle. The literature provides similar results for experiments on small-sized MEAs with starts from $-5\,^{\circ}\mathrm{C}$ and $-10\,^{\circ}\mathrm{C}$ [73, 212, 213]. Wang [214] concluded that the loss of ECSA is the major mechanism leading to cell voltage degradation at freeze-starts.

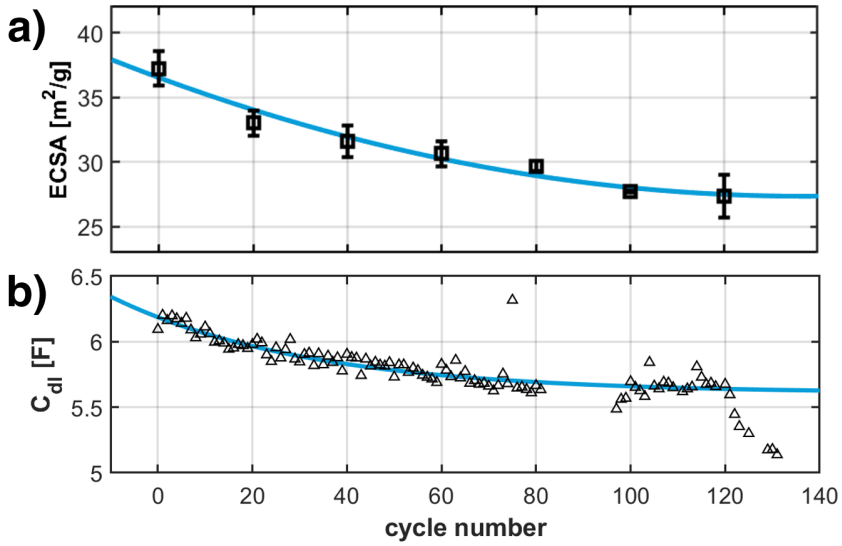

Figure 4.16 (a) Record of the ECSA from the BOL to cycle 120 by means of CV. (b) Record of the double layer capacitance values from the BOL to cycle 131 found by EIS at $j = 0.5\,\mathrm{A/cm^2}$. The solid lines serve as a guide for the eye.

The ECSA describes the area of active catalyst sites. Several phenomena can lead to the loss of active catalyst sites: platinum particles can come loose from the carbon support (platinum dissolution); platinum particles can migrate to form larger particles (Ostwald ripening); active sites can get blocked (platinum poisoning); the carbon support can corrode (carbon corrosion), and platinum particles can lose contact to the ionomer (ionomer degradation).[212, 215] For a detailed overview of typical degradation mechanisms, please refer to the supporting information A.4. Still, it is clear that we need more information to resolve the issue of which degradation mechanisms are responsible for the ECSA loss.

In Figure 4.16 (b), the record of the double layer capacitance C_{dl} over the course of the experiment is plotted. The double layer capacitance is calculated from EIS recordings and is associated with the interface between electron- and ion-conducting material. As the ionomer-carbon interface is considerably larger than the ionomer-platinum interface, loss of C_{dl} is usually associated

with either carbon corrosion or ionomer degradation.

After a slight increase during the 1st cycle, the double layer capacitance decreases from cycle 1 to cycle 121 by $9.8\,\%$. Therefore, one can conclude that the ionomer-carbon interface area is decreasing. Either the carbon support corrodes, the ionomer degrades, or both.

The spatial distribution of the double layer capacitance varies between each measurement. No pattern of change over the course of 131 cycles is visible. Also, the distribution is mainly shaped by the differences between the four groups of measurement points. Since the groups were measured with a time lag, the distribution might be shaped by capacity changes in time rather than in space.

4.2.4 Local Changes in Proton Conduction

Another EIS parameter that can be associated with certain degradation mechanisms is the uncompensated resistance. Figure 4.17 displays the history of the uncompensated resistance R_u. The uncompensated resistance is associated with the proton transport through the ionomer and interfacial resistances. It exhibits a decrease of $14.8\,\%$ from cycle 1 to cycle 121, indicating improved proton conduction. The largest part of the improvement ($9.8\,\%$) is seen in the first 20 cycles. This correlates with the voltage improvement seen in the first 20 cycles of the experiment.

However, improved proton transport can also be an indication of ionomer degradation. Paradoxically, ionomer degradation usually leads to improved proton conduction as the membrane thickness decreases. A thinner membrane leads to shorter proton pathways but also promotes

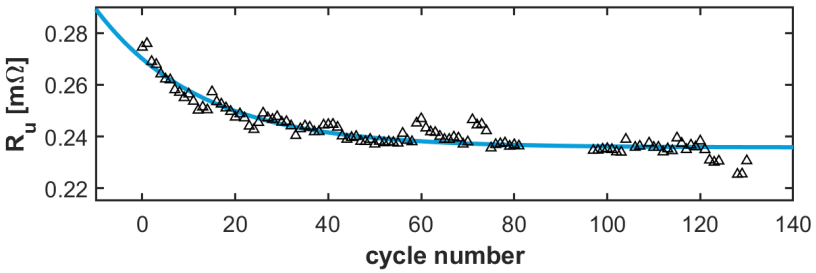

Figure 4.17 (a) Record of the uncompensated resistance R_u from the BOL to cycle 120 determined by EIS at $j = 0.5\,\mathrm{A/cm^2}$. The solid line serves as a guide for the eye.

hydrogen crossover and the formation of hotspots. Ultimately, ionomer degradation can lead to the formation of pinholes.

In contrast, Sabawa and Bandarenka [212] attributed the increased proton conduction to carbon corrosion. They argued that carbon corrosion reduces catalyst layer thickness and results in a higher ionomer-to-carbon ratio in the catalyst layer. As a consequence, the proton conduction in the catalyst layer improves.

Figure 4.18 (a) and (b) display the distribution of the uncompensated resistance at the BOL and after 120 cycles, looking at the active area from above. Again, yellow areas indicate high values and blue regions indicate low values. One can already see slight changes in the spatial distribution from the two distributions. Those become clearer when looking at the color map in Figure 4.18 (c), plotting the absolute change at each spot in color.

The uncompensated resistance decreases over the whole surface of the MEA. Still, one can see a more pronounced decline in edge regions and at two spots in the center of the cell. If we compare the color map to its counterpart for the current density in Figure 4.15 (c), we can see a similar pattern. The two spots in the middle of the cell correlate to the maxima in current density. Regions with high current densities and regions subject to the most negative temperature values

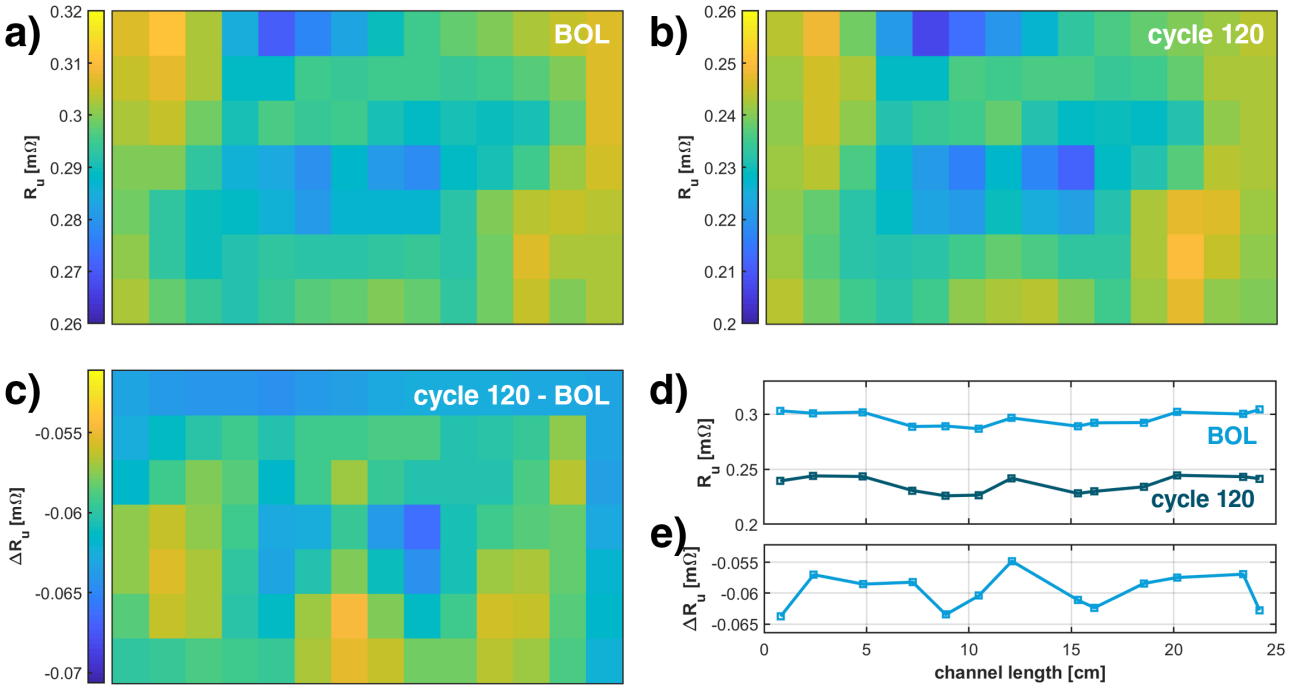

Figure 4.18 The uncompensated resistance distribution at $0.5\,\mathrm{A/cm^2}$ at the BOL (a), and after cycle 120 (b). The color map in (c) displays the absolute change in the uncompensated resistance distribution between BOL and cycle 120. The corresponding profiles along the flow channel for the BOL (light blue) and the 120th cycle (dark blue) are plotted in (d). The change in the uncompensated resistance profile can be seen in (e).

experience the strongest decrease in uncompensated resistance.

Figure 4.18 (d) and (e) show the profiles of R_u along the airflow direction at the BOL and after 120 cycles, as well as the difference between both curves. In the profile in Figure 4.18 (e), the argument becomes even more evident. Edge regions show a stronger decrease in uncompensated resistance than the average. One can attribute this to the freeze with a realistic temperature gradient from $-8\,°\mathrm{C}$ to $2\,°\mathrm{C}$. The outer cell areas experience the biggest temperature differences, leading to increased thermal and mechanical stress. Increased degradation rates in the outer regions promote membrane thinning, the formation of hotspots, and, ultimately, pinholes in the membrane. In cycle 132, the cell did not achieve an OCV above $0.85\,\mathrm{V}$, which was defined as EOL criterion. Ex-situ examination revealed the formation of pinholes in the outer areas of the active area. Pinholes promote hydrogen crossover, which reduces the OCV.

To conclude this chapter, all trends indicate that membrane thinning and the formation of pinholes is a dominant degradation mechanism in realistic freeze-start cycle experiments. It explains both the break-in behavior at the beginning of the experiment and the EOL after 131 cycles.

4.2.5 Faradaic Contributions

Lastly, we will look for signs of degradation in the fitting parameters associated with the faradaic reaction. Figure 4.19 displays the parameters R_{ct} (a), Aw (b), B (c). All three parameters stay fairly constant throughout the experiment. An increase in R_{ct} and Aw can be observed for the last few cycles.

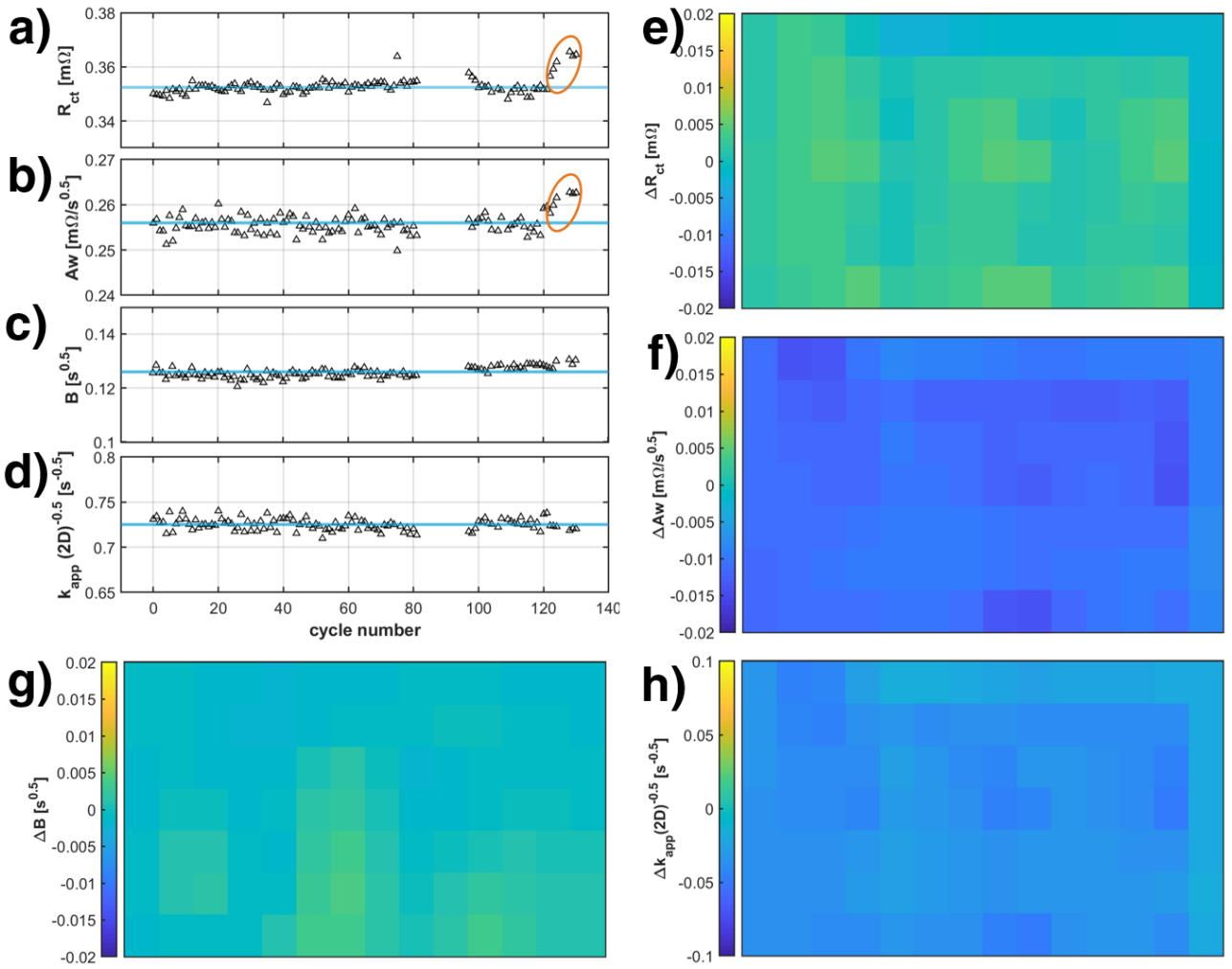

Figure 4.19 The history over 131 cycles for the charge transfer resistance R_{ct} (a), the Warburg short parameters Aw (b) and B (c), and the apparent rate coefficient k_{app} (d). The blue lines mark the average value; the orange circle marks the incline in R_{ct} and Aw in the last 10 cycles. The corresponding parameter changes between BOL and cycle 131 are displayed as color maps in (e)-(h).

The Warburg short parameter B is associated with the diffusion constant D and the Nernst diffusion layer thickness δ. Both magnitudes would only change if there were dramatic changes within the catalyst layer. We, therefore, expect B to be constant.

The constant behavior of R_{ct} and Aw indicates that no changes in the reaction efficiency and the mass transport take place. Further, we can calculate the apparent rate coefficient k_{app} from R_{ct} and Aw if we assume that the diffusion constant D is constant. The corresponding plot is

shown in Figure 4.19 (d). The apparent rate coefficient measures the average reaction rate coefficient per active site. A change in k_{app} would suggest changes in the catalyst particle structure. However, the apparent rate coefficient is constant throughout the experiment. We can, therefore, exclude Ostwald ripening from the list of possible degradation mechanisms.
The rise in the charge transfer resistance R_{ct} and the Warburg short parameter Aw in the last cycles is not visible in k_{app}. Hence, the increase in faradaic losses can only be explained by mass transport issues that emerge from cycle 121 onward. We attribute the mass transport issues to increased hydrogen crossover due to the pinhole formation. Increased hydrogen crossover leads to enhanced mass transport losses on the cathode side [216, 217].

In the spatially resolved analysis of the four discussed faradaic parameters in Figure 4.19 (e-h) we can not observe significant trends. As discussed, B and k_{app} are constant, with no meaningful compensation effects across the cell surface. R_{ct} and Aw reveal a slight but even increase in value over the whole active area.

4.2.6 Summary of the Observed Degradation Mechanisms

To summarize the chapter on freeze-start cycling degradation, we will give an overview over different degradation mechanisms and their relevance during freeze-start cycling. The following six mechanisms will be discussed: platinum dissolution, Ostwald ripening, platinum poisoning, carbon corrosion, ionomer degradation, interfacial delamination, and evolving mass transport issues.

Platinum dissolution was not determined as a major issue in the freeze-start cycle experiment. It can, however, contribute to the loss of ECSA. **Ostwald ripening** would resolve in a change in

the apparent rate coefficient k_{app}, which can not be observed in the experiment. We can not completely neglect **platinum poisoning**. Nevertheless, freeze-start cycling introduces no additional cause for platinum poisoning. ECSA loss and improved proton transport can both be caused by **carbon corrosion**. It is, therefore, thought to be a major contribution to the degradation in our experiment. The ultimate EOL caused by the formation of pinholes originates from **ionomer degradation**. Local improvements in the uncompensated resistance can track membrane thinning in the edge regions subject to the most negative temperatures. Ionomer degradation might also contribute to the loss of ECSA. **Interfacial delamination** was observed in previous experiments [212, 218], but did not occur in our experiment. The **mass transport issues** that evolved shortly before reaching EOL are attributed to the increased hydrogen crossover rate and not structural mass transport limitations.

4.3 Electrochemical Impedance Spectroscopy at Low Hydrogen Partial Pressure

A significant cost factor in PEMFC stack and system production lines is quality control. Conventional quality testing strategies are time-consuming and require high safety measures due to the operation with hydrogen. Reducing the hydrogen concentration in the anode stream would significantly reduce the safety requirements and, hence, costs for quality testing. However, reduced hydrogen partial pressures' impact must be fully understood to develop testing strategies at reduced hydrogen concentrations.

In the scope of this work, the dependency between hydrogen partial pressure (hpp) and fuel cell performance was investigated through polarization curve measurements and EIS in a range from 36 kPa to 190 kPa hpp. For the interpretation of the EIS data, a new equivalent circuit model (ECM) was developed and validated.

4.3.1 The Influence of Hydrogen Partial Pressure on Fuel Cell Performance

First, we look at the relation between voltage and hpp. Figure 4.20 (a) shows the polarization curves for $p_{H_2} = 36$ kPa, 116 kPa and 190 kPa. The hpp was reduced by diluting the hydrogen stream with nitrogen. The total pressure and the hydrogen flow were kept constant. During the $j = 2.5\,\mathrm{A/cm^2}$ hold at a hpp of 36 kPa, the cell voltage dropped below 0.3 V, which was defined as a safety limit in the test protocol. Therefore, the voltage value at $2.5\,\mathrm{A/cm^2}$ does not appear in the plot.

In the polarization curves, one can differentiate between the activation region at low current den-

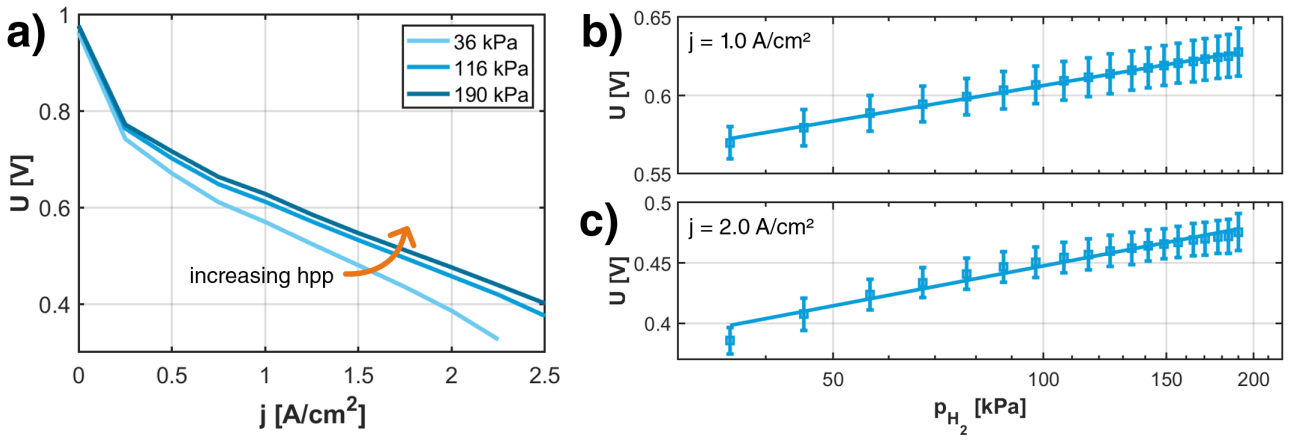

Figure 4.20 (a) Polarization curves at a hpp of $36\,\mathrm{kPa}$, $116\,\mathrm{kPa}$ and $190\,\mathrm{kPa}$. (b) The voltage at $j = 1.0\,\mathrm{A/cm^2}$ as a function of hpp. (c) The voltage at $j = 2.0\,\mathrm{A/cm^2}$ as a function of hpp. The solid lines in (b) and (c) display logarithmic fits to the experimental data.

sities and the ohmic region at intermediate current densities. A mass transport region can not be differentiated. The curves demonstrate a pronounced decline in performance with decreasing hpp at all current densities. Still, the losses become more apparent at high current densities. Zhang et al. [219] simulated the effect of anodic backpressure on the cell voltage. They found that the voltage change rate $\partial U/\partial p_{H_2}$ increases with increasing current density. Similar effects were also observed in high-temperature PEMFCs [220].

In Figure 4.20 (b), the average voltage at $j = 1.0\,\mathrm{A/cm^2}$ is plotted as a function of the hpp. The solid line is a logarithmic fit, highlighting the logarithmic relation between voltage and partial pressure. The voltage difference between the operation with pure hydrogen compared to a hpp of $36\,\mathrm{kPa}$ is $54\,\mathrm{mV}$. The same plot is displayed in Figure 4.20 (c) for a current density of $j = 2.0\,\mathrm{A/cm^2}$. The voltage difference between $36\,\mathrm{kPa}$ and $190\,\mathrm{kPa}$ of $107\,\mathrm{mV}$ is twice as high as at $j = 1.0\,\mathrm{A/cm^2}$. The logarithmic fit is still within the errorbars, but we see a slight deviation from the straight line in the semi-logarithmic plot.

At OCV, the Nernst equation states that the voltage is a logarithmic function of the partial pressure

of the reactants. However, the relation becomes more complicated as we move towards higher current densities. Kinetic losses from anode and cathode, mass transport, and ohmic losses all decrease cell voltage. If we assume that the hydrogen partial pressure does not influence proton transport and cathodic processes and neglect hydrogen diffusion, we arrive at

$$U = U_0 + \frac{RT}{nF} \ln\left(\frac{p_{H_2} p_{O_2}^{0,5}}{p_{H_2O}}\right) + \frac{RT}{\alpha F} \ln\left(\frac{j}{F k_0 a c_{0,H_02}}\right) \tag{4.1}$$

for large anodic overpotentials. The surface concentration c_0 depends on the hpp. Hence, one can get a second logarithmic contribution that increases with increasing current density. We will later see that those assumptions oversimplify the impact of the hpp. Still, this gives a good approximation for evaluating the observed trends in the cell voltage.

4.3.2 Validation of a New Equivalent Circuit Model for Low Hydrogen Partial Pressure

To understand the reasons for the observed voltage dependency, electrochemical impedance spectra were recorded at each hpp. The EIS was conducted at $j = 1.0\,\mathrm{A/cm^2}$ in the frequency range $3\,\mathrm{Hz}$ to $10\,000\,\mathrm{Hz}$. Exemplary spectra for $36\,\mathrm{kPa}$, $116\,\mathrm{kPa}$, and $190\,\mathrm{kPa}$ are plotted in the Nyquist plot in Figure 4.21.

The low-frequency intercept with the x-axis increases with decreasing hpp. In the high-frequency range, an additional feature evolves at low partial pressures. A similar feature was observed in the literature for MEAs with a very low platinum loading on the anode side [199, 221].

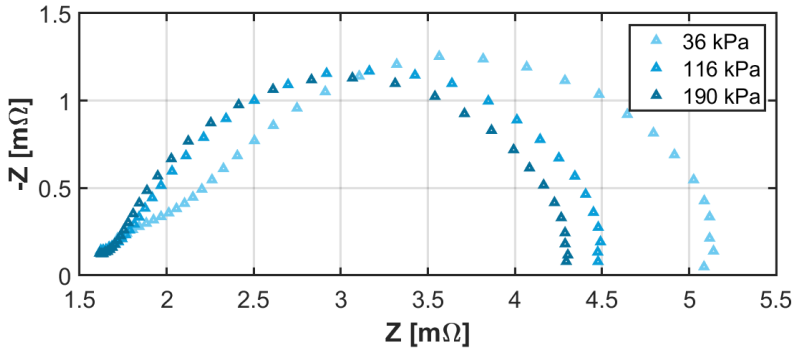

Figure 4.21 Exemplary Nyquist plot of EIS recordings at a hpp of $36\,$kPa, $116\,$kPa, and $190\,$kPa. The data was obtained at $j = 1.0\,\mathrm{A/cm^2}$ in the frequency range $3\,$Hz to $10\,000\,$Hz.

Therefore, we propose a new equivalent circuit model (ECM) for PEMFCs operated at low hydrogen partial pressure. The model comprises a cathode contribution, an anode contribution, and an uncompensated resistance for ohmic losses. The cathode contribution is based on the Randles ECM with a Warburg short element to account for oxygen diffusion. An additional Randles part with an anodic charge transfer resistance for the HOR and an anodic double layer capacitance is introduced to simulate the anode processes. Figure 4.22 displays the ECM together with the resulting fits for $36\,$kPa, $116\,$kPa and $190\,$kPa.

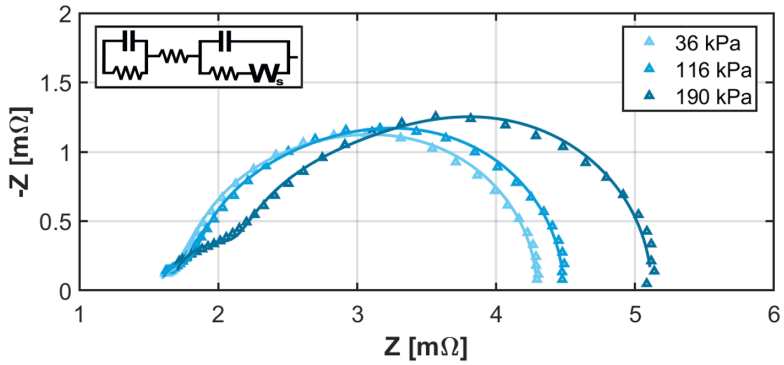

Figure 4.22 Exemplary Nyquist plot of EIS recordings at a hpp of $36\,$kPa, $116\,$kPa, and $190\,$kPa with the corresponding ECM fits. The ECM is shown in the top left corner. The data was obtained at $j = 1.0\,\mathrm{A/cm^2}$in the frequency range $3\,$Hz to $10\,000\,$Hz.

The fit with the proposed model shows good agreement with the experimental data. The relative

residuals are below $5\,\%$ at all hpp levels. With the new ECM, one can now analyze the impedance response for different hpps quantitatively. In Figure 4.23 (a), the anode charge transfer resistance is plotted against the hpp.

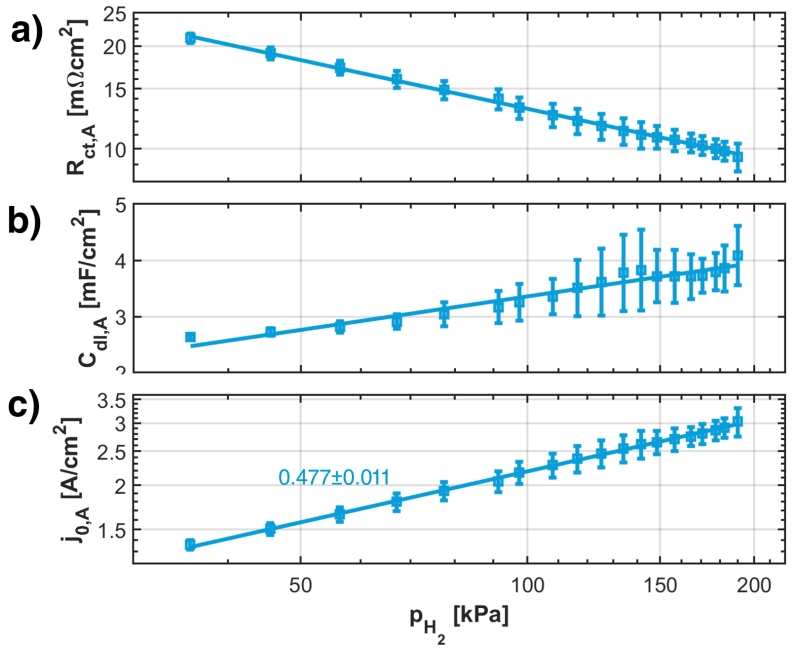

Figure 4.23 (a) Double-logarithmic plot of the anodic charge transfer resistance $R_{ct,A}$ against the hpp. (b) Semi-logarithmic plot of the anodic double layer capacitance $C_{dl,A}$ against the hpp. The solid lines serve as a guide for the eye. (c) Double-logarithmic plot of the anodic exchange current density $j_{0,A}$ versus the hpp. The fit reveals a reaction order of 0.477 ± 0.011.

The anodic charge transfer resistance increases by $123\,\%$ from $190\,$kPa to $36\,$kPa. We expect a dependency between reaction kinetics and partial pressure from the theory. From the linearized Butler-Volmer equation (eq. 2.19), we can derive an equation connecting the anodic charge transfer resistance $R_{ct,A}$ and the anodic exchange current density $j_{0,A}$:

$$R_{ct,A} = \frac{\partial \mu_{HOR}}{\partial j} = \frac{RT}{F j_{0,A}} \tag{4.2}$$

The exchange current density depends on the hydrogen concentration on the catalyst surface c_{H_2}, which is directly proportional to the partial pressure p_{H_2}.

$$\frac{j_{0,A}}{j^*_{0,A}} = \left(\frac{c_{H_2}}{c^*_{H_2}}\right)^m = \left(\frac{p_{H_2}}{p^*_{H_2}}\right)^m \tag{4.3}$$

Here, $j^*_{0,A}$, $c^*_{H_2}$, and $p^*_{H_2}$ denote reference values. m is the reaction order. Hence, we can calculate the reaction order from the slope of the double logarithmic plot of the exchange current density shown in Figure 4.23 (c).

The resulting value for the reaction order is 0.477 ± 0.011. Previous publications found similar reaction orders from micro-polarization measurements in a hydrogen pumping configuration [194, 199, 222]. For the first time, we report a value calculated from EIS measurements in hydrogen/air operation.

The relation between anodic double layer capacitance and hpp is plotted in Figure 4.23 (b). We see a trend of decreasing capacitance values with decreasing partial pressure. Note that low hpp is always associated with high volume flow and high flow velocities in our experiment setup. If we neglect degradation effects or changes in the catalyst layer structure, increasing double layer capacitance indicates a higher water content within the anode [223]. Thus, we conclude that the relation between the anodic double layer and hpp is an effect of increased flow velocities.

Figure 4.24 shows the same effect in the uncompensated resistance. The proton conduction improves with rising hpp. Again, we do not consider structural changes that are highly unlikely in this setup. In that case, improved proton conduction is correlated with a higher water content

within the ionomer [224, 225]. Since we keep the hydrogen flow constant and increase the nitrogen flow to adjust the hpp, low hpp translates to high volume flows in the anode stream. Higher flow velocities at low hpps draw water from the anode catalyst layer. Due to electro-osmotic drag, the water is further drained from the ionomer, worsening the proton conduction.

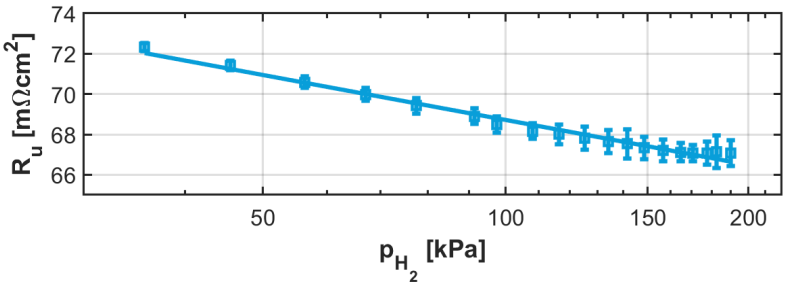

Figure 4.24 Semi-logarithmic plot of the uncompensated resistance R_u as a function of the hpp.

Figure 4.25 depicts the cathodic fitting parameters plotted against the hpp. No clear trend is observable from the semi-logarithmic plot of the cathodic charge transfer resistance $R_{ct,C}$ in (a). Even though the values of the cathodic charge transfer resistance are one order of magnitude larger than the anodic resistance values, the values at high hpp do not differ significantly from those at low hpp. The other three cathodic fitting parameters displayed in (b)-(d) show a dependency on the hpp. The trends are smaller than the relations observed in the anodic fitting parameters. Still, the fact that the partial pressure on the anode side affects cathodic processes is surprising.

As previously described, one can calculate the apparent rate coefficient of the ORR $k_{app,C}$ from

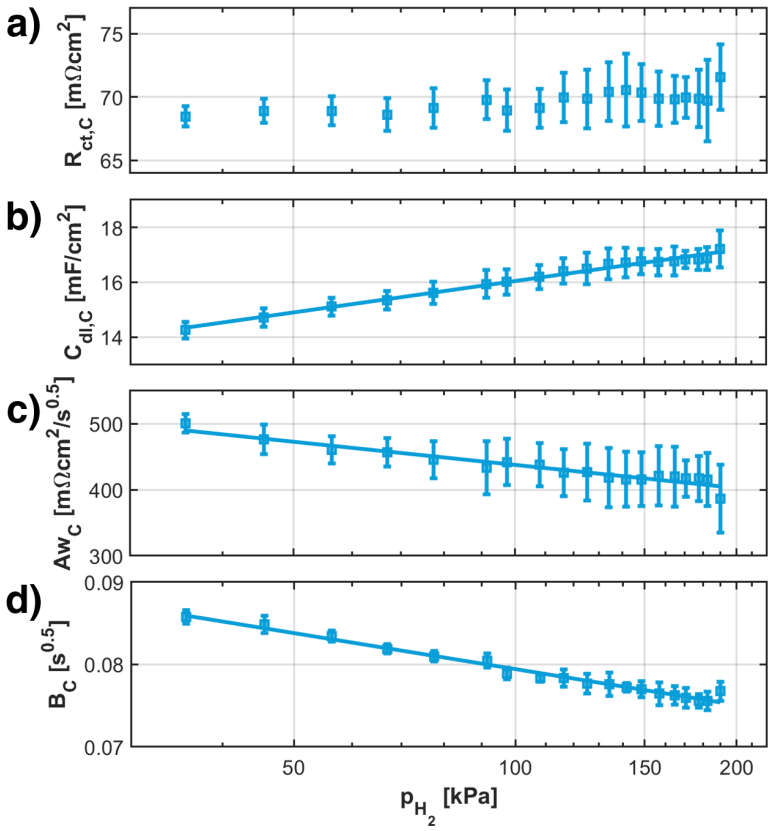

Figure 4.25 Semi-logarithmic plots of the cathodic charge transfer resistance $R_{ct,C}$ (a), the cathodic double layer capacitance $C_{dl,C}$ (b) and the Warburg short parameters Aw_C (c) and B_C (d) as a function of the hpp.

the charge transfer resistance $R_{ct,C}$, and the Warburg short parameter Aw_C. Additionally, one can utilize the second Warburg parameter B to estimate the Nernst diffusion layer thickness δ.

$$\frac{k_{app,C}}{(2D)^{0.5}} = \frac{Aw_C}{R_{ct,C}} \tag{4.4}$$

$$\delta = B \cdot D^{0.5} \tag{4.5}$$

We assume that the main contribution to mass transport losses arises from oxygen diffusion through accumulated water in the catalyst layer [226]. Therefore, the diffusion constant $D = 4.6 \times 10^{-5}\,\mathrm{cm}^2/\mathrm{s}$ for oxygen through water at $60\,^{\circ}\mathrm{C}$ was used for calculations [209, 227]. The calculated Nerst diffusion layer thickness values range between $\sim 5.50\,\mu\mathrm{m}$ and $\sim 6.24\,\mu\mathrm{m}$ (see

Figure 4.26 (b)) and are in line with expected water film thicknesses [228, 229]. Other publications also suggest that diffusion through thin ionomer films is dominant in oxygen transport losses [230, 231]. However, the diffusion layer thicknesses calculated with the diffusion constant of oxygen through Nafion ($D = 7.8 \times 10^{-6}\,\mathrm{cm}^2/\mathrm{s}$ at $60\,^{\circ}\mathrm{C}$) are considerably larger than expected thin film thicknesses [232, 233].

The resulting values of $k_{app,C}$ are plotted as a function of the hpp in Figure 4.26 (a). The calculated values are in the range of previously reported values [73, 212]. A slight trend of increasing apparent rate coefficients with decreasing hpp indicates that the change in hydrogen partial pressure has global effects on cell performance. Various effects can contribute to the trends seen in cathodic EIS fitting parameters: As the overpotential at the anode increases, the cathode potential is affected, too. Already, slightly different cathode potentials can impact the reaction kinetics. Further residual effects of the increased volume flow on the anode side introduce additional aspects, including changes in the hydrogen crossover rate and water management.

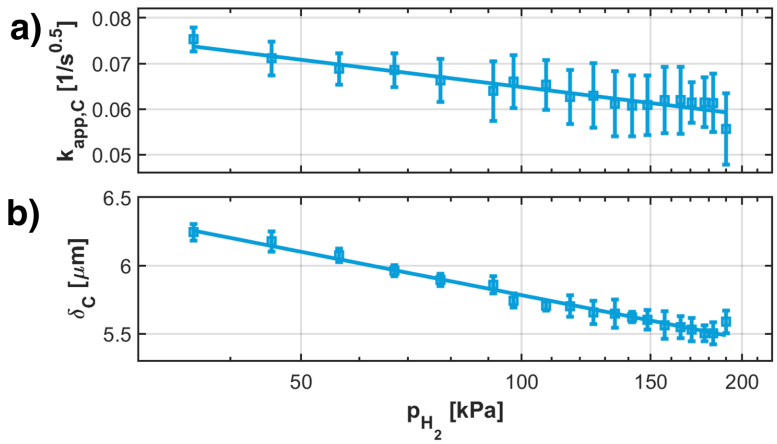

Figure 4.26 Semi-logarithmic plots of the cathodic apparent rate coefficient $k_{app,C}$ (a) and the cathodic Nernst diffusion layer thickness δ_C as a function of the hpp.

5 Conclusion

This study explores applications for electrochemical impedance spectroscopy (EIS) to accelerate the industrialization of fuel cell electric vehicles (FCEVs). As we move from small-series to mass production of polymer electrolyte membrane fuel cells (PEMFCs), time cycles in the design development and production lines become critical. EIS provides a well-established, non-intrusive, and fast measurement method that can be implemented in numerous development processes and into fuel cell quality testing to reduce costs. To understand the fundamentals of EIS in a broader field of applications, experiments on spatially resolved EIS, local degradation effects, and the impact of reduced hydrogen concentrations were investigated.

A new, cost-effective setup for spatially resolved EIS in automotive-sized PEMFCs was designed, implemented, and tested. The results bridge the gap between simulations and industrial fuel cell experiments. High current density regions can be associated with low proton resistance due to high water production. Adjustments in relative humidities of the gas supply can alter this observation. At low relative humidity, the features become additionally pronounced, while high relative humidities reduce the impact of water production. Decreasing the cathodic stoichiometry introduces high mass transport issues at the air outlet, which can be seen in the distribution of the

current density and the Warburg short parameter Aw. The anodic stoichiometry, in contrast, affects the fuel cell performance only marginally for $\lambda_A > 1.1$.

For the first time, local differences in degradation patterns due to temperature gradients during PEMFC cold starts were reported. A realistic freeze-start cycle experiment was conducted with a temperature gradient simulating the gradual cooling of the fuel cell stack during parking in sub-zero temperatures. Higher degradation in the outer regions of the cell, subject to the lowest temperatures, was observed through changes in the current density and uncompensated resistance distribution. EIS measurements indicate that carbon corrosion and ionomer degradation are the main degradation mechanisms. Ultimately, pinholes in the edge regions led to the failure to achieving the required open-circuit voltage (OCV) after 131 cycles. The findings can aid in developing advanced simulations and future operating strategies.

In order to reduce the time and investments spent on quality testing, the study of EIS at low hydrogen partial pressures provides valuable insights for new testing strategies. The cell voltage depends logarithmically on the hydrogen partial pressure. A new equivalent circuit model was presented and validated to interpret EIS at low hydrogen partial pressures. By applying the model, literature values for the anodic reaction order, the cathodic apparent rate coefficient, and the cathodic Nernst diffusion layer thickness were successfully reproduced. The anodic charge transfer resistance, found by fitting the new model to the EIS data, depends on the hydrogen partial pressure with an exponential factor of $m = -0.477$. Further, various effects, including proton availability, potential shifts, and water management, affect the properties of cathode processes as well.

In this work, we showed that EIS can reduce costs in the development phase and the production of PEMFCs. Spatially resolved EIS provides a tool to gain additional insights into fuel cell degradation and the testing of flow field designs. Quality testing strategies based on EIS can decrease the testbench time in the production line. Further, applying EIS at low hydrogen partial pressures can also meet the safety requirements in the production environment. Together, these efforts highlight EIS as a cost-effective tool for development and production and underscore its potential in advancing the industrialization of PEMFC.

A Supplementary Material

A.1 Fuel Cell Types

Since 1839, when the first fuel cell was invented by Grove, several fuels and materials have developed using the principles of a fuel cell [110, 234, 235]. A short overview of the most common fuel cell types is given below.

AFC

Alkaline fuel cells (AFCs) represent one the simplest concept in terms of electrocatalysis. The system consists of two electrodes linked by an aqueous solution of KOH or NaOH absorbed in a matrix. The overall reaction is composed of the hydrogen oxidation reaction (HOR) at the anode and the oxygen reduction reaction (ORR) at the cathode.

$$\mathrm{H_2} + 2\,\mathrm{OH^-} \longrightarrow 2\,\mathrm{H_2O} + 2\,\mathrm{e^-} \qquad \text{anodic reaction} \qquad \text{(A.1)}$$

$$\frac{1}{2}\,\mathrm{O_2} + \mathrm{H_2O} + 2\,\mathrm{e^-} \longrightarrow 2\,\mathrm{OH^-} \qquad \text{cathodic reaction} \qquad \text{(A.2)}$$

$$\mathrm{H_2} + \frac{1}{2}\,\mathrm{O_2} \longrightarrow \mathrm{H_2O} \qquad \text{overall reaction} \qquad \text{(A.3)}$$

The ORR in alkaline environment exhibits lower reaction losses than in acid environment. Therefore, higher efficiencies and specific energy densities can be generated. On top, many metals are stable in an alkaline agent and, hence, the material costs are lower since no expensive noble catalyst materials are needed. However, even atmospheric concentrations of CO_2 cause problems by degrading the electrolyte, which makes mobile applications using air as source for oxygen challenging. Further, sophisticated designs are needed to prevent electrolyte dilution through product water.

Solutions like CO_2 scrubbers or continuous electrolyte supply make AFCs economically uninteresting for mobile applications. Still, the AFC is established in aerospace applications, where high power densities are needed.

PEMFC

PEMFCs utilize a proton conducting polymer membrane as electrolyte. Protons are transferred between the anode and cathode. Accordingly, the water is produced at the cathode side.

$$\mathrm{H_2} \longrightarrow 2\,\mathrm{H^+} + 2\,\mathrm{e^-} \qquad \text{anodic reaction} \qquad \text{(A.4)}$$

$$\frac{1}{2}\,\mathrm{O_2} + 2\,\mathrm{H^+} + 2\,\mathrm{e^-} \longrightarrow \mathrm{H_2O} \qquad \text{cathodic reaction} \qquad \text{(A.5)}$$

$$\mathrm{H_2} + \frac{1}{2}\,\mathrm{O_2} \longrightarrow \mathrm{H_2O} \qquad \text{overall reaction} \qquad \text{(A.6)}$$

The ORR and HOR are catalyzed by platinum nanoparticles on a carbon support. Water management is crucial for PEMFCs as the perfluorinated sulfonic acid (PFSA) electrolyte shows increased proton conduction with rising humidification levels. The main advantage compared to AFCs is that poisoning by CO_2 is negligible and as a consequence air can be used as oxygen

source. CO_2 tolerance and fast startup times make PEMFCs a promising candidate for mobile applications.

DMFC

A similar concept with a polymer electrolyte membrane (PEM) can be used with methanol as fuel. A bi-functional catalyst is needed to split water for the carbon oxidation. Typically a bi- or tri-metal with platinum as basis and Ru, Sn, Mo or a combination of two of them is used as catalyst material. With direct methanol fuel cells (DMFCs) it is possible to directly utilize methanol in a fuel cell (Eq. A.7). However, poisoning of the catalyst surface by intermediates of the carbon oxidation remains a challenge.

$$\mathrm{CH_3OH + H_2O \longrightarrow CO_2 + 6\,H^+ + 6\,e^-} \qquad \text{anodic reaction} \qquad \text{(A.7)}$$

$$\frac{3}{2}\,\mathrm{O_2 + 6\,H^+ + 6\,e^- \longrightarrow 3\,H_2O} \qquad \text{cathodic reaction} \qquad \text{(A.8)}$$

$$\mathrm{CH_3OH + \frac{3}{2}\,O_2 \longrightarrow 2\,H_2O + CO_2} \qquad \text{overall reaction} \qquad \text{(A.9)}$$

PAFC

The phosphoric acid fuel cell (PAFC) was the first fuel cell concept to be commercially available. The name stems from the water-free phosphoric acid used as electrolyte. The acid is contained in an inorganic diaphragm. Phosphoric acid exhibits tolerance to CO_2 and a high conductivity at temperatures above approximately $150\,^{\circ}\mathrm{C}$. The reaction is the same as in a PEMFC (Eq. A.4) and the most widely used catalyst is platinum.

While the lower temperature limit is defined by the temperature depended ion conductivity, above

$220\,°C$ H_3PO_4 undergoes a phase transition, making it unsuitable as electrolyte. Due to evaporation especially at high operating temperatures, H_3PO_4 must be continually refilled.

MCFC

The high temperature molten carbon fuel cell (MCFC) utilizes molten alkali carbonates like Li_2CO_3 or K_2CO_3 absorbed in a $LiAlO_2$ matrix as electrolyte. Carbonate ions ${CO_3}^{2-}$ act as the charge carrier between cathode and anode.

$$\mathrm{H_2} + {\mathrm{CO_3}}^{2-} \longrightarrow \mathrm{CO_2} + \mathrm{H_2O} + 2\,\mathrm{e^-} \qquad \text{anodic reaction} \qquad \text{(A.10)}$$

$$\frac{1}{2}\,\mathrm{O_2} + \mathrm{CO_2} + 2\,\mathrm{e^-} \longrightarrow {\mathrm{CO_3}}^{2-} \qquad \text{cathodic reaction} \qquad \text{(A.11)}$$

$$\mathrm{H_2} + \frac{1}{2}\,\mathrm{O_2} \longrightarrow \mathrm{H_2O} \qquad \text{overall reaction} \qquad \text{(A.12)}$$

CO_2 is consumed at the anode side and produced at the cathode. The produced CO_2 is extracted from the exhaust gas and fed back to the anode. The high operating temperature of $\sim 650\,°C$ enables internal reforming of carbon fuels. The catalysts at both electrodes is normally nickel based and doesn't require noble metals. Startup/shutdown cycles induce high stresses in the electrolyte. Therefore, MCFC are mostly applied for stationary, continuous power applications.

SOFC

In a solid oxid fuel cell (SOFC) a oxygen-ion-conducting ceramic oxide is employed as electrolyte, with yttria-stabilized zirconia being the most popular material. The reaction is split up into the following reactions at anode and cathode.

$$\mathrm{H_2} + \mathrm{O^{2-}} \longrightarrow \mathrm{H_2O} + 2\,\mathrm{e^-} \qquad \text{anodic reaction} \qquad \text{(A.13)}$$

$$\frac{1}{2}\,\mathrm{O_2} + 2\,\mathrm{e^-} \longrightarrow \mathrm{O^{2-}} \qquad \text{cathodic reaction} \qquad \text{(A.14)}$$

$$\mathrm{H_2} + \frac{1}{2}\,\mathrm{O_2} \longrightarrow \mathrm{H_2O} \qquad \text{overall reaction} \qquad \text{(A.15)}$$

High operating temperatures from $600\,^\circ\mathrm{C}$ to $1000\,^\circ\mathrm{C}$ provide challenges for material requirements, but enables fuel flexibility and high efficiencies.. Due to long startup times, the commercial focus is on stationary applications. Perovskites like lanthanum–strontium cobaltite or strontium-doped lanthanum manganite are used as cathode materials and nickel catalyzes the anodic reaction. Intermediate temperature SOFCs, operating at $400\,^\circ\mathrm{C}$ to $700\,^\circ\mathrm{C}$, could reduce material requirements but the search for intermediate temperature ionic conductors is challenging.

A.2 Fuel Cell Electric Vehicles

The Fuel Cell System

The fuel cell stack is usually complemented by peripheral components to regulate the operating conditions. An overview over important components is shown in A.1. These can be summarized in four sub-systems [40, 236]:

- **air management**

  Oxygen for the cathode supply is sourced from the ambient air. To eliminate contamination an air filter is commonly integrated. Subsequently the air is preconditioned by a compressor and a humidifier. Hence, pressure and humidification can be controlled. Mass flow controllers enable the regulation of the gas flow.

- **fuel management**

  Hydrogen is stored at $200\,\mathrm{bar}$ to $700\,\mathrm{bar}$ in a hydrogen fuel tank. Valves regulate the pressure to the operating pressure. As for the air management, the media interface unit preconditions the hydrogen. A recirculation pump feeds hydrogen from the exhaust back to the anode inlet for optimum usage of the costly hydrogen.

- **thermal management**

  Thermal management is a critical design aspect. Most commonly, coolant is utilized in FCEVs. A high voltage coolant pump transports the coolant through a heat exchanger and further through cooling channels in the bipolar plates (BPPs).

- **power and control units**

  The voltage of the fuel cell stack must at all times provide the supply voltage for the electric

motor. Therefore a DC/DC converter regulates the output voltage to the required value. A fuel cell control unit translates the power requirements from the vehicle into operating parameters for all fuel cell system components.

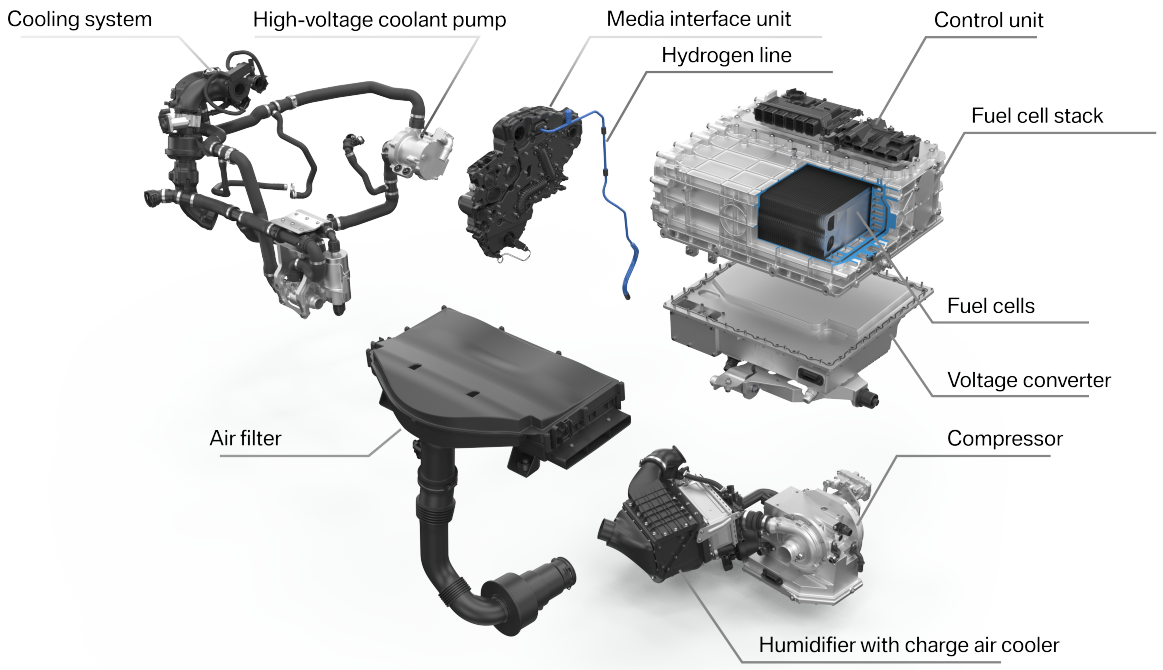

Figure A.1 Schematic representation of the components of a fuel cell system (FCS). Adapted from BMW Group 2022 [45]. © Copyright BMW AG.

Periphery in Automotive Applications

Fuel cell electric vehicles (FCEVs) are a complex system with the PEMFC only being one part. For the fuel supply, hydrogen must be stored within the car in high-pressure vessels. Commonly, a battery buffers changes in power demand and enables immediate throttle response and recuperation. The battery supplies an electric motor. The concept is visualized in Figure A.2.

Hydrogen is stored at $200\,\mathrm{bar}$ to $700\,\mathrm{bar}$ in a hydrogen fuel tank. Therefore, tank materials must withstand strong forces and provide safety even in case of a crash. Carbon fiber-reinforced plas-

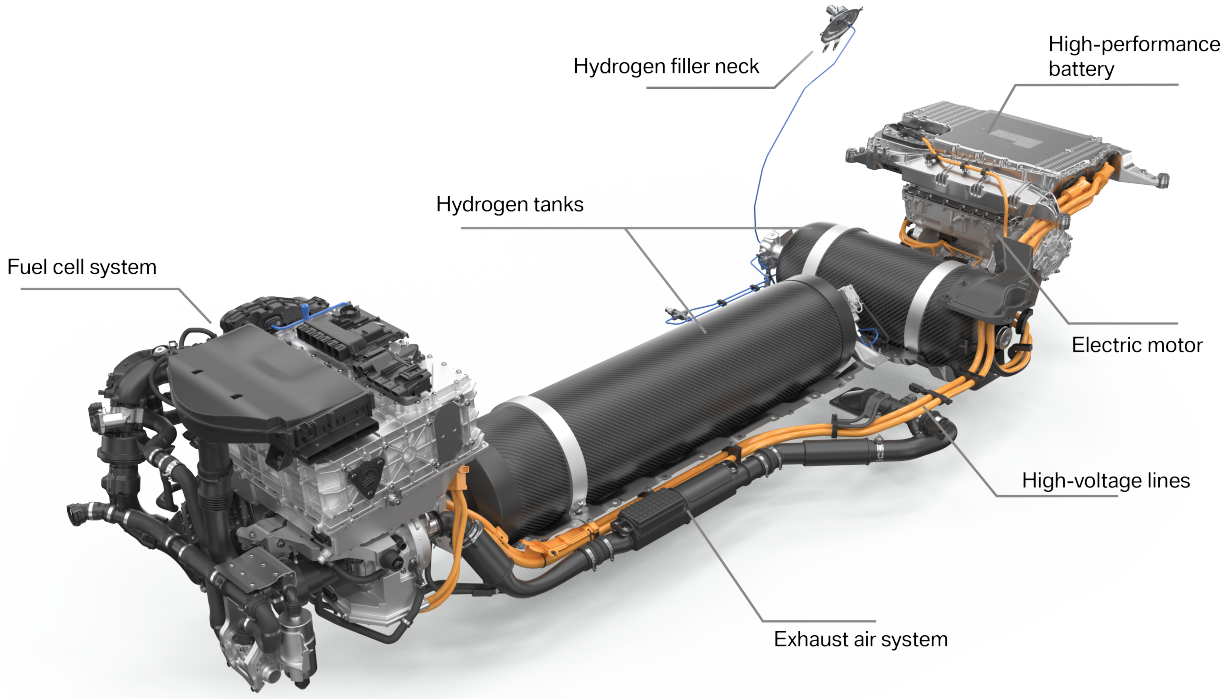

Figure A.2 Schematic representation of the concept of a FCEV. Adapted from BMW Group 2022 [45]. © Copyright BMW AG.

tic composites are most commonly used for compressed hydrogen storage. The hydrogen tank can be refueled via the hydrogen filler neck and the corresponding hydrogen lines and valves. In commercial vehicles, a high-performance lithium-ion battery complements the fuel cell system. An electric motor converts electrical power into mechanical power. An AC/DC converter and a power conditioner complete the drive train. High-voltage lines connect all components. Modern electrical cars are commonly operated at $400\,\mathrm{V}$ to $800\,\mathrm{V}$.

A.3 The Concept of Impedance

Electrochemical impedance measurements of a fuel cell are often modulated by an electric circuit diagram. Therefore, it is crucial to understand the underlying fundamentals of alternating current (AC) electric circuits to interpret obtained impedance spectra.

Alternating Current Circuits

Alternating current (AC) refers to a current periodically alternating with time. The period of the periodic wave T is defined as the time needed for one complete cycle. The frequency f of an AC is the reciprocal value of the period. From the frequency, we can further define the angular frequency ω.

$$f = \frac{1}{T} \tag{A.16}$$

$$\omega = 2\pi f \tag{A.17}$$

For simplicity, we will only discuss sinusoidal waves. However, the principles are directly transferable to other forms of periodic waves. The voltage and current in sinusoidal AC circuits can be written as

$$V(t) = V_m \sin(2\omega t + \theta) \tag{A.18}$$

$$I(t) = I_m \sin(2\omega t + \phi), \tag{A.19}$$

where V_m and I_m are the amplitudes of the voltage and the current, and θ and ϕ the corresponding phase shifts.

Resistors in AC Circuits

Applying Ohm's law to an AC circuit yields

$$V(t) = I(t)R = I_m R \sin(2\omega t + \phi) \tag{A.20}$$

and comparing it to equation A.18 we obtain

$$\phi = \theta \tag{A.21}$$

$$V_m = I_m R. \tag{A.22}$$

Capacitors in AC Circuits

Similary, we can derive a relation between current and voltage for a capacitor in an AC circuit.

$$I(t) = C\frac{dV(t)}{dt} = CV_m \cos(2\omega t + \theta) \cdot \omega = \omega C V_m \sin(2\omega t + \theta + \pi/2) \tag{A.23}$$

The relation of amplitudes and phase shifts is given by

$$\phi = \theta + \pi/2 \tag{A.24}$$

$$I_m = \omega C V_m. \tag{A.25}$$

Inductors in AC Circuits

For an inductance I we arrive at:

$$V(t) = L\frac{dI(t)}{dt} = LI_m \cos(2\omega t + \phi) \cdot \omega = \omega C V_m \sin(2\omega t + \phi + \pi/2). \tag{A.26}$$

Once again comparing to equation A.18 yields

$$\phi = \theta - \pi/2 \tag{A.27}$$

$$V_m = \omega L I_m. \tag{A.28}$$

Impedance

Complex algebra is often used to describe AC circuit problems. Before we introduce the concept of impedance, we quickly recall the most important formulas for a complex number Z.

$$Z = Re(Z) + i \cdot Im(Z) \qquad Z = |Z| \exp i\phi \tag{A.29}$$

$$|Z| = \sqrt{Re(Z)^2 + Im(Z)^2} \qquad \phi = \tan^{-1}(Im(Z)/Re(Z)) \tag{A.30}$$

$Re(Z)$ is the real part and $Im(Z)$ is the imaginary part of a complex number. $|Z|$ denotes the absolute value and ϕ is the angle or argument of Z.

Since the concept of resistance is limited to direct current (DC) applications, the electrical impedance

was introduced for AC circuits. It extends the concept of resistance to complex numbers. The definition of the impedance of an electric circuit is based on the Ohm's law:

$$Z = \frac{V(t)}{I(t)} \tag{A.31}$$

If we substitute $V(t)$ and $I(t)$ in this equation by the corresponding formulas A.18 and A.19 and use the relations of phase shifts and amplitudes obtained for resistors, capacitors and inductors, we obtain the impedance for each of these elements.

$$Z_R = R \qquad \text{resistor} \tag{A.32}$$

$$Z_C = \frac{1}{i\omega C} \qquad \text{capacitor} \tag{A.33}$$

$$Z_L = i\omega L \qquad \text{inductor} \tag{A.34}$$

A.4 PEM Fuel Cell Degradation Mechanisms and Mitigation Strategies

Besides cost reduction, degradation and durability are major challenges for automotive fuel cell development. The target lifetime for automotive fuel cells set by the U.S. Department of Energy (DOE) is 5,000 h. In combination with operational requirements and cost constraints the DOE target aims for fuel cells to be competitive against other energy storage and conversion technologies [47]. In this chapter, degradation mechanisms and mitigation strategies for each component of a PEMFC will be discussed.

Membrane

PEMs require high protonic conductivity, low reactant gas permeability, and good thermal, mechanical, and chemical stability. Membrane degradation and hydrogen crossover can lead to a failure of an entire stack. Although research into alternative membrane materials is increasing, this chapter will focus on the degradation mechanisms of PFSA membranes. Three main degradation modes can be distinguished: mechanical, thermal and chemical/electrochemical degradation [61, 135, 166, 237–239].

Membrane failure occurs when degradation leads to the formation of pinholes. Pinholes, in turn, lead to a locally increased gas crossover, combustion, and consequently rapid expansion of the pinhole. The critical value for membrane failure is often defined as a hydrogen crossover current roughly ten times higher than for new membranes ($j > 20\,\mathrm{mA/m^2}$) [61, 240].

Mechanical Degradation

Degradation mechanisms Mechanical degradation diminishes membrane integrity due to built-in, assembly, and operational stresses. Assembly stresses are mainly caused by the applied clamping pressure. The clamping pressure ensures good electrical contact and seals the edges. However, local unevennesses like the flow channels or smaller irregularities from the gas diffusion layers (GDLs) and the electrodes may lead to local stresses that significantly exceed the nominal clamping pressure. These high-pressure points lead to perforations and possible weak spots [], particularly in thinner membranes ($10\,\mu m$ to $50\,\mu m$), which are more susceptible to early-life failure from built-in and assembly stresses.[135, 166, 237, 238]

During operation, volume changes of the membrane and physical constraints by the electrodes, GDLs and BPPs induce additional stresses. The volume of PFSA membranes strongly depends on its water content. [61]

Local humidity differences and constraints induce stress and strain under relative humidity (rh) cycling, leading to the formation of micro defects and dimensional changes. Ex-situ analysis reveal characteristic craze-like defects after rh cycling. These craze-like defects develop into cracks and pinholes. The degradation under rh cycling is roughly proportional to the cycling amplitude [135].

Mitigation strategies To minimize assembly stress induced by contact pressure and operational stresses, uniformity and the absence of foreign particles in the production process are essential. [135, 166]. Chemical modifications like membrane annealing, uniaxial stretching, and chemical cross-linking of the polymer reduce swelling and enhance mechanical stability [239]. To prevent high operational stresses due to local humidity differences, flow field design plays

an important role in the mitigation of mechanical stresses. Reinforcement with a polytetrafluoroethylene (PTFE) backbone can extend the lifetime of one order of magnitude compared to conventional PFSA membranes [237].

Thermal Degradation

Degradation mechanisms In mobile applications fuel cells are operated in a wide temperature range, including sub-freezing temperatures. While the freezing point of chemically bound water in Nafion is at approximately $-120\,^{\circ}\mathrm{C}$, free water within the membrane and at the interface between membrane and electrode freezes at $0\,^{\circ}\mathrm{C}$ [237, 239]. The phase transition weakens the PFSA membrane itself and the interface with the electrodes. Consequences are a decrease in ionic conductivity, gas permeability, and mechanical strength [241].

PEMFCs generally operate most effectively between $60\,^{\circ}\mathrm{C}$ and $80\,^{\circ}\mathrm{C}$. Above a temperature of $80\,^{\circ}\mathrm{C}$ conventional PFSA membranes undergo a glass transition, diminishing proton conduction [237]. Recently, much effort has been made to develop high temperature PEM fuel cells to enhance kinetics, water management, and CO tolerance [242]. Nevertheless, dry conditions due to low humidity levels at elevated temperatures may degrade cell performance [62].

Mitigation strategies To mitigate freeze-start degradation, shut down and startup strategies aim to reduce the water content in the fuel cell. During shut down, the electrodes are purged with dry gas to eliminate free water within the cell [237, 243, 244]. Startup strategies pre-heat the fuel cell stack, maintain relatively dry conditions, and slowly increase the current [245–247].

Chemical Degradation

Degradation mechanisms PFSA can decompose by peroxide ($HO\cdot$) and hydroperoxide ($HHO\cdot$) radical attack. Transition metal ions like Fe^{2+}, originating from corrosion of stack elements, catalyse the production of radicals in PEMFCs [239]. Further, radicals are also formed by a direct formation with only H_2, O_2 and Pt involved [248, 249].

The chemical degradation involves four primary pathways: attacks on carboxylic acid end groups, C-S bonds, tertiary carbon atoms, and ether groups. All four mechanisms contribute to the chemical degradation with the contribution of each mechanism depending on the operating conditions [239, 250].

Foreign catalytic ions also degrade the ionomer by adsorbing at sulfonic acid groups and, as a consequence, blocking active sites for the proton conduction. This effect is, however, only significant beyond $50\,\%$ blocked sulfonic acid groups [166, 237, 238].

Mitigation strategies Several methods have been developed to mitigate chemical degradation. Stabilizing the most vulnerable polymer groups, such as chemically stabilizing carboxylic acid end groups, can achieve better stability against radical attack. So-called short side chain ionomers aim to minimize radical attack on the side chains by eliminating the tertiary carbon ($-CF$) and one of the ether bonded carbon atoms ($-O-CF_2$). Additionally, incorporating radical scavengers is highly effective in minimizing chemical degradation [239].

Studies have shown that the use of components free of iron significantly reduces chemical degradation due to the absence of the catalyst Fe^{2+} [251].

Electrodes

As outlines in Chapter 2.2.4, an electrode is composed of catalyst nanoparticles, a carbon support, and a binder. All three materials, platinum, carbon, and ionomer, might be subject to degradation. Most relevant are four mechanisms: platinum dissolution, platinum poisoning, carbon corrosion, and ionomer decomposition [166, 237]. A combination of these mechanisms also leads to pore collapse and interfacial delamination.

Platinum Dissolution and Deposition

Degradation mechanisms latinum atoms on the particle surface oxidize at a potential of $1.188\,\mathrm{V}$ (eq. A.35). The dissolved platinum atoms dissolute, leading to two main degradation issues: The platinum ions might either migrate into the membrane, forming a platinum that increases the proton resistance, or they might agglomerate to bigger particles. The particle growth leads to a decrease in electrochemical active surface area (ECSA), and therefore performance degradation [62, 166, 237]. This process is known as Oswald ripening. It is significantly enhanced by repeated changes of the cathode potential [252].

$$\mathrm{Pt} \longrightarrow \mathrm{Pt}^{2+} + 2\,\mathrm{e}^- \qquad 1.188\,\mathrm{V} \qquad \text{(A.35)}$$

$$\mathrm{Pt}^{2+} + 2\,\mathrm{e}^- \longrightarrow \mathrm{Pt} \qquad 0.70\,\mathrm{V} \qquad \text{(A.36)}$$

Mitigation strategies Since platinum dissolution is strongly tied to cathodic potential changes, stable operation reduces the degradation rates [62, 166, 237]. Therefore, applications that rely on quick load changes, like, for example FCEVs, can profit from buffering fluctuations with an

additional battery. In terms of material choice, Pt-alloy catalysts, particularly Pt-Co, have shown better stability compared to pure platinum catalysts [237].

Platinum Poisoning

Degradation mechanisms PEMFCs are exposed to impurities from the hydrogen and the air either from the supply or from the degradation of the fuel cell system. Impurities containing species with strong adsorption behavior on platinum may, such as carbon monoxide and hydrogen sulfide, alter the catalytic activity by blocking active sites and change electronic properties and surface structure [253].

Carbon monoxide directly binds on platinum via the carbon atom (eq. A.37). However, it may be removed in the presence of oxygen gas (eq. A.39) or by electrochemical oxidation (eq. A.38).

$$\mathrm{CO} + \mathrm{Pt} \longrightarrow \mathrm{Pt{-}CO} \tag{A.37}$$

$$\mathrm{CO_{Pt}} + \mathrm{H_2O} \longrightarrow \mathrm{CO_2} + 2\,\mathrm{H^+} + 2\,\mathrm{e^-} \tag{A.38}$$

$$\mathrm{CO_{Pt}} + \frac{1}{2}\,\mathrm{O_2} \longrightarrow \mathrm{CO_2} \tag{A.39}$$

The CO electrooxidation reaction typically proceeds at potentials above $0.6\,\mathrm{V}$ and thus can only be triggered by introducing air to the anode upon shutdown or in highly polarized stacks.
Hydrogen sulfide adsorbes under the formation of protons via a dissociative mechanism.

$$\mathrm{H_2S} + \mathrm{Pt} \longrightarrow \mathrm{Pt{-}S} + 2\,\mathrm{H^+} + 2\,\mathrm{e^-} \tag{A.40}$$

Contaminant levels as low as 25 ppb reduces the fuel cell performance significantly [253].

Mitigation strategies Fuel gas scrubbing and pre-filtration are strategies to prevent poisoning of the platinum catalyst. Further, improving the catalyst CO tolerance by alloying platinum shows promising results for CO poisoning [253].

Carbon Corrosion

Degradation mechanisms Besides degradation of the platinum catalyst itself, the carbon support can also corrode. Carbon can be electrochemical oxidized at comparably low potentials and is accelerated by the presence of platinum catalyst [166, 254, 255].

$$\mathrm{C} + \mathrm{H_2O} \longrightarrow \mathrm{CO_2} + 4\,\mathrm{H^+} + 4\,\mathrm{e^-} \qquad 0.205\,\mathrm{V} \tag{A.41}$$

Though the reaction kinetics are slow at typical operating temperatures of a PEMFC between $60\,^{\circ}\mathrm{C}$ and $120\,^{\circ}\mathrm{C}$, numerous studies have shown severe degradation on the cathode side due to local fuel-starvation [62, 252, 255]. Fuel distribution problems might arise from flow-field design, water-management, or blocked channels due to ice formation at sub-zero temperatures. In fuel-starvation can lead to a current-reversal and potentials as high as $1.2\,\mathrm{V}$ to $1.5\,\mathrm{V}$, promoting carbon corrosion and oxygen evolution [254–256].

Due to the corrosion of the carbon support, the platinum particle may lose contact and the ECSA decreases. Additionally, the support loses its structural integrity, limiting mass transfer through the electrode [62]. The rate of carbon corrosion depends on the partial water pressure and is most severe at the fuel outlet [252].

Mitigation strategies Since carbon corrosion is mainly assigned to fuel-starvation, optimized fuel cell operation can mitigate the degradation of the carbon support. Furthermore, startup

strategies reducing the probability of hydrogen-air fronts lead to improvements [252].

Alternatives to porous carbon powder, like multi-walled carbon tubes, show higher resistance to electrochemical oxidation and nearly two times lower degradation rates [237].

Pore Collapse and Interfacial Delamination

Degradation mechanisms At sub-zero temperatures, ice formation within the porous electrode structure can cause severe damage, leading to pore collapse and subsequent mass transport issues [245, 246]. Additionally, residual water at the interface between the catalyst layer and the membrane freezes at sub-zero temperatures, leading to interfacial delamination [245, 257, 258].

Mitigation strategies Operational strategies, such as gas purging during shutdown and pre-heating before startup, help minimize ice formation and protect the structural integrity of both the electrode and electrode-membrane interface [245–247].

A.5 Publications

In the following, the two peer-reviewed publications that are the base for this dissertation are presented:

Publication 1

F. Haimerl, J. P. Sabawa, T. A. Dao and A. S. Bandarenka, Spatially Resolved Electrochemical Impedance Spectroscopy of Automotive PEM Fuel Cells, ChemElectroChem, 2022, 9, e202200069.

Publication 2

F. Haimerl, S. Kumar, M. Heere and A. S. Bandarenka, Electrochemical impedance spectroscopy of PEM fuel cells at low hydrogen partial pressures: efficient cell tests for mass production, RSC Industrial Chemistry & Materials, 2024, 2, 132-140.

ChemElectroChem

Research Article
doi.org/10.1002/celc.202200069

Chemistry Europe
European Chemical Societies Publishing

www.chemelectrochem.org

Spatially Resolved Electrochemical Impedance Spectroscopy of Automotive PEM Fuel Cells

Felix Haimerl,*[a, b] Jarek P. Sabawa,[a, b] Tuan A. Dao,[a] and Aliaksandr S. Bandarenka*[b, c]

Fuel cell electric vehicles (FCEVs), which use polymer electrolyte membrane fuel cells (PEMFCs), provide a prospect to add to a future of harmful-emission-free mobility. However, an in-depth understanding of degradation mechanisms and contributions to performance losses is needed to commercialize FCEVs further. Most previous PEMFC degradation research has focused on global indicators of the cell condition. Still, failure occurs typically due to inhomogeneities in production or operation, leading to localized regions of high degradation rates. Despite simulations indicating that local degradation effects are significantly more pronounced at larger scales, experimental studies only exist for small-sized laboratory fuel cells so far. Here, we present the results of a comprehensive study of spatial distributions of essential PEMFC parameters using electrochemical impedance spectroscopy across the cell surface of automotive-size fuel cells with an active area of 285 cm^2. In particular, the results reveal increasing mass transport problems with increasing distance from the air inlet and a tendency of lower proton resistances in the center of the cell. One hundred twenty realistic freeze-start cycles degenerated the cell performance drastically. The outer cell regions, subject to the lowest temperatures, showed the most substantial degradation rates, partly compensated by central cell regions with slightly higher temperatures. These findings bridge the gap between simulation and experiment and provide valuable insights for future fuel cell design and operating strategies.

Introduction

Several car manufacturers, such as Hyundai, Honda, and Toyota, released commercially available FCEVs in the last decade.[1–3] BMW plans to start series production of a commercial FCEV by the end of this decade.[4] However, there remain general challenges to making FCEVs a viable alternative to widely used combustion engines and battery electric vehicles. Besides cost reduction, the U.S. Department of Energy names durability the main challenge for automotive PEMFC applications. Critical factors in addressing this issue are improving the understanding of degradation mechanisms and corresponding mitigation strategies.[5–6]

Three main degradation modes can be distinguished in PEMFCs: Dissolution and aggregation of the platinum catalyst, corrosion of the carbon support, and degradation of the proton-conducting ionomer. The degradation rates depend on the operating conditions, with the potential, temperature, and relative humidity as crucial parameters.[7–8] However, these operational parameters are not uniform across the cell surface. Relative humidity and the partial pressure of the reactants vary along the flow channels. The current density increases due to rising humidity levels with increasing distance from the gas inlets at a low relative humidity of the gas supply. At a higher inlet gas humidity, flooding effects reduce the current density close to the gas outlets and shift the maximum current density towards the middle of the cell.[9] Differences in current density lead to inhomogeneous waste heat production.

Additionally, experimental studies found gas temperature gradients of up to 6 K in a PEMFC stack due to the thermal mass of the stack.[10] Carbon corrosion and catalyst dissolution become more distinct at high temperatures leading to non-uniform degradation rates.[7] Local shortages of reactants due to blocked flow channels or uneven reactant distribution are other reasons for fuel cell degradation. Starvation of hydrogen or oxygen may lead to voltage reversal, accelerating carbon corrosion and radical formation. At low stoichiometries, the decrease of partial pressure along the flow channel results in shortages of oxygen and hydrogen close to the gas outlets, increasing degradation rates and diminishing performance. All of these factors contribute to local differences in the performance and degradation of PEMFCs.

Electrochemical Impedance Spectroscopy (EIS) provides a possibility to get deep insights into the electrochemical processes in a working fuel cell.[11–12] Extensive research went into studying the impedance response of a PEMFC and the effect of different operating parameters.[13–15] In recent years, sophisticated measurement methods have been developed to account for local performance and degradation issues. Scanning electrochemical microscopy-based measurements are, for in-

[a] F. Haimerl, Dr. J. P. Sabawa, T. A. Dao
BMW AG, Petuelring 130, 80809 München, Germany
E-mail: felix.haimerl@tum.de
[b] F. Haimerl, Dr. J. P. Sabawa, Prof. A. S. Bandarenka
Department of Physics
Technical University of Munich
James-Franck-Str. 1, 85748 Garching, Germany
[c] Prof. A. S. Bandarenka
Catalysis Research Center TUM
Technical University of Munich
Ernst-Otto-Fischer-Straße 1, 85748 Garching b. München, Germany
E-mail: bandarenka@ph.tum.de

Supporting information for this article is available on the WWW under https://doi.org/10.1002/celc.202200069

stance, used to characterize fundamental processes in half cells with high resolution, but it lacks functionality for industrial fuel cells[16–18]. For a complete membrane electrode assembly (MEA), the local impedance response is usually recorded by either measuring with a segmented fuel cell[19–23] or by adding a printed circuit board (PCB) to the setup[24–25]. Segmented cells are based on segmented flow fields and current collectors, with each segment being electronically isolated from its neighbors. In contrast, a PCB is only added to the cell setup between the cathode bipolar plate and the cathodic current collector.

Most studies on spatially resolved EIS in PEMFCs focus on flow field effects. Brett et al.[19] analyzed the proton resistance along a single channel PEMFC and concluded that there is no local effect on the membrane. Still, Hakenjos and Hebling[23] showed that reaction starvation along the flow field diminishes the cell performance. The effect of reactant contributions in a line vertical to the flow channels was investigated by Schneider et al..[22] They found that mass transport limitations underneath flow field ribs significantly affect cell performance at high cell currents. Gerteisen et al.[21] analyzed the influence of flow configuration, flow rate, and relative humidity on the local high-frequency resistance. Finally, Liu et al.[24–25] proposed the new setup with the added PCB and investigated the effect of the cathode stoichiometry on the local cell impedance.

Overall, there has been a growing interest in spatially resolved EIS measurements of PEMFCs. Findings indicate a strong relation of the spatial distribution of the impedance on the flow field design. However, the literature only provides studies of small-sized fuel cells with limited spatial resolution. An in-depth investigation of local impedance effects for a PEMFC with commercial FCEV applications is missing. This work aims to fill the gap and improve the understanding of the performance and degradation of automotive-sized PEMFCs. The two main model tests that were carried out in the context of this work are a parametric analysis of the influence of operating parameters on the local impedance response and a freeze-cycle degradation test. A new temperature control hardware[26] was used to realize the freeze cycles more realistically and faster than before.

Results and Discussion

For the parametric analysis and the freeze-cycle degradation tests, the current distribution and the dependencies of EIS equivalent circuit parameters were recorded at the average current corresponding to the current density of $j = 0.5\ A/cm^2$ for each parameter set / after each cycle.

The resulting impedance spectra were fitted with a modified Randles equivalent circuit shown in Figure 1a.[27–28] The physical model represented in Figure 1 shows a proton resistance (R_{proton}), being the inverse of the conductivity through the perflourosulfonic acid (PFSA) polymer membrane and connected in series with a parallel combination of elements representing the electrochemical processes (Faradaic impedance) at the electrode-electrolyte interfaces and the response of the interfaces themselves. The Faradaic impedance response

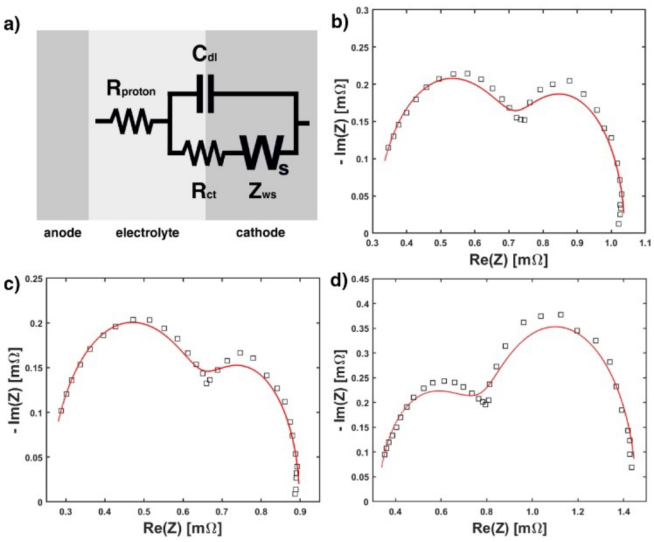

Figure 1. (a) The equivalent electric circuit applied to fit the data with the proton resistance (R_{proton}), the double layer capacitance (C_{dl}), the charge transfer resistance (R_{ct}), and a Warburg "short" element (Z_{ws}). (b)-(d) Exemplary impedance spectra and the resulting fits at the air outlet at (b) $j = 0.5$ A/cm^2, $T_{cell} = 60\,°C$, $T_{gas} = 85\,°C$, $p = 2$ bar, $\lambda_{H2} = 2$, $\lambda_{air} = 2$, $rh = 50\,\%$, (c) $j = 0.5$ A/cm^2, $T_{cell} = 80\,°C$, $T_{gas} = 85\,°C$, $p = 2$ bar, $\lambda_{H2} = 2$, $\lambda_{air} = 2$, $rh = 50\,\%$, and (d) $j = 0.5$ A/cm^2, $T_{cell} = 80\,°C$, $T_{gas} = 85\,°C$, $p = 2$ bar, $\lambda_{H2} = 2$, $\lambda_{air} = 1.5$, $rh = 50\,\%$.

is mainly dominated by the cathodic interface and the processes there. The cathode impedance is modeled by a capacitance accounting for the double layer (C_{dl}), a charge transfer resistance (R_{ct}), and the diffusion Warburg "short" (Z_{Ws}) element:

$$Z_{Ws}(\omega) = \frac{Aw}{\sqrt{\omega}}(1-j)\tanh\left(B\sqrt{j\omega}\right)$$

where the Aw is the Warburg coefficient and $B = d/D^{0.5}$ (d – Nernst diffusion layer thickness and D – diffusion coefficient of the electroactive species).

Anode processes are neglected due to the fact that the anodic hydrogen evolution is significantly faster than the cathodic oxygen reduction. In other words, one assumes that the total impedance at the anode is so much smaller if compared to the cathode that it possible to neglect it. Figure 1b–d shows Illustrative examples that the fits are in good agreement with the measured data points, with the relative residuals being in the range of $\pm 5\,\%$.

Subsequently, the obtained values for the circuit elements were further processed to obtain the "distribution maps" for each parameter across the cell surface.

General Relations of the Cell Descriptors

Figure 2a illustrates the origin of the resulting color maps. The x-y-plane displays the surface of the MEA, and the corresponding current density values are plotted as a color map. The flow channels are oriented in horizontal lines parallel to the x-axis.

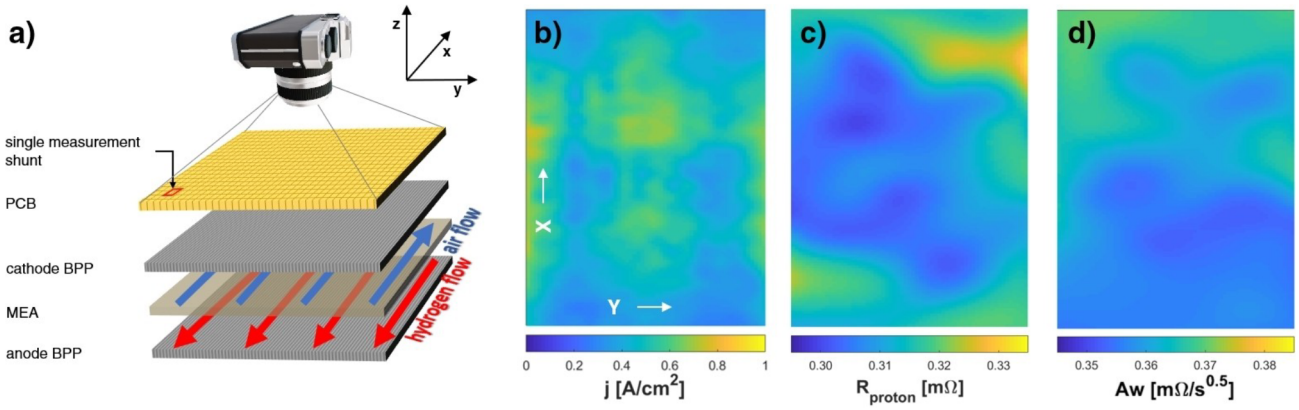

Figure 2. (a) Visualization of the measurement setup and the coordinate system. (b)-(d) Distribution maps of the current density j, the proton resistance R_{proton}, and the Warburg coefficient Aw. The data were obtained from local EIS at $j = 0.5$ A/cm^2, $T_{cell} = 80$ °C, $T_{gas} = 85$ °C, $p = 2$ bar, $\lambda_{H2} = 2$, $\lambda_{air} = 2$, $rh = 50$ %, in a frequency range from 0.3 Hz to 300 Hz

Hydrogen and air are supplied in a counter-flow, with hydrogen flowing from top to bottom in the graphic and air from bottom to top. Figure 2 shows exemplary maps of the current density (Figure 2b), the proton resistance (Figure 2c), and the Warburg coefficient (Figure 2d) at typical operating conditions with high stoichiometries ($\lambda_{H2} = 2$, $\lambda_{air} = 2$), a cell temperature of 80 °C and relative humidity of the supplied reactants of 50 %.

The recorded current distribution is typical for reasonable high cathodic stoichiometries. Following the x-axis, the current increases with increasing distance from the hydrogen and air inlets, leading to the highest values in the center region of the cell. Two distinct maxima are visible along with other fine structures, especially at the sides of the assembly. Simulations predicted similar distributions with two distinct peaks along the flow channel for counter-flow configurations with humid air as cathode gas.[29] Previous research found one maximum in the current distribution along the flow channels. However, literature mostly provides current distribution measurements of small-sized 5 cm × 5 cm PEM fuel cells.[21,23,30] Perpendicular to the flow channels, variations of the reactant distribution between gas channels result in an inhomogeneous current density.

The corresponding proton resistance distribution in figure 2c exhibits smaller values in the center of the cell surface. The outer regions, especially along the x-axis, show higher resistance values. The surface mirrors the current distribution along the flow channels in figure 2b. High proton resistance values roughly correspond to lower current densities. Variations in the charge transfer resistance are less pronounced but follow the same trends along the x-axis.

The Warburg coefficient, which accounts for the mass transfer to the catalyst-ionomer interface, is displayed in figure 2d. We observe a gradient of A_w from smaller values at the air inlet (bottom in the graphic) to higher values at the air outlet (top). The trend of a decreasing partial pressure of oxygen and therefore increased mass transport problems with increasing distance from the air inlet is well documented in the literature.[31–32] The second Warburg parameter B, which is directly associated with the diffusion constant, was reasonably constant across the surface.

Figure 3 shows the average values along the flow channels of the current density j and the resistances associated with proton conduction and charge transfer, as well as the Warburg coefficient. The graphic reinforces that both proton resistance and charge transfer resistance mirror the current distribution trends. We can see the two maxima in current distribution and corresponding minima in proton resistance and charge transfer resistance. The charge transfer resistance is directly associated with the current density. Therefore, a higher charge transfer resistance leads to a lower current density. The high current densities lead to higher temperatures, which in turn impact the charge transfer rate. However, the differences in charge transfer are too small to explain the large variations in current density. We, therefore, assume that the inhomogeneity in charge transfer resistance originates from slight temperature differences due to current density gradients.

The proton resistance is an immediate measure of the humidification of the PFSA ionomer. High humidification provides high proton conductivity. The humidification of the ionomer is enhanced by the high relative humidity of the supplied reactants and by the water production at the cathode side. Local maxima in current density enhance the water production and hence correspond to regions of increased proton conductivity. At the same time, a reduced proton

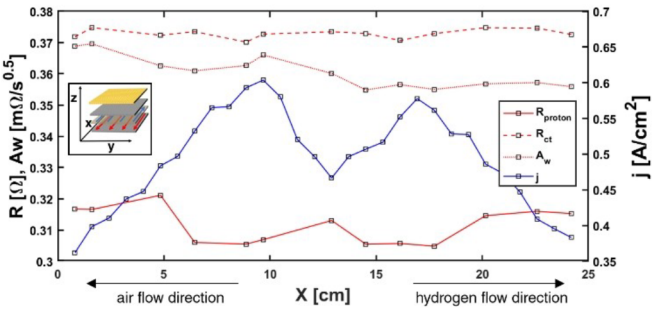

Figure 3. Average values along the flow channels of the current density j (blue) and the resistances associated with proton transfer (red solid) and charge transfer (red dashed), as well as the Warburg coefficient associated with mass transport (red dotted). Connecting lines are guides for the eyes.

resistance leads to higher current densities. Water transport and production characteristics make the predicted current distribution with two distinct maxima.

Parametric Analysis of Cell Descriptors

The impact of the cell's operating temperature was investigated at different levels of relative humidity ranging from 30% to 90%. The cell voltage increases at all humidity levels up to a temperature of 70 °C (Figure S-4a). The trend reverses from 70 °C upwards. The trend reversal is more pronounced at the low relative humidity of the supplied reactants. Analyzing the cell impedance, the proton resistance, the charge transfer resistance, and the parameter A_w are all influenced by the temperature (Figure S-4b–c).

The charge transfer resistance shows a clear downward trend for the temperature region between $T = 50$ °C and $T = 70$ °C and thus can explain the rise of voltage (Figure S-4c). The charge transfer resistance relates to the reaction rate of chemical reactions and is directly dependent on the temperature. The Butler-Volmer equation indicates an exponential increase in current density with increased temperatures at a specified overpotential. However, the effects of temperature on faradaic processes are diverse since mass transport phenomena play an essential role in sustaining the electrochemical reaction. Factors influenced by the cell temperature include effective oxygen diffusion, the mass fraction of oxygen, and water transport. Oxygen diffusivity and water transport increase with elevated temperatures. The mass fraction of oxygen decreases in contrast. Water transport mechanisms influence oxygen transport once again.[33] Esfeh et al. concluded that the partial pressure of oxygen decreases with increased temperature, leading to performance losses.[34] Indeed, the Warburg parameter, A_w, associated with oxygen diffusion, shows a rise for all relative humidities at elevated temperatures (Figure S-4d).

Spatially resolved impedance measurements reveal an evenly distributed increase in proton resistance from $T = 50$ °C to $T = 80$ °C for low relative humidity but a decrease for high relative humidity. Figure 4a shows the proton resistance for cell temperatures of 50 °C and 80 °C at $rh = 30\%$ and $rh = 90\%$ plotted over the cell area. The color maps show a tendency of lower values in the middle of the cell. The two distinct minima right at the center are pronounced at low temperatures combined with low relative humidity. The absolute water content transported into the cell is the smallest in this case.

Additionally, the airflow is sluggish, and the capacity of water uptake of cooler air is low. Consequently, the differences in local water production directly transform to differences in membrane hydration and, therefore, proton conduction. We do not see a general trend of increasing proton resistance along the flow direction, indicating that humidification of the ionomer does not decrease with increasing distance from the air inlet. This is consistent with previous counter-flow experiments by Gerteisen et al.[21] at a current density of $j = 0.5$ A/cm^2.

Oxygen supply and transport are assumed to influence the performance of a PEMFC significantly. Mass transport problems are especially prominent if an air feed supplies oxygen. We see a strong correlation between cathodic stoichiometry and cell voltage (Figure S-7a). Only at very low humidity, the cell voltage reaches a maximum at a stoichiometry of $\lambda_{air} = 1.3$, followed by a slight decrease in cell voltage for higher stoichiometries. We

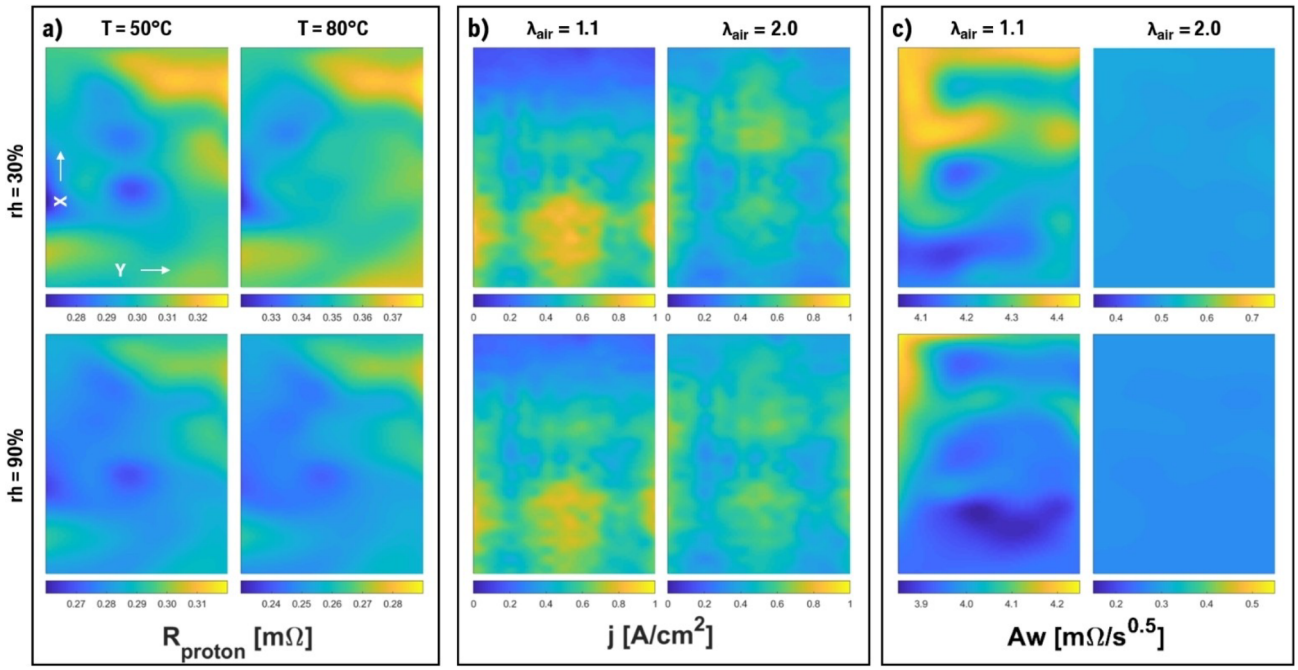

Figure 4. (a) Distribution maps of the proton resistance R_{proton} for $T_{cell} = 50$ °C and $T_{cell} = 80$ °C at $rh = 30\%$ and $rh = 90\%$. (b) Distribution maps of the current density for $\lambda_{air} = 1.1$ and $\lambda_{air} = 2.0$ at $rh = 30\%$ and $rh = 90\%$. (c) Distribution maps of the Warburg short parameter Aw for $\lambda_{air} = 1.1$ and $\lambda_{air} = 2.0$ at $rh = 30\%$ and $rh = 90\%$.

can explain both effects when looking at the individual impedance contributions and their spatial distributions.

Figure 4b shows the current distribution at a cathodic stoichiometry of $\lambda_{air}=2.0$ and $\lambda_{air}=1.1$ at $rh=30\,\%$ and $rh=90\,\%$. A shift of the current density maximum closer to the air inlet is apparent for low stoichiometries. At the air outlet, the current density is close to zero. Distribution maps of the Warburg coefficient Aw for $\lambda_{air}=2.0$ and $\lambda_{air}=1.1$ (Figure 4c) indicate that the shift in current density originates from mass transport problems at the air outlet. At $rh=30\,\%$, one can observe a general increase of Aw from an average value of ca 0.49 $m\Omega/s^{0.5}$ to an average value of 4.33 $m\Omega/s^{0.5}$, but we also see an increase of the gradient along the x-axis. The gradient increases from ca 0.08 $m\Omega/ms^{0.5}$ at $\lambda_{air}=2.0$ to ca 0.88 $m\Omega/ms^{0.5}$ at $\lambda_{air}=1.1$. The corresponding average values along the x-axis and linear fits are shown in figure S-8. The low stoichiometry leads to mass transfer problems and ultimately reactant starvation at regions far from the inlet. Simulations show that the partial pressure of oxygen decreases significantly along the flow channel.[31,35] The resulting mass transport problems at low cathodic stoichiometries are clearly visible from the results obtained in this study.

The influence of relative humidity on the Warburg coefficient is comparably small, suggesting that water transport is not an issue. Nevertheless, ionomer humidification seems to become a problem at low humidity and high stoichiometries. Figure S-7b shows the dependency of proton resistance on the cathodic stoichiometry. The proton conductivity decreases with rising stoichiometries. High stoichiometries mean high gas velocities. Hence, the water produced at the cathode is transported off faster and cannot humidify the ionomer. This effect is pronounced for low relative humidity. The increase in proton resistance gives rise to the maximum cell voltage at $\lambda_{air}=1.3$ for a rh of 30 %, which was also reported in the previous research.[36]

Anode processes are usually thought to have minimal contributions to PEMFC losses. Thus, the anode is usually not considered in equivalent circuit models. The impact of the anodic stoichiometry on the cell impedance was investigated to verify such a simplification. As expected, we do not see a general relation between mass transport and anodic stoichiometry. We do, however, see a trend in the fitting parameters R_{ct} and R_{proton} for the first semi-circle in the Nyquist plot. The charge transfer resistance parameter and the proton resistance parameter are shown in figure S-6. For both parameters, we see a general dependency on the anodic stoichiometry at low humidity and a spike in resistance for a stoichiometry of $\lambda_{H2}=1.1$. The spike of the fitting parameters might indicate that anodic mass transport limitations contribute to the first semi-circle in the Nyquist plot at a very low anodic stoichiometry. Therefore, the fitting with only one electrode-electrolyte interface oversimplifies the system in this case and leads to deviating parameter values.

Note that stoichiometry is directly related to the volume flow of hydrogen. Therefore, a decreased stoichiometry means smaller flow velocities and a lower absolute water content brought into the cell. A lower water content brought into the cell might explain the general trend of a slight increase of both proton and charge transfer resistance with decreasing anodic stoichiometry. In contrast to the cathode side, no water is produced by the fuel cell reaction at the anode side. Hence it is critical to humidify the anode externally. A dry anode leads to a loss of protonic conductivity. As a consequence of a dry anode, the back-diffusion of water through the membrane from the cathode to the anode is dominant, resulting in a water deficiency at the cathode.[37] Hence, the humidity of the anode affects the cell globally. Drying out of the cathode decreases the ECSA by eliminating proton pathways to the catalyst surface, leading to an additional increase in charge transfer resistance.[38]

Local Degradation Due to Freeze-Start Cycling

Starting from sub-zero temperatures is a major issue for PEMFCs in FCEVs. Therefore, a realistic freeze-start cycling test with moderate temperatures of 2 °C at the middle of the cell and lower temperatures of −8 °C in the outer regions was carried out to extend the scope of this study. The cell reached its end of life (EOL) after 131 cycles. In cycle 132, the cell did not achieve an open circuit voltage above 0.85 V. This correlates with the voltage history at a current density of $j=0.5$ A/cm^2 shown in figure 5a. After a sharp increase in cell voltage from the beginning of life (BOL) to the measurement after the first cycle, the trend tends to reverse for the rest of the cycling experiment. Three distinct phases are distinguishable. A sharp increase after cycle one and a much slower rise in cell voltage for cycles 1–20 (phase 1) are followed by a relatively constant voltage for cycles 21–60 (phase 2). Then, around cycle 60, the trend is reversed, and the cell voltage decreases from cycle 61 forwards (phase 3). Phase 1 seems to add to the break-in of the cell, even though an extensive break-in procedure was conducted before. The break-in behavior might even balance degradation effects in phase 2.

The voltage degradation strongly depends on the ionomer-to-carbon weight ratio. Sabawa and Bandarenka[28] found a similar voltage record for low ionomer-to-carbon weight ratios. They attributed the break-in behavior to a decrease in cathode catalyst layer thickness and thus a higher ionomer-to-carbon weight ratio, leading to better proton transport. This is supported by the change in ECSA shown in figure 5b. Over the course of 120 cycles, the ECSA reduced from ca 37.29 m^2/g to ca 27.33 m^2/g, which equals a relative loss of ~26.7 %. Previous experiments with thermal cycling from 80 °C to −10 °C and starts from −5 °C and −10 °C obtained similar results.[39,27]

Compensation of local degradation by regions subject to more moderate operating conditions might also contribute to the rather stable voltage course in phase 2.

Current distribution measurements across the MEA clarify these compensation effects. The absolute change in current distribution over 120 cycles is displayed in figure 5c. The outer cell regions showed a decrease in current density, which was compensated by large parts of the central cell area. The current density in peripheral regions at the air outlet degenerated most

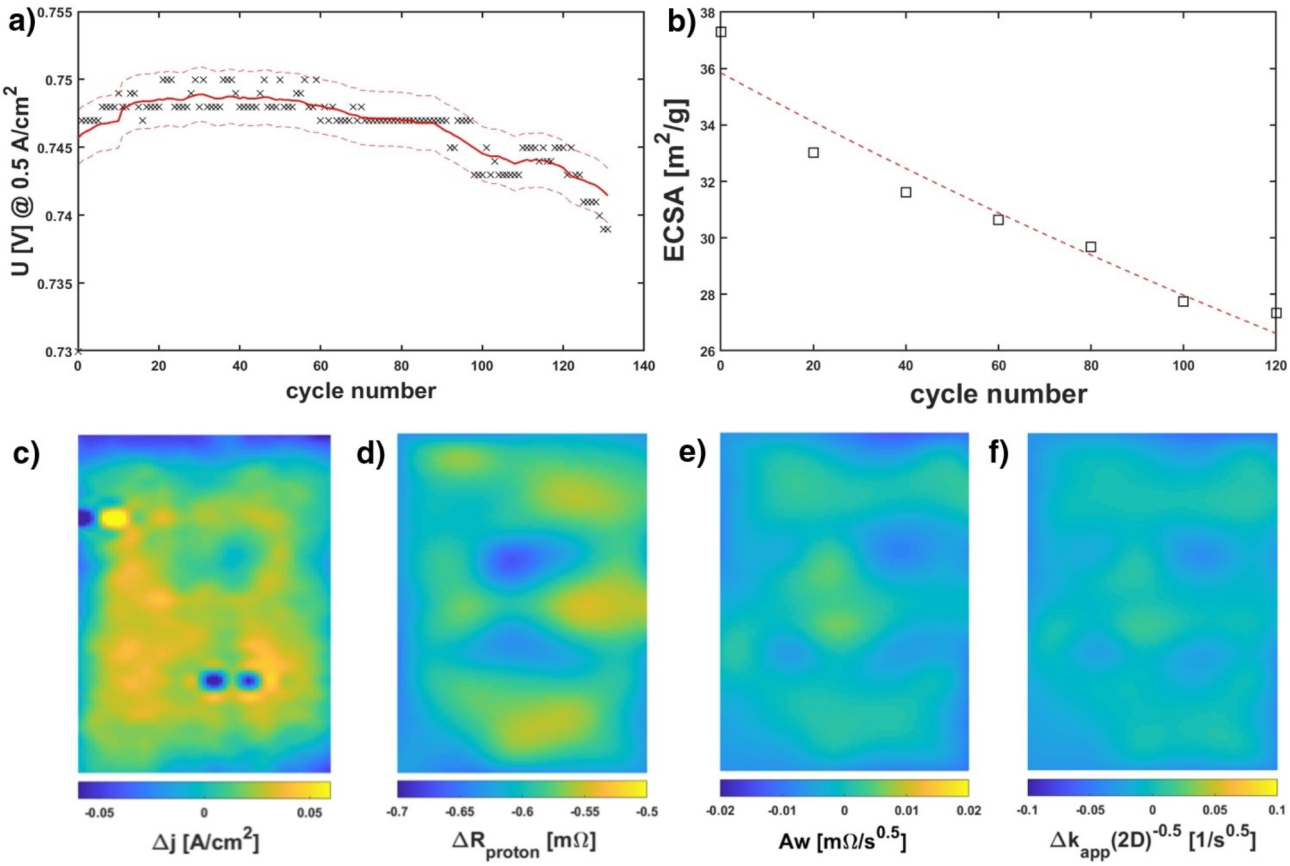

Figure 5. (a) Voltage history at $j = 0.5\ A/cm^2$ over the course of 131 freeze-cycles. (b) Colour map of the absolute change in current density distribution across the cell surface from BOL to cycle 120. Blue areas decreased in current density, and yellow areas increased in current density. (c) Colour map of the absolute change in proton resistance distribution across the cell surface from BOL to cycle 120. (d) The plot of the ECSA against the cycle number (dashed line is a guide for the eye). (e) Colour map of the absolute change of the Warburg short parameter *Aw* across the cell surface from BOL to cycle 120. (f) Colour map of the absolute change of the reaction coefficient k_{app} across the cell surface from BOL to cycle 120.

significantly by up to 0.05 A/cm^2. Additionally, the regions in the center of the cell, which previously showed the highest current densities, degraded more severely than regions subject to lower current densities. Two spots with a sharp decrease in current density are especially pronounced.

Throughout 131 cycles, the average proton resistance decreased by ~22.1%. The decrease, however, can mainly be attributed to the first 40 cycles. Figure 5d shows the distribution of the absolute change of proton resistance between the BOL and cycle 120. The resistance at the very edge of the cell and the high current spots reduce most significantly. The differences, even though small, might originate from higher carbon corrosion in regions of high current densities and low temperatures. This might sound counterintuitive, but high carbon corrosion rates lead to higher ionomer-to-carbon ratios and hence might improve the ionomer network in the catalyst layer.

Local changes in charge transfer resistance and double layer capacitance due to degradation are not noticeable. Instead, an even distribution is retained throughout 131 freeze-start cycles. Similarly, no pattern of change is visible in the Warburg short parameter A_w (Figure 5e).

From *Aw* and R_{ct} we can calculate the apparent reaction rate coefficient k_{app}, which is the area-independent average reaction rate coefficient per active site[28]:

$$\sqrt{2D}\,\frac{Aw(E)}{R_{ct}(E)} = k_{app}(E)$$

The diffusion coefficient *D* is unknown, but one can assume that it is constant throughout the cell. The resulting color map of the absolute change of $k_{app}/(2D)^{0.5}$ is shown in figure 5f. This parameter is fairly constant (considering its values between 0.9 and 1.1 $s^{-0.5}$), both across the MEA surface and in time during the freeze-start degradation test.[28] Hence, one can conclude that the local reaction kinetics was not significantly degraded by frost-starts. Since changes in the Pt catalyst structure or poisoning of specific Pt sites would lead to an altered apparent rate coefficient, we can attribute the loss of ECSA to carbon corrosion. We, therefore, propose carbon corrosion due to local reactant starvation and voltage reversal during the start-up from sub-zero temperatures as the main degradation mechanism in this case.

Conclusions

In this work, a study on the influence of operating parameters on the spatially resolved impedance of an automotive size fuel cell was conducted, and the impact of realistic temperature gradients on freeze-start cycling degradation was investigated. The results bridge the gap between small-sized lab-scale studies on spatially resolved PEMFC descriptors and simulations for larger-scale applications. As predicted by simulations, the current distribution reveals two distinct maxima along the flow direction due to water management. Local impedance measurements show that high current density areas directly translate to low proton resistance. The relation is pronounced for low flow velocities and low inlet gas humidity. Mass transport problems increase with increasing distance from the air inlet. The average value of the corresponding Warburg coefficient *Aw*, as well as the gradient along the flow channels, increase significantly when reducing the cathodic stoichiometry. Realistic freeze-start cycles with a temperature gradient across the MEA surface proved for the first time that uneven temperature distributions in a stack lead to characteristic degradation patterns. Repeated measurements of the current distribution revealed compensation effects leading to higher current densities in regions held at considerate temperatures and lower current densities in areas subject to −8 °C. Even though the cell reached its EOL after 131 cycles, no significant degradation was visible in the charge transfer resistance, and the Warburg parameter *Aw* associated with diffusion problems. In contrast, the proton resistance decreased throughout the freeze-start cycling experiment. That might be explained by a decrease in catalyst layer thickness and a resulting improvement of the ionomer network at the cathode.

Acknowledgements

Funded by the Deutsche Forschungsgemeinschaft (DFG, German Research Foundation) under Germany's Excellence Strategy – EXC 2089/1 – 390776260. The project (INSPIRE) has received funding from the Fuel Cells and Hydrogen 2 Joint Undertaking under grant agreement No 700127. This Joint Undertaking receives support from the European Union's Horizon 2020 research and innovation programme, Hydrogen Europe and Hydrogen Europe Research. Open Access funding enabled and organized by Projekt DEAL.

Conflict of Interest

The authors declare no conflict of interest.

Data Availability Statement

The data that support the findings of this study are available from the corresponding author upon reasonable request.

Keywords: electrochemical impedance spectroscopy · PEM fuel cells · electrocatalysis · fuel cell degradation mechanisms · temperature effects

[1] Y. Wang, D. F. Ruiz Diaz, K. S. Chen, Z. Wang, X. C. Adroher, *Mater. Today* **2020**, *32*, 178–203.
[2] Hyundai Motor Deutschland GmbH, "Der Hyundai NEXO" to be found under https://www.hyundai.de/modelle/nexo/, **2021**.
[3] American Honda Motor Co, "The Clarity Series" to be found under https://automobiles.honda.com/clarity, **2021**.
[4] BMW Group, "BMW i Hydrogen Next. Unser Brennstoffzellen-Entwicklungsfahrzeug" to be found under https://www.bmwgroup.com/de/unternehmen/bmw-group-news/artikel/BMWi Hydrogen NEXT.html, **2019**.
[5] U. S. Department of Energy, "DOE Hydrogen and Fuel Cells Program" to be found under https//www.???.???, **2019**.
[6] U. S. Department of Energy, "Department of Energy Hydrogen Program Plan" to be found under https://www.hydrogen.energy.gov/pdfs/hydrogen-program-plan-2020.pdf, **2020**.
[7] T. Madden, M. Perry, L. Protsailo, M. Gummalla, S. Burlatsky, N. Cipollini, S. Motupally, T. Jarvi in *Handbook of fuel cells*, Vol. 9, Hoboken, NJ, Wiley Interscience, **2010**, p. 3904.
[8] J. Zhao, X. Li, *Energy Convers. Manage.* **2019**, *199*, 112022.
[9] D. H. Jeon, K. N. Kim, S. M. Baek, J. H. Nam, *Int. J. Hydrogen Energy* **2011**, *36*, 12499–12511.
[10] J. Park, X. Li, *J. Power Sources* **2006**, *162*, 444–459, 2006.
[11] A. J. Bard, L. R. Faulkner, Electrochemical methods, Vol. 2, Hoboken, NJ: Wiley, **2001**, p. 833.
[12] X.-Z. Yuan, C. Song, H. Wang, J. Zhang, *Electrochemical Impedance Spectroscopy in PEM Fuel Cells*, London: Springer London, **2010**, p. 428.
[13] S. Asghari, A. Mokmeli, M. Samavati, *Int. J. Hydrogen Energy* **2010**, *35*, 9283–9290.
[14] A. Weiß, S. Schindler, S. Galbiati, M. A. Danzer, R. Zeis, *Electrochim. Acta* **2017**, *230*, 391–398.
[15] X. Yuan, J. C. Sun, M. Blanco, H. Wang, J. Zhang, D. P. Wilkinson, *J. Power Sources* **2006**, *161*, 2, 920–928.
[16] Y. Wang, X. Shan, N. Tao, *Faraday Discuss.* **2016**, *193*, 9–39.
[17] K. McKelvey, M. A. Edwards, P. R. Unwin, *Anal. Chem.* **2010**, *82*, 15, 6334–6337.
[18] T. Kai, C. G. Zoski, A. J. Bard, *Chem. Commun.* **2018**, *54*, 1934–1947.
[19] D. J. L. Brett, S. Atkins, N. P. Brandon, V. Vesovic, N. Vasileiadis, A. Kucernak, *J. Electrochem. Soc.* **2003**, *6*, A63.
[20] D. Gerteisen, W. Mérida, T. Kurz, P. Lupotto, M. Schwager, C. Hebling, *Fuel Cells* **2011**, *11*, 2, 339–349.
[21] D. Gerteisen, N. Zamel, C. Sadeler, F. Geiger, V. Ludwig, C. Hebling, *Int. J. Hydrogen Energy* **2012**, *37*, 7736–7744.
[22] P. Schneider, C. Sadeler, A.-C. Scherzer, N. Zamel, D. Gerteisen, *J. Electrochem. Soc.* **2019**, *166*, 322–333.
[23] A. Hakenjos, C. Hebling, *J. Power Sources* **2005**, *145*, 307–311.
[24] D. Liu, R. Lin, B. Feng, L. Han, Y. Zhang, M. Ni, S. Wu, *Appl. Energy* **2019**, *254*, 113712.
[25] D. Liu, R. Lin, B. Feng, Z. Yang, *Int. J. Hydrogen Energy* **2019**, *44*, 7564–7573.
[26] J. P. Sabawa, F. Haimerl, F. Riedmann, T. Lochner, A. S. Bandarenka, *Eng. Rep.* **2020**, *32*, 178.
[27] J. P. Sabawa, A. S. Bandarenka, *Electrochim. Acta* **2019**, *311*, 21–29.
[28] J. P. Sabawa, A. S. Bandarenka, *Int. J. Hydrogen Energy* **2021**, *95*, 704.
[29] S. Dutta, S. Shimpalee, J. W. van Zee, *J. Appl. Electrochem.* **2000**, *30*, 135–146.
[30] M. Geske, M. Heuer, G. Heideck, Z. A. Styczynski, *Energies* **2010**, *3*, 770–783.
[31] S. Shimpalee, S. Hirano, M. DeBolt, V. Lilavivat, J. W. Weidner, Y. Khunatorn, *J. Electrochem. Soc.* **2017**, *164*, E3073-E3080.
[32] E. Engebretsen, G. Hinds, Q. Meyer, T. Mason, E. Brightman, L. Castanheira, P. R. Shearing, D. J. Brett, *J. Power Sources* **2018**, *382*, 38–44.
[33] M. Coppo, N. P. Siegel, M. v. Spakovsky, *J. Power Sources* **2006**, *159*, 560–569.
[34] H. K. Esfeh, M. K. A. Hamid, *Energy Procedia* **2014**, *61*, 2617–2620.
[35] L. Xia, C. Zhang, M. Hu, S. Jiang, C. S. Chin, Z. Gao, Q. Liao, *Int. J. Hydrogen Energy* **2018**, *43*, 23441–23449.
[36] H. Chen, B. Liu, R. Liu, Q. Weng, T. Zhang, P. Pei, *Energy Convers. Manage.* **2020**, *205*, 112398.
[37] L. Wang, *Int. J. Hydrogen Energy* **2003**, *28*, 1263–1272.

[38] D. Malevich, E. Halliop, B. Peppley, J. Pharoah, K. Karan, *ECS Trans.* **2009**, *16*, 1763–1774.
[39] E. Cho, J.-J. Ko, H. Y. Ha, S.-A. Hong, K.-Y. Lee, T.-W. Lim, I.-H. Oh, *J. Power Sources* **2003**, *150*, A1667.
[40] M. Oszcipok, D. Riemann, U. Kronenwett, M. Kreideweis, M. Zedda, *J. Power Sources* **2005**, *145*, 407–415.
[41] F. Barbir in *PEM Fuel Cells*, Vol. 142, Elsevier, **2013**, p. 33–72.
[42] BMW Group, "Wasserstoffauto: Alles, was Sie jetzt wissen sollten" to be found under https://www.bmw.com/de/innovation/so-funktionieren-wasserstoffautos.html, **2020**.
[43] IPCC, *Climate Change 2014: Synthesis Report*, Geneva, Switzerland: IPCC, **2014**.
[44] United Nations, "Paris Agreement" to be found under https://unfccc.int/sites/default/files/english_paris_agreement.pdf, **2015**.
[45] T. Lochner, R. Kluge, J. Fichtner, H. El-Sayed, B. Garlyyev, A. Bandarenka, *ChemElectroChem* **2020**, *7*, 3545–3568.

Manuscript received: January 19, 2022
Revised manuscript received: April 4, 2022
Accepted manuscript online: April 13, 2022

Industrial Chemistry & Materials

ROYAL SOCIETY OF CHEMISTRY

PAPER

View Article Online
View Journal | View Issue

Cite this: *Ind. Chem. Mater.*, 2024, **2**, 132

Electrochemical impedance spectroscopy of PEM fuel cells at low hydrogen partial pressures: efficient cell tests for mass production†

Felix Haimerl,‡*[ab] Sunil Kumar,‡[bc] Michael Heere[c] and Aliaksandr S. Bandarenka*[ad]

Quality testing costs hinder the large-scale production of PEM fuel cell systems due to long testing times and high safety measures for hydrogen. While eliminating both issues, electrochemical impedance spectroscopy at low hydrogen concentrations can provide valuable insights into fuel cell processes. However, the influence of high anode stream dilutions on PEM fuel cell performance is not yet completely understood. This study presents a new equivalent circuit model to analyze impedance spectra at low hydrogen partial pressures. The proposed model accurately describes the impedance response and explains the performance decrease at low hydrogen concentrations. First, the reduced availability of hydrogen at the anode leads to rising reaction losses from the hydrogen side. Further, the resulting losses lead to potential changes also influencing the cathode processes. The findings indicate that impedance spectroscopy at low hydrogen partial pressure might provide a reliable fuel cell quality control tool, simplifying production processes, reducing costs, and mitigating risks in fuel cell production.

Keywords: PEM fuel cells; Electrochemical impedance spectroscopy; EIS; Large scale PEMFC production; Anodes; Cathodes.

Received 10th July 2023,
Accepted 25th September 2023

DOI: 10.1039/d3im00075c

rsc.li/icm

1 Introduction

Decarbonizing the transportation sector is crucial in achieving a renewable energy transition, as transport emissions have been growing faster than any other end-use sector.[1] Fuel cells offer a clean alternative to fossil fuel combustion for many transport applications. For road applications, such as cars, trucks, and buses, polymer electrolyte membrane fuel cells (PEMFCs) have emerged as the most promising technology. Over the past decade, rapid developments in fuel cell materials, integration, and manufacturing have fueled commercial interest in fuel cell electric vehicles (FCEVs).[2,3] Prominent original equipment manufacturers (OEMs), such as the BMW Group, Daimler, Volkswagen, Toyota, and Hyundai, have actively engaged in extensive research, development, and demonstration endeavors in this field.[4–8]

Despite the progress, further technological advancements are necessary to maximize FCEVs' viability and widespread adoption.[9] As the emphasis shifts to PEMFC mass production, there is a growing need to develop stable and cost-effective production processes with short cycle times. Within the value chain of FCEVs, several intermediate quality checks are standard since companies usually focus on only one or two of the production steps shown in Fig. 1. These quality checks are a significant obstacle to further commercializing FCEVs.[10–14] Testing protocols must identify and isolate manufacturing flaws in the production process, including quality control checks on individual components, the fuel cell stack, and the fuel cell system while keeping the cost of production low. The IEC 62282-2-100 standard mandates the conduct of routine quality control tests that need to be carried out on every unit.[15] Those tests at the end of the production line are frequently called "End-of-Line" (EoL) or "Factory Acceptance Test" (FAT). They are contractually obligated to customers to verify that the unit meets the specified requirements.[16,17]

[a] *Technical University of Munich, School of Natural Sciences, Department of Physics, Professorship of Physics of Energy Conversion and Storage, 85748 Garching, Germany*
[b] *BMW AG, Petuelring 130, 80809 München, Germany. E-mail: felix.haimerl@bmw.de*
[c] *Technical University Braunschweig, Faculty of Mechanical Engineering, Institute of Internal Combustion Engines and Fuel Cells, 38108 Braunschweig, Germany*
[d] *Technical University of Munich, Catalysis Research Center TUM, Ernst-Otto-Fischer-Straße 1, 85748 Garching, Germany. E-mail: bandarenka@ph.tum.de*
† Electronic supplementary information (ESI) available. See DOI: https://doi.org/10.1039/d3im00075c
‡ Equally contributing authors.

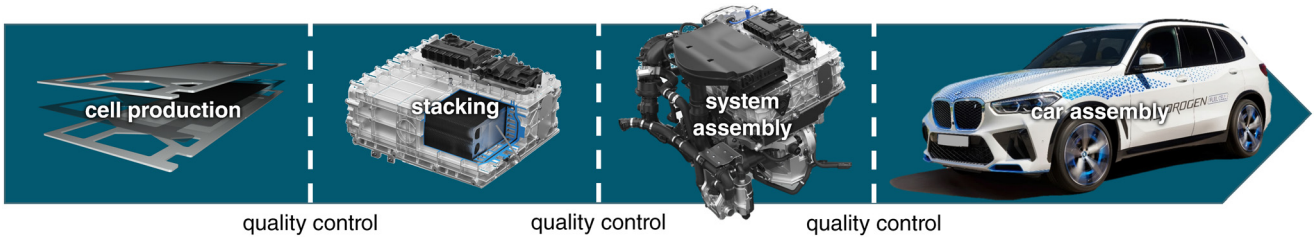

Fig. 1 Visualization of the value chain of a fuel cell electric vehicle. After each production step, a quality control step ensures the safety and performance of the product.

State-of-the-art quality control procedures mostly rely on the operation with hydrogen. However, hydrogen poses safety concerns as it can detonate at a volumetric concentration ratio as low as 4.3% and has high permeability through various materials.[18,19] Consequently, stringent safety measures must be implemented during hydrogen testing, leading to cost inefficiencies in the manufacturing process.[20] Therefore, test strategies that require lower security measures are necessary. For fuel cell components, including catalyst layers, membranes, gas diffusion layers (GDLs), and bipolar plates, optical tools provide a solution. Recent advances in this field include through-plane reactive excitation techniques for detecting pinholes in membrane electrode assemblies,[21] infrared thermography studies to detect membrane irregularities[22] or electrode defects,[23,24] and deep learning implementations.[16,25] However, optical measures are limited to component testing, and alternative methods must be employed for fuel cell stack and fuel cell system testing.

Electrochemical impedance spectroscopy (EIS) offers a well-established method to gain insights into fuel cells for simultaneous fast and non-invasive measurements. By subjecting the fuel cell to small amplitude sinusoidal perturbations, EIS can reveal important information about the charge transfer kinetics, mass transport limitations, and the overall electrochemical behavior of the cell.[26–30] In particular, EIS is a widespread tool to monitor degradation in PEM fuel cells[31–33] and is also applied in FCEVs for on-road state-of-health monitoring.[34,35] Applying EIS at low hydrogen partial pressure (hpp) might provide valuable insights while mitigating safety and cost concerns. However, since the cathode side in a PEM fuel cell is usually rate-determining, few studies investigate the impact of reduced hpp on the fuel cell performance. Stühmeier *et al.*[37] studied the hydrogen oxidation reaction (HOR) pressure dependence in the range 100–400 kPa using hydrogen pump measurements and found a dependency of the apparent activation energy of the HOR on the hpp. In contrast, a full factorial study by Gerling *et al.*[41] found no dependency of the apparent activation energy on the hpp in the range 4–100 kPa. Both studies did, however, only focus on the impact on the anodic reaction.

Through this study, we aim to enhance the understanding of fuel cell behavior under varying hydrogen concentrations using impedance analysis and contribute to developing improved diagnostic techniques and strategies for fuel cell system manufacturing.

2 Results and discussion

The membrane electrolyte assemblies (MEAs) were operated at various levels of anode inlet gas dilution corresponding to different hydrogen partial pressures (hpps) to investigate the correlation between hpp and performance. Polarization curves and impedance spectra were recorded for hpps between 36 kPa and 190 kPa. Fig. 2 shows the resulting polarization curves at 190 kPa (solid curve), 98 kPa (dashed curve), and 36 kPa (dotted curve) hydrogen partial pressure. The dilution was achieved by mixing nitrogen gas into the anode gas stream while the hydrogen flow remained constant. Humidified air was used as the cathode gas.

The polarization curves demonstrate a pronounced decline in performance with decreasing partial pressure across the entire range of current densities. Comparing the polarization curves, the voltage losses are more apparent at higher current densities. In Fig. 3a, the resulting voltage values at j = 1.0 A cm^{-2} are plotted against the hydrogen partial pressure. We see a logarithmic dependency with a voltage difference of 54 mV between 190 kPa and 36 kPa hpp, respectively. For the voltage values at j = 2.0 A cm^{-2} (Fig. 3b), we found a logarithmic dependency with a total voltage drop of 107 mV at 36 kPa partial pressure. The voltage difference at j = 2.0 A cm^{-2} is twice as high as at j = 1.0 A cm^{-2}.

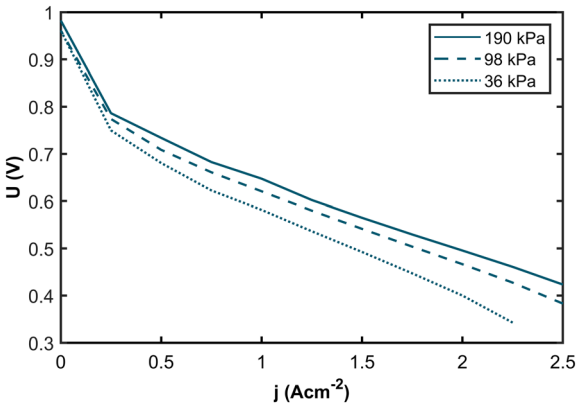

Fig. 2 Polarization curves for partial hydrogen pressures of 190 kPa (solid curve), 98 kPa (dashed curve), and 36 kPa (dotted curve). At 36 kPa, the maximum current density of 2.5 A cm^{-2} was not achieved without the cell voltage dropping below 0.3 V, which was specified as the lower voltage limit to ensure low degradation.

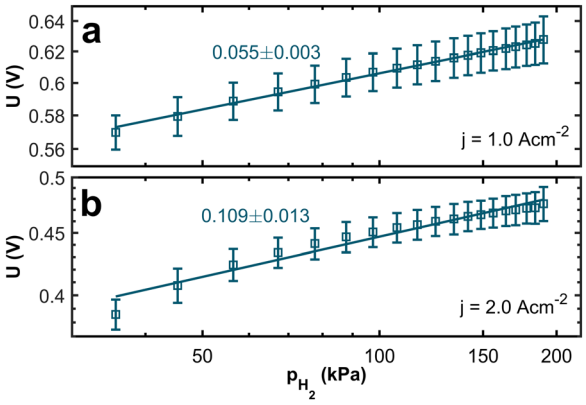

Fig. 3 Logarithmic plot of the voltage at a current density of (a) 1.0 A cm^{-2} and (b) 2.0 A cm^{-2} against the hydrogen partial pressure. The lines serve as a guide for the eye.

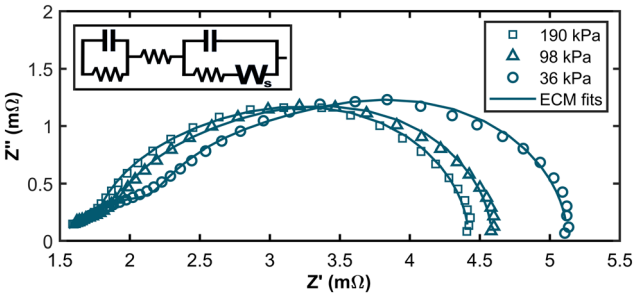

Fig. 4 Nyquist plot of the impedance spectra for hydrogen partial pressures of 36 kPa, 98 kPa, and 190 kPa. The experimental data points (markers) were recorded in a frequency range between 3 and 10 kHz at a current density of 1.0 A cm^{-2}. The corresponding fits are displayed as solid curves. The ECM for fitting the impedance data is displayed in the top-left corner.

From the Nernst equation (eqn (1)), we can see a theoretical logarithmic dependency of the open circuit voltage U_{OCV} on the partial pressure of hydrogen p_{H_2}:

$$U_{OCV} = U_0 + \frac{RT}{2F} \cdot \ln\left(\frac{p_{H_2} p_{O_2}^{0.5}}{p_{H_2O}}\right) \quad (1)$$

Here, U_0 is the theoretical open circuit voltage at standard conditions. R is the universal gas constant, T is the temperature, F is the Faraday constant, and p_{O_2} and p_{H_2O} are the corresponding partial pressures of oxygen and water. Additionally, the partial pressure of reactant gases also influences hydrogen crossover, exchange current densities, and the limiting current density of electrode reactions. The polarization curve can be described by

$$U_{cell} = U_{OCV} - \eta_{HOR} - \eta_{ORR} - \eta_{MT} - \eta_{\Omega} \quad (2)$$

with the overpotentials of the hydrogen oxidation reaction (HOR), the oxygen reduction reaction (ORR), the mass transport losses (MT), and ohmic losses. Zhang *et al.*[36] simulated the effects of different back pressures on the anode, which can directly be transferred to the influence of hpp. They found that the back pressure influences the cell voltage at high current densities significantly more than it does at low current densities, which agrees with the data from our experiments.

To investigate the origins of the voltage losses related to decreased hpp, electrochemical impedance spectra were recorded for each partial pressure value at a current density of j = 1.0 A cm^{-2}. The frequencies spanned 36 logarithmically distributed points between 3 Hz and 10 kHz. In total, twelve spectra were recorded for each partial pressure. The Kramers–Kronig check was performed to ensure high data quality.

Exemplary Nyquist plots are shown in Fig. 4 (For all EIS spectra, please refer to the ESI†). It is apparent that the low-frequency intercept with the x-axis, associated with overall fuel cell losses, increased at low hpp. A pronounced feature in the high-frequency range becomes visible as the partial pressure decreases. Previous studies found a similar feature for extremely low platinum loadings at the anode, contributing to anode reaction losses.[37,38] Therefore, we propose a new equivalent circuit model (ECM) for fitting the impedance data of PEM fuel cells at low hpp. The ECM consists of an uncompensated resistance equalling all ohmic resistances in the cell and a parallel circuit of a charge transfer resistance, and a double layer capacitance mimicking the electrochemical response in the cathode layer. In series with the charge transfer resistance, a Warburg short element simulates gas diffusion losses in the cathode. To account for increasing anode contributions to the cell overpotential at high anode stream dilutions, we added a parallel connection of a charge transfer resistance for the HOR and a capacitance for the double layer forming at the anode interface. The ECM and the resulting fits are shown in Fig. 4 for 36 kPa, 98 kPa, and 190 kPa partial pressure.

The Bode plots and the corresponding residuals of the fits are displayed in Fig. 5. The ECM fits show good agreement with the experimental data across all partial pressure values, with all relative residuals below 5%.

In Fig. 6a, we can see the relation between the uncompensated resistance, which is dominated by proton transport, and the partial pressure. We observe a trend of increasing resistance with decreasing hydrogen concentration. Theoretically, we do not expect a dependency between the uncompensated resistance and the partial pressure. However, the relationship between the water content of the ionomer and proton conduction is well established.[39,40] Since we keep the stoichiometry constant and adjust the nitrogen flow, flow velocities increase significantly at low hydrogen concentrations. Thus, the electro-osmatic drag might drain water from the ionomer and increase the resistance associated with proton transport.

In contrast, the theory does predict a dependency of the anodic charge transfer resistance on the hpp.[16] The double-logarithmic plot in Fig. 6b reveals the proportionality, validating the chosen ECM. The Butler–Volmer equation describes the relation between current density and anode

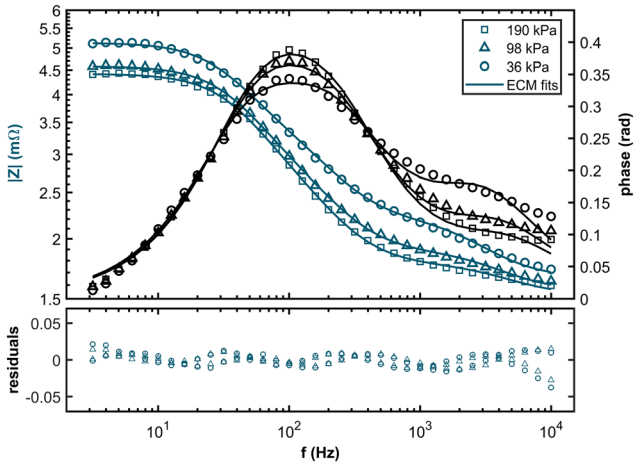

Fig. 5 Bode plot of the impedance spectra for hydrogen partial pressures of 36 kPa, 98 kPa, and 190 kPa. The experimental data points (markers) were recorded in a frequency range between 3 Hz and 10 kHz at a current density of 1.0 A cm^{-2}. The corresponding fits are displayed as solid curves. The corresponding relative residuals of the fits are displayed below.

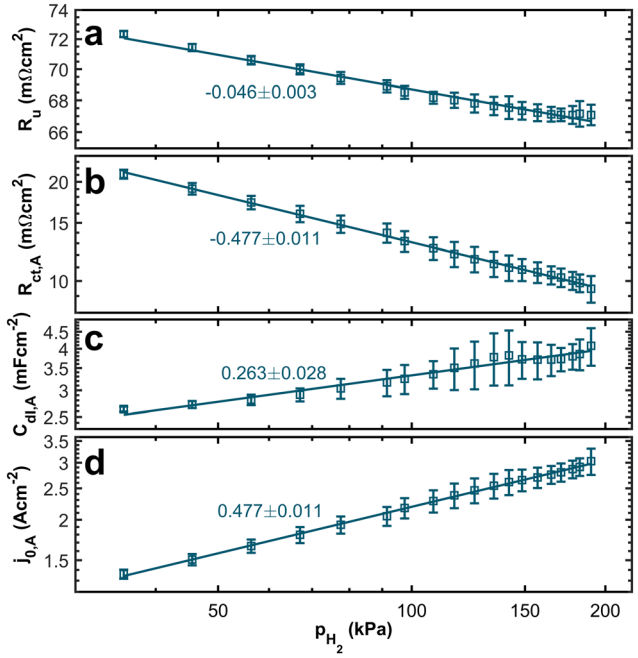

Fig. 6 Double-logarithmic plots of (a) the uncompensated resistance; (b) the charge transfer resistance at the anode; (c) the double-layer capacitance of the anode; and (d) the effective exchange current density of the HOR. All against the hydrogen partial pressure.

overpotential. For small overpotentials, we can linearize the equation. Hence, the voltage loss at the anode can be described by

$$\eta_{HOR} = j \cdot \frac{RT}{Fj_{0,A}(\alpha_A + \alpha_C)} \quad (3)$$

with the current density j and the exchange current density $j_{0,A}$ with respect to the geometric surface area. The anodic and cathodic transfer coefficients α_A, α_C cannot be determined here. Therefore, the sum $\alpha_A + \alpha_C$ is set to unity.[37] From the linearized Butler–Volmer equation, we can derive an expression for the impedance of the anodic charge transfer.

$$R_{A,ct} = \frac{\partial \eta_{HOR}}{\partial j} = \frac{RT}{Fj_{0,A}} \quad (4)$$

We can calculate the exchange current density from the charge transfer resistance at the anode. The exchange current density depends on the hydrogen concentration on the catalyst surface and, therefore, should be directly proportional to the hpp according to Henry's Law.

$$\frac{j_{0,A}}{j^*_{0,A}} = \left(\frac{c_{H_2}}{c^*_{H_2}}\right)^m = \left(\frac{p_{H_2}}{p^*_{H_2}}\right)^m \quad (5)$$

Here, $j^*_{0,A}$ is the calculated exchange current density at a reference concentration $c^*_{H_2}$ referring to a reference partial pressure $p^*_{H_2}$. Hence, we can determine the reaction order m of the HOR from the slope in a double logarithmic plot of the exchange current density against the hpp. The corresponding plot is shown in Fig. 6d. We obtain a reaction order of 0.477 ± 0.011, which is in line with previous publications.[37,41,42] Stühmeier *et al.*[37] found a reaction order of 0.39 ± 0.05 at 60 °C calculated from micro-polarization measurements in a hydrogen pumping configuration. Therefore, it was shown that we could indeed analyze anode contributions to the fuel cell performance by reducing the hpp.

A trend of higher capacities at higher partial pressures (see Fig. 6c) supports the idea that the electro-osmotic drag at high flow velocities dries out the ionomer. High water content in the catalyst layer is generally associated with high double-layer capacities.[34,43] Hence, drying of the anode catalyst layers at high flow velocities leads to reduced double layer capacities.

Fig. 7 depicts the dependence of cathode characteristics on the hpp in the anode stream. No clear trend is visible from the double-logarithmic plot of the charge transfer resistance associated with the ORR in Fig. 7a. While the absolute values of the cathodic charge transfer resistance are nearly one order of magnitude higher than those for the anodic charge transfer resistance, the measured values at low hpps equal those at high partial pressures within the error bars. Therefore, the dependency of the anodic reaction on the hydrogen concentration is, as expected, more significant than that of the ORR charge transfer resistance. Fig. 7b–d displays the other fitting parameters $C_{dl,C}$, Aw_C, B_C associated with the cathode. All three parameters show a dependency on the hpp. Even though the trend is smaller than those seen for parameters associated with the anode, the effect of the hydrogen concentration at the anode on the double layer capacitance and the diffusion at the cathode side is surprising. We will therefore analyze the origin further.

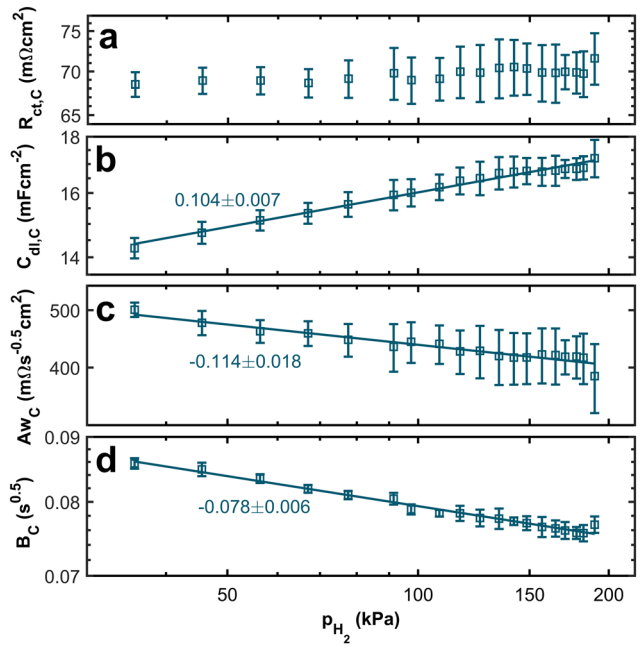

Fig. 7 Double-logarithmic plots of (a) the cathodic charge transfer resistance; (b) the double layer capacitance $C_{dl,C}$; (c) the first Warburg short parameter Aw_C; and (d) the second Warburg short parameter B_c *vs.* p_{H_2}.

From the correlation between the Warburg short parameter Aw_C and the charge transfer resistance $R_{ct,C}$, we can calculate the apparent rate coefficient k_{app}.

$$\frac{Aw_C}{R_{ct,C}} = \frac{k_{app}}{\sqrt{2D}} \quad (6)$$

Also, we can deduce the Nernst diffusion layer thickness δ from the second Warburg short parameter B, assuming the diffusion coefficient D is constant.

$$\delta = B \cdot \sqrt{D} \quad (7)$$

Diffusion losses of oxygen can generally stem from three factors: oxygen diffusion in the gas mixture, diffusion through a layer of liquid water that forms at high currents or humidified gases, and diffusion through the ionomer in the catalyst layer. Hence, the determination of the diffusion coefficient is not straightforward. Caulk & Baker measured a jump in oxygen transport resistance at elevated current densities and contributed to the sudden increase in the formation of a water layer. For similar operating conditions and a similar GDL compared to this study, the main contribution to the oxygen transport resistance was the diffusion through a thin water layer.[44] Therefore, the diffusion constant for oxygen through water $D = 5.31 \times 10^{-5}$ cm^2 s^{-1} was used for calculations.[45] The calculated Nernst diffusion layer thickness ranges from ~5.50 μm to ~6.24 μm. The values are within the range of literature values and compare well with expected water film thickness values.[46,47] Other publications also suggest that a significant mass transport resistance contribution arises from the diffusion through a thin ionomer layer.[48] However, the diffusion layer values calculated with the diffusion constant of the ionomer ($D = 7.81 \times 10^{-6}$ cm^2 s^{-1} at 60 °C)[49] are considerably different (2.11 μm to 2.40 μm) than expected ionomer film thicknesses.[50]

The resulting trends of the apparent rate coefficient k_{app} and the Nernst diffusion layer thickness δ are displayed in Fig. 8. The values for the ratio $Aw_C/R_{ct,C}$ vary between ~5.4 $s^{-0.5}$ and ~7.3 $s^{-0.5}$, which is in accordance with previously reported values.[32,33,51] We can see a slight dependence of the apparent rate coefficient and the Nernst diffusion layer thickness on the hpp. Since the cell is operated in galvanostatic mode, the potential changes with the partial pressure (compare Fig. 3). The reaction kinetics and the mass transport depend on the electrode potential. Also, hydrogen crossover might increase due to higher flow velocities on the anode side. An increase in the rate of hydrogen crossover correlates with increased mass transport issues on the cathode side.[52,53]

3 Conclusions

The study focused on investigating the correlation between hydrogen partial pressure (hpp) and the performance of PEMFCs, which can help in testing the fuel cells under low hydrogen partial pressure. Polarization curves and impedance spectra were recorded for a wide range of hpps between 36 kPa and 190 kPa by diluting the hydrogen stream with nitrogen while keeping the hydrogen flow constant.

The polarization curves and impedance spectra obtained from the experiments showed a pronounced decline in performance with decreasing hpp across the entire range of current densities. The voltage losses were more significant at higher current densities.

The impedance spectra analysis revealed that the low-frequency intercept associated with overall fuel cell losses increased at low hpp, while a prominent feature in the high-frequency range became visible. An ECM was proposed to fit

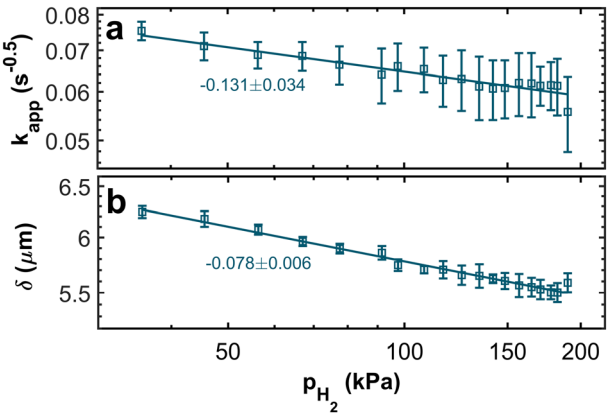

Fig. 8 Double-logarithmic plots of (a) the apparent rate coefficient k_{app} and (b) the Nernst diffusion layer thickness δ in relation to the hydrogen partial pressure.

the impedance data, including a part for anode contributions. The fits showed good agreement with the experimental data. As predicted from theory, the charge transfer resistance associated with the anode showed an exponential dependency on hpp. The calculated anodic reaction order confirmed results from previous studies based on micro-polarization measurements. We, therefore, proved the validity of the chosen ECM. The cathode characteristics, including charge transfer resistance, double-layer capacitance, and Warburg short parameters, also showed dependencies on the hpp, although smaller than those observed for the anode. While hpp does not influence cathode processes directly, the induced performance losses lead to electrode potential changes since the current was kept constant. The unsaturated resistance, dominated by proton transport, showed an increasing trend with decreasing hydrogen concentrations, potentially attributed to increased electro-osmotic drag.

Overall, the research findings contribute to understanding the relationship between hpp and the performance of PEMFCs. Improved knowledge of testing with low hydrogen concentrations should pave the way to simplify processes, reduce costs, and mitigate risks in fuel cell production.

4 Experimental section

4.1 Cell preparation

The MEAs were assembled manually and subsequently hot-pressed for 240 s at 160 °C to ensure optimal electric contact. A proton exchange membrane supplied by Gore (M775.15) was utilized. For anode and cathode, commercial platinum/Vulcan catalyst layers with weight loadings of 0.08 mg cm^{-2} and 0.4 mg cm^{-2}, respectively, were applied. The MEA configuration is complemented by two gas diffusion layers by Toray with a thickness of 150/180 μm for anode/cathode. The effective active area of the MEAs is 43.56 cm^2. In the context of the experiment, each fuel cell in the experimental setup consisted of a single MEA sandwiched between two graphite flow fields. The flow fields were arranged in a parallel counter-flow configuration, allowing for efficient gas flow and reaction pathways. Each side of the cell setup is completed by a copper current collector plated with gold, an isolation plate, and compression hardware. The compression plates evenly compress the cell to a pressure of 900 kPa. The cell setup is visualized in Fig. 9.

Electrochemical measurements

Tests were performed on the single-cell test station Evaluator C50-LT from HORIBA FuelCon AG (Germany). During the experimental procedures, the fuel cell was operated automatically with TestWork by HORIBA FuelCon AG. The anode was supplied with a mixture of hydrogen (99.999% purity) and nitrogen (99.999% purity), and the cathode was fed with air. The hydrogen flow was kept at 19.2 cm^2 s^{-1}, equalling a stoichiometric factor of 1.5 for the maximum current density of 2.5 A cm^{-2}. Similarly, to ensure an ample

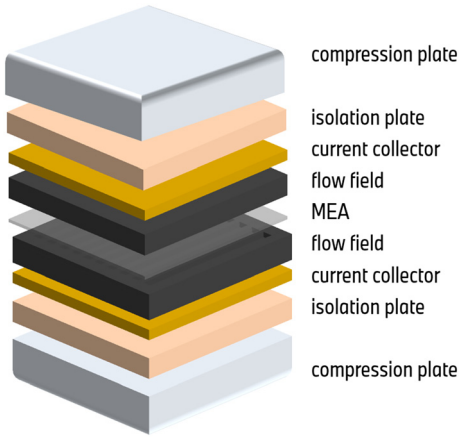

Fig. 9 Visualization of the cell setup.

air supply at the cathode and mitigate losses, the air was supplied at a flow rate of 168.6 cm^2 s^{-1} corresponding to a stoichiometry of 5.5 at 2.5 A cm^{-2}. While the hydrogen flow was limited by the maximum total flow rates of the testbench, the air stoichiometry was chosen to minimize the effect of mass transport limitations. The supplied gases were conditioned to a constant relative humidity of 50% throughout the experiments at a cell temperature of 60 °C. The back pressure was kept at 200 kPa at both the anode and cathode. For better comparability, the set of operating parameters was adapted from common operating conditions in the literature. The hpp was varied by adapting the nitrogen flow while the supply of hydrogen and air was kept constant. Starting from 190 kPa, equaling no added nitrogen supply, going down to 36 kPa partial pressure, equaling a nitrogen flow rate of 87.7 cm^2 s^{-1}, and going back up to pure hydrogen. The whole procedure was repeated two times so that the measurements for all hpps were carried out in total four times. This way, it was ensured that the data was not affected by any degradation effects.

Before conducting the measurements, a comprehensive 9 h activation step based on potential cycling was carried out to prepare the cell for optimal functioning. A purging process was implemented with a predetermined high gas concentration to minimize any potential fluctuations. This purging process was intended to stabilize the cell and create a controlled environment for reliable measurements.

At each hpp step, a polarization curve was recorded. The experimental procedure involved gradually increasing the cell's current density up to 2.5 A cm^{-2}. Potentials were recorded at each defined current density while ramping the current density downward. The standard duration for holding each current density was typically 60 s to ensure accurate and reliable measurements. However, shorter durations were employed for lower densities and open circuit voltages to minimize the risk of potential cell degradation. Minimizing the exposure time under these specific conditions mitigated the risk of any adverse effects on the cell's performance and integrity. A 4800 s hold was introduced after every change in

hpp to ensure consistent experimental conditions. This time interval allowed the system to stabilize before measuring each polarization curve.

Impedance measurements were subsequently conducted after each polarization curve while keeping the nitrogen dilution and operating parameters constant. A Zahner Zennium workstation was utilized for these measurements, capturing spectra ranging from 3 Hz to 10 kHz at 1.0 A cm^{-2} with five points per decade. After a stabilization time of 600 s, three impedance spectra are recorded with a 600 s waiting time between each other.

Data processing

For the polarization curves, the voltage values were averaged over 25 s for each current hold. The resulting cell voltages were averaged over the four polarization curves measured for each partial pressure for error analysis.

Prior to the fitting process, all impedance spectra were checked for validity by applying the Kramers–Kronig check. The impedance spectra were fitted with MATLAB using a non-linear least square fitting algorithm. Subsequently, the fitting parameters were averaged over twelve impedance spectra taken for each hpp. Regression models for the relations of voltage values and fitting parameters on the partial pressure were also fitted using a non-linear least square algorithm. Uncertainties for the cell descriptors deduced from the fitting parameters were calculated by applying error propagation rules.

Partial pressure values were calculated by subtracting the water vapor pressure from the back pressure and dividing the resulting value of 190 kPa according to the volumetric ratios of hydrogen and nitrogen.

Conflicts of interest

The authors declare no conflict of interest.

Acknowledgements

We acknowledge financial funding from the Deutsche Forschungsgemeinschaft (DFG, German Research Foundation) under Germany's Excellence Strategy – EXC 2089/1 – 390776260 (e-conversion) & – EXC 2163/1 – 390881007 (Sustainable and Energy Efficient Aviation). We also acknowledge the BMW AG, Germany for supporting the research.

References

1 Transport, International Energy Agency, **https://www.iea.org/reports/transport**, (23.08.2023).
2 D. A. Cullen, K. C. Neyerlin, R. K. Ahluwalia, R. Mukundan, K. L. More, R. L. Borup, A. Z. Weber, D. J. Myers and A. Kusoglu, New roads and challenges for fuel cells in heavy-duty transportation, *Nat. Energy*, 2021, **6**, 462–474.
3 B. G. Pollet, S. S. Kocha and I. Staffell, Current status of automotive fuel cells for sustainable transport, *Curr. Opin. Electrochem.*, 2019, **16**, 90–95.
4 *Automobility in transition? a socio-technical analysis of sustainable transport*, ed. F. W. Geels, Routledge, New York, 2012.
5 B. Budde, F. Alkemade and K. M. Weber, Expectations as a key to understanding actor strategies in the field of fuel cell and hydrogen vehicles, *Technol. Forecast. Soc. Change*, 2012, **79**, 1072–1083.
6 Y. Luo, Y. Wu, B. Li, T. Mo, Y. Li, S.-P. Feng, J. Qu and P. K. Chu, Development and application of fuel cells in the automobile industry, *J. Energy Storage*, 2021, **42**, 103124.
7 T. Yoshida and K. Kojima, Toyota MIRAI fuel cell vehicle and progress toward a future hydrogen society, *Interface Mag.*, 2015, **24**, 45–49.
8 G. Trencher and A. Edianto, Drivers and barriers to the adoption of fuel cell passenger vehicles and buses in Germany, *Energies*, 2021, **14**, 833.
9 O. Saritas, D. Meissner and A. Sokolov, A transition management roadmap for fuel cell electric vehicles (FCEVs), *J. Knowl. Econ.*, 2019, **10**, 1183–1203.
10 A. Kampker, P. Ayvaz, C. Schön, J. Karstedt, R. Förstmann and F. Welker, Challenges towards large-scale fuel cell production: Results of an expert assessment study, *Int. J. Hydrogen Energy*, 2020, **45**, 29288–29296.
11 J. Marcinkoski, B. D. James, J. A. Kalinoski, W. Podolski, T. Benjamin and J. Kopasz, Manufacturing process assumptions used in fuel cell system cost analyses, *J. Power Sources*, 2011, **196**, 5282–5292.
12 M. Ulsh, B. Sopori, N. V. Aieta and G. Bender, Challenges to high-volume production of fuel cell materials: Quality control, *ECS Trans.*, 2013, **50**, 919–926.
13 J. Wang, H. Wang and Y. Fan, Techno-economic challenges of fuel cell commercialization, *Engineering*, 2018, **4**, 352–360.
14 M. Miller and A. Bazylak, A review of polymer electrolyte membrane fuel cell stack testing, *J. Power Sources*, 2011, **196**, 601–613.
15 International Electrotechnical Commission, Fuel cell technologies: Part 2–100: Fuel cell modules – Safety, **https://webstore.iec.ch/publication/59780**, (23.08.2023).
16 F. Sasse, G. Fischer, N. Eschner and G. Lanza, Improving End-Of-Line Quality Control of Fuel Cell Manufacturing Through Machine Lerning Enabled Data Analysis, *PhD thesis*, Technische Universität Chemnitz, Chemnitz, 2022.
17 M. Killcross, in *Chemical and Process Plant Commissioning Handbook*, Elsevier, 2021, pp. 203–212.
18 M. Molnarne and V. Schroeder, Hazardous properties of hydrogen and hydrogen containing fuel gases, *Process Saf. Environ. Prot.*, 2019, **130**, 1–5.
19 C. Henager, in *Materials for the Hydrogen Economy*, ed. R. Jones and G. Thomas, CRC Press, 2007, pp. 181–190.
20 E. Abohamzeh, F. Salehi, M. Sheikholeslami, R. Abbassi and F. Khan, Review of hydrogen safety during storage, transmission, and applications processes, *J. Loss Prev. Process Ind.*, 2021, **72**, 104569.

21 M. Ulsh, A. DeBari, J. M. Berliner, I. V. Zenyuk, P. Rupnowski, L. Matvichuk, A. Z. Weber and G. Bender, The development of a through-plane reactive excitation technique for detection of pinholes in membrane-containing MEA sub-assemblies, *Int. J. Hydrogen Energy*, 2019, **44**, 8533–8547.
22 M. Wang, S. Medina, J. Ochoa-Lozano, S. Mauger, S. Pylypenko, M. Ulsh and G. Bender, Visualization, understanding, and mitigation of process-induced-membrane irregularities in gas diffusion electrode-based polymer electrolyte membrane fuel cells, *Int. J. Hydrogen Energy*, 2021, **46**, 14699–14712.
23 M. Ulsh, J. M. Porter, D. C. Bittinat and G. Bender, Defect detection in fuel cell gas diffusion electrodes using infrared thermography, *Fuel Cells*, 2016, **16**, 170–178.
24 P. K. Das, A. Z. Weber, G. Bender, A. Manak, D. Bittinat, A. M. Herring and M. Ulsh, Rapid detection of defects in fuel-cell electrodes using infrared reactive-flow-through technique, *J. Power Sources*, 2014, **261**, 401–411.
25 A. Yan, P. Rupnowski, N. Guba and A. Nag, Towards deep computer vision for in-line defect detection in polymer electrolyte membrane fuel cell materials, *Int. J. Hydrogen Energy*, 2023, **48**, 18978–18995.
26 X.-Z. Yuan, C. Song, H. Wang and J. Zhang, *Electrochemical Impedance Spectroscopy in PEM Fuel Cells*, Springer London, London, 2010.
27 M. A. Rubio, A. Urquia and S. Dormido, Diagnosis of performance degradation phenomena in PEM fuel cells, *Int. J. Hydrogen Energy*, 2010, **35**, 2586–2590.
28 R. R. Gaddam, L. Katzenmeier, X. Lamprecht and A. S. Bandarenka, Review on physical impedance models in modern battery research, *Phys. Chem. Chem. Phys.*, 2021, **23**, 12926–12944.
29 S. M. Rezaei Niya and M. Hoorfar, Study of proton exchange membrane fuel cells using electrochemical impedance spectroscopy technique – A review, *J. Power Sources*, 2013, **240**, 281–293.
30 T. Lochner, M. Perchthaler, F. Hnyk, D. Sick, J. P. Sabawa and A. S. Bandarenka, Analysis of the capacitive behavior of polymer electrolyte membrane fuel cells during operation, *ChemElectroChem*, 2021, **8**, 96–102.
31 T. Lochner, L. Hallitzky, M. Perchthaler, M. Obermaier, J. Sabawa, S. Enz and A. S. Bandarenka, Local degradation effects in automotive size membrane electrode assemblies under realistic operating conditions, *Appl. Energy*, 2020, **260**, 114291.
32 J. P. Sabawa and A. S. Bandarenka, Investigation of degradation mechanisms in PEM fuel cells caused by low-temperature cycles, *Int. J. Hydrogen Energy*, 2021, **46**, 15951–15964.
33 J. P. Sabawa and A. S. Bandarenka, Degradation mechanisms in polymer electrolyte membrane fuel cells caused by freeze-cycles: Investigation using electrochemical impedance spectroscopy, *Electrochim. Acta*, 2019, **311**, 21–29.
34 T. Lochner, M. Perchthaler, J. T. Binder, J. P. Sabawa, T. A. Dao and A. S. Bandarenka, Real-time impedance analysis for the on-road monitoring of automotive fuel cells, *ChemElectroChem*, 2020, **7**, 2784–2791.
35 S. Dirkes, J. Leidig, P. Fisch and S. Pischinger, Prescriptive Lifetime Management for PEM fuel cell systems in transportation applications, Part II: On-board operando feature extraction, condition assessment and lifetime prediction, *Energy Convers. Manage.*, 2023, **283**, 116943.
36 J. Zhang, C. Song, J. Zhang, R. Baker and L. Zhang, Understanding the effects of backpressure on PEM fuel cell reactions and performance, *J. Electroanal. Chem.*, 2013, **688**, 130–136.
37 B. M. Stühmeier, M. R. Pietsch, J. N. Schwämmlein and H. A. Gasteiger, Pressure and temperature dependence of the hydrogen oxidation and evolution reaction kinetics on Pt electrocatalysts via PEMFC-based hydrogen-pump measurements, *J. Electrochem. Soc.*, 2021, **168**, 064516.
38 A. Huth, B. Schaar and T. Oekermann, A "proton pump" concept for the investigation of proton transport and anode kinetics in proton exchange membrane fuel cells, *Electrochim. Acta*, 2009, **54**, 2774–2780.
39 L. Wu, Z. Zhang, J. Ran, D. Zhou, C. Li and T. Xu, Advances in proton-exchange membranes for fuel cells: An overview on proton conductive channels (PCCs), *Phys. Chem. Chem. Phys.*, 2013, **15**, 4870.
40 P. Knauth and M. L. Di Vona, Hydration and proton conductivity of ionomers: The model case of sulfonated aromatic polymers, *Front. Energy Res.*, 2014, **2**, 50.
41 C. Gerling, M. Hanauer, U. Berner and K. A. Friedrich, PEM single cells under differential conditions: Full factorial parameterization of the ORR and HOR kinetics and loss analysis, *J. Electrochem. Soc.*, 2022, **169**, 014503.
42 K. C. Neyerlin, W. Gu, J. Jorne and H. A. Gasteiger, Study of the exchange current density for the hydrogen oxidation and evolution reactions, *J. Electrochem. Soc.*, 2007, **154**, B631.
43 S. A. Watzele, L. Katzenmeier, J. P. Sabawa, B. Garlyyev and A. S. Bandarenka, Temperature dependences of the double layer capacitance of some solid/liquid and solid/solid electrified interfaces. An experimental study, *Electrochim. Acta*, 2021, **391**, 138969.
44 D. A. Caulk and D. R. Baker, Heat and Water Transport in Hydrophobic Diffusion Media of PEM Fuel Cells, *J. Electrochem. Soc.*, 2010, **157**, B1237.
45 K. R. Harris and L. A. Woolf, Pressure and temperature dependence of the self diffusion coefficient of water and oxygen-18 water, *J. Chem. Soc., Faraday Trans. 1*, 1980, **76**, 377.
46 J. W. Darbyshire and J. B. Lawrence, An electrochemically based electrical fuel cell model. In an electrochemically based electrical fuel cell model, *AUPEC*, 2004.
47 T. Hoshiko, H. Nakajima, T. Konomi, T. Kitahara and S. Kita, Estimation of Water Layer Thickness Adjacent to the Cathode Catalyst Layer of a PEFC (Analysis Using Electrochemical Impedance Spectroscopy), *ECS Trans.*, 2008, **16**, 2117–2123.
48 N. Nonoyama, S. Okazaki, A. Z. Weber, Y. Ikogi and T. Yoshida, Analysis of oxygen-transport diffusion resistance in proton-exchange-membrane fuel cells, *J. Electrochem. Soc.*, 2011, **158**, B416.

49 L. Zhang, C. Ma and S. Mukerjee, Oxygen reduction and transport characteristics at a platinum and alternative proton conducting membrane interface, *J. Electroanal. Chem.*, 2004, **568**, 273–291.
50 Z. Fang, M. S. Lee, J. Y. Kim, J. H. Kim and T. F. Fuller, The effect of carbon support surface functionalization on PEM fuel cell performance, durability, and ionomer coverage in the catalyst layer, *J. Electrochem. Soc.*, 2020, **167**, 064506.
51 F. Haimerl, J. P. Sabawa, T. A. Dao and A. S. Bandarenka, Spatially resolved electrochemical impedance spectroscopy of automotive PEM fuel cells, *ChemElectroChem*, 2022, **9**, e20220006.
52 B. Ghorbani, J. DeVaal, G. Afonso and K. Vijayaraghavan, Use of reduced-voltage EIS to establish a relation between oxygen concentration and EIS responses of large commercial PEM fuel cell modules, *Int. J. Hydrogen Energy*, 2023, S0360319923021791.
53 R. Omrani and B. Shabani, Hydrogen crossover in proton exchange membrane electrolysers: The effect of current density, pressure, temperature, and compression, *Electrochim. Acta*, 2021, **377**, 138085.

Acronyms

AC alternating current

AFC alkaline fuel cell

BEV battery electric vehicle

BOL begin of life

BPP bipolar plate

CAD computer-aided design

CNLS complex non-linear least square

CPE constant phase element

CV cyclic voltammetry

DC direct current

DMFC direct methanol fuel cell

DOE U.S. Department of Energy

ECM equivalent circuit model

ECSA electrochemical active surface area

EIS electrochemical impedance spectroscopy

EOL end of life

FCEV fuel cell electric vehicle

FCS fuel cell system

FS full scale

GDL gas diffusion layer

HFR high-frequency resistance

HOR hydrogen oxidation reaction

hpp hydrogen partial pressure

ICEV internal combustion engine vehicle

MCFC molten carbon fuel cell

MEA membrane electrode assembly

MFC mass flow controller

MPL microporous layer

OCV open-circuit voltage

ORR	oxygen reduction reaction
PAFC	phosphoric acid fuel cell
PCB	printed circuit board
PEM	polymer electrolyte membrane
PEMFC	polymer electrolyte membrane fuel cell
PEN	polyethylene naphthalate
PFSA	perfluorinated sulfonic acid
PHEV	plugin hybrid electric vehicle
ppb	parts per billion
PTFE	polytetrafluoroethylene
RD	reading
rh	relative humidity
SOFC	solid oxid fuel cell
SOP	stable operation point
TCP	temperature control plate
UN	United Nations
wt	weight

List of Figures

List of Tables

Bibliography

[1] K. Vohra, E. A. Marais, W. J. Bloss, J. Schwartz, L. J. Mickley, M. Van Damme, L. Clarisse, and P.-F. Coheur, “Rapid rise in premature mortality due to anthropogenic air pollution in fast-growing tropical cities from 2005 to 2018,” *Science Advances*, vol. 8, no. 14, p. eabm4435, 2022.

[2] W. Hill, E. L. Lim, C. E. Weeden, C. Lee, M. Augustine, K. Chen, F.-C. Kuan, F. Marongiu, E. J. Evans, D. A. Moore, F. S. Rodrigues, O. Pich, B. Bakker, H. Cha, R. Myers, F. van Maldegem, J. Boumelha, S. Veeriah, A. Rowan, C. Naceur-Lombardelli, T. Karasaki, M. Sivakumar, S. De, D. R. Caswell, A. Nagano, J. R. M. Black, C. Martínez-Ruiz, M. H. Ryu, R. D. Huff, S. Li, M.-J. Favé, A. Magness, A. Suárez-Bonnet, S. L. Priestnall, M. Lüchtenborg, K. Lavelle, J. Pethick, S. Hardy, F. E. McRonald, M.-H. Lin, C. I. Troccoli, M. Ghosh, Y. E. Miller, D. T. Merrick, R. L. Keith, M. Al Bakir, C. Bailey, M. S. Hill, L. H. Saal, Y. Chen, A. M. George, C. Abbosh, N. Kanu, S.-H. Lee, N. McGranahan, C. D. Berg, P. Sasieni, R. Houlston, C. Turnbull, S. Lam, P. Awadalla, E. Grönroos, J. Downward, T. Jacks, C. Carlsten, I. Malanchi, A. Hackshaw, K. Litchfield, TRACERx Consortium, J. F. Lester, A. Bajaj, A. Nakas, A. Sodha-Ramdeen, K. Ang, M. Tufail, M. F. Chowdhry, M. Scotland, R. Boyles, S. Rathinam, C. Wilson, D. Marrone, S. Dulloo, D. A. Fennell, G. Matharu, J. A. Shaw, J. Ri-

ley, L. Primrose, E. Boleti, H. Cheyne, M. Khalil, S. Richardson, T. Cruickshank, G. Price, K. M. Kerr, S. Benafif, K. Gilbert, B. Naidu, A. J. Patel, A. Osman, C. Lacson, G. Langman, H. Shackleford, M. Djearaman, S. Kadiri, G. Middleton, A. Leek, J. D. Hodgkinson, N. Totten, A. Montero, E. Smith, E. Fontaine, F. Granato, H. Doran, J. Novasio, K. Rammohan, L. Joseph, P. Bishop, R. Shah, S. Moss, V. Joshi, P. Crosbie, F. Gomes, K. Brown, M. Carter, A. Chaturvedi, L. Priest, P. Oliveira, C. R. Lindsay, F. H. Blackhall, M. G. Krebs, Y. Summers, A. Clipson, J. Tugwood, A. Kerr, D. G. Rothwell, E. Kilgour, C. Dive, H. J. W. L. Aerts, R. F. Schwarz, T. L. Kaufmann, G. A. Wilson, R. Rosenthal, P. Van Loo, N. J. Birkbak, Z. Szallasi, J. Kisistok, M. Sokac, R. Salgado, M. Diossy, J. Demeulemeester, A. Bunkum, A. Stewart, A. M. Frankell, A. Karamani, A. Toncheva, A. Huebner, B. Chain, B. B. Campbell, C. Castignani, C. Puttick, C. Richard, C. T. Hiley, D. R. Pearce, D. Karagianni, D. Biswas, D. Levi, E. Hoxha, E. L. Cadieux, E. Colliver, E. Nye, F. Gálvez-Cancino, F. Athanasopoulou, F. Gimeno-Valiente, G. Kassiotis, G. Stavrou, G. Mastrokalos, H. Zhai, H. L. Lowe, I. G. Matos, J. Goldman, J. L. Reading, J. Herrero, J. K. Rane, J. Nicod, J. M. Lam, J. A. Hartley, K. S. Peggs, K. S. S. Enfield, K. Selvaraju, K. Thol, K. W. Ng, K. Dijkstra, K. Grigoriadis, K. Thakkar, L. Ensell, M. Shah, M. V. Duran, M. Litovchenko, M. W. Sunderland, M. Dietzen, M. Leung, M. Escudero, M. Angelova, M. Tanić, O. Chervova, O. Lucas, O. Al-Sawaf, P. Prymas, P. Hobson, P. Pawlik, R. K. Stone, R. Bentham, R. E. Hynds, R. Vendramin, S. Saghafinia, S. López, S. Gamble, S. K. A. Ung, S. A. Quezada, S. Vanloo, S. Zaccaria, S. Hessey, S. Ward, S. Boeing, S. Beck, S. K. Bola, T. Denner, T. Marafioti, T. P. Mourikis, T. B. K. Watkins, V. Spanswick, V. Barbè, W.-T. Lu, W. K. Liu, Y. Wu, Y. Naito, Z. Ramsden, C. Veiga, G. Royle, C.-A. Collins-Fekete, F. Fraioli, P. Ashford, T. Clark, M. D. Forster, S. M. Lee, E. Borg, M. Falzon, D. Papadatos-Pastos,

J. Wilson, T. Ahmad, A. J. Procter, A. Ahmed, M. N. Taylor, A. Nair, D. Lawrence, D. Patrini, N. Navani, R. M. Thakrar, S. M. Janes, E. M. Hoogenboom, F. Monk, J. W. Holding, J. Choudhary, K. Bhakhri, M. Scarci, M. Hayward, N. Panagiotopoulos, P. Gorman, R. Khiroya, R. C. M. Stephens, Y. N. S. Wong, S. Bandula, A. Sharp, S. Smith, N. Gower, H. K. Dhanda, K. Chan, C. Pilotti, R. Leslie, A. Grapa, H. Zhang, K. AbdulJabbar, X. Pan, Y. Yuan, D. Chuter, M. MacKenzie, S. Chee, A. Alzetani, J. Cave, L. Scarlett, J. Richards, P. Ingram, S. Austin, E. Lim, P. De Sousa, S. Jordan, A. Rice, H. Raubenheimer, H. Bhayani, L. Ambrose, A. Devaraj, H. Chavan, S. Begum, S. I. Buderi, D. Kaniu, M. Malima, S. Booth, A. G. Nicholson, N. Fernandes, P. Shah, C. Proli, M. Hewish, S. Danson, M. J. Shackcloth, L. Robinson, P. Russell, K. G. Blyth, C. Dick, J. Le Quesne, A. Kirk, M. Asif, R. Bilancia, N. Kostoulas, M. Thomas, J. DeGregori, M. Jamal-Hanjani, and C. Swanton, “Lung adenocarcinoma promotion by air pollutants,” *Nature*, vol. 616, no. 7955, pp. 159–167, 2023.

[3] I. C. Dedoussi, S. D. Eastham, E. Monier, and S. R. H. Barrett, “Premature mortality related to United States cross-state air pollution,” *Nature*, vol. 578, no. 7794, pp. 261–265, 2020.

[4] D. Liu, R. Lin, B. Feng, L. Han, Y. Zhang, M. Ni, and S. Wu, “Localised electrochemical impedance spectroscopy investigation of polymer electrolyte membrane fuel cells using Print circuit board based interference-free system,” *Applied Energy*, vol. 254, p. 113712, 2019.

[5] M. Zhou, J. C. Feistner, N. Li, S. S. Araya, G. Cinti, and V. Liso, “Experimental and numerical investigations of high-temperature PEM fuel cells under different anode dilution levels and varying temperatures,” *International Journal of Hydrogen Energy*, vol. 55, pp. 1383–1392, 2024.

[6] A. Pietri, F. Colas, R. Mogollon, J. Tam, and D. Gutierrez, “Marine heatwaves in the Humboldt current system: From 5-day localized warming to year-long El Niños,” *Scientific Reports*, vol. 11, no. 1, p. 21172, 2021.

[7] E. A. Schuur, B. W. Abbott, R. Commane, J. Ernakovich, E. Euskirchen, G. Hugelius, G. Grosse, M. Jones, C. Koven, V. Leshyk, D. Lawrence, M. M. Loranty, M. Mauritz, D. Olefeldt, S. Natali, H. Rodenhizer, V. Salmon, C. Schädel, J. Strauss, C. Treat, and M. Turetsky, “Permafrost and Climate Change: Carbon Cycle Feedbacks From the Warming Arctic,” *Annual Review of Environment and Resources*, vol. 47, no. 1, pp. 343–371, 2022.

[8] T. Geng, F. Jia, W. Cai, L. Wu, B. Gan, Z. Jing, S. Li, and M. J. McPhaden, “Increased occurrences of consecutive La Niña events under global warming,” *Nature*, vol. 619, no. 7971, pp. 774–781, 2023.

[9] X. Yuan, Y. Wang, P. Ji, P. Wu, J. Sheffield, and J. A. Otkin, “A global transition to flash droughts under climate change,” *Science*, vol. 380, no. 6641, pp. 187–191, 2023.

[10] L. Gudmundsson, J. Boulange, H. X. Do, S. N. Gosling, M. G. Grillakis, A. G. Koutroulis, M. Leonard, J. Liu, H. Müller Schmied, L. Papadimitriou, Y. Pokhrel, S. I. Seneviratne, Y. Satoh, W. Thiery, S. Westra, X. Zhang, and F. Zhao, “Globally observed trends in mean and extreme river flow attributed to climate change,” *Science*, vol. 371, no. 6534, pp. 1159–1162, 2021.

[11] IPCC, “Climate Change 2023: Synthesis Report. Contribution of Working Groups I, II and III to the Sixth Assessment Report of the Intergovernmental Panel on Climate Change [Core Writing Team, H. Lee and J. Romero (eds.)],” tech. rep., IPCC, Geneva, Switzerland, 2023.

[12] M. Lynas, B. Z. Houlton, and S. Perry, “Greater than 99% consensus on human caused climate change in the peer-reviewed scientific literature,” *Environmental Research Letters*, vol. 16, no. 11, p. 114005, 2021.

[13] S. Manabe, “Role of greenhouse gas in climate change,” *Tellus A: Dynamic Meteorology and Oceanography*, vol. 71, no. 1, p. 1620078, 2019.

[14] D. Kweku, O. Bismark, A. Maxwell, K. Desmond, K. Danso, E. Oti-Mensah, A. Quachie, and B. Adormaa, “Greenhouse Effect: Greenhouse Gases and Their Impact on Global Warming,” *Journal of Scientific Research and Reports*, vol. 17, no. 6, pp. 1–9, 2018.

[15] J. Tollefson, “Top climate scientists are sceptical that nations will rein in global warming,” *Nature*, vol. 599, no. 7883, pp. 22–24, 2021.

[16] S. Hsiang, R. Kopp, A. Jina, J. Rising, M. Delgado, S. Mohan, D. J. Rasmussen, R. Muir-Wood, P. Wilson, M. Oppenheimer, K. Larsen, and T. Houser, “Estimating economic damage from climate change in the United States,” *Science*, vol. 356, no. 6345, pp. 1362–1369, 2017.

[17] D. Steel, C. T. DesRoches, and K. Mintz-Woo, “Climate change and the threat to civilization,” *Proceedings of the National Academy of Sciences*, vol. 119, no. 42, p. e2210525119, 2022.

[18] D. I. Armstrong McKay, A. Staal, J. F. Abrams, R. Winkelmann, B. Sakschewski, S. Loriani, I. Fetzer, S. E. Cornell, J. Rockström, and T. M. Lenton, “Exceeding 1.5°C global warming could trigger multiple climate tipping points,” *Science*, vol. 377, no. 6611, p. eabn7950, 2022.

[19] NASA, “Global Temperature.” https://climate.nasa.gov/vital-signs/global-temperature/, 2023.

[20] H. Ritchie, P. Rosado, and M. Roser, “CO_2 and Greenhouse Gas Emissions,” *Our World in Data*, 2023.

[21] REN21, “Renewables 2023 Global Status Report,” tech. rep., REN21, Bonn, Germany, 2023.

[22] United Nations Framework Convention on Climate Change (UNFCCC), “The Paris Agreement,” 2016.

[23] W. J. Ripple, C. Wolf, T. M. Newsome, P. Barnard, and W. R. Moomaw, “World Scientists’ Warning of a Climate Emergency,” *BioScience*, p. biz088, 2019.

[24] European Commission, “The European Green Deal,” tech. rep., European Commission, 2019.

[25] IEA, “Electric car sales, 2016-2023,” tech. rep., IEA, Paris, 2023.

[26] M. Victoria, E. Zeyen, and T. Brown, “Speed of technological transformations required in Europe to achieve different climate goals,” *Joule*, vol. 6, no. 5, pp. 1066–1086, 2022.

[27] P. Sorknæs, R. M. Johannsen, A. D. Korberg, T. B. Nielsen, U. R. Petersen, and B. V. Mathiesen, “Electrification of the industrial sector in 100% renewable energy scenarios,” *Energy*, vol. 254, p. 124339, 2022.

[28] M. Wei, C. A. McMillan, and S. de la Rue du Can, “Electrification of Industry: Potential, Challenges and Outlook,” *Current Sustainable/Renewable Energy Reports*, vol. 6, no. 4, pp. 140–148, 2019.

[29] IEA, “World Energy Outlook 2023,” tech. rep., IEA, Paris, 2023.

[30] M. Muratori, M. Alexander, D. Arent, M. Bazilian, P. Cazzola, E. M. Dede, J. Farrell, C. Gearhart, D. Greene, A. Jenn, M. Keyser, T. Lipman, S. Narumanchi, A. Pesaran, R. Sioshansi, E. Suomalainen, G. Tal, K. Walkowicz, and J. Ward, “The rise of electric vehicles—2020 status and future expectations,” *Progress in Energy*, vol. 3, no. 2, p. 022002, 2021.

[31] Y. Liu, Y. Bai, W. Jaegermann, R. Hausbrand, and B.-X. Xu, “Impedance Modeling of Solid-State Electrolytes: Influence of the Contacted Space Charge Layer,” *ACS Applied Materials & Interfaces*, vol. 13, no. 4, pp. 5895–5906, 2021.

[32] A. König, L. Nicoletti, D. Schröder, S. Wolff, A. Waclaw, and M. Lienkamp, “An Overview of Parameter and Cost for Battery Electric Vehicles,” *World Electric Vehicle Journal*, vol. 12, no. 1, p. 21, 2021.

[33] A. Wanitschke and S. Hoffmann, “Are battery electric vehicles the future? An uncertainty comparison with hydrogen and combustion engines,” *Environmental Innovation and Societal Transitions*, vol. 35, pp. 509–523, 2020.

[34] T. Selmi, A. Khadhraoui, and A. Cherif, “Fuel cell–based electric vehicles technologies and challenges,” *Environmental Science and Pollution Research*, vol. 29, no. 52, pp. 78121–78131, 2022.

[35] Y. Luo, Y. Wu, B. Li, T. Mo, Y. Li, S.-P. Feng, J. Qu, and P. K. Chu, “Development and application of fuel cells in the automobile industry,” *Journal of Energy Storage*, vol. 42, p. 103124, 2021.

[36] Y. Wang, H. Yuan, A. Martinez, P. Hong, H. Xu, and F. R. Bockmiller, “Polymer electrolyte membrane fuel cell and hydrogen station networks for automobiles: Status, technology, and perspectives,” *Advances in Applied Energy*, vol. 2, p. 100011, 2021.

[37] B. G. Pollet, S. S. Kocha, and I. Staffell, “Current status of automotive fuel cells for sustainable transport,” *Current Opinion in Electrochemistry*, vol. 16, pp. 90–95, 2019.

[38] A. G. Olabi, T. Wilberforce, and M. A. Abdelkareem, “Fuel cell application in the automotive industry and future perspective,” *Energy*, vol. 214, p. 118955, 2021.

[39] M. A. Aminudin, S. K. Kamarudin, B. H. Lim, E. H. Majilan, M. S. Masdar, and N. Shaari, “An overview: Current progress on hydrogen fuel cell vehicles,” *International Journal of Hydrogen Energy*, vol. 48, no. 11, pp. 4371–4388, 2023.

[40] Y. Wang, E. Gordon, and H. Ren, “Mapping the Potential of Zero Charge and Electrocatalytic Activity of Metal–Electrolyte Interface via a Grain-by-Grain Approach,” *Analytical Chemistry*, vol. 92, no. 3, pp. 2859–2865, 2020.

[41] Y. Nonobe, “Development of the fuel cell vehicle mirai,” *IEEJ Transactions on Electrical and Electronic Engineering*, vol. 12, no. 1, pp. 5–9, 2017.

[42] B. K. Hong and S. H. Kim, “Recent Advances in Fuel Cell Electric Vehicle Technologies of Hyundai,” *ECS Transactions*, vol. 86, no. 13, pp. 3–11, 2018.

[43] S. Tanaka, K. Nagumo, M. Yamamoto, H. Chiba, K. Yoshida, and R. Okano, “Fuel cell system for Honda CLARITY fuel cell,” *eTransportation*, vol. 3, p. 100046, 2020.

[44] B. K. Hong, S. H. Kim, and C. M. Kim, “Powering the Future through Hydrogen and Polymer Electrolyte Membrane Fuel Cells: Current commercialisation and key challenges with focus

on work at Hyundai," *Johnson Matthey Technology Review*, vol. 64, no. 3, pp. 236–251, 2020.

[45] BMW Group, "Launch of the BMW iX5 Hydrogen Pilot Fleet." https://www.bmwgroup.com/en/news/general/2023/BMWiX5Hydrogen.html, 2023.

[46] A. Kampker, H. Heimes, M. Kehrer, S. Hagedorn, P. Reims, and O. Kaul, "Fuel cell system production cost modeling and analysis," *Energy Reports*, vol. 9, pp. 248–255, 2023.

[47] U.S. Department of Energy,, "Department of Energy Hydrogen Program Plan," tech. rep., U.S. Department of Energy, 2020.

[48] R. R. Gaddam, L. Katzenmeier, X. Lamprecht, and A. S. Bandarenka, "Review on physical impedance models in modern battery research," *Physical Chemistry Chemical Physics*, vol. 23, no. 23, pp. 12926–12944, 2021.

[49] S. M. Rezaei Niya and M. Hoorfar, "Study of proton exchange membrane fuel cells using electrochemical impedance spectroscopy technique – A review," *Journal of Power Sources*, vol. 240, pp. 281–293, 2013.

[50] C. Wang and J. S. Spendelow, "Recent developments in Pt–Co catalysts for proton-exchange membrane fuel cells," *Current Opinion in Electrochemistry*, vol. 28, p. 100715, 2021.

[51] N. A. Ivanova, D. D. Spasov, A. A. Zasypkina, O. K. Alekseeva, E. V. Kukueva, E. A. Vorobyeva, E. S. Kudinova, R. G. Chumakov, P. Millet, and S. A. Grigoriev, "Comparison of the performance and durability of PEM fuel cells with different Pt-activated microporous layers," *International Journal of Hydrogen Energy*, vol. 46, no. 34, pp. 18093–18106, 2021.

[52] R. L. Borup, A. Kusoglu, K. C. Neyerlin, R. Mukundan, R. K. Ahluwalia, D. A. Cullen, K. L. More, A. Z. Weber, and D. J. Myers, “Recent developments in catalyst-related PEM fuel cell durability,” *Current Opinion in Electrochemistry*, vol. 21, pp. 192–200, 2020.

[53] M. Rubio, A. Urquia, and S. Dormido, “Diagnosis of performance degradation phenomena in PEM fuel cells,” *International Journal of Hydrogen Energy*, vol. 35, no. 7, pp. 2586–2590, 2010.

[54] E. Pahon, D. Hissel, and N. Yousfi-Steiner, “A review of accelerated stress tests dedicated to proton exchange membrane fuel cells – Part I: Fuel cell component level,” *Journal of Power Sources*, vol. 546, p. 231895, 2022.

[55] V. Shokhen, L. Strandberg, M. Skoglundh, and B. Wickman, “Impact of Accelerated Stress Tests on the Cathodic Catalytic Layer in a Proton Exchange Membrane (PEM) Fuel Cell Studied by Identical Location Scanning Electron Microscopy,” *ACS Applied Energy Materials*, vol. 5, no. 9, pp. 11200–11212, 2022.

[56] P. Ren, P. Pei, Y. Li, Z. Wu, D. Chen, and S. Huang, “Degradation mechanisms of proton exchange membrane fuel cell under typical automotive operating conditions,” *Progress in Energy and Combustion Science*, vol. 80, p. 100859, 2020.

[57] E. Colombo, A. Baricci, D. Mora, L. Guetaz, and A. Casalegno, “An innovative accelerated stress test representative of automotive PEMFC degradation mechanisms validated on 1000 hours real-world operation,” *Journal of Power Sources*, vol. 580, p. 233376, 2023.

[58] P. Ahmadi, S. H. Torabi, H. Afsaneh, Y. Sadegheih, H. Ganjehsarabi, and M. Ashjaee, “The effects of driving patterns and PEM fuel cell degradation on the lifecycle assessment

of hydrogen fuel cell vehicles," *International Journal of Hydrogen Energy*, vol. 45, no. 5, pp. 3595–3608, 2020.

[59] R. Marić, C. Gebauer, M. Nesselberger, F. Hasché, and P. Strasser, "Towards a Harmonized Accelerated Stress Test Protocol for Fuel Starvation Induced Cell Reversal Events in PEM Fuel Cells: The Effect of Pulse Duration," *Journal of The Electrochemical Society*, vol. 167, no. 12, p. 124520, 2020.

[60] P. Thiele, Y. Yang, S. Dirkes, M. Wick, and S. Pischinger, "Realistic accelerated stress tests for PEM fuel cells: Test procedure development based on standardized automotive driving cycles," *International Journal of Hydrogen Energy*, vol. 52, pp. 1065–1080, 2024.

[61] T. Madden, M. Perry, L. Protsailo, M. Gummalla, S. Burlatsky, N. Cipollini, S. Motupally, and T. Jarvi, "Proton exchange membrane fuel cell degradation: Mechanisms and recent progress," in *Handbook of Fuel Cells* (W. Vielstich, A. Lamm, H. A. Gasteiger, and H. Yokokawa, eds.), Wiley, 1 ed., 2010.

[62] J. Zhao and X. Li, "A review of polymer electrolyte membrane fuel cell durability for vehicular applications: Degradation modes and experimental techniques," *Energy Conversion and Management*, vol. 199, p. 112022, 2019.

[63] M. Geske, M. Heuer, G. Heideck, and Z. A. Styczynski, "Current Density Distribution Mapping in PEM Fuel Cells as An Instrument for Operational Measurements," *Energies*, vol. 3, no. 4, pp. 770–783, 2010.

[64] D. H. Jeon, K. N. Kim, S. M. Baek, and J. H. Nam, "The effect of relative humidity of the cathode on the performance and the uniformity of PEM fuel cells," *International Journal of Hydrogen Energy*, vol. 36, no. 19, pp. 12499–12511, 2011.

[65] T. Lochner, L. Hallitzky, M. Perchthaler, M. Obermaier, J. Sabawa, S. Enz, and A. S. Bandarenka, “Local degradation effects in automotive size membrane electrode assemblies under realistic operating conditions,” *Applied Energy*, vol. 260, p. 114291, 2020.

[66] Y. S. Kim, D. K. Kim, K. Y. Ahn, and M. S. Kim, “Parametric study on the local current distribution of polymer electrolyte membrane fuel cell with counter flow channel under pressurized condition,” *Journal of Mechanical Science and Technology*, vol. 34, no. 5, pp. 2189–2198, 2020.

[67] I. Alaefour, G. Karimi, K. Jiao, and X. Li, “Measurement of current distribution in a proton exchange membrane fuel cell with various flow arrangements – A parametric study,” *Applied Energy*, vol. 93, pp. 80–89, 2012.

[68] Y. Hou, J. Schall, S. Dietze, T. Kurz, and D. Gerteisen, “An experimental and numerical study of spatial and temporal catalyst degradation during start-up and shut-down of PEM fuel cells,” *Journal of Power Sources*, vol. 591, p. 233780, 2024.

[69] L. Dubau, L. Castanheira, F. Maillard, M. Chatenet, O. Lottin, G. Maranzana, J. Dillet, A. Lamibrac, J.-C. Perrin, E. Moukheiber, A. ElKaddouri, G. De Moor, C. Bas, L. Flandin, and N. Caqué, “A review of PEM fuel cell durability: Materials degradation, local heterogeneities of aging and possible mitigation strategies,” *WIREs Energy and Environment*, vol. 3, no. 6, pp. 540–560, 2014.

[70] T. Lochner, M. Perchthaler, J. T. Binder, J. P. Sabawa, T. A. Dao, and A. S. Bandarenka, “Real-Time Impedance Analysis for the On-Road Monitoring of Automotive Fuel Cells,” *ChemElectroChem*, vol. 7, no. 13, pp. 2784–2791, 2020.

[71] T. Chu, M. Xie, Y. Yu, B. Wang, D. Yang, B. Li, P. Ming, and C. Zhang, “Experimental study of the influence of dynamic load cycle and operating parameters on the durability of PEMFC,” *Energy*, vol. 239, p. 122356, 2022.

[72] M. Prokop, M. Drakselova, and K. Bouzek, “Review of the experimental study and prediction of Pt-based catalyst degradation during PEM fuel cell operation,” *Current Opinion in Electrochemistry*, vol. 20, pp. 20–27, 2020.

[73] J. P. Sabawa and A. S. Bandarenka, “Degradation mechanisms in polymer electrolyte membrane fuel cells caused by freeze-cycles: Investigation using electrochemical impedance spectroscopy,” *Electrochimica Acta*, vol. 311, pp. 21–29, 2019.

[74] Y. Wang, X. Shan, and N. Tao, “Emerging tools for studying single entity electrochemistry,” *Faraday Discussions*, vol. 193, pp. 9–39, 2016.

[75] K. McKelvey, M. A. Edwards, and P. R. Unwin, “Intermittent Contact-Scanning Electrochemical Microscopy (IC-SECM): A New Approach for Tip Positioning and Simultaneous Imaging of Interfacial Topography and Activity,” *Analytical Chemistry*, vol. 82, no. 15, pp. 6334–6337, 2010.

[76] T. Kai, C. G. Zoski, and A. J. Bard, “Scanning electrochemical microscopy at the nanometer level,” *Chemical Communications*, vol. 54, no. 16, pp. 1934–1947, 2018.

[77] D. J. L. Brett, S. Atkins, N. P. Brandon, V. Vesovic, N. Vasileiadis, and A. Kucernak, “Localized Impedance Measurements along a Single Channel of a Solid Polymer Fuel Cell,” *Electrochemical and Solid-State Letters*, vol. 6, no. 4, p. A63, 2003.

[78] D. Gerteisen, W. Mérida, T. Kurz, P. Lupotto, M. Schwager, and C. Hebling, “Spatially Resolved Voltage, Current and Electrochemical Impedance Spectroscopy Measurements,” *Fuel Cells*, vol. 11, no. 2, pp. 339–349, 2011.

[79] D. Gerteisen, N. Zamel, C. Sadeler, F. Geiger, V. Ludwig, and C. Hebling, “Effect of operating conditions on current density distribution and high frequency resistance in a segmented PEM fuel cell,” *International Journal of Hydrogen Energy*, vol. 37, no. 9, pp. 7736–7744, 2012.

[80] P. Schneider, C. Sadeler, A.-C. Scherzer, N. Zamel, and D. Gerteisen, “Fast and Reliable State-of-Health Model of a PEM Cathode Catalyst Layer,” *Journal of The Electrochemical Society*, vol. 166, no. 4, pp. F322–F333, 2019.

[81] A. Hakenjos and C. Hebling, “Spatially resolved measurement of PEM fuel cells,” *Journal of Power Sources*, vol. 145, no. 2, pp. 307–311, 2005.

[82] E. Engebretsen, G. Hinds, Q. Meyer, T. Mason, E. Brightman, L. Castanheira, P. R. Shearing, and D. J. Brett, “Localised electrochemical impedance measurements of a polymer electrolyte fuel cell using a reference electrode array to give cathode-specific measurements and examine membrane hydration dynamics,” *Journal of Power Sources*, vol. 382, pp. 38–44, 2018.

[83] T. Schmitt, R. Bligny, G. Maranzana, and U. Sauter, “Rapid and Local EIS on a Segmented Fuel Cell: A New Method for Spatial and Temporal Resolution,” *Journal of The Electrochemical Society*, vol. 169, no. 9, p. 094504, 2022.

[84] T. Goosmann, P. Oppek, and A. Weber, “Method for Systematic Validation of a Physically Based PEMFC Model By Spatially Resolved Impedance Measurements,” *ECS Meeting Abstracts*, vol. MA2023-02, no. 38, pp. 1837–1837, 2023.

[85] C. Liu, R. Chen, F. Sera, A. M. Vicedo-Cabrera, Y. Guo, S. Tong, M. S. Coelho, P. H. Saldiva, E. Lavigne, P. Matus, N. Valdes Ortega, S. Osorio Garcia, M. Pascal, M. Stafoggia, M. Scortichini, M. Hashizume, Y. Honda, M. Hurtado-Díaz, J. Cruz, B. Nunes, J. P. Teixeira, H. Kim, A. Tobias, C. Íñiguez, B. Forsberg, C. Åström, M. S. Ragettli, Y.-L. Guo, B.-Y. Chen, M. L. Bell, C. Y. Wright, N. Scovronick, R. M. Garland, A. Milojevic, J. Kyselý, A. Urban, H. Orru, E. Indermitte, J. J. Jaakkola, N. R. Ryti, K. Katsouyanni, A. Analitis, A. Zanobetti, J. Schwartz, J. Chen, T. Wu, A. Cohen, A. Gasparrini, and H. Kan, “Ambient Particulate Air Pollution and Daily Mortality in 652 Cities,” *New England Journal of Medicine*, vol. 381, no. 8, pp. 705–715, 2019.

[86] D. Liu, R. Lin, B. Feng, and Z. Yang, “Investigation of the effect of cathode stoichiometry of proton exchange membrane fuel cell using localized electrochemical impedance spectroscopy based on print circuit board,” *International Journal of Hydrogen Energy*, vol. 44, no. 14, pp. 7564–7573, 2019.

[87] A. Kampker, P. Ayvaz, C. Schön, J. Karstedt, R. Förstmann, and F. Welker, “Challenges towards large-scale fuel cell production: Results of an expert assessment study,” *International Journal of Hydrogen Energy*, vol. 45, no. 53, pp. 29288–29296, 2020.

[88] J. Marcinkoski, B. D. James, J. A. Kalinoski, W. Podolski, T. Benjamin, and J. Kopasz, “Manufacturing process assumptions used in fuel cell system cost analyses,” *Journal of Power Sources*, vol. 196, no. 12, pp. 5282–5292, 2011.

[89] M. Ulsh, B. Sopori, N. V. Aieta, and G. Bender, “Challenges to High-Volume Production of Fuel Cell Materials: Quality Control,” *ECS Transactions*, vol. 50, no. 2, pp. 919–926, 2013.

[90] J. Wang, H. Wang, and Y. Fan, “Techno-Economic Challenges of Fuel Cell Commercialization,” *Engineering*, vol. 4, no. 3, pp. 352–360, 2018.

[91] X.-Z. Yuan, C. Nayoze-Coynel, N. Shaigan, D. Fisher, N. Zhao, N. Zamel, P. Gazdzicki, M. Ulsh, K. A. Friedrich, F. Girard, and U. Groos, “A review of functions, attributes, properties and measurements for the quality control of proton exchange membrane fuel cell components,” *Journal of Power Sources*, vol. 491, p. 229540, 2021.

[92] M. Ulsh, A. DeBari, J. M. Berliner, I. V. Zenyuk, P. Rupnowski, L. Matvichuk, A. Z. Weber, and G. Bender, “The development of a through-plane reactive excitation technique for detection of pinholes in membrane-containing MEA sub-assemblies,” *International Journal of Hydrogen Energy*, vol. 44, no. 16, pp. 8533–8547, 2019.

[93] Y. Wang, H. Yuan, A. Martinez, P. Hong, H. Xu, and F. Bockmiller, “Polymer Electrolyte Membrane Fuel Cell and Hydrogen Station Network for Automobiles: Status, Technology, and Perspectives,” *Advances in Applied Energy*, vol. 2, p. 100011, 2021.

[94] M. Ulsh, J. M. Porter, D. C. Bittinat, and G. Bender, “Defect Detection in Fuel Cell Gas Diffusion Electrodes Using Infrared Thermography,” *Fuel Cells*, vol. 16, no. 2, pp. 170–178, 2016.

[95] P. K. Das, A. Z. Weber, G. Bender, A. Manak, D. Bittinat, A. M. Herring, and M. Ulsh, “Rapid detection of defects in fuel-cell electrodes using infrared reactive-flow-through technique,” *Journal of Power Sources*, vol. 261, pp. 401–411, 2014.

[96] I. V. Zenyuk, N. Englund, G. Bender, A. Z. Weber, and M. Ulsh, “Reactive impinging-flow technique for polymer-electrolyte-fuel-cell electrode-defect detection,” *Journal of Power Sources*, vol. 332, pp. 372–382, 2016.

[97] F. Sasse, G. Fischer, N. Eschner, and G. Lanza, “Improving End-Of-Line Quality Control of Fuel Cell Manufacturing Through Machine Lerning Enabled Data Analysis,” in *FC^3 Fuel Cell Conference.*, (Chemnitz), Universitätsverlag Chemnitz, Chemnitz, 2022.

[98] A. Yan, P. Rupnowski, N. Guba, and A. Nag, “Towards deep computer vision for in-line defect detection in polymer electrolyte membrane fuel cell materials,” *International Journal of Hydrogen Energy*, vol. 48, no. 50, pp. 18978–18995, 2023.

[99] M. Killcross, “Factory acceptance testing,” in *Chemical and Process Plant Commissioning Handbook*, pp. 203–212, Elsevier, 2021.

[100] M. Wolter, G. Fauser, C. Bretthauer, and M. A. Roscher, “End-of-line testing and formation process in Li-ion battery assembly lines,” in *International Multi-Conference on Systems, Signals & Devices*, (Chemnitz, Germany), pp. 1–3, IEEE, 2012.

[101] S. M. Lambert, M. Armstrong, P. S. Attidekou, P. A. Christensen, J. D. Widmer, C. Wang, and K. Scott, “Rapid Nondestructive-Testing Technique for In-Line Quality Control of Li-Ion Batteries,” *IEEE Transactions on Industrial Electronics*, vol. 64, no. 5, pp. 4017–4026, 2017.

[102] Xiaoyu Li, Tiansi Wang, Lei Pei, Chunbo Zhu, and Bingliang Xu, “A comparative study of sorting methods for Lithium-ion batteries,” in *2014 IEEE Conference and Expo Transportation Electrification Asia-Pacific (ITEC Asia-Pacific)*, (Beijing, China), pp. 1–6, IEEE, 2014.

[103] X. C. A. Chacón, S. Laureti, M. Ricci, and G. Cappuccino, “A Review of Non-Destructive Techniques for Lithium-Ion Battery Performance Analysis,” *World Electric Vehicle Journal*, vol. 14, no. 11, p. 305, 2023.

[104] M. Ank, P. Bilfinger, N. Grube-Doiz, and M. Lienkamp, “Economic potential assessment of multi-cell testing in lithium-ion cell production and electric vehicle application,” *Procedia CIRP*, vol. 120, pp. 243–248, 2023.

[105] M. Ank, J. Göhmann, and M. Lienkamp, “Multi-Cell Testing Topologies for Defect Detection Using Electrochemical Impedance Spectroscopy: A Combinatorial Experiment-Based Analysis,” *Batteries*, vol. 9, no. 8, p. 415, 2023.

[106] M. Ank, S. Stock, N. Wassiliadis, T. Burger, R. Daub, and M. Lienkamp, “Influence analysis of production defects of lithium-ion cells using single-cell and multi-cell characterization,” *Journal of Energy Storage*, vol. 62, p. 106938, 2023.

[107] M. Molnarne and V. Schroeder, “Hazardous properties of hydrogen and hydrogen containing fuel gases,” *Process Safety and Environmental Protection*, vol. 130, pp. 1–5, 2019.

[108] C. Henager, “Hydrogen Permeation Barrier Coatings,” in *Materials for the Hydrogen Economy* (R. Jones and G. Thomas, eds.), pp. 181–190, CRC Press, 2007.

[109] E. Abohamzeh, F. Salehi, M. Sheikholeslami, R. Abbassi, and F. Khan, “Review of hydrogen safety during storage, transmission, and applications processes,” *Journal of Loss Prevention in the Process Industries*, vol. 72, p. 104569, 2021.

[110] A. Hamnett, “Introduction to fuel-cell types,” in *Handbook of Fuel Cells* (W. Vielstich, A. Lamm, H. A. Gasteiger, and H. Yokokawa, eds.), Wiley, 1 ed., 2010.

[111] F. Barbir, *PEM Fuel Cells: Theory and Practice*. London: Academic Press, 2nd ed ed., 2013.

[112] S. Srinivasan, *Fuel Cells: From Fundamentals to Applications*. New York: Springer, 2006.

[113] R. O'Hayre, S.-W. Cha, W. Colella, and F. B. Prinz, *Fuel Cell Fundamentals*. Hoboken, NJ, USA: John Wiley & Sons, Inc, 2016.

[114] A. Lavacchi, H. Miller, and F. Vizza, *Nanotechnology in Electrocatalysis for Energy*, vol. 170 of *Nanostructure Science and Technology*. New York, NY: Springer New York, 2013.

[115] X. Li, M. Ahmadi, L. Collins, and S. V. Kalinin, "Deconvolving distribution of relaxation times, resistances and inductance from electrochemical impedance spectroscopy via statistical model selection: Exploiting structural-sparsity regularization and data-driven parameter tuning," *Electrochimica Acta*, vol. 313, pp. 570–583, 2019.

[116] J. Zhang, Y. Tang, C. Song, J. Zhang, and H. Wang, "PEM fuel cell open circuit voltage (OCV) in the temperature range of 23°C to 120°C," *Journal of Power Sources*, vol. 163, no. 1, pp. 532–537, 2006.

[117] J. K. Nørskov, J. Rossmeisl, A. Logadottir, L. Lindqvist, J. R. Kitchin, T. Bligaard, and H. Jónsson, "Origin of the Overpotential for Oxygen Reduction at a Fuel-Cell Cathode," *The Journal of Physical Chemistry B*, vol. 108, no. 46, pp. 17886–17892, 2004.

[118] H. S. Taylor, "A theory of the catalytic surface," *Proceedings of the Royal Society of London. Series A, Containing Papers of a Mathematical and Physical Character*, vol. 108, no. 745, pp. 105–111, 1925.

[119] F. Calle-Vallejo, J. I. Martínez, J. M. García-Lastra, P. Sautet, and D. Loffreda, "Fast Prediction of Adsorption Properties for Platinum Nanocatalysts with Generalized Coordination Numbers," *Angewandte Chemie International Edition*, vol. 53, no. 32, pp. 8316–8319, 2014.

[120] F. Calle-Vallejo, J. Tymoczko, V. Colic, Q. H. Vu, M. D. Pohl, K. Morgenstern, D. Loffreda, P. Sautet, W. Schuhmann, and A. S. Bandarenka, "Finding optimal surface sites on heterogeneous catalysts by counting nearest neighbors," *Science*, vol. 350, no. 6257, pp. 185–189, 2015.

[121] B. Garlyyev, J. Fichtner, O. Piqué, O. Schneider, A. S. Bandarenka, and F. Calle-Vallejo, "Revealing the nature of active sites in electrocatalysis," *Chemical Science*, vol. 10, no. 35, pp. 8060–8075, 2019.

[122] F. J. Perez-Alonso, D. N. McCarthy, A. Nierhoff, P. Hernandez-Fernandez, C. Strebel, I. E. L. Stephens, J. H. Nielsen, and I. Chorkendorff, "The Effect of Size on the Oxygen Electroreduction Activity of Mass-Selected Platinum Nanoparticles," *Angewandte Chemie International Edition*, vol. 51, no. 19, pp. 4641–4643, 2012.

[123] A. S. Alabi, A. P. I. Popoola, O. M. Popoola, N. R. Mathe, and M. Abdulwahab, "Materials for electrocatalysts in proton exchange membrane fuel cell: A brief review," *Frontiers in Energy Research*, vol. 11, p. 1091105, 2023.

[124] S. Wang, J. Zhang, O. Gharbi, V. Vivier, M. Gao, and M. E. Orazem, "Electrochemical impedance spectroscopy," *Nature Reviews Methods Primers*, vol. 1, no. 1, p. 41, 2021.

[125] V. Čolić and A. S. Bandarenka, "Pt Alloy Electrocatalysts for the Oxygen Reduction Reaction: From Model Surfaces to Nanostructured Systems," *ACS Catalysis*, vol. 6, no. 8, pp. 5378–5385, 2016.

[126] C. Zhu, Q. Shi, B. Z. Xu, S. Fu, G. Wan, C. Yang, S. Yao, J. Song, H. Zhou, D. Du, S. P. Beckman, D. Su, and Y. Lin, “Hierarchically Porous M–N–C (M = Co and Fe) Single-Atom Electrocatalysts with Robust MN $_x$ Active Moieties Enable Enhanced ORR Performance,” *Advanced Energy Materials*, vol. 8, no. 29, p. 1801956, 2018.

[127] H. Xu, L. Zhang, and Department of Building Environment and Energy Engineering, Xi’an Jiaotong University, Xi’an 710049, China, “Influences of space charge layer effect on oxygen vacancy transport adjacent to three phase boundaries within solid oxide fuel cells,” *Acta Physica Sinica*, vol. 70, no. 12, p. 128801, 2021.

[128] S. Liu, M. Rasinski, Y. Lin, K. Wippermann, A. Everwand, and W. Lehnert, “Effects of constant load operations on platinum bands formation and cathode degradation in high-temperature polymer electrolyte fuel cells,” *Electrochimica Acta*, vol. 289, pp. 354–362, 2018.

[129] R. Nandan, G. Raj, and K. K. Nanda, “FeCoNiMnCr High-Entropy Alloy Nanoparticle-Grafted NCNTs with Promising Performance in the Ohmic Polarization Region of Fuel Cells,” *ACS Applied Materials & Interfaces*, vol. 14, no. 14, pp. 16108–16116, 2022.

[130] R. Martínez-Hincapié and V. Čolić, “Electrocatalysts for the Oxygen Reduction Reaction: From Bimetallic Platinum Alloys to Complex Solid Solutions,” *ChemEngineering*, vol. 6, no. 1, p. 19, 2022.

[131] L. Dai, Y. Xue, L. Qu, H.-J. Choi, and J.-B. Baek, “Metal-Free Catalysts for Oxygen Reduction Reaction,” *Chemical Reviews*, vol. 115, no. 11, pp. 4823–4892, 2015.

[132] C. Hu and L. Dai, “Doping of Carbon Materials for Metal-Free Electrocatalysis,” *Advanced Materials*, vol. 31, no. 7, p. 1804672, 2019.

[133] S. V. Sawant, A. W. Patwardhan, J. B. Joshi, and K. Dasgupta, “Boron doped carbon nanotubes: Synthesis, characterization and emerging applications – A review,” *Chemical Engineering Journal*, vol. 427, p. 131616, 2022.

[134] J. Masa, W. Xia, M. Muhler, and W. Schuhmann, “On the Role of Metals in Nitrogen-Doped Carbon Electrocatalysts for Oxygen Reduction,” *Angewandte Chemie International Edition*, vol. 54, no. 35, pp. 10102–10120, 2015.

[135] X. Huang and K. Reifsnider, “Durability of PEM Fuel Cell Membranes,” in *Modeling and Diagnostics of Polymer Electrolyte Fuel Cells* (C.-Y. Wang and U. Pasaogullari, eds.), pp. 1–43, New York, NY: Springer New York, 2009.

[136] A. de Frank Bruijn and G. J. M. Janssen, “PEM Fuel Cell Materials: Costs, Performance and Durability,” in *Fuel Cells* (K.-D. Kreuer, ed.), pp. 249–303, New York, NY: Springer New York, 2013.

[137] A. Kusoglu and A. Z. Weber, “New Insights into Perfluorinated Sulfonic-Acid Ionomers,” *Chemical Reviews*, vol. 117, no. 3, pp. 987–1104, 2017.

[138] A. Iiyama, K. Shinohara, S. Iguchi, and A. Daimaru, “Membranes and catalyst performance targets for automotive fuel cells,” in *Handbook of Fuel Cells* (W. Vielstich, A. Lamm, H. A. Gasteiger, and H. Yokokawa, eds.), Wiley, 1 ed., 2010.

[139] A. Kraytsberg and Y. Ein-Eli, “Review of Advanced Materials for Proton Exchange Membrane Fuel Cells,” *Energy & Fuels*, vol. 28, no. 12, pp. 7303–7330, 2014.

[140] R. Hiesgen, T. Morawietz, M. Handl, M. Corasaniti, and K. A. Friedrich, “Insight into the Structure and Nanoscale Conductivity of Fluorinated Ionomer Membranes,” *Journal of The Electrochemical Society*, vol. 161, no. 12, pp. F1214–F1223, 2014.

[141] Z. Luo, Z. Chang, Y. Zhang, Z. Liu, and J. Li, “Electro-osmotic drag coefficient and proton conductivity in Nafion® membrane for PEMFC,” *International Journal of Hydrogen Energy*, vol. 35, no. 7, pp. 3120–3124, 2010.

[142] K. Miyatake, “Membrane Electrolytes, from Perfluorosulfonic Acid (PFSA) to Hydrocarbon Ionomers,” in *Encyclopedia of Sustainability Science and Technology* (R. A. Meyers, ed.), pp. 1–32, New York, NY: Springer New York, 2015.

[143] Y. Garsany, R. W. Atkinson, M. B. Sassin, R. M. E. Hjelm, B. D. Gould, and K. E. Swider-Lyons, “Improving PEMFC Performance Using Short-Side-Chain Low-Equivalent-Weight PFSA Ionomer in the Cathode Catalyst Layer,” *Journal of The Electrochemical Society*, vol. 165, no. 5, pp. F381–F391, 2018.

[144] Y.-C. Park, K. Kakinuma, H. Uchida, M. Watanabe, and M. Uchida, “Effects of short-side-chain perfluorosulfonic acid ionomers as binders on the performance of low Pt loading fuel cell cathodes,” *Journal of Power Sources*, vol. 275, pp. 384–391, 2015.

[145] S. So, H. Kang, D. Choi, and K.-H. Oh, “Tunable aggregation of short-side-chain perfluorinated sulfonic acid ionomers for the catalyst layer in polymer electrolyte membrane fuel cells,” *International Journal of Hydrogen Energy*, vol. 45, no. 38, pp. 19891–19899, 2020.

[146] R. Liu, Q. Jia, B. Zhang, Z. Lai, and L. Chen, “Protective coatings for metal bipolar plates of fuel cells: A review,” *International Journal of Hydrogen Energy*, vol. 47, no. 54, pp. 22915–22937, 2022.

[147] S. Garner, S. Bhattacharya, J. Dong, J. Li, and E. Kjeang, “Effects of Reinforcement Type on the Structure and Properties of Perfluorosulphonic Acid Membranes for Polymer Electrolyte Membrane Fuel Cells,” *ECS Meeting Abstracts*, vol. MA2022-01, no. 35, pp. 1442–1442, 2022.

[148] L. Guo, A. Masuda, and K. Miyatake, “Reinforcement effect in tandemly sulfonated, partially fluorinated polyphenylene PEMs for fuel cells,” *RSC Advances*, vol. 13, no. 16, pp. 11225–11233, 2023.

[149] J. Gao, X. Dong, Q. Tian, and Y. He, “Carbon nanotubes reinforced proton exchange membranes in fuel cells: An overview,” *International Journal of Hydrogen Energy*, vol. 48, no. 8, pp. 3216–3231, 2023.

[150] Y. Pang, Y. Duan, Q. Li, B. Liu, X. Hu, Q. Liu, and C. Zhao, “Immobilized hindered amine radical scavenger for durability enhancement of perfluorosulfonic acid membrane in PEMFCs,” *Journal of Membrane Science*, vol. 686, p. 121999, 2023.

[151] T. Agarwal, S. Adhikari, Y. S. Kim, S. Komini Babu, D. Tian, C. Bae, N. N. T. Pham, S. G. Lee, A. K. Prasad, S. G. Advani, A. Sievert, W. P. Rasika Liyanage, T. E. Hopkins, A. Park, and R. Borup, “Fluoroalkyl phosphonic acid radical scavengers for proton exchange membrane fuel cells,” *Journal of Materials Chemistry A*, vol. 11, no. 18, pp. 9748–9754, 2023.

[152] G. Byun, J. Kim, N. Kim, Y. Cho, and C. Park, “Molecular engineering of hydrocarbon membrane to substitute perfluorinated sulfonic acid membrane for proton exchange membrane fuel cell operation,” *Materials Today Energy*, vol. 17, p. 100483, 2020.

[153] A. Katzenberg, A. Chowdhury, M. Fang, A. Z. Weber, Y. Okamoto, A. Kusoglu, and M. A. Modestino, “Highly Permeable Perfluorinated Sulfonic Acid Ionomers for Improved Electro-

chemical Devices: Insights into Structure–Property Relationships," *Journal of the American Chemical Society*, vol. 142, no. 8, pp. 3742–3752, 2020.

[154] S. A. Berlinger, B. D. McCloskey, and A. Z. Weber, "Inherent Acidity of Perfluorosulfonic Acid Ionomer Dispersions and Implications for Ink Aggregation," *The Journal of Physical Chemistry B*, vol. 122, no. 31, pp. 7790–7796, 2018.

[155] Y. Sun, S. Polani, F. Luo, S. Ott, P. Strasser, and F. Dionigi, "Advancements in cathode catalyst and cathode layer design for proton exchange membrane fuel cells," *Nature Communications*, vol. 12, no. 1, p. 5984, 2021.

[156] K. Malek, T. Mashio, and M. Eikerling, "Microstructure of Catalyst Layers in PEM Fuel Cells Redefined: A Computational Approach," *Electrocatalysis*, vol. 2, no. 2, pp. 141–157, 2011.

[157] W. Olbrich, T. Kadyk, U. Sauter, M. Eikerling, and J. Gostick, "Structure and conductivity of ionomer in PEM fuel cell catalyst layers: A model-based analysis," *Scientific Reports*, vol. 13, no. 1, p. 14127, 2023.

[158] M. Grandi, K. Mayer, M. Gatalo, G. Kapun, F. Ruiz-Zepeda, B. Marius, M. Gaberšček, and V. Hacker, "The Influence Catalyst Layer Thickness on Resistance Contributions of PEMFC Determined by Electrochemical Impedance Spectroscopy," *Energies*, vol. 14, no. 21, p. 7299, 2021.

[159] L. Zhao, H. Yuan, J. Xie, S. Jiang, X. Wei, W. Tang, P. Ming, and H. Dai, "Inconsistency evaluation of vehicle-oriented fuel cell stacks based on electrochemical impedance under dynamic operating conditions," *Energy*, vol. 265, p. 126162, 2023.

[160] N. Bevilacqua, T. Asset, M. Schmid, H. Markötter, I. Manke, P. Atanassov, and R. Zeis, "Impact of catalyst layer morphology on the operation of high temperature PEM fuel cells," *Journal of Power Sources Advances*, vol. 7, p. 100042, 2021.

[161] M. F. Mathias, J. Roth, J. Fleming, and W. Lehnert, "Diffusion media materials and characterisation," in *Handbook of Fuel Cells* (W. Vielstich, A. Lamm, H. A. Gasteiger, and H. Yokokawa, eds.), Wiley, 1 ed., 2010.

[162] J. P. Owejan, J. E. Owejan, W. Gu, T. A. Trabold, T. W. Tighe, and M. F. Mathias, "Water Transport Mechanisms in PEMFC Gas Diffusion Layers," *Journal of The Electrochemical Society*, vol. 157, no. 10, p. B1456, 2010.

[163] J. M. Morgan and R. Datta, "Understanding the gas diffusion layer in proton exchange membrane fuel cells. I. How its structural characteristics affect diffusion and performance," *Journal of Power Sources*, vol. 251, pp. 269–278, 2014.

[164] J. Wind, A. LaCroix, S. Braeuninger, P. Hedrich, C. Heller, and M. Schudy, "Metal bipolar plates and coatings," in *Handbook of Fuel Cells* (W. Vielstich, A. Lamm, H. A. Gasteiger, and H. Yokokawa, eds.), Wiley, 1 ed., 2010.

[165] G. O. Mepsted and J. M. Moore, "Performance and durability of bipolar plate materials," in *Handbook of Fuel Cells* (W. Vielstich, A. Lamm, H. A. Gasteiger, and H. Yokokawa, eds.), Wiley, 1 ed., 2010.

[166] F. A. de Bruijn, V. A. T. Dam, and G. J. M. Janssen, "Review: Durability and Degradation Issues of PEM Fuel Cell Components," *Fuel Cells*, vol. 8, no. 1, pp. 3–22, 2008.

[167] L. Liu, Y. Xing, Y. Li, Z. Fu, Z. Li, and H. Li, “Enhanced mechanical durability of perfluorosulfonic acid proton-exchange membrane based on a double-layer ePTFE reinforcement strategy,” *International Journal of Hydrogen Energy*, vol. 47, no. 67, pp. 29014–29026, 2022.

[168] N. F. Asri, T. Husaini, A. B. Sulong, E. H. Majlan, and W. R. W. Daud, “Coating of stainless steel and titanium bipolar plates for anticorrosion in PEMFC: A review,” *International Journal of Hydrogen Energy*, vol. 42, no. 14, pp. 9135–9148, 2017.

[169] K. Scott, “Mass transfer in flow fields,” in *Handbook of Fuel Cells* (W. Vielstich, A. Lamm, H. A. Gasteiger, and H. Yokokawa, eds.), Wiley, 1 ed., 2010.

[170] S. Shimpalee, S. Hirano, M. DeBolt, V. Lilavivat, J. W. Weidner, and Y. Khunatorn, “Macro-Scale Analysis of Large Scale PEM Fuel Cell Flow-Fields for Automotive Applications,” *Journal of The Electrochemical Society*, vol. 164, no. 11, pp. E3073–E3080, 2017.

[171] B. H. Lim, E. H. Majlan, W. R. W. Daud, T. Husaini, and M. I. Rosli, “Effects of flow field design on water management and reactant distribution in PEMFC: A review,” *Ionics*, vol. 22, no. 3, pp. 301–316, 2016.

[172] M. Ohring, *Engineering Materials Science*. Elsevier Science, 2014.

[173] T. Lochner, M. Perchthaler, F. Hnyk, D. Sick, J. P. Sabawa, and A. S. Bandarenka, “Analysis of the Capacitive Behavior of Polymer Electrolyte Membrane Fuel Cells during Operation,” *ChemElectroChem*, vol. 8, no. 1, pp. 96–102, 2021.

[174] X.-Z. Yuan, C. Song, H. Wang, and J. Zhang, *Electrochemical Impedance Spectroscopy in PEM Fuel Cells*. London: Springer London, 2010.

[175] A. J. Bard and L. R. Faulkner, *Electrochemical Methods: Fundamentals and Applications*. New York: Wiley, 2nd ed ed., 2001.

[176] A. S. Bandarenka, "Exploring the interfaces between metal electrodes and aqueous electrolytes with electrochemical impedance spectroscopy," *The Analyst*, vol. 138, no. 19, p. 5540, 2013.

[177] M. Urquidi-Macdonald, S. Real, and D. D. Macdonald, "Applications of Kramers—Kronig transforms in the analysis of electrochemical impedance data—III. Stability and linearity," *Electrochimica Acta*, vol. 35, no. 10, pp. 1559–1566, 1990.

[178] A. Weiß, S. Schindler, S. Galbiati, M. A. Danzer, and R. Zeis, "Distribution of Relaxation Times Analysis of High-Temperature PEM Fuel Cell Impedance Spectra," *Electrochimica Acta*, vol. 230, pp. 391–398, 2017.

[179] M. Schönleber, D. Klotz, and E. Ivers-Tiffée, "A Method for Improving the Robustness of linear Kramers-Kronig Validity Tests," *Electrochimica Acta*, vol. 131, pp. 20–27, 2014.

[180] X. Yuan, H. Wang, J. Colinsun, and J. Zhang, "AC impedance technique in PEM fuel cell diagnosis—A review," *International Journal of Hydrogen Energy*, vol. 32, no. 17, pp. 4365–4380, 2007.

[181] A. A. Kulikovsky, "PEM Fuel Cell Impedance at Open Circuit," *Journal of The Electrochemical Society*, vol. 163, no. 5, pp. F319–F326, 2016.

[182] M. Kondratenko and A. Kulikovsky, "Impedance Spectroscopy Study of the Dependence of High-temperature Polymer Electrolyte Membrane Fuel Cell Parameters on Current," *Fuel Cells*, vol. 18, no. 6, pp. 748–754, 2018.

[183] Y. Tsai, “Nonlinear least-squares analyses of complex impedance and admittance data for solid electrolytes,” *Solid State Ionics*, vol. 7, no. 2, pp. 129–139, 1982.

[184] E. Warburg, “Ueber das Verhalten sogenannter unpolarisirbarer Elektroden gegen Wechselstrom,” *Annalen der Physik*, vol. 303, no. 3, pp. 493–499, 1899.

[185] J. Huang, “Diffusion impedance of electroactive materials, electrolytic solutions and porous electrodes: Warburg impedance and beyond,” *Electrochimica Acta*, vol. 281, pp. 170–188, 2018.

[186] J. E. B. Randles, “Kinetics of rapid electrode reactions,” *Discussions of the Faraday Society*, vol. 1, p. 11, 1947.

[187] A. C. Lazanas and M. I. Prodromidis, “Electrochemical Impedance Spectroscopy-A Tutorial,” *ACS Measurement Science Au*, vol. 3, no. 3, pp. 162–193, 2023.

[188] A. Lasia, “The Origin of the Constant Phase Element,” *The Journal of Physical Chemistry Letters*, vol. 13, no. 2, pp. 580–589, 2022.

[189] H. J. Yang, D. Han, J. Kim, Y. H. Kim, and J. H. Bae, “Constant phase element affected by ion transport in nanoporous electrodes,” *Journal of Electroanalytical Chemistry*, vol. 922, p. 116766, 2022.

[190] S. M. Gateman, O. Gharbi, H. Gomes de Melo, K. Ngo, M. Turmine, and V. Vivier, “On the use of a constant phase element (CPE) in electrochemistry,” *Current Opinion in Electrochemistry*, vol. 36, p. 101133, 2022.

[191] C. L. Alexander, B. Tribollet, and M. E. Orazem, “Contribution of Surface Distributions to Constant-Phase-Element (CPE) Behavior: 1. Influence of Roughness,” *Electrochimica Acta*, vol. 173, pp. 416–424, 2015.

[192] C. L. Alexander, B. Tribollet, and M. E. Orazem, “Contribution of Surface Distributions to Constant-Phase-Element (CPE) Behavior: 2. Capacitance,” *Electrochimica Acta*, vol. 188, pp. 566–573, 2016.

[193] C. L. Alexander, B. Tribollet, V. Vivier, and M. E. Orazem, “Contribution of Surface Distributions to Constant-Phase-Element (CPE) Behavior: 3. Adsorbed Intermediates,” *Electrochimica Acta*, vol. 251, pp. 99–108, 2017.

[194] C. Gerling, M. Hanauer, U. Berner, and K. Andreas Friedrich, “PEM Single Cells under Differential Conditions: Full Factorial Parameterization of the ORR and HOR Kinetics and Loss Analysis,” *Journal of The Electrochemical Society*, vol. 169, no. 1, p. 014503, 2022.

[195] P. Moçotéguy, B. Ludwig, D. Beretta, and T. Pedersen, “Study of the impact of water management on the performance of PEMFC commercial stacks by impedance spectroscopy,” *International Journal of Hydrogen Energy*, vol. 45, no. 33, pp. 16724–16737, 2020.

[196] U. Cano-Castillo, A. Ortiz, S. Manzo, L. G. Arriaga, and G. Orozco, “Parameter Changes During Gradual Flooding of a PEM Fuel Cell through EIS Studies,” *ECS Transactions*, vol. 3, no. 1, pp. 931–939, 2006.

[197] B. Ghorbani, J. DeVaal, G. Afonso, and K. Vijayaraghavan, “Use of reduced-voltage EIS to establish a relation between oxygen concentration and EIS responses of large commercial PEM fuel cell modules,” *International Journal of Hydrogen Energy*, p. S0360319923021791, 2023.

[198] H. Gasteiger, J. Panels, and S. Yan, “Dependence of PEM fuel cell performance on catalyst loading,” *Journal of Power Sources*, vol. 127, no. 1-2, pp. 162–171, 2004.

[199] B. M. Stühmeier, M. R. Pietsch, J. N. Schwämmlein, and H. A. Gasteiger, “Pressure and Temperature Dependence of the Hydrogen Oxidation and Evolution Reaction Kinetics on Pt Electrocatalysts via PEMFC-based Hydrogen-Pump Measurements,” *Journal of The Electrochemical Society*, vol. 168, no. 6, p. 064516, 2021.

[200] S. Dierickx, A. Weber, and E. Ivers-Tiffée, “How the distribution of relaxation times enhances complex equivalent circuit models for fuel cells,” *Electrochimica Acta*, vol. 355, p. 136764, 2020.

[201] A. M. Dhirde, N. V. Dale, H. Salehfar, M. D. Mann, and T.-H. Han, “Equivalent Electric Circuit Modeling and Performance Analysis of a PEM Fuel Cell Stack Using Impedance Spectroscopy,” *IEEE Transactions on Energy Conversion*, vol. 25, no. 3, pp. 778–786, 2010.

[202] “Environmental Testing - Part 3-6: Supporting Documentation and Guidance - Confirmation of the Performance of Temperature/Humidity Chambers (IEC 60068-3-6:2018),” 2018.

[203] Angelantoni Test Technologies, “New Climatic and Thermostatic Chambers,” 2020.

[204] CTS GmbH, “CTS-Temperature Test Chambers,” 2020.

[205] D. Sonntag, “Important new values of the physical constants of 1986, vapor pressure formulations based on the ITS-90, and psychrometer formulae,” *5*, vol. 70, pp. 340–344, 1990.

[206] S. Dutta, S. Shimpalee, and J. Van Zee, “[No title found],” *Journal of Applied Electrochemistry*, vol. 30, no. 2, pp. 135–146, 2000.

[207] J. Zhang, ed., *PEM Fuel Cell Electrocatalysts and Catalyst Layers: Fundamentals and Applications*. London: Springer London, 2008.

[208] D. Malevich, E. Halliop, B. Peppley, J. Pharoah, and K. Karan, "Effect of Relative Humidity on Electrochemical Active Area and Impedance Response of PEM Fuel Cell," *ECS Transactions*, vol. 16, no. 2, pp. 1763–1774, 2008.

[209] K. R. Harris and L. A. Woolf, "Pressure and temperature dependence of the self diffusion coefficient of water and oxygen-18 water," *Journal of the Chemical Society, Faraday Transactions 1: Physical Chemistry in Condensed Phases*, vol. 76, no. 0, p. 377, 1980.

[210] H. Chen, B. Liu, R. Liu, Q. Weng, T. Zhang, and P. Pei, "Optimal interval of air stoichiometry under different operating parameters and electrical load conditions of proton exchange membrane fuel cell," *Energy Conversion and Management*, vol. 205, p. 112398, 2020.

[211] L. Xia, C. Zhang, M. Hu, S. Jiang, C. S. Chin, Z. Gao, and Q. Liao, "Investigation of parameter effects on the performance of high-temperature PEM fuel cell," *International Journal of Hydrogen Energy*, vol. 43, no. 52, pp. 23441–23449, 2018.

[212] J. P. Sabawa and A. S. Bandarenka, "Investigation of degradation mechanisms in PEM fuel cells caused by low-temperature cycles," *International Journal of Hydrogen Energy*, vol. 46, no. 29, pp. 15951–15964, 2021.

[213] M. Oszcipok, D. Riemann, U. Kronenwett, M. Kreideweis, and M. Zedda, "Statistic analysis of operational influences on the cold start behaviour of PEM fuel cells," *Journal of Power Sources*, vol. 145, no. 2, pp. 407–415, 2005.

[214] Y. Wang, “Analysis of the Key Parameters in the Cold Start of Polymer Electrolyte Fuel Cells,” *Journal of The Electrochemical Society*, vol. 154, no. 10, p. B1041, 2007.

[215] Y. Li, Z. Zheng, X. Chen, Y. Liu, M. Liu, J. Li, D. Xiong, and J. Xu, “Carbon corrosion behaviors and the mechanical properties of proton exchange membrane fuel cell cathode catalyst layer,” *International Journal of Hydrogen Energy*, vol. 45, no. 43, pp. 23519–23525, 2020.

[216] C. Francia, V. S. Ijeri, S. Specchia, and P. Spinelli, “Estimation of hydrogen crossover through Nafion® membranes in PEMFCs,” *Journal of Power Sources*, vol. 196, no. 4, pp. 1833–1839, 2011.

[217] Q. Tang, B. Li, D. Yang, P. Ming, C. Zhang, and Y. Wang, “Review of hydrogen crossover through the polymer electrolyte membrane,” *International Journal of Hydrogen Energy*, vol. 46, no. 42, pp. 22040–22061, 2021.

[218] E. Cho, J.-J. Ko, H. Y. Ha, S.-A. Hong, K.-Y. Lee, T.-W. Lim, and I.-H. Oh, “Characteristics of the PEMFC Repetitively Brought to Temperatures below 0°C,” *Journal of The Electrochemical Society*, vol. 150, no. 12, p. A1667, 2003.

[219] J. Zhang, C. Song, J. Zhang, R. Baker, and L. Zhang, “Understanding the effects of back-pressure on PEM fuel cell reactions and performance,” *Journal of Electroanalytical Chemistry*, vol. 688, pp. 130–136, 2013.

[220] M. G. Waller, M. R. Walluk, and T. A. Trabold, “Performance of high temperature PEM fuel cell materials. Part 1: Effects of temperature, pressure and anode dilution,” *International Journal of Hydrogen Energy*, vol. 41, no. 4, pp. 2944–2954, 2016.

[221] A. Huth, B. Schaar, and T. Oekermann, “A “proton pump” concept for the investigation of proton transport and anode kinetics in proton exchange membrane fuel cells,” *Electrochimica Acta*, vol. 54, no. 10, pp. 2774–2780, 2009.

[222] K. C. Neyerlin, W. Gu, J. Jorne, and H. A. Gasteiger, “Study of the Exchange Current Density for the Hydrogen Oxidation and Evolution Reactions,” *Journal of The Electrochemical Society*, vol. 154, no. 7, p. B631, 2007.

[223] S. Watzele, L. Katzenmeier, J. Sabawa, B. Garlyyev, and A. Bandarenka, “Temperature Dependences of the Double Layer Capacitance of Some Solid / Liquid and Solid / Solid Electrified Interfaces. An Experimental Study,” *Electrochimica Acta*, vol. 391, p. 138969, 2021.

[224] L. Wu, Z. Zhang, J. Ran, D. Zhou, C. Li, and T. Xu, “Advances in proton-exchange membranes for fuel cells: An overview on proton conductive channels (PCCs),” *Physical Chemistry Chemical Physics*, vol. 15, no. 14, p. 4870, 2013.

[225] P. Knauth and M. L. Di Vona, “Hydration and Proton Conductivity of Ionomers: The Model Case of Sulfonated Aromatic Polymers,” *Frontiers in Energy Research*, vol. 2, p. 50, 2014.

[226] D. A. Caulk and D. R. Baker, “Heat and Water Transport in Hydrophobic Diffusion Media of PEM Fuel Cells,” *Journal of The Electrochemical Society*, vol. 157, no. 8, p. B1237, 2010.

[227] W. Xing, M. Yin, Q. Lv, Y. Hu, C. Liu, and J. Zhang, “Oxygen Solubility, Diffusion Coefficient, and Solution Viscosity,” in *Rotating Electrode Methods and Oxygen Reduction Electrocatalysts*, pp. 1–31, Elsevier, 2014.

[228] J. W. Darbyshire and J. B. Lawrence, “An Electrochemically based Electrical Fuel Cell Model. In An Electrochemically based Electrical Fuel Cell Model,” *AUPEC 2004*, 2004.

[229] T. Hoshiko, H. Nakajima, T. Konomi, T. Kitahara, and S. Kita, “Estimation of Water Layer Thickness Adjacent to the Cathode Catalyst Layer of a PEFC (Analysis Using Electrochemical Impedance Spectroscopy),” *ECS Transactions*, vol. 16, no. 2, pp. 2117–2123, 2008.

[230] N. Nonoyama, S. Okazaki, A. Z. Weber, Y. Ikogi, and T. Yoshida, “Analysis of Oxygen-Transport Diffusion Resistance in Proton-Exchange-Membrane Fuel Cells,” *Journal of The Electrochemical Society*, vol. 158, no. 4, p. B416, 2011.

[231] W. Aït-Idir, P. Wu, R. Sgarbi, Q. Labarde, S. Touhami, M. Daoudi, A. El kaddouri, J.-C. Perrin, J. Dillet, C. Marty, F. Micoud, M. Chatenet, O. Lottin, and J. Mainka, “Oxygen diffusion impedance in proton exchange membrane fuel cells – insights into electrochemical impedance spectra and equivalent electrical circuit modeling,” *Electrochimica Acta*, vol. 472, p. 143430, 2023.

[232] L. Zhang, C. Ma, and S. Mukerjee, “Oxygen reduction and transport characteristics at a platinum and alternative proton conducting membrane interface,” *Journal of Electroanalytical Chemistry*, vol. 568, pp. 273–291, 2004.

[233] Z. Fang, M. S. Lee, J. Y. Kim, J. H. Kim, and T. F. Fuller, “The Effect of Carbon Support Surface Functionalization on PEM Fuel Cell Performance, Durability, and Ionomer Coverage in the Catalyst Layer,” *Journal of The Electrochemical Society*, vol. 167, no. 6, p. 064506, 2020.

[234] W. Grove, “XXIV. *On voltaic series and the combination of gases by platinum*,” *The London, Edinburgh, and Dublin Philosophical Magazine and Journal of Science*, vol. 14, no. 86-87, pp. 127–130, 1839.

[235] G. G. Scherer, “Fuel Cell Types and Their Electrochemistry,” in *Encyclopedia of Sustainability Science and Technology* (R. A. Meyers, ed.), pp. 3872–3886, New York, NY: Springer New York, 2012.

[236] S. H. Kim, Y. B. Kum, K. C. Lee, T. W. Lim, J. C. Park, J. Ferro, and D. M. Flanaghan, “Development of Hyundai’s Tucson FCEV,” in *SAE 2005 World Congress & Exhibition*, pp. 2005–01–0005, 2005.

[237] J. Wu, X. Z. Yuan, J. J. Martin, H. Wang, J. Zhang, J. Shen, S. Wu, and W. Merida, “A review of PEM fuel cell durability: Degradation mechanisms and mitigation strategies,” *Journal of Power Sources*, vol. 184, no. 1, pp. 104–119, 2008.

[238] A. B. LaConti, M. Hamdan, and R. C. McDonald, “Mechanisms of membrane degradation,” in *Handbook of Fuel Cells* (W. Vielstich, A. Lamm, H. A. Gasteiger, and H. Yokokawa, eds.), Wiley, 1 ed., 2010.

[239] M. Zatoń, J. Rozière, and D. J. Jones, “Current understanding of chemical degradation mechanisms of perfluorosulfonic acid membranes and their mitigation strategies: A review,” *Sustainable Energy & Fuels*, vol. 1, no. 3, pp. 409–438, 2017.

[240] S. Kreitmeier, M. Michiardi, A. Wokaun, and F. N. Büchi, “Factors determining the gas crossover through pinholes in polymer electrolyte fuel cell membranes,” *Electrochimica Acta*, vol. 80, pp. 240–247, 2012.

[241] R. McDonald, C. Mittelsteadt, and E. Thompson, “Effects of Deep Temperature Cycling on Nafion® 112 Membranes and Membrane Electrode Assemblies,” *Fuel Cells*, vol. 4, no. 3, pp. 208–213, 2004.

[242] D. Schonvogel, M. Rastedt, P. Wagner, M. Wark, and A. Dyck, “Impact of Accelerated Stress Tests on High Temperature PEMFC Degradation,” *Fuel Cells*, vol. 16, no. 4, pp. 480–489, 2016.

[243] P. Xu and S. Xu, “A Progress Review on Gas Purge for Enhancing Cold Start Performance in PEM Fuel Cell,” in *WCX World Congress Experience*, pp. 2018–01–1312, 2018.

[244] E. Schießwohl, T. von Unwerth, F. Seyfried, and D. Brüggemann, “Experimental investigation of parameters influencing the freeze start ability of a fuel cell system,” *Journal of Power Sources*, vol. 193, no. 1, pp. 107–115, 2009.

[245] C. Y. Wang, X. G. Yang, Y. Tabuchi, and F. Kagami, “Cold-start durability of membrane-electrode assemblies,” in *Handbook of Fuel Cells* (W. Vielstich, A. Lamm, H. A. Gasteiger, and H. Yokokawa, eds.), Wiley, 1 ed., 2010.

[246] Z. Wan, H. Chang, S. Shu, Y. Wang, and H. Tang, “A Review on Cold Start of Proton Exchange Membrane Fuel Cells,” *Energies*, vol. 7, no. 5, pp. 3179–3203, 2014.

[247] P. Liu and S. Xu, “A Progress Review on Heating Methods and Influence Factors of Cold Start for Automotive PEMFC System,” in *WCX SAE World Congress Experience*, pp. 2020–01–0852, 2020.

[248] V. O. Mittal, H. Russell Kunz, and J. M. Fenton, “Is H[sub 2]O[sub 2] Involved in the Membrane Degradation Mechanism in PEMFC?,” *Electrochemical and Solid-State Letters*, vol. 9, no. 6, p. A299, 2006.

[249] H. S. Casalongue, S. Kaya, V. Viswanathan, D. J. Miller, D. Friebel, H. A. Hansen, J. K. Nørskov, A. Nilsson, and H. Ogasawara, “Direct observation of the oxygenated species during oxygen reduction on a platinum fuel cell cathode,” *Nature Communications*, vol. 4, no. 1, p. 2817, 2013.

[250] L. Ghassemzadeh and S. Holdcroft, “Quantifying the Structural Changes of Perfluorosulfonated Acid Ionomer upon Reaction with Hydroxyl Radicals,” *Journal of the American Chemical Society*, vol. 135, no. 22, pp. 8181–8184, 2013.

[251] A. Pozio, R. Silva, M. De Francesco, and L. Giorgi, “Nafion degradation in PEFCs from end plate iron contamination,” *Electrochimica Acta*, vol. 48, no. 11, pp. 1543–1549, 2003.

[252] T. Zhang, P. Wang, H. Chen, and P. Pei, “A review of automotive proton exchange membrane fuel cell degradation under start-stop operating condition,” *Applied Energy*, vol. 223, pp. 249–262, 2018.

[253] F. H. Garzon and F. A. Uribe, “Effects of contaminants on catalyst activity,” in *Handbook of Fuel Cells* (W. Vielstich, A. Lamm, H. A. Gasteiger, and H. Yokokawa, eds.), Wiley, 1 ed., 2010.

[254] K. G. Gallagher, R. M. Darling, and T. F. Fuller, “Carbon-support corrosion mechanisms and models,” in *Handbook of Fuel Cells* (W. Vielstich, A. Lamm, H. A. Gasteiger, and H. Yokokawa, eds.), Wiley, 1 ed., 2010.

[255] J. P. Meyers and R. M. Darling, “Model of Carbon Corrosion in PEM Fuel Cells,” *Journal of The Electrochemical Society*, vol. 153, no. 8, p. A1432, 2006.

[256] Y. Shao, G. Yin, and Y. Gao, “Understanding and approaches for the durability issues of Pt-based catalysts for PEM fuel cell,” *Journal of Power Sources*, vol. 171, no. 2, pp. 558–566, 2007.

[257] S. Huo, K. Jiao, and J. W. Park, “On the water transport behavior and phase transition mechanisms in cold start operation of PEM fuel cell,” *Applied Energy*, vol. 233–234, pp. 776–788, 2019.

[258] Q. Yan, H. Toghiani, Y.-W. Lee, K. Liang, and H. Causey, “Effect of sub-freezing temperatures on a PEM fuel cell performance, startup and fuel cell components,” *Journal of Power Sources*, vol. 160, no. 2, pp. 1242–1250, 2006.

[259] F. Haimerl, J. P. Sabawa, T. A. Dao, and A. S. Bandarenka, “Spatially Resolved Electrochemical Impedance Spectroscopy of Automotive PEM Fuel Cells,” *ChemElectroChem*, vol. 9, no. 10, 2022.

[260] F. Haimerl, S. Kumar, M. Heere, and A. S. Bandarenka, “Electrochemical impedance spectroscopy of PEM fuel cells at low hydrogen partial pressures: Efficient cell tests for mass production,” *Industrial Chemistry & Materials*, vol. 2, no. 1, pp. 132–140, 2024.